THE ROLE OF HYDROGEN IN THE ENVIRONMENTAL FAILURE OF HIGH STRENGTH ALUMINIUM ALLOYS

A Thesis submitted for the degree of

Doctor of Philosophy

in the University of London

by

Leontios Christodoulou

Department of Metallurgy and Materials Science,
Imperial College of Science and Technology
London, SW7 2AZ.

TO MY PARENTS.

ABSTRACT

An investigation into the effect of exposure of Al-Zn-Mg alloys to water vapour has shown that hydrogen, produced by the reaction is absorbed by both the alloy grain boundaries and matrix. The amount of absorbed hydrogen depends on the local chemistry at the metal/oxide interface and is influenced by alloying additions. Attainment of a critical concentration of dissolved hydrogen in the boundaries leads to brittle intergranular fracture on the subsequent application of stress. Attainment of a critical hydrogen concentration in the matrix leads to transgranular cleavage fracture.

Depending upon the alloy composition and heat treatment bubbles of gaseous hydrogen can be formed at suitable sites within the alloys such as grain boundary particles. The formation of grain boundary bubbles reduces embrittlement by reducing the local concentration of dissolved hydrogen.

It is proposed that the interaction of stress and environmental variables with the above criteria governsthe environmental failure of Al-Zn-Mg alloys in aqueous and water vapour containing environments. It is suggested that such failures are hydrogen embrittlement dominated.

TABLE OF CONTENTS

	Page
ABSTRACT	3
CONTENTS	4
1. INTRODUCTION	7
2. LITERATURE REVIEW	9
2.1. Alloy Microstructure	10
2.2. Mechanical Strength and Deformation Behaviour.	13
2.3. Quaternary Alloying Additions.	14
2.4. Environment Assisted Fracture.	15
2.5. Effect of Metallurgical Variables on Environment-Sensitive Behaviour.	17
2.5.1. Microstructure	17
2.5.2. Alloy content.	17
2.5.3. Solution heat treatment temperature	19
2.5.4. Quench rate	21
2.5.5. Ageing	23
2.6. Mechanical Aspects of Environmental Failure	25
2.6.1. Stress effects	25
2.6.2. Strain rate	32
2.7. Environmental Aspects of Failure	38
2.7.1. Oxide films	38
2.7.2. Aluminium-water reaction	42
2.7.3. Direct evidence of hydrogen entry into Al-Zn-Mg alloys in aqueous systems	51
2.7.4. Gaseous environments	53
2.7.5. Organic liquids	55
2.7.6. Electrical potential	55
2.7.7. Stress corrosion crack growth in hydrogen atmospheres	59
2.8. Pre-exposure Embrittlement	60
2.9. Electron Irradiation Induced Corrosion	63
3. EXPERIMENTAL PROCEDURE	66
3.1. Alloys and Heat Treatments	66
3.2. Exposure Tests	66
3.3. Cathodic Charging	68
3.4. Mechanical Testing	68

		Page
3.5.	C.T.E.M. Sample Preparation Techniques	68
3.6.	Electron Metallography	69
3.7.	"In-situ" High Voltage Electron Microscopy	71
3.7.1.	Environment	72
3.7.2.	Temperature	75
3.7.3.	Electron flux density	76
3.7.4.	Image recording	76
3.7.5.	Contamination	77
3.7.6.	In-situ straining	77
3.8.	Bulk Surface Studies	78
4.	RESULTS	81
4.1.	Exposure Tests	81
4.1.1.	Isochronally aged 6/3 base alloy at 70°C	81
4.1.2.	Isothermally aged high purity 6/3 base alloy at 120°C: solution treated condition	85
4.1.3.	Isothermally aged high purity 6/3 base alloy at 120°C: aged condition	95
4.1.4.	Isothermally aged 6/3 Cu alloy	104
4.1.5.	Isothermally aged 6/3 Cr alloy	125
4.2.	Cathodic Charging	131
4.3.	"In-situ" Electron Microscopy	131
4.3.1.	6/3 base alloy	144
4.3.2.	6/3 Cu alloy	153
4.3.3.	6/3 Cr alloy	158
4.3.4.	"In-situ" straining experiments	175
4.4.	Surface Reaction	182
4.4.1.	Reaction of Al-Zn-Mg (Cu/Cr) alloys with water vapour	182
4.4.2.	Surface oxide on tensile samples exposed to moist environments	221
5.	DISCUSSION	224
5.1.	Proposed Mechanism of Failure	224
5.2.	Discussion of results: Surface reaction during exposure	230
5.3.	Pre-exposure Embrittlement Tests	236
5.3.1.	Isochronal exposure: 6/3 base alloy	236
5.3.2.	Isothermal exposure 6/3 base alloy	239
5.3.3.	6/3 Cu alloy	249
5.3.4.	6/3 Cr alloy	251
5.3.5.	Cathodic charging	253

	Page
5.4. "In-situ" observations	254
5.4.1. Displacement damage	254
5.4.2. Irradiation induced temperature rise	257
5.4.3. Helium injection	258
5.4.4. Ionisation damage	259
5.4.5. Radiation damage in the oxide and its contribution to the accelerated surface reaction observed.	259
5.4.6. Proposed mechanism for the radiation enhanced surface reaction	262
5.4.7. Surface reaction kinetics	266
5.4.8. Deductions from the "in-situ" reaction experiments	267
5.4.9. Discussion of the straining stage "in-situ" experiments	269
5.5. Extension of the Proposed Mechanism to S.C.C.	271
5.5.1. Metallurgical effects	272
5.5.2. Stress effects	274
5.5.3. The role of oxide films	275
6. CONCLUSIONS AND SUGGESTIONS FOR FURTHER WORK	276
ACKNOWLEDGEMENTS	281
REFERENCES	282

INTRODUCTION

The mechanism of environment-sensitive fracture in high strength aluminium alloys is subject to controversy at the present time. In spite of the very extensive past research into the metallurgical, mechanical and environmental aspects of the phenomenon there is no consensus as to the mechanism involved.

Two basic and fundamentally different mechanisms of failure have been advanced. The first, and perhaps most widely accepted, identifies the process of failure as one of a highly localised anodic dissolution reaction under the combined influence of stress and environment. The alternative model postulates that the phenomenon is controlled by a hydrogen embrittlement event. Hydrogen is believed to be generated as a consequence of the alloy/environment interaction, absorbed into the alloy and be responsible for the brittle fracture event.

Many variations on the basic theme of electrochemical dissolution introduced by E.H. Dix in the "1949 Edward DeMille Campbell Memorial Lecture" (Trans. A.S.M. Vol. 42 p.1057 1950) have been presented in the intervening years and many workers have interpreted their results via the dissolution control models. These vary from the metallurgically biased preferential dissolution of grain boundary precipitates (62) or precipitate free zones (14) through oxide film rupture and dissolution (86-90), including effects of coplanar slip (30, 31) models, to theories of stress (85) or strain (86) assisted dissolution. Similarly a range of hydrogen embrittlement theories have been extended to Al-Zn-Mg alloys from other systems covering such concepts as hydrogen adsorption (214) hydrogen absorption (92) and void pressurisation (168).

A view that is rapidly gaining support among many workers is the one that considers that both dissolution and hydrogen mechanisms (with the appropriate modifications for any one system under consideration) can operate either in parallel or in competition. Certainly the available literature would not contradict such a view.

The aims of the current study were to examine the conditions of generation, entry and effect of hydrogen on the environment-sensitive fracture event in a water vapour environment and to establish the mechanism of failure. It was further proposed to assess the potential of any developed mechanism to explain other results reported in the literature.

The study has been confined to three alloys based on the Al-Zn-Mg system (7000 series alloys). A high purity Al-6%Zn-3%Mg alloy was examined together with two quaternary compositions, based on the above, containing copper and chromium additions respectively.

The investigation has been largely based on electron microscopical techniques. Both standard and specialised transmission electron microscopy techniques were employed to study the alloy/environment interaction. In particular, "in-situ" high voltage electron microscopy was used extensively to monitor directly the reaction of the experimental alloys with water vapour, both in the presence and absence of stress. The technique was shown to be a most powerful tool of investigation and furnished direct evidence of hydrogen penetration into Al-Zn-Mg alloys.

Susceptibility to embrittlement was assessed by extensive mechanical testing of samples exposed to water vapour and fractographic studies using high resolution scanning electron microscopy.

On the basis of the presented results a model of failure, derived from previous proposals (42,77), was developed. In its basic form it is capable of explaining many of the observed phenomena. It indicates that an absorbed hydrogen embrittlement mechanism can satisfactorily explain the environmental failure behaviour of Al-Zn-Mg alloys under most conditions.

2. LITERATURE REVIEW

The literature on the environment sensitive failure of high strength aluminium alloys (H.S.A.A.) is extensive and has been comprehensively reviewed (1, 2, 3, 4, 5, 6). In the presence of these recent and detailed reviews it would serve little purpose to present an extended literature review here. It is proposed instead, to generally confine this review to specific topics with immediate relevance to the experimental techniques and results whilst still employing the wealth of information available in the overall discussion. Throughout this review it will be assumed to some extent that the reader is familiar with the basic concepts of stress corrosion cracking behaviour of the Al-Zn-Mg system. More specialised topics however, such as "in-situ" High Voltage Electron Microscopy will, where appropriate, be discussed in more detail.

The contributions to the literature may be broadly divided into three main categories:

(1) Those dealing with the metallurgical variables such as alloy composition and microstructure (3,5).

(2) Those dealing with the mechanical aspects of the phenomenon both on the macro and micro scale (e.g. applied stress and crack tip stress intensity) (1, 2, 6).

(3) Perhaps the most voluminous, those dealing with environmental effects (e.g. solution chemistry, applied potential, etc.) (1, 2, 4, 6).

In the following literature review an outline of all of the above will be given. In particular the generation of hydrogen as a result of the environment/stress/alloy interaction and its subsequent absorption/evolution will be examined.

2.1. Alloy Microstructure

The mechanical properties of the Al-Zn-Mg system are derived from a precipitation hardening sequence of (7)

Supersaturated Solid Solution → G.P. Zones → Intermediate Phase →

Equilibrium phase.

Despite copious literature the exact precipitation sequence and phases present at any temperature are in dispute (8,9). In the more commercially important alloys (those containing up to 6% Zn and 3% Mg) the sequence of precipitation is generally accepted as being (7)

Supersaturated Solid Solution → G.P. Zones → η' → $\eta(MgZn_2)$ → $T(Mg_3Zn_3Al_2)$

The Guinier-Preston zones are spherical or elliptical segregations of Mg and Zn of a size between 20-35A. Their presence has been reported by many workers either as a result of direct or indirect measurements (7,10,12,13,14,15,11). At low temperatures (22°C) the presence of two types of zones has been suggested (16). On continued ageing the zones are replaced by platelets or rods of η' (7,11,8,17,18,19). The orientation relationship between the η' and matrix is given as (17)

$$(0001)_{\eta'}//(1\bar{1}1)_{Al} \cdot (10\bar{1}0)_{\eta'}//(110)_{Al}$$

The structure of η' is hexagonal and the suggested composition is given as $Mg_4Zn_{11}Al$ (17).

The equilibrium η ($MgZn_2$) phase is formed by transformation from η' (8) and also exhibits a hexagonal structure. A large number of variants have been reported (7,8,9).

η	Al	η	Al
(100)	(001)	(001)	(110)
(001)	$(1\bar{1}\bar{1})$	(100)	(110)
(001)	$(1\bar{1}\bar{1})$	(110)	(110)
(001)	(110)	$(\bar{1}20)$	$(1\bar{1}\bar{1})$
$(\bar{1}20)$	$(1\bar{1}\bar{1})$	(302)	(110)
$(\bar{1}20)$	$(1\bar{1}\bar{1})$	(201)	$(1\bar{1}2)$
$(\bar{1}20)$	$(1\bar{1}\bar{1})$	(104)	(110)
$(\bar{1}20)$	$(1\bar{1}2)$	(001)	$(31\bar{1})$
$(\bar{1}20)$	(001)	(001)	(110)

The T phase (actual composition $(AlZn)_{49}Mg_{32}$ and not the $Zn_3Mg_3Al_2$ commonly referred to (7)) forms only during slow cooling from the

solution treatment temperatures. An intermediate T' phase has also been discussed by some workers (7,9,11,20,21). No reports of T phase precipitates have been made regarding material quenched and aged in the temperature range of 100-150°C.

Grain boundary precipitation occurs very rapidly on ageing in quenched Al-Zn-Mg alloys. Only the equilibrium η ($MgZn_2$) or T ($(AlZn)_{49}Mg_{32}$) phases are formed (22). It is possible for nucleation to occur during the quench, leading to a bi-modal precipitate size distribution of grain boundary particles (22). The size and density of the precipitates is a function of grain boundary type. Unwin and Nicholson (22) found that the nucleation density was related to the deviation from boundary coincidence. Few particles were observed at very low angle (<2°) boundaries or in high angle boundaries where the misorientation was close to a coincidence site lattice relationship. The greatest number of particles were found on random high angle boundaries.

The growth of the grain boundary precipitates involves the cooperative transport of solute along the boundary and diffusion from the adjacent matrix (21,23). Butler and Swann (23) using a High Voltage Electron Microscope were able to show conclusively that the size and density of the grain boundary precipitates was insensitive to the presence of excess vacancy defects. They concluded, along with Unwin and Nicholson, that the differences in the grain boundary precipitate nucleation rate and initial growth between different solution heat treatment temperatures are due to changes in the level of solute segregation.

The development of grain boundary precipitates is associated with the formation of precipitate free zones (P.F.Z.) adjacent to the grain boundaries. Considerable interest has been expressed in the origin of these zones (15,24,25,26). P.F.Z.s in rapidly quenched material are formed as a result of vacancy diffusion and annihilation at grain boundaries. The loss of excess vacancies to the boundary from the immediately surrounding matrix gives rise to a vacancy concentration profile. The extent of the vacancy depletion depends on the solution heat treatment temperature and the quench rate (15) (Figure 2.1). Since the nucleation of G.P. zones, at any temperature, below the G.P. solvus (25) is dependent on the existence of a critical concentration of excess vacancies, precipitation will not occur in the zones adjacent to the grain boundaries. Due to the loss of the vacancies to the boundary, these sites are not sufficiently vacancy supersaturated. The resulting precipitate

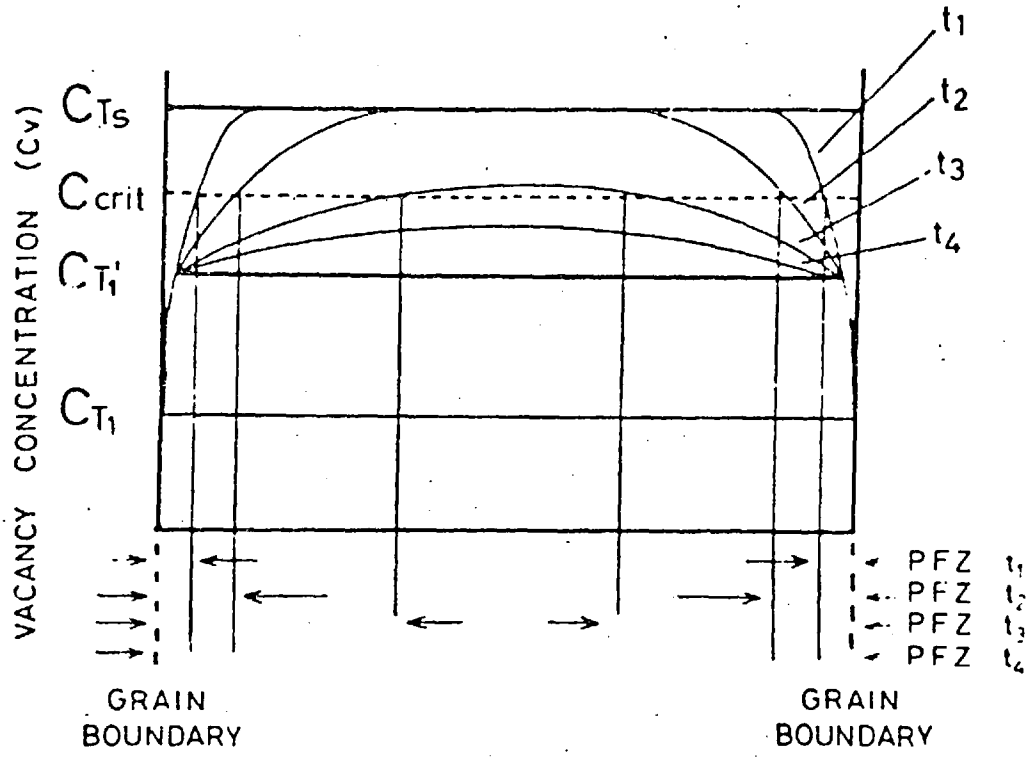


Figure 2.1. Schematic representation of the vacancy concentration profiles and subsequent P.F.Z. widths after various quench interruption times. (After Unwin et al (24))

C_{crit} = critical vacancy concentration to nucleate precipitates.

C_{T_s} = equilibrium vacancy concentration at the solution treatment temperature.

C_{T_1} = equilibrium vacancy concentration at the quench. interruption temperature.

C_{T_1} = equilibrium vacancy concentration at the ageing temperature.

For short interruption times t_1 and t_2 a narrow P.F.Z. is formed but this widens with increasing holding time until at interruption time t_4 C_{crit} is not exceeded and only heterogeneous nucleation occurs.

free zone is solute supersaturated. On subsequent ageing this solute diffuses to the grain boundary (20,21,22,23) and contributes to the growth of the grain boundary precipitates. The solute content of the P.F.Z. therefore in a quenched and aged sample should vary with ageing time and temperature.

In slowly cooled or quench interrupted samples a solute profile is established in addition to the vacancy profile. Under these conditions the solute diffuses to the boundary and is precipitated out as large grain boundary precipitates. Thus a solute depleted zone is formed. The width of the P.F.Z. is determined by the type of grain boundary present via the effect the latter has on the growth of the grain boundary precipitates. The exact mechanism of solute-vacancy interaction is in dispute (25,26) but both of the advanced models arrive at the same qualitative conclusions. With the advent of microanalysis techniques many workers (21,11,27,28) have examined the P.F.Z. of Al-Zn-Mg alloys using X-ray microanalysis and energy loss spectroscopy, and the results are in agreement with the ideas of Lorimer et al (26) and Jacobs and Pashley et al (25). Solute depletion as a result of quench interruption and ageing has been found.

2.2. Mechanical Strength and Deformation Behaviour

Peak strength in the Al-Zn-Mg system occurs with a microstructure consisting predominantly of G.P. zones mixed with η', η being present at the grain boundaries (1,2,3). This corresponds to a heat treatment of rapid quench from the single phase region and subsequent ageing at 120^{o}C for 25 hours (T6 temper).

It is a common observation that during deformation of the peak strength microstructure slip is concentrated in narrow bands. (16,29,30, 31,32). Dislocation motion involves the shearing of the matrix precipitates (G.P. zones and η'). Planar slip is developed on ageing; the as quenched structure exhibits a fairly homogeneous distribution of dislocations. Overaged microstructures revert to a less heterogeneous deformation behaviour ("wavy"slip)

Preferential deformation has not been found to occur in the P.F.Z. (16,30,29,32). High fracture toughness is favoured by a low yield stress and is associated with high proportions of transgranular fracture. (33,34). It is insensitive to the width of the P.F.Z. The proportion of intergranular fracture increases with increasing area fraction of

grain boundary precipitate. The intercrystalline fracture surfaces are dimpled indicating ductile failure (33,34). The proportion of intergranular fracture increases with increasing grain size (35).

2.3. Quaternary Alloy additions

The minor alloying elements added to the Al-Zn-Mg alloys can have two effects;
(a) Form intermetallic particles which pin grain boundaries and stabilise the wrought structure (i.e. reduce recrystallisation and severely inhibit grain growth), and/or
(b) Affect the precipitation of the second phase by altering the kinetics and morphology of the precipitation sequence.

Elements in group (a) include Cr, Mn, and Zr but both Cr and Mn give rise to heterogeneous second phase (η) precipitation, the intermetallic particles acting as favourable sites for nucleation (36,37,38). Zr additions produce more homogeneous dispersoids and result in higher fracture toughness (39,40). Less of the original cast structure is retained in Zr containing alloys (41). Fracture toughness is also increased if impurities such as Fe and Si, normally present in commercial alloys, are kept to a minimum (3,4,39).

It is interesting to note that small additions of In and Cd (<0.01 at%) give rise to grain boundary embrittlement of Al-Zn-Mg alloys (36). The crack path was found to run "along the precipitates on the grain boundary" and within the P.F.Z. (cf. S.C.C. cracks). No additional precipitates were found and the author concluded that embrittlement was caused by grain boundary segregation by these elements (36). Embrittlement was insensitive to heat treatment.

The most notable minor alloying addition belonging to group (b) is copper. Copper additions are made to the majority of commercial alloys and, provided they are at the 1% level or above, improve the strength, ductility and stress corrosion cracking resistance significantly (1,2,3, 4,5). Copper encourages the formation and stabilisation of G.P. zones and η'. It substitutes into $MgZn_2$ to form $Mg(CuZn)_2$. (1,2,11,37,38). The overall precipitation processes in Cu containing alloys are not significantly different from those found in the ternary system. Small quantities of S phase (Al_2CuMg) have been reported in alloys containing more than $\sim$2.0%Cu (11). Copper is only omitted from commercial alloys due to its adverse effect on weldability (3). Silver acts in a similar

manner (38,41). It is believed that silver atoms cluster at a fast rate and enhance the formation of G.P. zones. Ag imparts severe quench sensitivity to commercial alloys (3,5).

A large number of other alloying additions either intentionally added or present as impurity traces have been examined. For a recent review the reader is referred to the review of Mondolfo (7) and the work of Yoshi Baba (36,38)

2.4. Environment Assisted Fracture

The major limitation to the use of high strength Al-Zn-Mg based alloys arises as a result of their susceptibility to premature failure in the presence of an aggressive environment. The most common corrosive agent is water but specific ions such as halides accelerate the failure. This phenomenon has come to be known as stress corrosion cracking. This name had in the past been taken to imply failure in aqueous solutions, often containing halides, exclusively, but the current use of the term incompasses environment assisted failure in other environments, (liquid metals, cathodic charging, etc.). In this work the term stress corrosion cracking (S.C.C.) will be used according to the latter definition, implying environment sensitive failure.

The fracture path in environment sensitive failure is almost exclusively intergranular (1,2,3). The only direct evidence available on the crack propagation path is that of Montgrain and Swann (42) and it is clear from their results that failure occurs along the grain boundary particle/matrix interface. It does not involve precipitate dissolution or significant dislocation production (even though some dislocations may have been lost from the thin foils examined). Middleton and Parkins (43) concluded that the crack path was coincident with the grain boundaries rather than the adjacent precipitate free zone. Decohesion along the precipitate/matrix interface was reported by Watkinson and Scully (44). Discontinuous propagation (with audible cracking!) was also reported by those workers. Gruhl (45) had already noted such behaviour and was able to record the signal using an ordinary microphone/audio recording system. Astonishingly the above researchers (44,45) came to opposite conclusions. Gruhl attributed the discontinuous cracking events to hydrogen embrittlement, whilst Watkinson and Scully favoured a dissolution model which they could not pinpoint. ("The corrosion process directly responsible for cracking has not been determined in this study.")

In a recent study using high resolution scanning microscopy Scamans (46) found that samples of an Al-5%Zn-2.5%Mg alloy (7017, 7018) exhibited striations on essentially brittle fracture facets, if stressed under a variety of environments including distilled water and sodium chloride solutions.

The striations were interpreted in terms of a discontinuously growing crack which did not cause the dissolution of either grain boundary precipitates or intermetallic dispersoids. The mechanism believed to be operative was one of hydrogen embrittlement. Hydrogen generated as a result of the surface reaction between the environment and alloys is absorbed into the boundary. When sufficient hydrogen has accumulated the cohesive strength of the boundary reduced to a value below the applied stress and brittle fracture occurs. The observed striations are believed to be the crack arrest sites where further corrosion must take place before further crack growth (46).

Similar striations were earlier reported by McEvily, Clark and Bond (47). These were interpreted as resulting from a repetitive two-stage dissolution process involving film formation and rupture.

Transgranular cleavage-type fracture in environment sensitive failures of Al-Zn-Mg alloys has been reported by Scully (48) and Nelson and Pugh (49). Some evidence also appears in Alani's thesis (50). Brittle transgranular fracture was observed by Gest and Troiano (51) after cathodic charging. The occurrence of cleavage in the f.c.c. structure is rather difficult to reconcile with the existence of multiple slip systems available and is more characteristic of lower symmetry structures such as b.c.c. or h.c.p. Nelson and Pugh attributed their results to intragranular hydrogen and using etch pit techniques concluded that the cleavage planes were either of {100} or {110} types. They also suggested that the cracking process was discontinuous.

It is interesting to note that the reported cleavage plane in gallium wetted single crystal aluminium is of the {100} type (52). This is predicted from Gilman (53) but the criterion of Burton and Jura (54) suggests that for most metals including aluminium the {111} type planes are of lowest energy and thus these would be expected to cleave first. In a very recent communication Old and Trevena (55) using single crystals were able to essentially reproduce the results of Westwood et al (52). It is interesting to compare the effect of ageing of high strength aluminium alloys on toughness and liquid metal embrittlement

(Figure 2.2.). The closely related increase of resistance to embrittlement with an increase at ageing times of ~10 hours at 160°C suggests that the liquid metal embrittlement phenomenon, generally believed to be due to an adsorption/decohesion event (52) is sensitive to microstructural variations produced after heating at 160°C.

Accepting Westwood's ideas that L.M.E. is an adsorption-decohesion event then the crucial parameter must be the 'decohesion' (or interfacial) energy. Significant changes in this 'decohesion energy' must therefore be associated with precipitation of the second phase particles.

2.5. Effect of Metallurgical Variables on Environment-Sensitive Behaviour

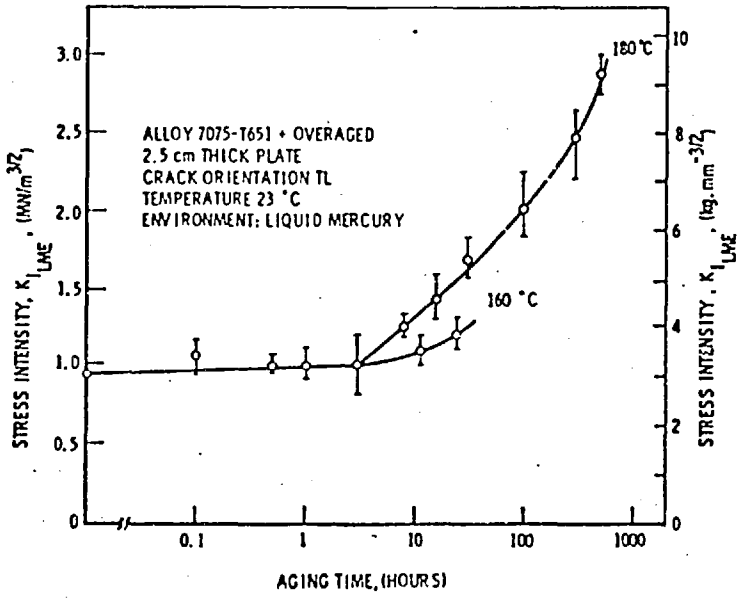
2.5.1. Microstructure

The environment-sensitive behaviour of Al-Zn-Mg alloys is strongly dependent on their microstructure. On the macroscopic grain structure scale, it is well established that commercially available alloys with an elongated grain structure (wrought products), exhibit severe stress corrosion cracking sensitivity when stressed in the short transverse orientation (1,2,3,4). Much slower crack propagation rates are observed when they are stressed in the longitudinal or long transverse directions. High purity alloys normally have a completely recrystallised structure and the anisotropic properties are not found. Grain size is an important variable; the larger the grain size the greater the susceptibility to stress corrosion (47,56). High purity, fully recrystallised alloys are the most susceptible to stress corrosion cracking.
The beneficial effect of most additions can be attributed, at least in part, to the grain refining role that such impurities may play. This is in addition to any specific effect that a particular element may have on the mechanism of failure be it anodic dissolution or hydrogen embrittlement.

2.5.2. Alloy Content

With regard to the effect of the two major alloying elements as a broad generalisation it can be stated that increasing the total amount of solute which can be put into supersaturated solid solution increases the susceptibility to S.C.C. (2,3,4,5,35).

The stress corrosion cracking susceptibility is also influenced by the ratio of Zn/Mg and optimum properties are found when this is in the



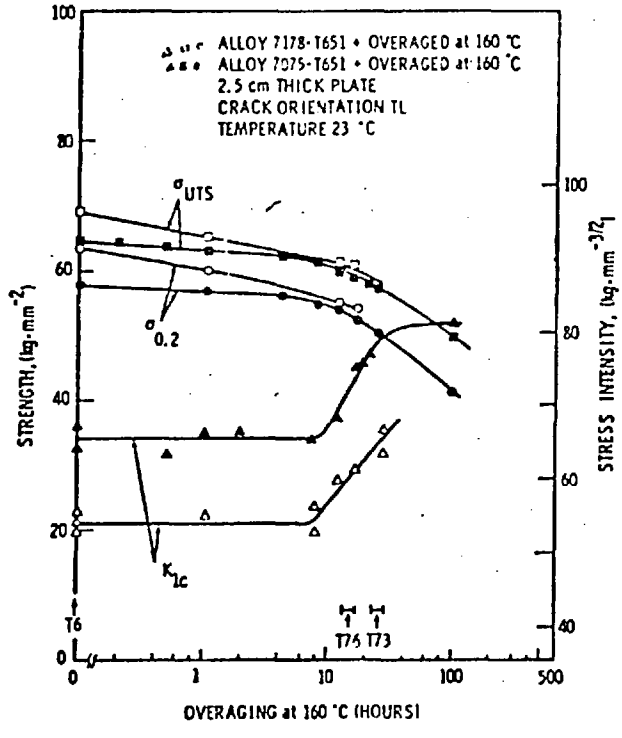


Figure 2.2. (a) Influence of overageing on resistence to liquid metal embrittlement and (b) on strength and fracture toughness. After Speidel (6).

region of 2.7 - 3 (35). Gruhl has deduced from this that it is the Mg and Zn content and distribution in the boundary that determine the embrittlement.

Minor alloying element additions improve the stress corrosion resistance of the alloys by either decreasing the grain size (35) or by specifically modifying the microstructure. For instance copper additions result in limited substitution of zinc by copper atoms in $MgZn_2$ and this is believed to be beneficial. The exact mechanism by which copper additions improve S.C.C. resistance is not known.

Doig et al (57) have suggested that it is the copper depletion of the P.F.Z. in the overaged condition that is responsible for the improvement. This is quite clearly wrong because it does not explain the beneficial effect of copper in underaged material. In any case an improvement in S.C.C. behaviour is obtained by overaging alloys without copper additions (see below).

Silver is believed to reduce S.C.C. susceptibility by affecting the size and distribution of the hardening precipitates (G.P. zones and η') (41). In this respect the silver additions act in the same manner as copper. Both stabilize the intermediate precipitate structure (2,3,7,8). The exact mechanism by which a more stabilized intermediate structure imparts greater stress corrosion cracking resistance is not known. Indeed an intermediate precipitate structure would be predicted by several theories (29,30,31) to be more susceptible . This is because an intermediate precipitate structure would favour planar slip and the above theories associate S.C.C. susceptibility with the occurrence of such planar slip.

Gruhl (58) found that additions of chromium to Al-Zn-Mg alloys significantly raised the time to failure of stressed samples (Figure 2.3).

The interpretation of their results was based partly on the indirect effect of Cr additions on the grain structure but a direct effect was also noted which they could not identify. The modification of the precipitation process, involving the η' and η phases, by the chromium additions was not considered to have any influence (58).

2.5.3. Solution Heat Treatment Temperature

Some workers indicate that a beneficial effect is obtained if the solution heat treatment temperature (S.H.T.) is raised (12,59,60). Scamans et al (77) found that the room temperature pre-exposure embrittlement characteristics of an Al-6%Zn-3%Mg alloy were adversely affected if samples

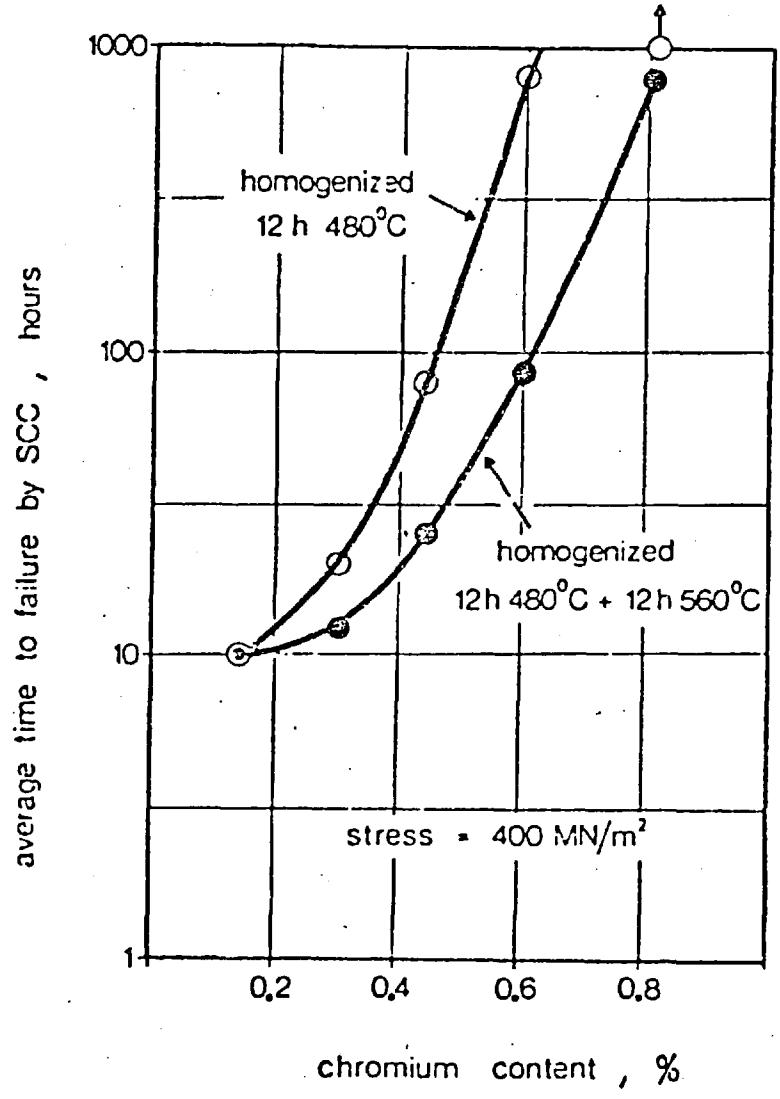


Figure 2.3. Effect of chromium content on the time to failure by S.C.C. of an Al-Zn-Mg alloy after quenching and ageing for 48 hours at 120°C. (Figure from Speidel (4))

were solution treated at 475°C. Both higher and lower tmperatures (500 and 450°C) resulted in more resistant alloys. Increasing the exposure temperature to 70°C eliminated the S.H.T. dependence

Current work on Al-Mg and Al-Zn-Mg alloys (60) suggests that susceptibility to water vapour embrittlement is related to S.H.T. Specifically the lower the temperature the greater the susceptibility. This is believed to be related to magnesium segregation effects (60).

It is difficult to understand why in a well annealed sample there should be a S.H.T. dependence. Quench rate would be expected to be of greater importance (see below) and the S.H.T. effect may simply reflect differences in the attained quench rates. However, if the S.H.T. dependence is real then two explanations can be advanced: Firstly it is possible that the effect is related to the oxide film that forms during solution treatment. Different temperatures may lead to differences in oxide chemistry and structure. In a mildly aggressive environment small differences in oxide character may play a significant role in the environmental failure by influencing crack initiation. (This would be most pronounced in smooth specimens). The second possible explanation may indeed involve segregation effects. However, segregation due to solution temperature alone would only result if the samples received short treatments (i.e. if not enough time was available for diffusion to even out any concentration profiles). This would be most likely if the S.H.T. was very close to the second phase solvus (~350°C). The recommended S.H.T. range in commercial Al-Zn-Mg alloys is 400-500°C (4). Solution treatment in this temperature range is believed to result in the optimum distribution of intermetallic particles of Cr Zr and Mn which retard recrystallisation and grain growth. Heating above 500°C results in agglomeration of the Cr rich particles and leads to less efficient inhibition of recrystallisation (4).

2.5.4. Quench Rate

It is well documented that stress corrosion cracking sensitivity of H.S.A.A. increases with increasing quench rate (4) (Figure 2.4.).

The effect of the quench rate is considered to be important for a number of reasons: Firstly it will determine the composition of material immediately adjacent to the boundary. Slow quenches will result in solute depletion of the P.F.Z. whilst fast cooling rates will produce solute supersaturation. The grain boundary particle character will also be determined by the cooling rate. Slowly cooled material exhibits large precipitates while a cold water quench results in precipitate free boundaries.

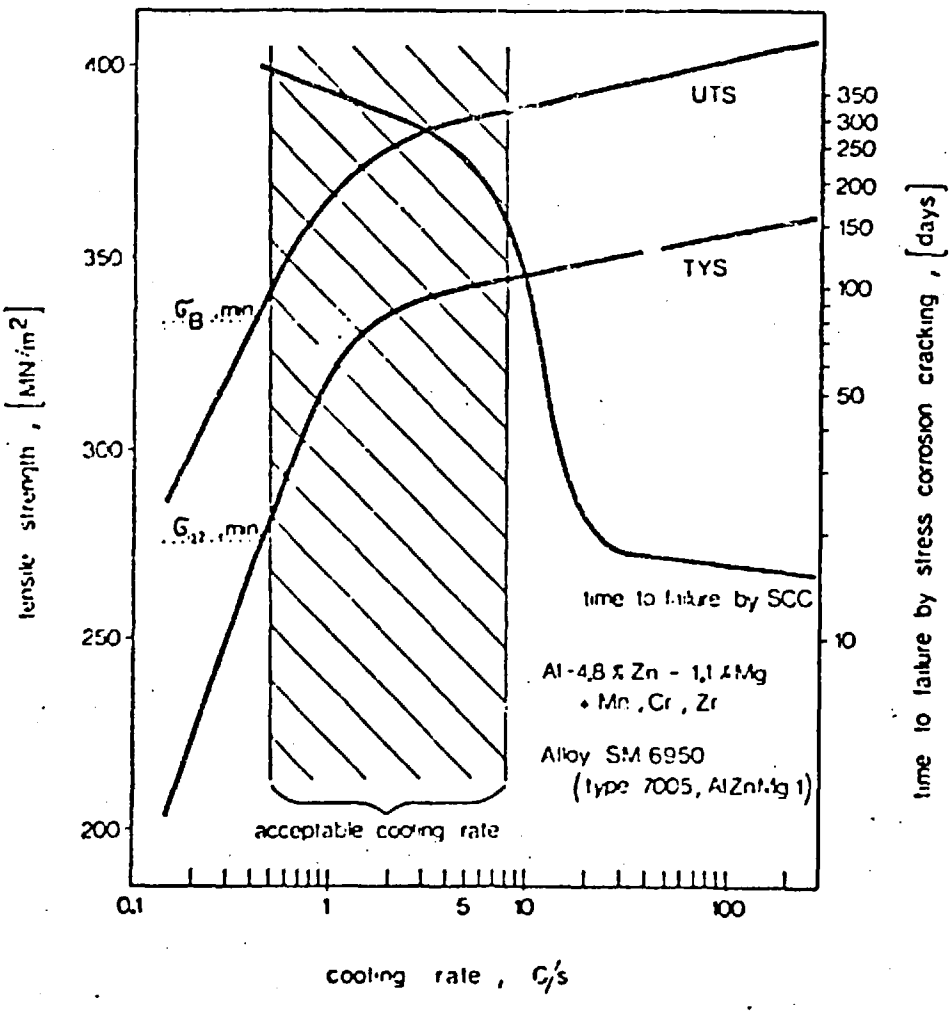


Figure 2.4. Effect of cooling rate from the solution annealing on strength and stress corrosion resistance of an alloy typical of the 7000 series alloys (Figure from Speidel (2))

Fast cooling rates are normally necessary in order to attain high strength. However, quench sensitivity (decrease in attainable tensile properties with decreasing cooling rate) is increased by alloying additions. (e.g. Cr, Zr, Mn) Silver is particularly harmful in this respect and this together with its high cost has inhibited its use in commercial alloys (3).

2.5.5. Ageing

Resistance to stress corrosion cracking is a strong function of the ageing condition in Al-Zn-Mg alloys. In general a maximum susceptibility is exhibited by structures consisting of G.P. zones and η'. This is normally found just before peak strength (Figure 2.5). Many attempts have been made to correlate the variation of S.C.C. susceptibility with metallurgical parameters which are known to vary with ageing conditions. These include:

(1) grain boundary precipitate size (8,43,44,61,62,63,64).
(2) grain boundary precipitate spacing (20,44,61,65,66).
(3) precipitate free zone width (14,67).
(4) preferential slip in the P.F.Z. (47,68,69).
(5) solute profile in P.F.Z. (8,20,61,57,70,71).
(6) matrix precipitate size/distribution (29,30,44,64,72).
(7) deformation characteristics (matrix) (29,30,31).

It is not the intention here to discuss in detail all of the above relationships. The reader is referred to the recent review by Bernstein and Thompson (3), which deals with the metallurgical variables of environment-assisted failure. The mechanisms proposed are also briefly discussed by the above authors in a different review (5).

Several points, however, need to be outlined at present. Specifically it should be appreciated that very few, if any, of the above parameters can be varied independently. For example, during the ageing of a quenched sample all of the above would be expected to vary. Consequently correlation of S.C.C. susceptibility with one parameter does not necessarily exclude the possibility of dependence on the others. (A detailed discussion of the effect of ageing on the environment-assisted failure will be given later under "Discussion".)

Of the direct observations reported in the literature those of Montgrain and Swann (42) and Ward and Lorimer (70) clearly show that grain boundary precipitate dissolution does not take place during the propagation of a stress corrosion crack. More recently Scamans (46) was able to match the

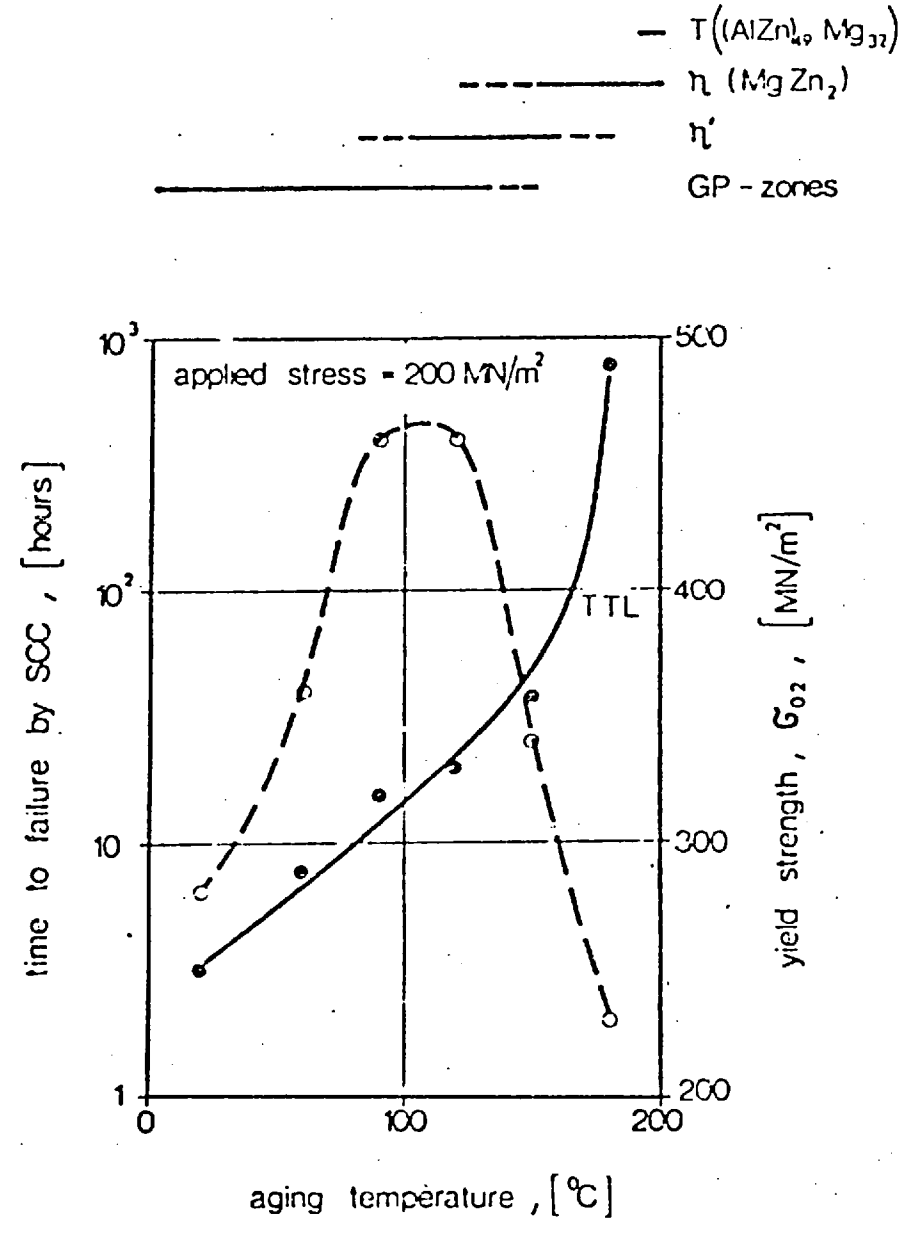


Figure 2.5. Effect of ageing on yield strength and time to failure by S.C.C. in an Al-Zn-Mg alloy (After Speidel (2))

two faces of an intergranular stress corrosion crack perfectly and came to the conclusion that no material was lost, i.e. no dissolution had taken place. His results certainly show that no particle dissolution had taken place. Many other authors have, in the past, come to the conclusion that very little corrosion is necessary for crack propagation to occur (2,3,43,44).

2.6. Mechanical Aspects

Stress corrosion cracking as implied by its name is dependent on the interaction of stress, environment and material. Aqueous S.C.C. constitutes the most important variant of the environmental failure phenomenon which also includes liquid metal embrittlement (L.M.E.) and embrittlement following exposure to aggressive media in the absence of the simultaneous action of stress. In this last category are included the "pre-exposure embrittlement" work of Gruhl et al (73,74,75) and Swann and co-workers (42,76,77), together with the cathodic charging experiments of Gest and Troiano (51) and others (78,79,80).

2.6.1. Stress Effects

On the "macro-stress" scale it is well established that increasing the stress leads to a reduced component life (1). Time to failure (T.T.F.) tests show an increase in component life as the tensile stress is decreased (1). A threshold stress below which no cracking occurs is often quoted (2). Using smooth specimens Gruhl (80) was able to correlate the life-time of a sample (L) with the stress level σ via a relationship:-

$$\frac{1}{L} = K_1 \exp(K_2 \sigma)$$

where K_1 and K_2 are constants.

The effect of stress has been more quantitatively established using pre cracked specimens of the double cantilever beam type (D.C.B.) (2,6,81). These have emphasised the importance of crack tip stress intensity (Figure 2.6).

The characteristic three region crack velocity vs crack tip intensity (V-K) curves (Figure 2.6) have been found in a variety of environments including liquid metals (6). Region III is normally regarded as being environment independent and is associated with ductile failure (at K_{IC}). The stress intensity independent region II extends over a large range of stress intensities and is followed by the stress intensity dependent region I which obeys a relationship of the form

$$V = V_o(\exp C_1 K) \quad \text{where}$$

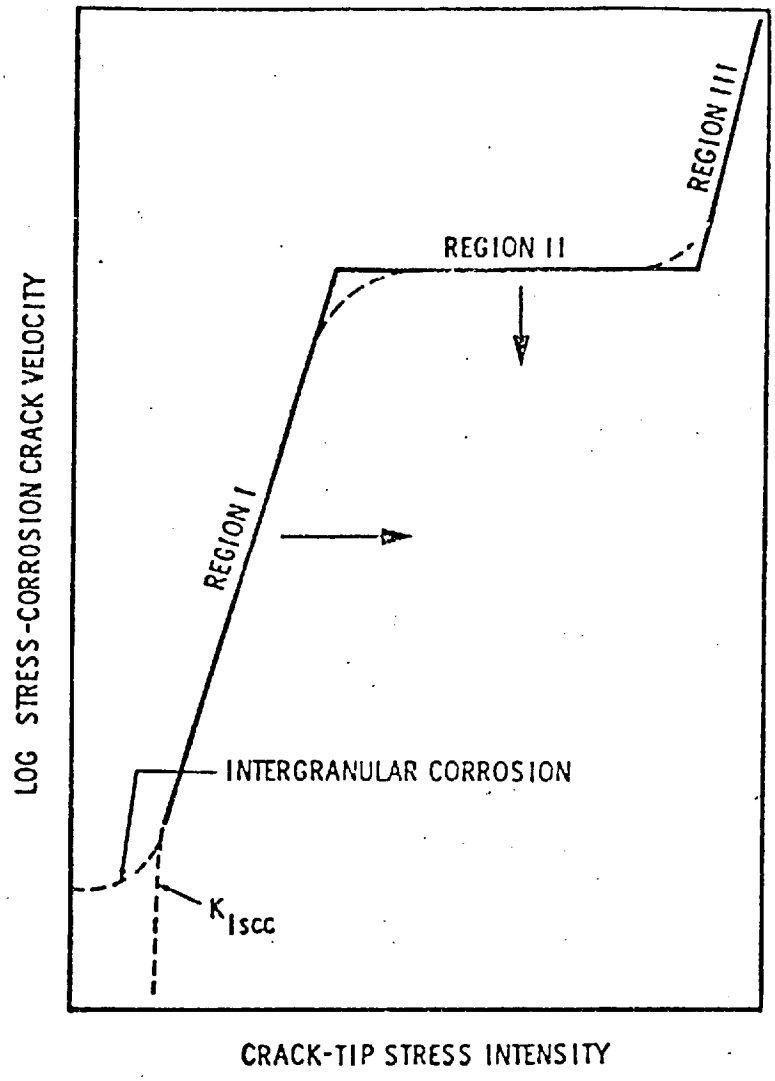


Figure 2.6. Schematic representation of the influence of stress intensity (K) on stress corrosion crack velocity (V). Arrows indicate the direction of displacement of the curve with overageing. The effect on region 1 is significantly greater than region 2. (6)

V = crack velocity

K = stress intensity

C_1, V_o = constants.

It is sometimes reported that a threshold stress intensity exists ($K_{1\ S.C.C.}$) below which no crack growth occurs (6,2).

The crack growth rate versus stress intensity curve is sensitive to alloy composition, ageing condition and environment (2,4,6). For instance overageing of alloys markedly displaces region I of the curve to higher K values. The same treatment also transfers the plateau region II to lower crack velocities but this effect is of lower magnitude (6) (Figure 2.6). In contrast to this environmental variables tend to have a more pronounced effect on the stress intensity independent regime (6). Some of the environmental aspects will be outlined in section 2.7.

The localised effects of the applied stress on an existing crack constitute the basis of most theories of stress corrosion cracking and some of these will be briefly outlined below. Before examining these however, it is fruitful to consider the stress state of a propagating crack in a thick sample.

Continuum plasticity solutions predict that stress levels ahead of cracks in a material under a tensile stress and plane strain, are much in excess of the tensile yield strength σ_o (Figure 2.7) (82,83). The peak in stress occurs at a distance of approximately $2\delta t$ ahead of the crack tip where δt is the amount that the crack has been opened by plastic deformation. These high stress levels, however, cannot exist <u>at</u> the crack tip as the triaxial stress conditions necessary for their existence cannot be maintained at the free surface. Plastic deformation at this region therefore establishes a "plastic zone" at the stress level approximating to the yield stress under uniaxial tension (σ_o). The radius of the plastic zone (r_p) is given by

$r_p = \frac{1}{2\pi}\left(\frac{K}{\sigma_o}\right)^2$ where K = stress intensity and is typically $\sim$ 40μm at $K_{I.S.C.C.}$:

(Assuming that $K_{I.S.C.C.} \sim$ 5 $MNm^{-3/2}$ and σ_o = 350 $MN.m^{-2}$)

It is conceivable that this deformed region constitutes an active path where dissolution may occur preferentially. This argument forms the basis of the dissolution control theories that are mainly concerned with the effect of stress. They propose that as a result of the applied stress and hence existence of a plastic zone, the energy barrier for dissolution

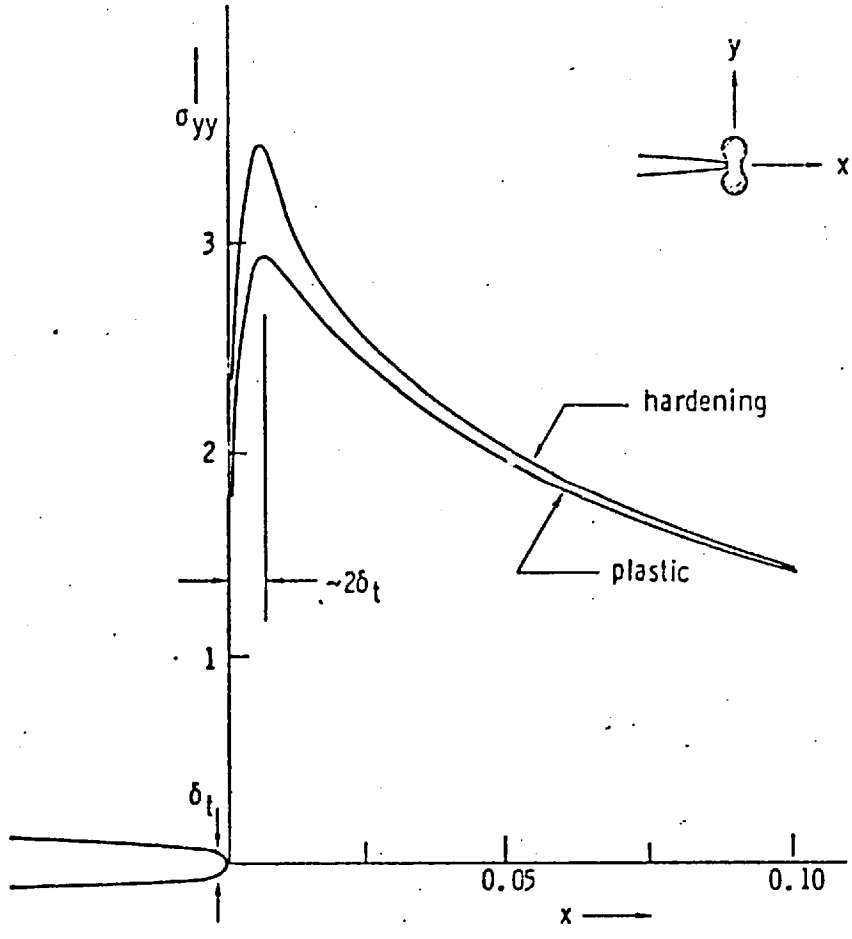


Figure 2.7. Dependence of maximum stress on distance ahead of the crack in units of $K^2/\sigma y$. Two cases are shown: ideal plastic material and hardening material with exponent of 0.1. Plane strain conditions.

is reduced leading to the preferential loss of the deformed metal (84,85, 86).

Others workers propose that the action of stress, and in particular localised deformation, provides a means of oxide film breakdown leading to accelerated dissolution (47,87,88,89,90). The most recent of these (90) attribute critical importance to the oxide film repair process following the breakdown of the existing film (see section 2.4.3.).

The existence of the high stresses ahead of the crack tip also constitutes the basis of the hydrogen embrittlement theories which are based on Troiano's so-called decohesion model (91) and its later modifications (92,93). Originally given as a mechanistic explanation of hydrogen embrittlement in steels the theory postulates that dissolved hydrogen accumulates in the region ahead of the crack tip as a result of the high triaxial stress that exists there. The cohesive strength of the lattice is then thought to be reduced by the presence of a critical hydrogen concentration. Crack growth occurs when the local tensile stress exceeds this lower level of strength (Figure 2.8). Crack extension is discontinuous and is caused by the repeated attainment of the critical hydrogen concentration (91). Under stress corrosion cracking conditions the hydrogen is generated as a result of the corrosion reaction and is transported to the region ahead of the crack tip by diffusion (91,92,93). The driving force for diffusion is provided by the assumed increased solubility of hydrogen at the region under triaxial stress (91).

Green et al (82) have carried out experiments in which the stress corrosion cracking susceptibility was assessed as a function of loading under torsion (mode III) and tension (mode I) conditions (Figure 2.9). They have argued that under torsional (mode III) loading conditions no hydrostatic stress distribution exists ahead of the crack tip (Figure 2.9) and thus if the S.C.C. of Al-Zn-Mg alloys is governed by a hydrogen embrittlement mechanism, then the alloys should be less sensitive to attack under those conditions. Their results are shown in Figure 2.10. In agreement with the above suggestion they show that susceptibility is greater in tension (mode I) than torsion (mode III). These results constitute some of the strongest evidence in support of a hydrogen embrittlement mechanism dominating in the environmental failure of Al-Zn-Mg alloys. It is generally considered (82,3) that a dissolution controlled failure should not be sensitive to loading mode thus no differences would be expected between the different stressing geometries. (This appears to be true in other systems such as α-brass in ammoniacal environments (82)).

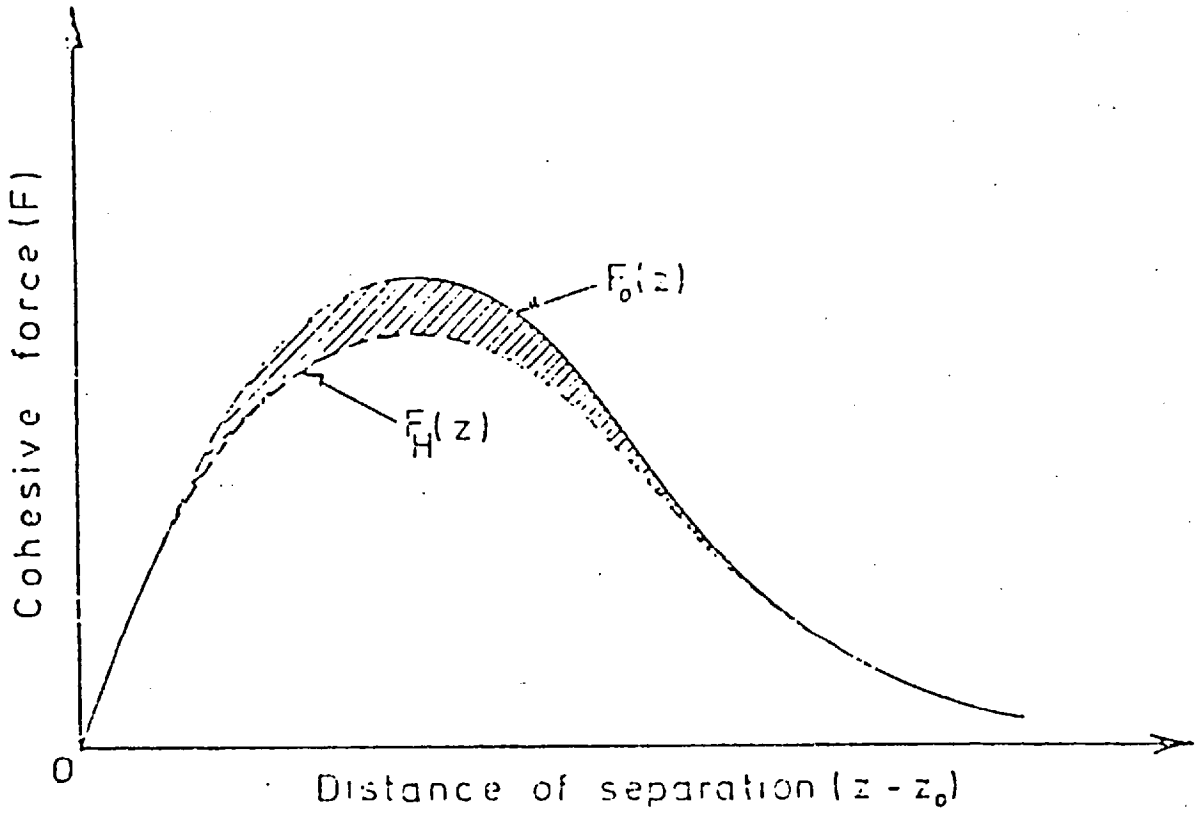
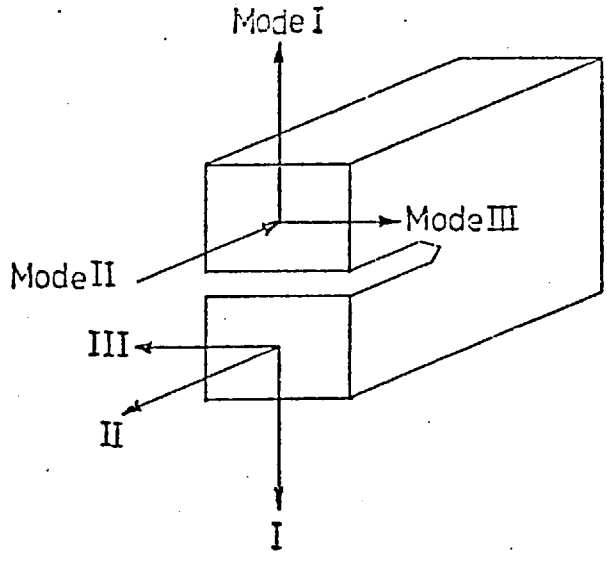


Figure 2.8. Schematic illustration of the cohesive force as a function of the distance of separation across a metal plane. The cohesive force at a given hydrogen concentration is represented by $F_H(Z)$ and is lower than the cohesive force in the absence of atomic hydrogen $F_0(Z)$.



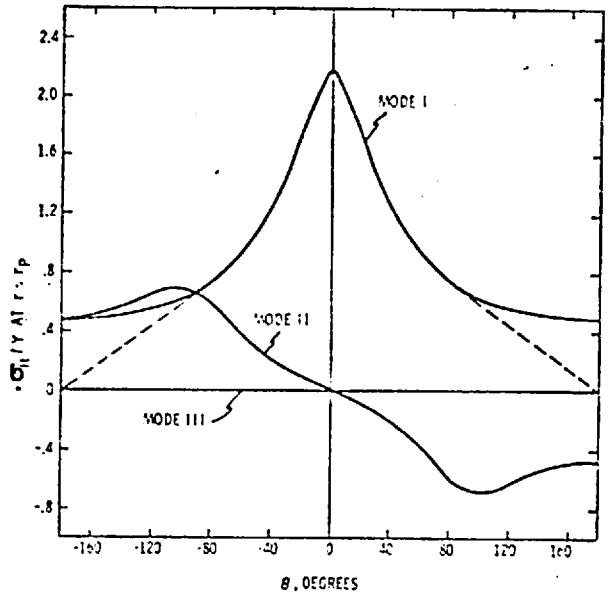


Figure 2.9. Three modes of loading of a pre-cracked specimen (a) and the proposed hydrostatic stress distribution ahead of the crack tip. Figure (a) after Bernstein and Thompson (2) and (b) after Green et al (81).

There are two more points worthy of consideration in Green's results: Firstly, it is clear that whilst susceptibility under torsion is severely reduced it is not eliminated. This suggests that there is a contribution to failure from some form of anodic dissolution process. Secondly, addition of arsenic (hydrogen recombination poison) to the saline solution was found to have opposite effects under the two different conditions (Figure 2.10). Under tension it was detrimental but under torsion beneficial (82). Green and co-workers rationalised this observation as follows: Under tensile loading arsenic additions are detrimental because they enhance the absorption of atomic hydrogen into the alloy. Segregation of the hydrogen ahead of the crack then enhances the embrittlement phenomenon. Under torsional loading however, there is insufficient hydrostatic stress to cause local concentration of hydrogen (and therefore embrittlement) and thus the dissolution mechanism controls the behaviour of the alloy. Under these conditions the arsenic restricts the cathodic reaction (i.e. $2H^+ + 2e^- \rightarrow H_2$) and via this the anodic (dissolution) reaction. Thus it is beneficial.

2.6.2. Strain Rate Effects

The effect of strain rate on the environment-sensitive behaviour of aluminium alloys has attracted much attention and strain rate tests have been utilised by various workers to examine both the internal hydrogen embrittlement behaviour (51,77,78,96), and the oxide film breakdown and repassivation process (44,90,95). Strain rate dependence in internal hydrogen embrittled systems is related to the time available for diffusion of hydrogen to the region of high triaxial stress as discussed previously (91,92,93). Under stress corrosion crack propagation conditions, much attention has been focussed on the dynamic breakdown of the surface oxide under a constant slow strain rate (44,90,94).

Slow strain rate tests have been used as accelerated tests for S.C.C. susceptibility and much useful information has been obtained for a variety of alloy systems / environment combinations (94)

Ugiansky et al (95) reported that the stress corrosion behaviour of 7075 plate is sensitive to strain rate (Figure 2.11). It is of interest to note that the sensitivity was only apparent in the metallurgically susceptible state, viz T6 condition (see section 2.4.) Their results confirm the previously reported work of Watkinson and Scully, who examined a high purity Al-6%Zn-3%Mg alloy (44) (Figure 2.12). In that work it was found that samples aged for 24 hours at 120°C, i.e. T6 condition,

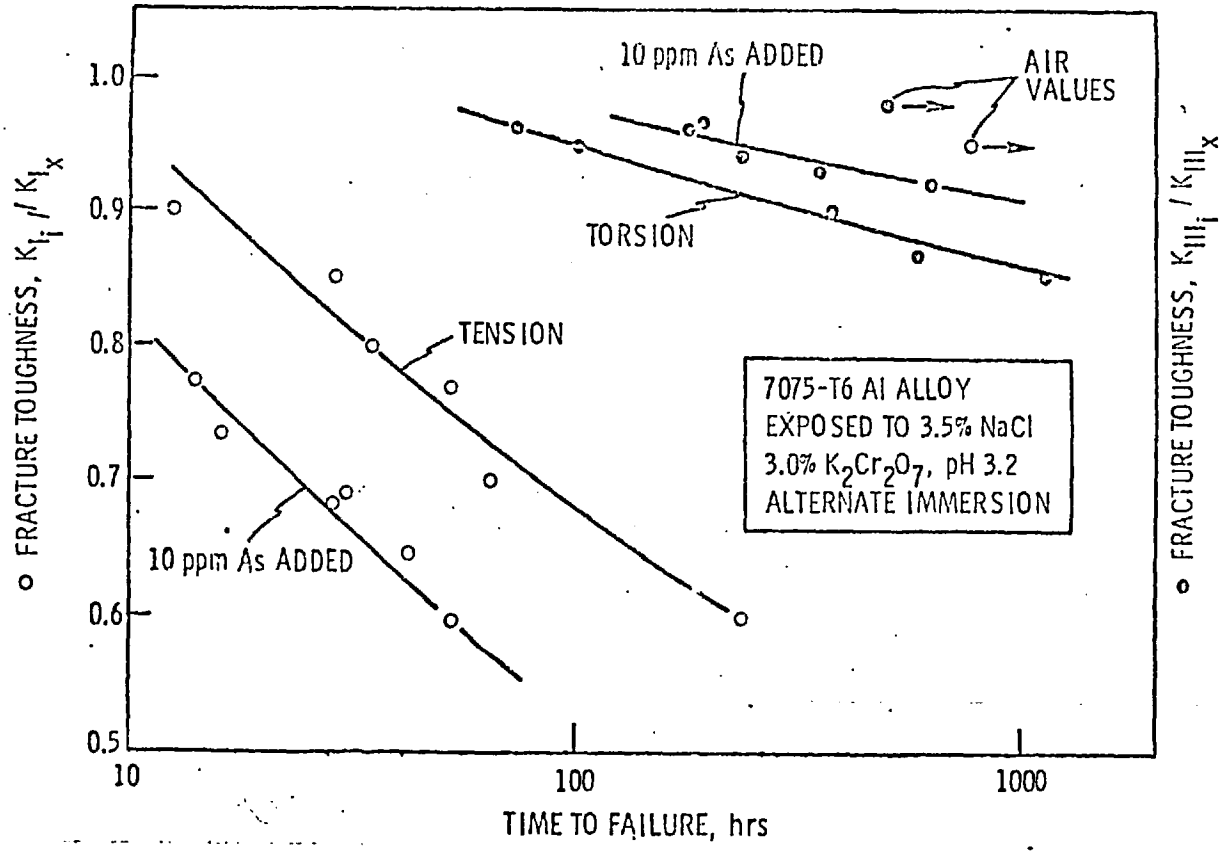


Figure 2.10. Susceptibility of 7075-T6 alloy to S.C.C. in an aqueous solution under both tensile and torsional loading. After Green et al (81)

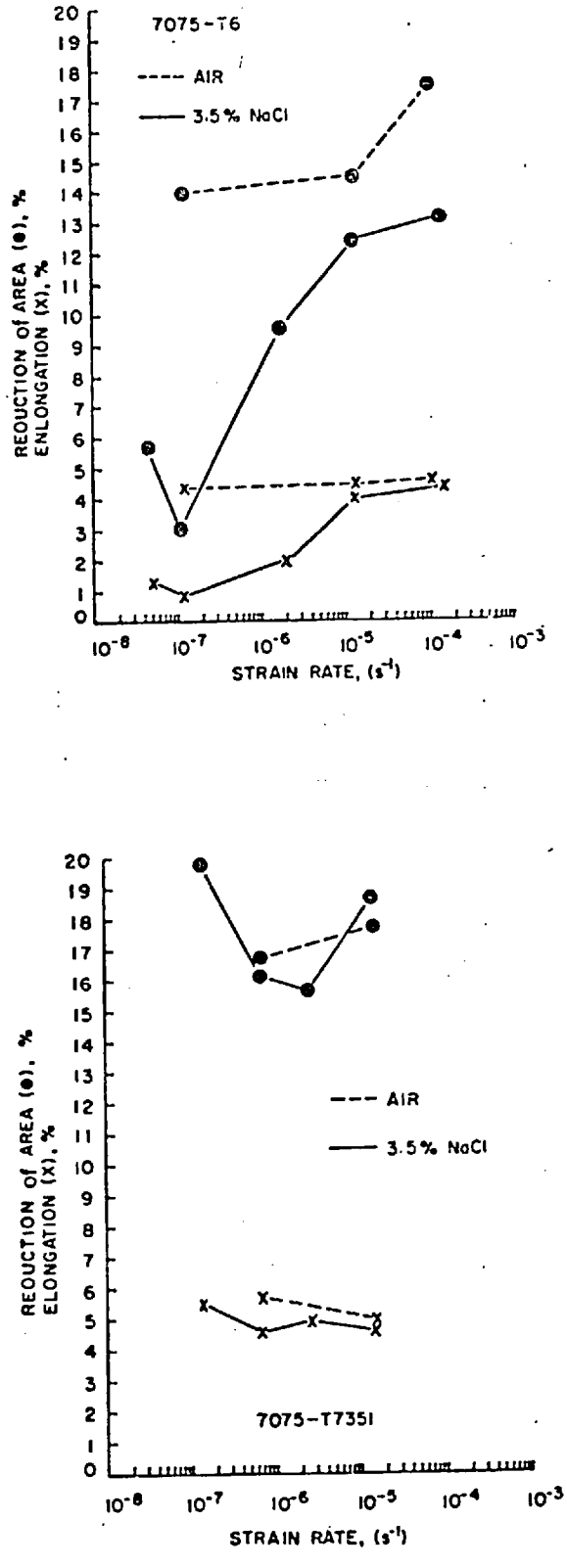


Figure 2.11. (a,b) Effect of strain rate on the S.C.C. of an 7075 alloy. Figure (a) represents the behaviour of a peak strength aged condition (T6) whilst Figure (b) refers to an overaged microstructural state (T7351). After Ugianski et al (95)

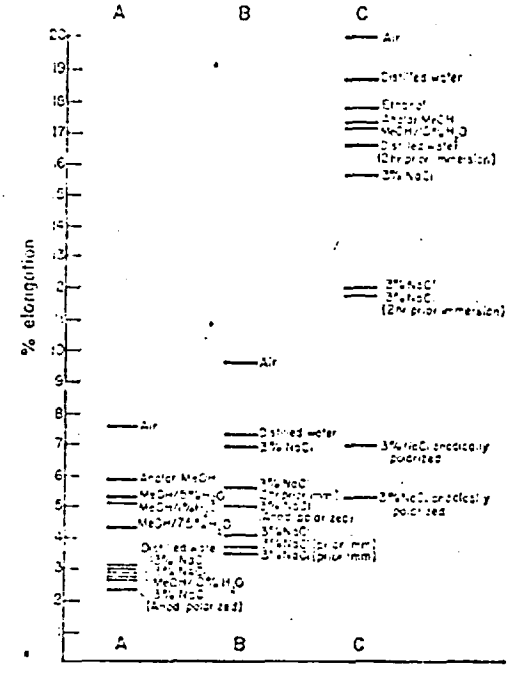


Figure 2.12. Results from Watkinson and Scully (44) on an Al-6%Zn-3%Mg from constant slow strain rate tests.

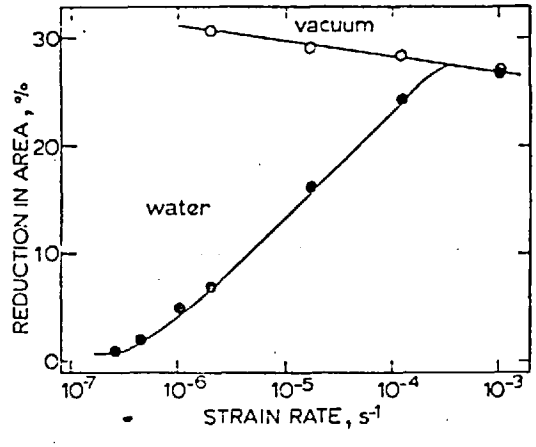


Figure 2.13. Strain rate sensitive behaviour in an 7179 alloy.

were most embrittled under slow constant rate straining in aggressive environments (Figure 2.12). Some very important points are evident from that work:

(i) Degree of embrittlement depends on heat treatment.

(ii) Loss of ductility in samples tested in organic environments (MeOH) is related to the water content of such media.

(iii) Loss of ductility is greater if samples are exposed to 3%NaCl solution prior to testing.

(iv) Anodic polarisation in general results in the lowest elongation values.

Furthermore, Watkinson and Scully (44) report no environmental sensitivity at strain rates greater than $3 \times 10^{-3} s^{-1}$. Hardie et al (96) have found strain rate sensitive behaviour in an 7179 alloy (Figure 2.13). At strain rates of $\sim 10^{-7}$ s^{-1} complete embrittlement is reported. Increasing the temperature of the corrosive medium (Newcastle tap water!) resulted in increased embrittlement.

The validity of the slow strain rate tests as a measure of S.C.C. susceptibility has been discussed by Buhl (97). Three possible types of behaviour are described by Buhl of which only 2 are attributed, at least partly, to S.C.C. (Figure 2.14). In cases where S.C.C. is involved there exists a critical strain rate above which no effect is observed (Figure 2.14). The explanation advanced for the insensitivity of the strain to fracture at very high strain rates to the environment is that the corrosion process cannot keep up with the very fast straining. This is quite reasonable. In cases where a minimum in the strain to fracture is observed at an intermediate strain rate (Figure 2.15) the explanation proposed is that this is due to variations in the repassivation rate. To verify this the author (97) postulates that if the minimum is sensitive to "environment, material, solvent, aggressive or inhibiting ions, electrode potential, etc." then it is the repassivation rate that is "responsible" for the phenomenon. The author also pre-supposes that failure occurs by an anodic dissolution mechanism. Whilst the repassivation rate is almost certainly sensitive to the above variables and may play an important role by determining the amount of corrosion taking place as discussed by Scully (90), the rate limiting step may be quite different if a hydrogen embrittlement mechanism operates. For instance Scamans et al (77) Parkins et al (96) and Gest and Troiano (51) have all found that pre-corroded samples recover their ductile properties if not mechanically tested immediately upon removal from

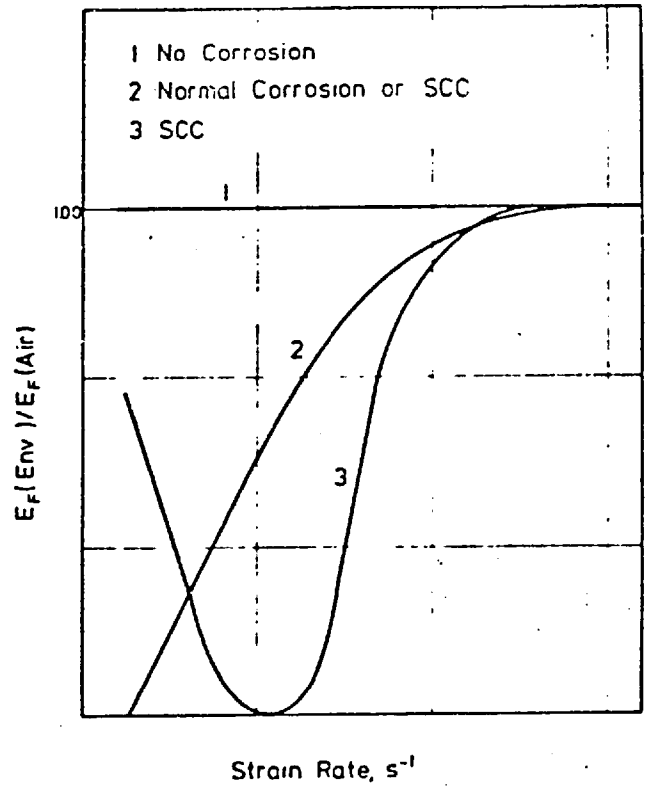


Figure 2.14. Three types of behaviour exhibited during slow strain rate testing of materials. E_F is the fracture energy. (After Buhl (97).

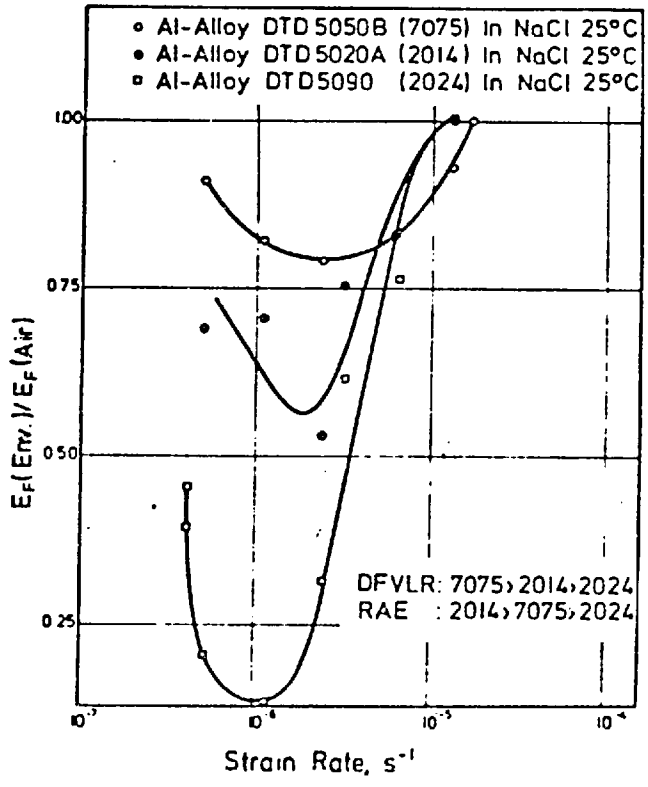


Figure 2.15. Results from various aluminium alloys. After Buhl (97)

the environment generating hydrogen. It is possible therefore that the observed minimum and subsequent increase in elongation values at very low strain rates is related to the loss or the internal re-arrangement of hydrogen and the effect of this on ductility. A second possible influential step under some conditions in a hydrogen embrittlement mechanism may be the adsorption/absorption event. This may well be related to the repassivation rate (90,99).

Gest and Troiano have reported strain rate sensitive behaviour of cathodically charged 7075 samples (51), whilst Scamans et al (77) were unable to detect such sensitivity in a high purity Al-6%Zn-3%Mg alloy that had been exposed to water vapour.

In their pre-exposure embrittlement tests Parkins et al (96) found that the phenomenon was strain rate sensitive, a result shared with later work by Scamans (98).

The implications of strain rate sensitivity of pre-exposed samples will be discussed later but it should be borne in mind that such sensitivity following cathodic charging constitutes some of the strongest evidence in support of hydrogen embrittlement mechanisms in iron base alloys (3,147). The occurrence of such phenomena in high strength aluminium alloys (51, 78, 79, 80) are strong indications in favour of a similar mechanism operating in this alloy system.

2.7. Environmental Aspects of Failure

2.7.1. Oxide Films

It is generally accepted that the oxide film covering Al-Zn-Mg alloys plays an important role in their stress corrosion cracking behaviour.

The breakdown of the oxide and subsequent repassivation of the bare metal under the influence of the environment forms the basis of a number of variants of the "dissolution control" model (86, 87, 88, 89, 90). Some of the authors (87,86) regard the breakdown step as critical while others consider the repassivation kinetics to be of primary importance (88,89,90). The early theories of Logan and Hoar postulated the absence of an oxide film at the crack tip as a result of continuous yield. This, it was believed, led to a very localised corrosion reaction. The later modifications of the above theories (47) dealt with the objection that under most S.C.C. conditions the crack tip would not be expected to remain bare. It was therefore suggested that repeated breakdown and growth of the oxide occurs. Further, to accommodate the intergranular nature of the process

it was postulated that this behaviour was restricted to the softer precipitate free zone (47). Much subsequent work has failed to provide evidence in support of such preferential deformation in the P.F.Z. (1, 2, 3, 44, 72).

Localised destruction of the oxide by emergent dislocations could easily occur at crack tips or other discontinuities before general breakdown. The occurrence of planar slip in the most susceptible condition would favour such a breakdown mechanism. However, the existence of non-susceptible tempers and alloys exhibiting planar slip suggests that whilst breakdown would appear to be necessary it does not seem to be a sufficient criterion for S.C.C. (99).

The subsequent reformation of the oxide and in particular the repassivation kinetics are considered to be of extreme significance (90,99). It has been argued by Scully that since the stable configuration of the surface is that it is covered by an oxide film, as soon as bare metal is revealed oxidation will commence. The time between the breakdown event and complete re-oxidation will control the amount of corrosion damage incurred by the alloy. The total charge associated with a particular breakdown/repassivation event will determine the amount of dissolution taking place (anodic reaction). However, it will also determine the amount of hydrogen produced as a result of the cathodic reaction. Hydrogen discharge is the cathodic reaction occurring in the vicinity of a propagating stress corrosion crack (oxygen starvation situation). Thus one or both of these processes could affect the stress corrosion cracking characteristics of the alloy.

Knowledge of the oxidation characteristics of the alloys at service conditions is therefore of interest. In the absence of any information on the low temperature oxidation of Al-Zn-Mg alloys a brief summary of the oxidation characteristics of pure aluminium is given below.

It is reported that an amorphous layer of alumina, 10Å thick, is formed as a result of room temperature oxidation of aluminium in dry oxygen (100). Coverage is complete within minutes. A similar film of comparable dimensions has also been found by Hunter and Fowle (101) following storage in laboratory air. De Brouchere (102) in an electron diffraction study, was unable to detect any oxide film on pure aluminium which had been oxidised at room temperature and concluded that the thickness be less than 100Å. A value of 40Å is put forward by Vernon (103).

On the theoretical side the models of film growth are based primarily on Wagner's assumptions (104). He proposed that during oxidation both metal ions and electrons diffuse through the oxide and react with oxygen at the oxide/air interface. The electrons are thought to penetrate the oxide via the quantum-mechanical tunnelling effect up to a maximum distance of 55A. Mott (105) points out that since thick oxide films on aluminium can only be obtained by anodising, a condition which requires the passage of aluminium ions through the superficial layer and electron transfer via the external circuit, then it is reasonable to assume that at room temperature aluminium ions can diffuse through Al_2O_3 but free electrons cannot do so.

It is suggested that low temperature thin films on aluminium show an abnormally high metal/oxygen ratio (106). This has been attributed to excess aluminium ions in the normally vacant cation sites (γ-alumina contains a very high proportion of uncharged vacant cation sites; only 21 1/3 of the available 24 sites in the spinel structure are occupied). Electrical neutrality is maintained by trapped electrons (106). The ionic defects that exist in the low temperature oxide can have significant effects on the properties of the film. In particular they can determine the nature of the dominant mobile species (106, 107). Alloying elements added to aluminium would be expected to modify the defect structure of the oxide by incorporation in the oxide film and would thereby influence the mobility of specific species. For instance doping of $\alpha.Al_2O_3$ with magnesium leads to the introduction of oxygen vacancies and/or aluminium interstitials (108). It is well known that the high temperature oxidation kinetics of Al-Mg alloys are significantly accelerated in comparison to pure Al (109, 110, 111).

With reference to low temperature oxidation, attention must also be given to the effect of the environment and in particular of specific species such as hydroxyl ions, chlorides, fluorides, etc. on the character and rate of film formation. The modification of the oxide by particular agents could be responsible for the acceleration of S.C.C. under specific conditions. A decrease in repassivation rate or even complete replacement of the oxide may lead to a change in the mechanism of attack.

Modification of the oxide by chloride and fluoride solution has been reported by Prior and co-workers (112, 113, 114) and more recently by Vallant and Nilson (115). Their results were interpreted on the basis of an increase in the number of defects in the oxide films due to exchange of oxygen ions from the oxide lattice with chloride, fluoride and hydroxyl

ions. The effect of the incorporated ions according to Beck et al (112) was to lower the ionic but not electronic resistivity of the film. The complete replacement of the oxide at the crack tip by a chloride film has been proposed as being responsible for the accelerated stress corrosion cracking behaviour of aluminium alloys in chloride environments (116, 117). Whilst there is no direct evidence to support the existence of such a chloride layer, the existence of a concentrated, acidified $AlCl_3$ solution at the crack tip would appear to be well founded (2, 118, 119, 120). Alternatively it might be that the existence of such an environment at the crack tip is sufficient to modify the oxide characteristics or repassivation rate (90, 99) sufficiently to be responsible for the acceleration of the phenomenon. Since the solubility limit of $AlCl_3$ is low (2) the possibility of a chloride layer forming at the crack tip cannot be excluded.

Scully (121) has tentatively suggested that the formation of a stable halide film of the crack tip influences the hydrolysis reaction and thereby modifies S.C.C. behaviour. Resistance to hydrolysis by fluoride films is suggested as the reason for the beneficial effect of fluoride.

Before conclusion of this section a brief reference should be made to the high temperature oxidation characteristics of Al-Zn-Mg alloys. High temperature oxides are important in as much as they may influence the initial step of the environment sensitive behaviour of the alloys. The primary role of the high temperature oxide is likely to be restricted to the initiation of a stress corrosion crack. Once the crack has been established repassivation will occur at the service temperature (normally below $120^{o}C$). The subsequent growth of the crack will depend on the environmental and mechanical factors existing at the service conditions and thus the crucial reaction must still be regarded as the low temperature oxidation.

In Al-Zn-Mg alloys oxidation in the range of 400-$520^{o}C$ results in the formation of MgO crystallites particularly at the grain boundaries (122, 123). It is conceivable that such regions constitute more reactive sites where preferential chemical attack may occur and where Mg diffusion to the surface is more rapid.

2.7.2. Aluminium-Water Reaction

The aluminium-water system has received considerable attention and the voluminous literature has been recently reviewed (124).

Depending upon the existing conditions, the products of the reaction have been reported as being bayerite, gibbsite or nordstrandite ($Al(OH)_3$), boehmite or diaspore (AlOOH), and γ-Al_2O_3 and corundum.

Some authors believe that the reaction involves the dissolution of the oxide, normally present on the aluminium substrate, and the subsequent precipitation of a hydroxide phase (125), whilst others believe that the reaction is one of condensation-polymerisation of the existing air formed film (126). This so called "ageing" process is thought to follow the sequence:

Oxide → amorphous hydroxide → oxyhydroxide Pseudoboehmite ($\begin{matrix}\text{boehmite}\\\text{diaspore}\end{matrix}$) → trihydroxide ($\begin{matrix}\text{bayerite}\\\text{gibbsite}\\\text{nordstrandite}\end{matrix}$)

The amorphous hydroxide is colloidal in nature and consists of discrete crystals, roughly spherical, with a diameter range between 30-200A (124).

Pseudoboehmite is the most kinetically accessible phase and it is the initial crystalline product. It forms in preference to the equilibrium boehmite/diaspore phases. It is an aluminium oxyhydroxide of a structure similar to that of boehmite but contains significant amounts of excess water (124, 127). The extra water is bound with hydrogen bonds between the layered structure of boehmite. The layers of boehmite are formed as a result of the octahedral arrangement of oxygen atoms around the metal atoms. The octahedra are interlocked to form a double layer and adjacent layers are linked by hydrogen bonds (Figure 2.16)(124).

The morphology of pseudoboehmite is characteristic and consists of very thin platelets which appear as fibrils (124, 125).

Bayerite is always present in a well developed crystalline form and exhibits diverse shapes. The structure of bayerite consists of a close packed hexagonal hydroxyl lattice with the aluminium atoms occupying two-thirds of the octahedral interstices.

Gibbsite and Nordstrandite have not been found in the absence of an alkali oxide or organic additives and there is no evidence to suggest that they constitute major products in aqueous solutions (124). Gibbsite takes the form of hexagonal plates or rods while Nordstrandite appears as a collection of very thin rectangular laths.

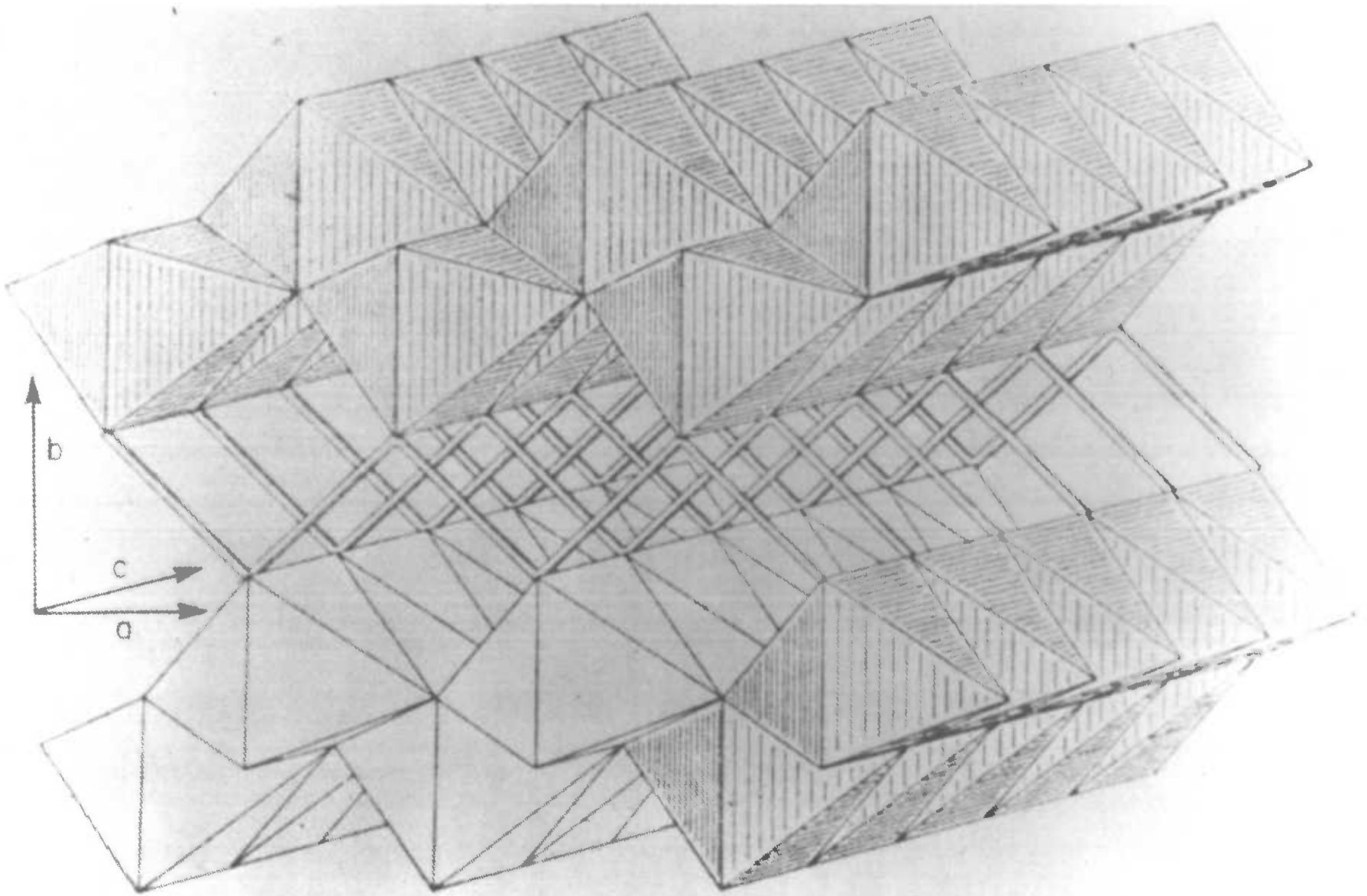


Figure 2.16. Boehmite structure. Hydrogen bonds link the octahedral arrangement of oxygen atoms around the metal atoms. Figure after Alwitt (124).

It is generally accepted that the reaction of aluminium with water results in a duplex surface film, consisting of an outer hydrated layer together with an amorphous barrier layer immediately adjacent to the metal (125, 127, 128). The hydrated oxide is most probably pseudoboehmite under most conditions (124) whilst the barrier oxide is commonly regarded as being amorphous. This amorphous layer has been compared to the oxide formed in air (125).

The mechanism of film growth is in dispute. Some authors (124, 128) regard the inward diffusion of hydrated species to be critical whilst others (125) consider that the rate limiting step to be the outward diffusion of aluminium ions.

The growth kinetics of the oxide formed on aluminium following immersion in water are as follows:-

(i) Incubation Period.

There exists an incubation period between the time of immersion and any visible reaction. This incubation period ranges from an interval of over 10 minutes at $40^{o}C$ to a few seconds at $80^{o}C$ (124).

The events responsible for this behaviour are not associated with the development of a particular solution chemistry within the liquid phase but rather with a hydration event at the solid surface. This has been clearly demonstrated in specimens which received successive immersions of individual periods less than the incubation period while the total time of exposure was greater. The net reaction was identical to that found if the specimens received one immersion treatment of total duration equaling the sum of the individual immersions (128). The duration of the incubation period is insensitive to solution pH variations over a wide range. It does, however, depend on the prior surface preparation treatment (128).

(ii) Rapid Growth Period.

Following the induction period film growth occurs at a rapid rate. This has been attributed to the redeposition of the dissolved oxide on the surface (125). Alwitt in his review concluded that both the induction period and initial rapid growth stage are controlled by the nucleation and spread of hydrolysis sites over the oxide originally present on the surface (124).

(iii) Slow Growth Period.

Following the rapid growth period the rate of growth is reduced. Vedder and Vermilyea (125) consider that the rate limiting step here is the outward diffusion of the aluminium ions through the oxide which react at the oxide/environment surface, whilst Alwitt (124) suggests that it is the inward diffusion of water (perhaps as H^+ and OH^-) that is the rate limiting step.

The cathodic reaction occurs primarily at the metal grain boundaries and this has been attributed to an increased electronic conductivity of the oxide film (125). The segregation of impurities at these sites is believed to be responsible (125).

Prolonged exposure of the pseudoboehmite film to water at temperatures up to 110°C results in the formation of bayerite (124). The bayerite crystals form on the surface of the pseudoboehmite and appear to grow independently of the pseudoboehmite (124, 128). Recently Rehal and Scamans (129) however, on the basis of microscopical studies, have suggested that the bayerite crystals were imbedded in the underlying metal.

The aspect of the Al-H_2O reaction most pertinent to this work, however, concerns the second product of the reaction; hydrogen.

Assuming that the reaction

$$2Al + 3H_2O = Al_2O_3 + 3H_2$$

occurs the pressure of the evolved hydrogen can be calculated. Using textbook values in the expansion

$$P_{H_2} = P_{H_2O} \exp\left[\frac{-\left(\Delta H^o_{fAl_2O_3} - 3\Delta H^o_{fH_2O}\right)}{3RT}\right]$$

where $\Delta H^o_{fAl_2O_3}$ and $\Delta H^o_{fH_2O}$ are the heats of formation of alumina and water respectively (and the activity of aluminium and water are taken as unity) the resulting calculated equilibrium pressure of hydrogen at 293K is of the order of 10^{40} atmospheres. Whilst this is an upper limiting equilibrium value and is generally unlikely to be achieved it clearly demonstrates that the metal/environment combination is capable of significant hydrogen production. It is also noteworthy that this value is not significantly affected by the activity of the water. Traces of water being sufficient to generate large amounts of hydrogen. Furthermore, the production of hydrogen is unlikely to be limited by high pressures.

The formation of hydrogen as a result of the reaction of aluminium with water containing environments opens the possibility of part of the hydrogen

being absorbed into the material rather than evolved as gas. It is this step that forms the initial (and crucial) aspect of the "pre-exposure embrittlement" tests and hydrogen embrittlement theories advanced by Gruhl and Swann. Pickup of hydrogen as a result of the above reaction has been accepted for many years (at least at high temperatures) and as early as 1957 Draley and Ruther (130) proposed a mechanism for hydrogen penetration of aluminium. An essentially identical mechanism was proposed later by Swann and co-workers to explain their pre-exposure embrittlement results (76). The basic mechanism of Draley and Ruther is outlined in Figure 2.17.

The oxidation (corrosion) reaction is assumed to occur by ionic migration through a barrier film.

The anodic processes occur by either outward Al^{3+} cation diffusion through the oxide or by inward $O^{=}$ anion migration.

The corresponding cathodic reactions proceeds by the outward diffusion of electrons and/or inward diffusion of protons. Draley and Ruther regard the last process as contributing significantly to the cathodic reaction whilst the anodic reaction is believed to involve the outward migration of Al^{3+}. The driving forces for proton migration are cited as the potential gradient together with a proton concentration gradient. Hydrogen is believed to be absorbed in the metal only in the atomic form (130).

The predictions and implications of the above mechanism are:
(i) Hydrogen uptake by the metal as a result of the reaction,
(ii) Formation of gaseous hydrogen at the metal/oxide interface causing increased corrosion provided the pressure is sufficiently high to cause the oxide to blister and rupture, and
(iii) Hydrogen in the metal increased by cathodic polarisation.

Draley and Ruther (130) provided evidence to support all of the above. A "considerable" increase in hydrogen content was reported in a sample exposed to water at 350°C for a "few" hours and acute surface damage was apparent. The above authors found that the addition of 1% nickel to their samples was sufficient to reduce the hydrogen pickup, under similar conditions, to non-detectable values. They attributed this beneficial effect to the ability of nickel to catalyse the formation of hydrogen gas which was believed lost to the environment (130). However, the authors were not able to determine whether the effect was due to the combination of H atoms beneath the oxide before atomic hydrogen could diffuse into the metal or whether the active liberation sites were at the oxide/moist environment interface.

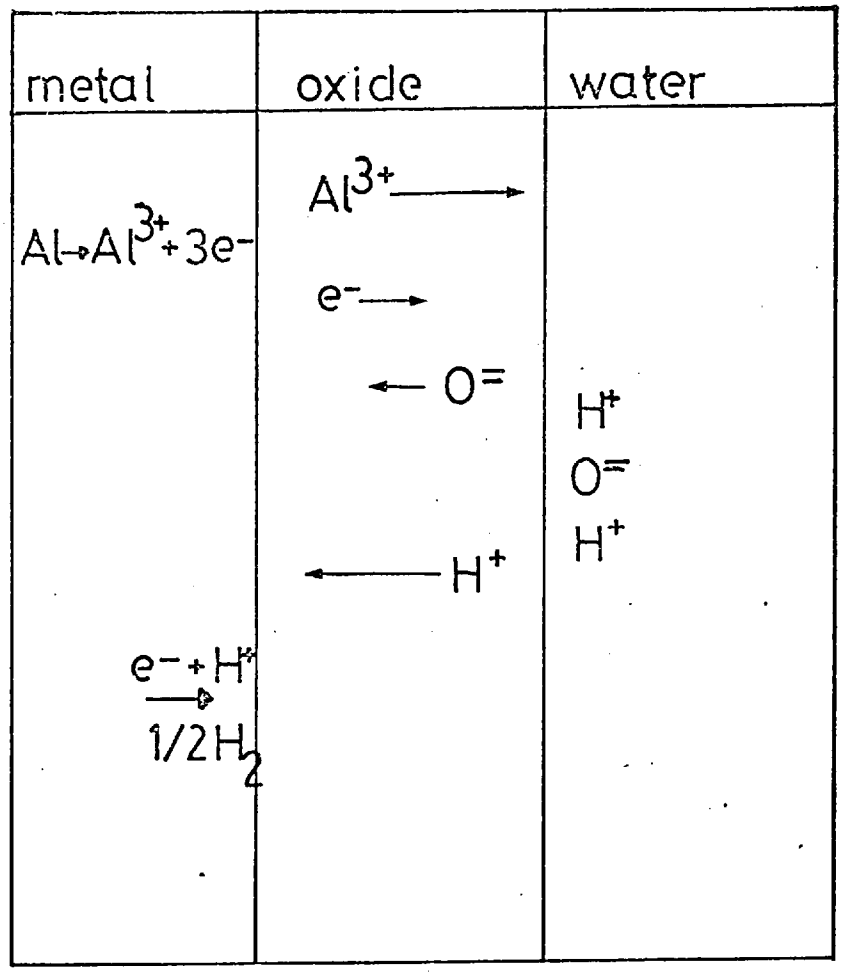


Figure 2.17. The essential steps in the introduction of hydrogen into aluminium following reaction with water. Redrawn from Draley and Ruther (130).

In support of the previous ideas several authors provide evidence showing that at high temperatures (120-520°C),
(i) the oxidation rate of aluminium is significantly increased in water vapour containing environments (131, 132, 134, 135).
(ii) the hydrogen content of samples oxidised in the presence of water vapour is appreciably increased (132, 133, 135, 136, 137).
(iii) surface blisters and internal hydrogen bubbles are formed in aluminium following attack by moist environments. Discontinuities such as grain boundaries act as preferential nucleation sites (131, 132, 133, 134, 137).

Cochran (138) examined the ability of various surface films to catalyse the atomic to molecular hydrogen reaction and thus inhibit hydrogen diffusion into the metal. Using an electrical glow discharge at reduced pressure of hydrogen he was able to show that films of tungsten, iron, cobalt, nickel, molybdenum and chromium reduce the permeability of hydrogen through the oxide. An aluminium-nickel alloy formed a film which was impermeable to hydrogen (138). Cochran has suggested that elements of high hydrogen overpotential catalyse the reaction,

$$H + H \rightarrow H_2$$

and thus reduce the amount of hydrogen absorbed in the metal. Andreev et al (139) carried out permeation studies in hydrated aluminium oxide films at high temperature and from their results concluded that hydrogen only diffuses via the defects that exist in the oxide. Indeed the role of the defects present in the oxide appear to play a crucial role in the transport characteristics of aluminium oxide. For instance it has been recently reported that additions of 0.2% MgO to α-Al_2O_3 increase the diffusion coefficient of tritium by "4 or 5 orders of magnitude" (140). The preferential oxidation of magnesium in Al-Zn-Mg alloys (109) is likely therefore to influence significantly the entry of hydrogen through the oxide.

There does appear to be some evidence in support of the proposal that diffusion of hydrogen through alumina is governed by the defect structure (139). Both Cochran (138) and Blackburn and Gulbransen (133) found that pre-treatment of aluminium samples with fluorides reduced hydrogen permeability and inhibited blister formation when such samples were oxidised at high temperatures under moist conditions. The effect of the fluoride ion was considered to be such that it inhibited the entry of hydrogen by producing an impervious surface layer of oxide/fluoride (130, 133, 138). Somewhat surprisingly pre-treatment with chloride (1M HCl solution) was also found to result in reduced blistering and hydrogen

absorption in the case of high purity aluminium (133). Eborral and Ransely (111) on the other hand, on examination of an Al-7% Mg alloy, found that inhibition of the blistering reaction was achieved by fluoride but not chloride treatments. Similarly Leidheiser and Nas (136) measured significant concentrations of hydrogen in aluminium following exposure to a 3.5% NaCl solution at 100°C for 24 hours (Table I). This value represented a substantial increase over the hydrogen content measured when similar specimens were immersed in distilled water (136) (Table I).

It appears therefore, that fluoride modification of the oxide results in a more "Protective" film which reduces hydrogen permeation. The behaviour of chloride modified oxide is less straightforward since it exhibits resistance to hydrogen permeation at high temperatures but appears to enhance hydrogen permeability in aqueous solution at lower temperatures. The low temperature behaviour can be rationalised in terms of the pitting phenomena which occur when aluminium is immersed in chloride solutions (116, 118). These result in breakdown of the oxide locally which then allows the cathodic reaction (H production) to introduce hydrogen into the metal.

The role played by HCl in the suppression of blisters at high temperatures is not clearly understood. Blackburn and Gulbransen (133) suggested that the treatment in hydrochloric acid may dissolve the impurities present in the oxide thus making it more protective. Alternatively they suggest that a chemisorbed layer of $AlCl_3$ may form which inhibits hydrogen permeation. The first suggestion is considered unlikely, especially in the light of Eborral's and Ransely's (111) results but there appears to be little evidence to guide comment on the second suggestion. The fact that blistering is not restricted in Al-Mg alloys would cast doubt on the existence of an $AlCl_3$ layer but it is not possible to accurately estimate the effect of the magnesium addition on the behaviour of the surface reactions. The existence of a chloride layer in aqueous solution is still unresolved (120, 121) but it is possible that no protection is afforded by such a layer in aqueous solutions due to a continuous hydrolysis reaction.

The observations outlined above would more clearly support a view which considers that it is the modification of the oxide by small amounts of incorporated chloride ions that control the permeability of hydrogen. Since hydrogen permeability is dependent on the defect structure of the oxide (139) it appears that in the case of pure aluminium chloride

TABLE I

HYDROGEN EXTRACTED FROM PURE ALUMINIUM AFTER EXPOSURE TO LIQUID WATER.
(from Leidheiser and Das (136))

Temperature of water	Exposure Time	Penetrated Hydrogen in ml at STP/100 g of Aluminium	
		Individual Expt. Values	Average Values
60^{o}	24 hrs.	0.146, .090, .132, .105, .097, .150	0.12
100^{o}	10 min.	0.159, .155, .138, .136, .201, .148	0.156
100^{o}	30 min.	0.156, .167, .201, .135, .140, .161	0.160
100^{o}	6 hrs.	0.130, .144, .192, .202, .168, .154	0.165
100^{o}	24 hrs.	0.172, .155, .162, .156, .170, .205	0.170
100^{o} (3.5%NaCl)	24 hrs.	0.442, .378, .540, .480, .385, .315	0.42

incorporation is sufficient to reduce or eliminate the defect mobility processes, which control the migration of hydrogen. In the case of the Al-7Mg alloy it would appear that the number of defects encouraging hydrogen mobility dominate even in the presence of chloride ions in the lattice. As outlined previously chloride ions, present in solution, strongly accelerate stress corrosion crack growth rates (1,26). Similarly additions of bromide and iodide (at concentrations greater than 10^{-2} moles/litre) increase S.C.C. susceptibility. In contrast to these the fluoride ion is conspicuous by its marginally beneficial effect (6).

These observations are consistent with the previous discussion. It seems that influencing hydrogen entry via the modification of the surface layer by the various anions induces changes in the stress corrosion cracking behaviour. Solutions that cause pitting, i.e. local oxide film breakdown (chlorides, bromides and iodides) increase the rate of attack whilst fluoride, which does not cause pitting is slightly beneficial.

Environment sensitive failure is independent of hydrogen ion concentration in chloride environments between pH values of 0-11 (6,2) (Figure 2.18). Above pH 12 general corrosion occurs. This behaviour properly reflects the theoretically predicted (118, 120) and experimentally observed (119) phenomenon of constant pH within an aluminium crack at 3.5. Sedriks et al (68) have associated this with the formation of $Al(OH)_3$ ("hydrolysis" reaction).

2.7.3. Direct Evidence of Hydrogen Entry into Aluminium-Zinc-Magnesium Alloys in Aqueous Systems

Direct evidence of hydrogen entry into Al-Zn-Mg alloys during stress corrosion conditions in aqueous systems has been provided by a number of workers (141, 142, 143, 144).

Electron microscopical studies by Alani and Swann (141) and Scamans (142) have shown that following exposure of Al-Zn-Mg alloy samples to water vapour at 70°C internal hydrogen bubbles are formed at grain boundaries. These were preferentially associated with second phase particles or dislocations if present (141). The bubbles were surrounded by strong elastic strain fields. It is also reported that bubble formation is enhanced if samples are exposed under a tensile stress (141).

The agent inside the bubbles was positively identified as hydrogen by mass spectroscopy following fracture of the samples in an evacuated chamber (77).

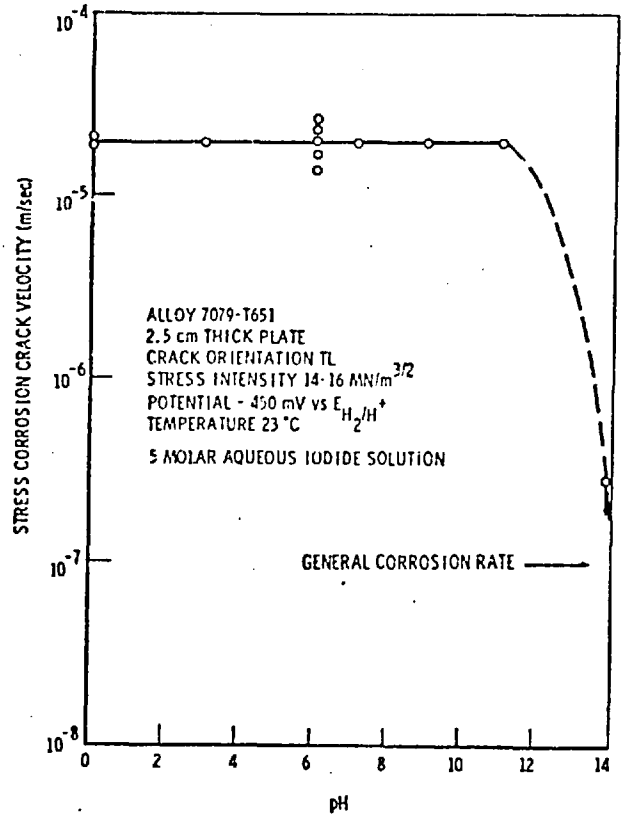


Figure 2.18. Effect of pH on region II velocity of stress corrosion cracks in a high strength aluminium alloy. After Speidel (6).

Haynie and Boyd (143) using an autoradiographic technique were able to detect hydrogen (tritium) enrichment at the boundaries of an Al-Zn-Mg alloy following exposure to a sodium sulphate solution containing Tritiated water. They also report that the application of stress to their samples increased the concentration of tritium at the grain boundaries. Cracking of some boundaries was evident in samples under stress (143).

In a similar study Grzemba and Gruhl (144) also detected tritium at the grain boundaries of a related alloy. However, they were only able to observe tritium enrichment at grain boundaries which exhibited fine cracks (144). In view of this it is not possible to establish the contribution of tritiated water to the autoradiographic labelling, and thus their results must be treated with caution (144).

From the results presented here and in the previous section (2.7.2.) it appears that hydrogen uptake can and does take place in environments which cause stress corrosion cracking of Al-Zn-Mg alloys. What needs to be resolved is the effect, if any, of the absorbed hydrogen. This will be examined in detail at a later stage, but it is interesting to note that, environment sensitive mechanical failure can occur if the prevailing conditions favour the entry of hydrogen (see subsequent sections).

2.7.4. Gaseous Environments

The effects of gaseous environments on the stress corrosion cracking behaviour of Al-Zn-Mg alloys have been summarised by Speidel (6).
The main observations are:

(i) Stress corrosion cracks neither initiate or propagate in dry gases.

(ii) Stress corrosion cracks initiate immediately from deliberately introduced pre-cracks in samples stressed to near K_{IC} and exposed to wet gases (Figure 2.19).

(iii) The path of stress corrosion cracks filled with moist gases is almost exclusively intergranular (similar to liquid metal, aqueous solution or organic solvent environments).

(iv) The general shape of the V-K curve is similar to the shape of the V-K curves in the other environments listed above.

(v) Region II (plateau) crack growth rate depends strongly on the water vapour partial pressure in the gas (Figure 2.20).

(vi) Metallurgical parameters have only a mild influence on region II crack growth.

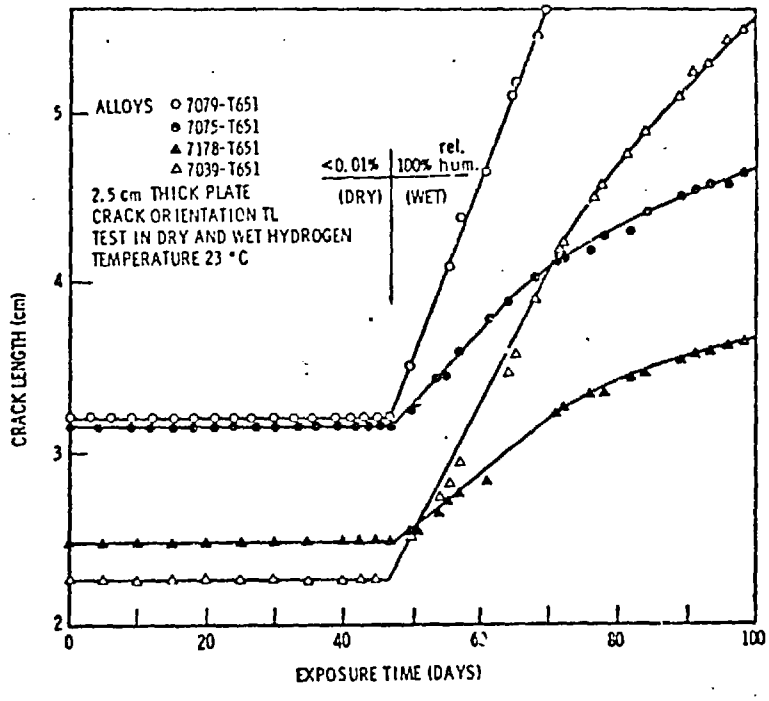


Figure 2.19. Effect of the introduction of water vapour on the crack growth rate of different aluminium alloys in hydrogen. After Speidel (6).

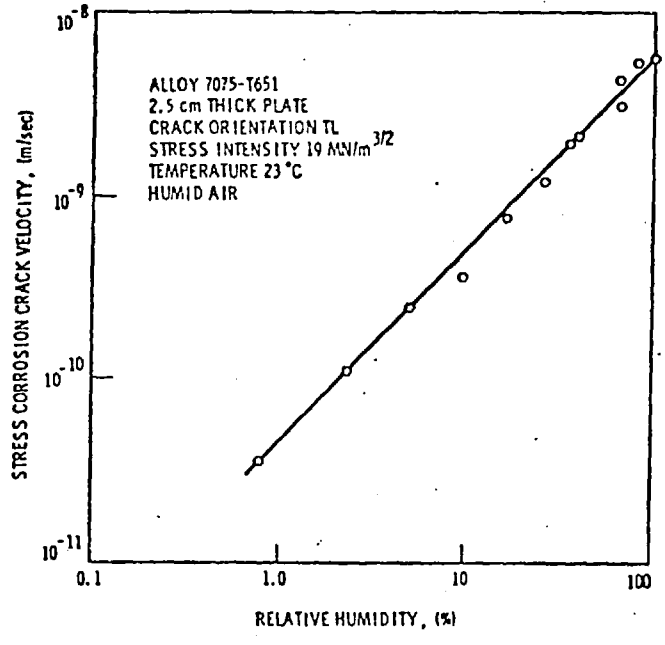


Figure 2.20. Effect of humidity of air on the stress independent S.C.C. velocity of a high strength aluminium alloy. After Speidel (6).

(vii) The stress dependent crack velocity in region I of the V-K curve for aluminium alloys is strongly influenced by the metallurgical parameters (see section 2.5).
(viii) Argon, nitrogen, oxygen and air all lead to the same kinetics of subcritical crack growth provided the humidity is the same.

It is evident from the above summary that the agent responsible for S.C.C. in gaseous environments is water vapour (Figure 2.19). In particular Speidel (149) has argued that the variation of crack velocity with relative humidity in region II (Figure 2.20) represents strong evidence that hydrogen, produced as a result of the reaction of water vapour with the alloy, is responsible for S.C.C. of Al-Zn-Mg alloys. He proposes that since condensation of water would not be expected at relative humidities below 30% then anodic dissolution cannot be responsible for crack propagation. The absence of any change in the behaviour at relative humidites greater than 30% suggests that a change of mechanism does not occur when condensation does occur in the crack. Therefore the mechanism must still be one involving hydrogen embrittlement (149). The close similarity of the stress intensity versus crack velocity curves for the majority of environments and alloys (2,6) has further suggested that the mechanism of failure under most conditions is of the same type.

2.7.5. Organic Liquids

Available results show that S.C.C. velocities in organic liquids fall into the same scatter band as those for tests in distilled water (6,44). Furthermore observations indicate that reduction of the water content of ethyl alcohol and acetone results in reduction of crack velocity. This strongly suggests that the subcritical crack growth in organic liquids is associated with the presence of water in such media. Arguments similar to those proposed for gaseous environments in support of a hydrogen embrittlement mechanism (section 2.7.4.) can be advanced here.

The fact that only traces of water give rise to crack growth rates (6) and embrittlements (44) approaching those found in distilled water is correctly predicted from the discussion in Section 2.7.2. In that it was shown that the pressure of hydrogen generated as a result of the Al/H_2O reaction does not greatly depend on the activity of the water.

2.7.6. Electrical Potential

It has been known that under cathodic polarisation the S.C.C. susceptibility is reduced (2) and this has been a major argument in favour

of an anodic dissolution mechanism operating in Al-Zn-Mg alloys.

However, more recent results show that the crack growth rate of a cathodically polarised sample can be directly related to the hydrogen permeability (6,51,146) (Figure 2.21).

The correlation between hydrogen permeability and crack growth rate, including the minimum at intermediate potentials, is a classic observation in high strength steels where there is general agreement that hydrogen embrittlement is responsible for the environment-assisted failure (3, 145). It is believed that the variation in permeability to hydrogen is governed by the oxide produced locally as a result of cathodic charging. Klimowitz and Latanision (147) suggest that cathodic charging results in the modification of the oxide which influences the access of hydrogen to the metal substrate. To support their view they have presented evidence which show that cathodic charging imposes severe embrittlement only if the electrolyte pH is allowed to rise (the oxide is believed to be less protective in highly alkaline solutions). (147).

Similar arguments were previously employed by Powell and Scully to explain the cathodic charging behaviour of titanium alloys (148).

The cathodic protection against S.C.C. at the intermediate potentials (Figure 2.21) has been attributed by Speidel (149) to a reduced dissolution (anodic) reaction with a concomitant reduction in the hydrogen production (cathodic reaction) process. Attention must also be drawn to the voltage drop (IR drop) that may be expected in a polarised sample containing deep cracks. The application of a particular potential at the surface of the specimen does not necessary imply attainment of that level of polarisation at the crack tip. The difference between the applied potential and that actually existing at the crack tip depends on the solution chemistry via the dependence on R.

The increase in hydrogen permeability and crack growth rate at anodic potentials is accommodated in the hydrogen embrittlement argument by advocating that enhanced corrosion, dissolution or pitting (expected under anodic conditions) leads to acidification and enhanced hydrogen evolution (149). Qualitative support for such a conjecture is furnished by the well known phenomenon of hydrogen pickup during electropolishing of metallic samples. (Anodic voltages run into tens of volts in most cases, and yet significant hydrogen pickup can occur.)

Discrimination between anodic dissolution and hydrogen embrittlement mechanisms cannot therefore be satisfactorily made on the evidence of

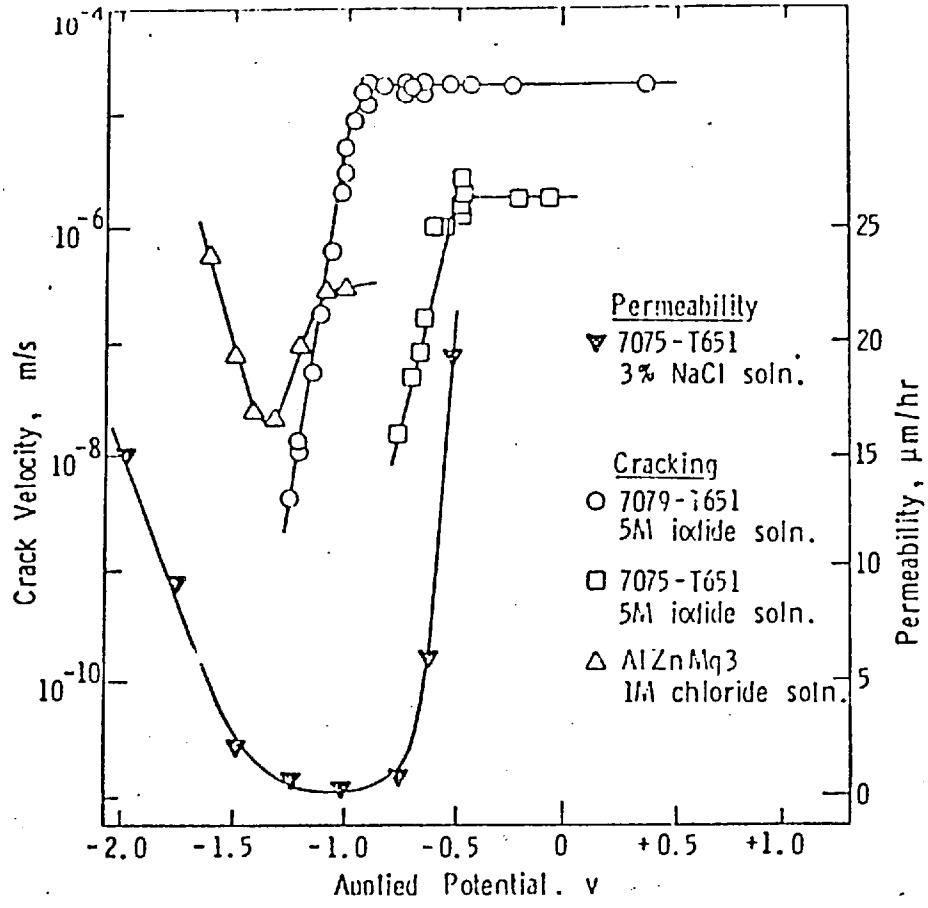


Figure 2.21. Dependence of crack velocity and hydrogen permeability on applied potential (volts vs S.C.E.) for several aluminium in various environments. From Bernstein and Thompson (3).

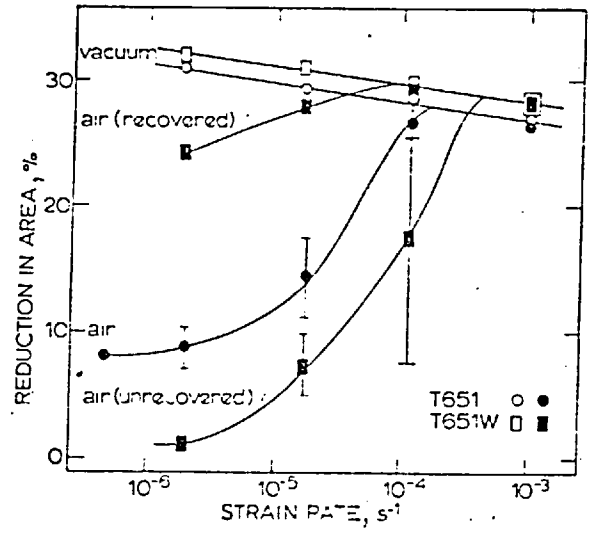


Figure 2.22. Strain rate sensitivity of pre-exposed samples. After Hardie et al (96).

polarisation tests. On examination of the electrochemical processes within cavities Ateya and Pickering (150) concluded that the electrode potential at the bottom of a cavity or crack converges toward a common value for either anodic or cathodic polarisation conditions at the outer surface. It is clear from their analysis that the nature and progress of the electrochemical processes in cracks would generally be different from those at the surface.

The effects of cathodically introduced hydrogen in Al-Zn-Mg alloys reported by Gest and Troiano (51) have been discussed (79) and successfully reproduced (78). The main observations are listed below:

(a) Absorbed hydrogen leads to brittle transgranular fracture.
(b) The degree of embrittlement is both strain rate and temperature dependent.
(c) The embrittlement is reversible.
(d) A lattice parameter expansion is associated with the uptake of hydrogen following polarisation.
(e) The permeability of hydrogen is polarisation dependent.
(f) Crack propagation is discontinuous.
(g) Ductility is restored by outgassing at room temperature.

These phenomena are classic observations of the hydrogen embrittlement behaviour of high strength steels (145, 91).

It is clear from the above results that one of the major objections to hydrogen embrittlement in Al-Zn-Mg alloys, that of cathodic protection, has been disposed of. The behaviour of the cathodically charged samples simply cannot be explained by any form of dissolution mechanism. However, the question "to what extent do the above relate to the S.C.C. case of these alloys?" can be raised. The relationship between cathodically charged samples and stress corrosion behaviour is probably quite distant, but nevertheless the importance of these results is not diminished. They conclusively prove that provided hydrogen has access to the alloys it will penetrate and cause embrittlement. An important step in the process is the transition between any adsorbed to absorbed hydrogen. The correlation between permeability and embrittlement is very important and indicates that the surface related processes are of significance.

Once hydrogen absorption occurs it is held intragranularly. This gives rise to an increase in lattice parameter. The straining of the lattice results in its embrittlement and upon application of stress brittle fracture is exhibited. The strain rate dependence and reversibility

of embrittlement suggests that the hydrogen is mobile and not associated with a hydride phase as suggested in a recent article (151). The operative mechanism would appear to approximate quite closely to Troiano's (91) original criterion which requires diffusion of hydrogen to the crack tip leading to discontinuous propagation.

2.7.7. Stress Corrosion Crack Growth in Hydrogen Atmospheres.

Nucleation and growth of subcritical cracks in high strength aluminium alloys has not been reported in dry hydrogen (2,3). This has been a significant objection to the involvement of hydrogen in S.C.C. in the past years. However, recent results show that under high pressures of high purity hydrogen (~300 Atmospheres) predeformed 7075 suffers a ductility loss when compared to samples exposed to helium (152). Koch (153) reported that the fracture surfaces of a 7075 alloy stressed in ionised hydrogen gas were very similar to those produced in a 3% NaCl solution. The author concluded that the failure mechanism was common to both environments and that it involved some type of hydrogen embrittlement effect.

It seems therefore that hydrogen gas may under some conditions induce embrittlement and fracture similar to that found in more traditional stress corrosion tests. Once again there appears to be a correlation between the opportunity of hydrogen to enter the alloy and the observed embrittlement. It should be noted that the results of Fidelle et al (150) could be regarded as achieving oxide film breakdown in the presence of hydrogen. The procedure consists of making the alloy of interest into a membrane which separates two evacuated chambers. The one chamber is filled with dry helium until the membrane is plastically deformed into a bow shape and the chamber is subsequently evacuated. Hydrogen is then pumped into the other chamber at high pressures so that the membrane is now deformed back towards the first chamber and the observed deformation compared to that observed if He is used instead of hydrogen. Embrittlement is not detected if hydrogen is simply pumped into one chamber till fracture without prior pressurisation from the opposite side. It is therefore likely that the deformation of the metal in the core of the membrane disrupts the oxide film on the outside surface which is damaged and thus allows entry of hydrogen when this is subsequently introduced.

2.8, Pre-exposure Embrittlement

Many of the results of the pre-exposure embrittlement tests have already been given, but since it was chosen in this work to assess S.C.C. susceptibility by employing such tests a summary of the previously reported results will be given below.

Typically during pre-exposure embrittlement tests the samples are separately exposed to the desired corrosive environment and subsequently mechanically tested to failure (42, 73-77, 80, 96). The resulting mechanical properties are then related to the combined but not simultaneous effect of stress and environment. The tests offer a number of advantages which include convenience and versatility. Post fracture corrosion is eliminated in these tests and thus fractographic and other metallographic techniques can be employed to examine specific aspects of the fracture. The tests also allow detection of any reversible effects of pre-corrosion. For this reason they have been most successful in detecting hydrogen embrittlement phenomena, such as reversibility of embrittlement and strain rate dependence of ductility (77, 96).

The pre-exposure embrittlement phenomenon was first reported by Gruhl (73) who found that exposure of Al-Zn-Mg samples to a 2%NaCl solution markedly reduced their stress corrosion lifetime during subsequent stress corrosion tests. The effect became more pronounced if stress was applied during the exposure treatment and could be eliminated by repeating the heat treatment cycle (73, 80). In other tests traces of water in non-aqeuous solutions were shown to be responsible for a similar effect. Gruhl considered that hydrogen was adsorbed onto the samples as a result of the corrosion reaction and that under the influence of the subsequently applied stress it diffused into the grain boundaries leading to embrittlement.

A similar pre-exposure effect has been reported by Watkinson and Scully (44) who found that exposure of an Al-6%Zn-3%Mg alloy to either a 3%NaCl solution or distilled water markedly reduced the recorded elongation of samples during subsequent slow strain rate tests.

The effect was attributed to surface pitting which provided suitable nuclei for crack initiation upon the subsequent application of stress. It is not possible to ascertain if hydrogen effects as previously suggested by Gruhl (80) played a role in this behaviour. It is not reported if storage after pre-exposure had any effect on the mechanical behaviour.

Swann and co-workers (42, 76, 77, 141) carried out mechanical tests on samples of a high purity Al-6%Zn-3%Mg alloy which had been previously

exposed to water vapour containing environments. Severe embrittlement of the samples was found. The authors concluded that deep penetration of hydrogen along the grain boundaries occurred which led to some form of low energy decohesion along the matrix/grain boundary precipitate interface (42, 76, 77).

The presence of hydrogen was shown by spectroscopically analysing the gas evolved upon fracture (42, 77) and by direct observation of hydrogen bubbles at the boundaries in an electron microscope (141). Similar observations were subsequently reported by Scamans (142).

The degree of embrittlement was found to be dependent on the temperature and relative humidity of the environment and was reduced to zero when samples were mechanically tested in vacuum (77). Quaternary additions of chromium and copper to the base alloy reduced the rate and degree of embrittlement. In the case of the chromium bearing alloy recovery of ductility could be achieved by storage in laboratory air (77). The rate of recovery was much higher than the rate of embrittlement. In agreement with the results of Gruhl the embrittlement was completely eliminated by repeating the heat treatment cycle. Embrittlement was not found to be strain rate sensitive.

The proposed mechanism (47, 76, 77) involves the penetration of hydrogen through the oxide film via a mechanism identical to that proposed by Draley and Ruther (130) which is outlined in section 2.7.2. The permeation of protons through the oxide film was assumed to be facilitated by the presence of MgO crystallites at the grain boundaries. The presence of an amorphous layer of Al_2O_3 produced by electropolishing of the samples was considered to act as a more efficient barrier to proton diffusion.

In contrast to Gruhl's proposals (80) the action of stress was not considered to be necessary for hydrogen penetration of the grain boundaries which was assumed to occur by an accelerated diffusion mechanism. Atomic hydrogen was considered as the damaging species (42, 77, 141).

In a later study Scamans and Tuck (154) carried out pre-exposure tests on Al-Zn-Mg and Al-Mg-Si alloys. They found that exposure to water-vapour saturated air at 70°C led to the development of a "brittle ring" in the Al-Zn-Mg alloy but not in the Al-Mg-Si. The "brittle ring" consisted of a zone of intergranular failure growing from the edge of the sample and was a function of sample heat treatment. The more metallurgically susceptible the alloy the greater the degree of brittle front penetration (154). The extent of the brittle front was related by the authors to a "zinc enrichment" of the boundaries which was caused

by the preferential oxidation of magnesium and aluminium at the surface. This, it was suggested, established zinc enrichment at the surface and under the influence of the resulting concentration profile zinc diffusion occurred back down the boundary. Zinc was assumed to increase the chemisorption of hydrogen leading to embrittlement.

In a very recent study Hardie et al (96) carried out experiments in an attempt to reproduce the results of Swann and co-workers in a commercial alloy. Their results which included immersion in various solutions before mechanically testing were in very good agreement with those earlier reported by Swann et al (77). Embrittlement of the samples was detected following immersion in water for periods in excess of five hours. Embrittlement was most easily detected at slow strain rates (below $10^{-5}s^{-1}$) and was completely reversible in vacuum and even in laboratory air, provided sufficient holding time was allowed (100 hours). The recovery of ductility was associated with a change in fracture mode (intergranular to 'ductile'). The rapid recovery under vacuum reported by Scamans et al (77) was also reproduced, suggesting rapid hydrogen removal (96). Both from their embrittlement and recovery rates Hardie et al calculated a hydrogen diffusion coefficient in the range of $9 \times 10^{-8} - 10^{-7}$ cm^2 s^{-1}. The lowest value is considered as an underestimate because it refers to the time necessary to observe intergranular fracture in the centre of the samples and does not take into account the incubation period necessary for the alloy/water reaction to occur (96). However, this should be short ~1 minute (124). The major deviation between Hardie's (96) and Scamans' et al (77) results is the strain rate sensitivity observed in the former case (Figure 2.22). A possible explanation for this deviation will be given in "Discussion" and it is believed that this is related to the difference in grain size between the alloys, It should be pointed out here that the tests of Hardie et al were carried out on a commercial alloy whilst Swann and co-workers dealt with high-purity samples. Significant differences in grain size should therefore be expected between these alloys (~150 μm in the high-purity alloy whilst the grain size of 7178 is unlikely to be more than 50 μm (on the basis of the presented micrograph this appears to be ~25 μm. No grain size measurements are given by the authors.)

During their pre-exposure tests Scamans and Tuck (154) investigated the penetration of hydrogen through a membrane of an Al-Zn-Mg alloy separating two gas tight chambers. The membrane was exposed to water vapour on one side and maintained dry on the other. Following exposure

times of 5-10 days hydrogen was detected in the dry chamber. This was attributed to the penetration of the membrane by hydrogen which was produced in the "wet" side as a result of the corrosion reaction between the alloy and water vapour. From their measurements the authors (154) calculated a diffusion coefficient at 70°C at 10^{-10} cm^2/sec. This is comparable to the values given by Gest and Troiano (51) (2×10^{-9} cm^2/sec) from their cathodic charging experiments and Montgrain and Swann (42) (5×10^{-10} cm^2/sec) from their pre-exposure embrittlement results.

Significantly no hydrogen penetration was evident if the membrane was made up of an AlMgSi alloy even though hydrogen generation had occurred (this was shown by analysis of the gases in the "wet" cell) (154). AlMgSi alloys do not suffer from S.C.C. (2). Furthermore, the buildup of hydrogen in the dry half-cell was increased when the Al-Zn-Mg membrane was heat treated to a stress corrosion susceptible condition.

The implications of these observations are important. Firstly, they indicate that non-susceptible alloys are not penetrated by hydrogen. Furthermore, susceptibility is related to the ease of permeation by hydrogen, a correlation not unlike that found from the polarisation tests (2, 51, 146) (see Section 2.7.6). It is not clear from Scamans' and Tucks (154) results if the rate limiting step is the diffusion of hydrogen through the oxide or the metal and therefore it is not possible to establish whether non susceptible alloys and tempers restrict diffusion of hydrogen by modification of the microstructure or inhibit hydrogen uptake at the hydrated oxide.

2.9. Electron Irradiation Induced Corrosion

A substantial part of the work carried out during the course of this research programme has been concerned with the examination of the Al-Zn-Mg/H_2O reaction "in-situ" in a high voltage electron microscope. As a consequence of the use of such a technique the corrosion reaction occurs under the influence of the electron beam and the effect of electron irradiation on the observed reaction must be considered. A detailed description and discussion of the experimental technique and possible irradiation effects is given in the appropriate sections in chapters 3 and 5 and thus will not be discussed now. However, an outline of the phenomenon will be given here.

The only previously reported work is that by Flower and Swann (155) and Flower (156). The examination of the Al-Zn-Mg/H_2O system to be

reported in this work forms an extension of the work reported in the above papers (155, 156) and during the discussion of the results extensive reference will be made to them.

The initial work on the electron irradiation induced corrosion phenomenon (155) was carried out on single crystals of silicon. It was found that at low temperatures the silicon substrate reacted with the deliberately introduced moisture in the electron microscope environmental cell (Chapter 3) under the influence of the electron beam. As a result of electron irradiation under the moist environment it was found that a surface reaction occurred which produced hydrated silica and hydrogen (155). The colloidal silica produced formed surface blisters which were internally pressurised by the hydrogen. The phenomenon was interpreted as arising from an ionisation damage mechanism operating on the Si-O bonds which involved the passage of water molecules through the silica and their subsequent reaction with the silicon surface.

Subsequent work on aluminium and magnesium (156) has shown that the phenomenon is not unique to silicon. The damage process responsible for the observed reaction (growth and blistering of the surface oxide) was identified as again involving ionisation damage to the oxide which is accompanied by lowering of the metal/oxide bond strength. This led to decohesion of the growing oxide under the influence of the high pressure hydrogen produced by the reaction(156). The critical blister diameter for decohesion was shown to be inversely proportional to temperature. It was shown in that work (156) that assuming that the decohesion of the oxide does not involve plastic deformation and using the standard Griffith equation, the pressure, P, of hydrogen required for decohesion is given by

$$P = 4d \sqrt{\frac{4E\gamma}{\pi}} \cdot b^{-3/2} \quad \text{where}$$

d = blister thickness

E = Youngs modulus

γ = metal/oxide interfacial energy

b = blister diameter

Furthermore by relating the amount of hydrogen produced to the amount of oxide reaction product it was also shown that

$$P = \frac{6n\ d\rho\ RT}{Mb} \quad \text{where}$$

ρ = oxide density

M = oxide molecular weight

n = number of moles of hydrogen produced per mole of oxide

Combining the above equations it was shown (156) that the blister diameter at decohesion was given by

$$b_{\text{decohesion}} = \frac{16E\gamma M^2}{9\pi n^2 \rho^2 R^2 T^2}$$

This equation correctly predicted the experimentally observed blister diameter/temperature dependence. An approximate surface energy value (γ) was also obtained from the above equation ($\sim 1 J/m^2$). It was observed in the above work that at any temperature initial, observable corrosion was detected at a constant total electron dose regardless of the dose rate (156).

3. EXPERIMENTAL PROCEDURE

3.1. Alloys and Heat Treatments

The alloys used in this investigation were based on a high purity Al-Zn-Mg alloy supplied by Alcan (UK). The compositions are shown in Table II which also shows the compositions of some related commercially available alloys.

25 mm slabs were sliced from the supplied cast billets and hot rolled to a thickness of 1 mm. The entry temperature was 450°C. Following homogenisation at 450°C the alloy strips were cold rolled down to a thickness of 0.50 mm.

The oxide formed during the working sequence was removed by chemical polishing either in a concentrated sodium hydroxide solution at 70°C or in a mixture of 15% Nitric acid and 85% Phosphoric acid at 85°C. The sodium hydroxide solution produced slight grain boundary etching.

Sheet tensile specimens of 15 mm gauge length were stamped out and given a further short polishing treatment, followed by a vigorous wash in successive baths of distilled water and finally ethanol. All samples were then given a final degreasing wash in an ultra-sonic cleaner using "inhibisol".

The standard heat treatment, following the working sequence consisted of a solution treatment at 450°C for 1 hour followed by a cold water quench. Selected samples of the copper bearing quaternary alloy were solution treated at 500°C, furnace cooled down to 450°C, held for 1 hour and then cold water quenched. This heat treatment was carried out in order to increase the grain size of the 6/3 Cu alloy to a value close to that of the high purity base material.

All solution heat treatments were carried out either under a flowing, dry, high purity argon atmosphere in a horizontal furnace (450°C treatments), or in sealed glass tubes containing dry argon (500°C treatments). All subsequent heat treatments were carried out in sealed tubes containing dry argon or dry air.

3.2. Exposure Tests

During the entire course of this work there was a firm commitment to minimise the time that samples were exposed to water vapour containing environments such as laboratory air, moist solvents, etc., other than as a result of deliberate experimental exposure. Such deliberate exposure was

TABLE II

Compositions (wt%) of experimental alloys and related commercially available alloys.

Alloy	Cr	Cu	Fe	Mg	Mn	Si	Ti	Zn	
High Purity Base (6/3)	0.01	0.002	0.01	2.9	0.002	0.01	0.01	6.1	Balance Al
Cu containing experimental alloy (6/3 Cu)	0.001	1.7	0.02	3.0	0.001	0.01	0.01	6.3	
Cr containing experimental alloy (6/3 Cr)	0.14	0.003	0.01	2.99	-	0.02	-	6.11	
Commercial 7075	0.11	1.4	0.3	2.6	0.2	0.15	-	6.2	
Commercial 7079	0.2	0.6	0.4	3.3	0.2	0.3	0.1	4.3	
Commercial 7178	0.o8	2.0	0.5	2.5	0.3	0.4	0.2	6.5	

carried out by placing samples above a pool of distilled water in sealed vessels. The environment was therefore water vapour saturated air (w.v.s.a.). Dry control specimens enclosed in sealed glass tubes were placed in the same vessels at positions adjacent to the exposed ones. Two temperatures of exposure were used: 70°C and 120°C. The 120°C exposure tests were carried out in an autoclave at a steam pressure of 2.06 bars. Temperature control was between +1 and -3°C. The 70°C series of tests were carried out in an oven with a temperature stability of ±1.5°C.

3.3. Cathodic Charging

Selected tensile samples were cathodically charged as a way of introducing hydrogen into the specimens. A current density of 0.2 A/cm^2 was used in a 2% solution of H_2SO_4 with a small amount of sodium arsenate as a hydrogen recombination poison. No potentiostatic control was employed.

3.4. Mechanical Testing

Immediately following their heat treatment (either wet or dry) the samples were tested in an "Instron" tensile testing machine. The majority of tests were carried out in laboratory air at a strain rate of $10^{-3}s^{-1}$. A small number of tests were carried out using a range of slower strain rates down to $10^{-5}s^{-1}$. During these tests the samples, both wet and dry, were surrounded by magnesium perchlorate powder in order to minimise the effect of any water vapour in the testing environment.

At least four samples were tested for each condition of heat treatment and exposure to water vapour. The larger grained high purity alloy showed the greatest scatter and it was deemed necessary to carry out at least six tests on material exposed at 120°C in order to increase the level of confidence in the results.

3.5. T.E.M. Specimen Preparation Techniques

Specimen preparation for transmission electron microscopy was carried out using standard surface preparation techniques. Two solutions were used : (i) 20% perchloric acid in ethanol at -20°C at a potential of 20 volts and (ii) 30% nitric acid solution in methanol. The temperature was kept below -30°C and the potential was controlled in the range of 12-13 volts. The perchloric acid solution resulted in excellent foils when used for the high purity and chromium containing alloys but was less satisfactory when used to polish copper bearing samples.

Copper was found to be redeposited on the surface of the foil. The 30% solution of nitric acid in methanol on the other hand performed equally well in all the alloys: therefore this was used to produce all subsequent foils employed. No copper redeposition was evident using this electrolyte.

The majority of thin foils examined were prepared by the "window" technique. Whilst this is a rather slow procedure it offers greater control of the thinning process and normally results in very large electron transparent areas. A small number of "disc type" thin foils were prepared using commercially available thinning equipment. A 20% solution of nitric acid in methanol at -20^{o}C was used. The resulting foils were of good quality and would be adequate for most routine investigations. Grain boundary etching and oxide film thickening were the most common defects, but these could be kept at a minimum by utilising low temperatures.

In order to determine whether the surface preparation techniques affected the results by introducing artifacts into the samples a number of specimens were ion beam thinned using an argon beam at 5.6 kV. The electron transparent foils resulting from this technique were of lower quality, due to displacement damage and oxidation by residual traces of oxygen in the chamber.

3.6. Electron Metallography

Electron metallographic techniques were used extensively in order to:

(1) Investigate hydrogen bubble formation in exposed material,
(2) Follow the microstructural changes that occurred as a result of ageing and exposure at 120^{o}C.
(3) Examine "in-situ" the reaction between the alloys and water vapour. and
(4) To relate the above to the "bulk" reaction between the alloys and water vapour.

Three instruments were employed. An AEI EM7 high voltage electron microscope (H.V.E.M.), a Philips EM301 and a JEOL 100 CX TEMSCAN. The instruments provide a range of facilities and between them offer the opportunity to carry out high resolution conventional transmission microscopy (CTEM), high resolution scanning and scanning transmission microscopy (SEM and STEM) and "in-situ" transmission microscopy.

3.6.1. Hydrogen bubble formation and microstructural changes

Standard techniques in transmission electron microscopy were used to examine the phenomenon of bubble formation and precipitation as a result of ageing treatments. High resolution CTEM of the samples was carried out in the Philips 301 and JEOL 100 CX microscopes but a large number of thicker foils were also examined in the HVEM.

All specimens used for hydrogen bubble investigations were prepared from material which had been exposed to water vapour containing environments in the bulk form, i.e. they were not less than 0.2 mm in thickness. The majority of examinations were carried out on specimens which were thinned from the standard tensile specimens used in mechanical testing.

Examination of thick foils was carried out in an attempt to minimise any atypical results arising from the use of very thin foils. Thin foils can give rise to atypical results as a consequence of their high surface/mass ratio. In particular, during in-situ experiments there exists a critical specimen thickness that must be exceeded before bulk behaviour can be anticipated. For instance recrystallisation of deformed aluminium does not occur at the foil edge and bulk characteristics are only found in regions of 1.5μm in thickness or greater (157). Additionally, depletion of a reactive alloying element in the course of a surface chemical reaction will be expected to occur more rapidly in thin foils than in thick ones.

Excessive loss of hydrogen to the surfaces of very thin foils, is another, specific example of a possible disadvantage relevant to this work.

A substantial increase in specimen penetration and hence maximum usable foil thickness, was achieved by using high accelerating voltages in the AEI EM7. An fourfold increase in specimen thickness is possible for equivalent resolutions between 100 and 1000 kV (158). In the environmental in-situ experiments where it was necessary for the beam to penetrate the test atmosphere as well as the sample the advantages of higher voltages were significant. However, accelerating voltages are limited by radiation damage effects which occur as a result of electron irradiation. These are of several types. Atomic displacement damage occurs if electrons are of sufficient energy to displace atoms from their lattice positions. There exists a threshold potential below which atomic displacement damage is not encountered (158). Above the threshold the rate of damage increases with electron energy. The primary defects produced

are vacancies and interstitials. In the case of aluminium it is reported that the threshold potential is 166 kV. In common with other crystalline solids it is orientation dependent (158).

The primary defects may collapse and form interstitial or vacancy loops and/or voids (secondary defects) which are visible in the electron microscope. The distribution of secondary defects is not uniform throughout the foil thickness as point defects generated close to the foil surfaces can escape to the surfaces and be annihilated (159).

Ionisation damage is a different form of damage that may occur. This involves the excitation of bonding electrons. It occurs at all accelerating voltages but since the ionisation cross-section decreases with increasing incident electron energy this form of damage decreases with increased operating voltage. The forms of visible damage that can result include polymerisation and depolymerisation of organic molecules and bond rupture and loss of crystallinity in inorganic and covalently bonded crystals.

Great care must therefore be exercised when carrying out in-situ experiments where the above effects could influence the reaction taking place.

In this work the primary objective was to simulate bulk behaviour and to obtain an insight into the mechanism of the phenomenon of environment sensitive failure. Possible atypical behaviour of very thin foils was therefore undesirable and examination of thick foils was mandatory. This inevitably required the use of accelerating voltages above the threshold for displacement damage. A compromise accelerating potential of 500 kV was generally employed with limited experiments at 300 kV and 100 kV to examine the influence of displacement damage. Operation at 500 kV allowed penetration of relatively thick samples (4μm) without excessively fast build up of visible displacement damage.

3.7. In-situ High Voltage Electron Microscopy

The in-situ examination of Al-Zn-Mg/H_2O vapour reaction in the gas reaction cell of the HVEM formed a substantial part of this work. A comprehensive review of the state-of-the-art in in-situ microscopy has recently been published and reference may be made to that for detailed discussion of the currently available techniques (160).

The experimental technique employed is based on the use of a differentially pumped, aperture type environmental cell, which can be placed in the objective pole piece of the microscope. A schematic

representation of the arrangement is shown in Figure 3.1.

3.7.1. Environment

The experimental arrangement allows the environment of interest to be introduced into the specimen directly as shown in Figure 3.2. The specimen chamber forms part of a large reservoir as indicated in Figure 3.1. The large volume (~500 ml) associated with the reservoir is needed to give good pressure stability at steady state conditions.

The pressure was varied by controlling the rate of gas entry into the reservoir by means of a needle valve. Measurement of pressure was carried out at the inlet port of the cell.

The first two apertures, above and below the specimen are of 100μm diameter and limit the leakage of gas into a differentially pumped region (Figure 3.2.) Differential pumping was carried out using a turbomolecular pump mechanically isolated via a bellows arrangement to minimise vibration. The use of a turbomolecular pump was preferred over other types (e.g. diffusion pumps) due to its relative cleanliness.

The differentially pumped region is itself separated from the high vacuum in the microscope column by two 200μm apertures. These reduce the leak rate into the column to a value which can be dealt with by the column pumping system. The high pressure region was therefore maintained at a state of dynamic equilibrium by balancing the gas flow with the leak rate through the apertures.

The particular cell used during the course of this work can be used at pressures approaching one atmosphere (161). However, the pressure used was limited to a value which was subjectively judged as providing adequate image resolution and contrast while maintaining environmental conditions not too far removed from those employed in the bulk studies.

Water vapour was introduced into the cell by using helium as an inert carrier gas. Electron scattering by helium is low and is associated with single scattering events as opposed to gases of higher atomic number where multiple effects are significant (161). Under these conditions a total gas pressure of 100 torr was employed. The partial pressure of water vapour present at any temperature is shown in Figure 3.3.

Specimen tilt of $\pm 20^{o}$ about the specimen rod axis was possible together with normal translation facilities. Tilting is essential as the contrast mechanisms operative result from diffraction. Diffraction

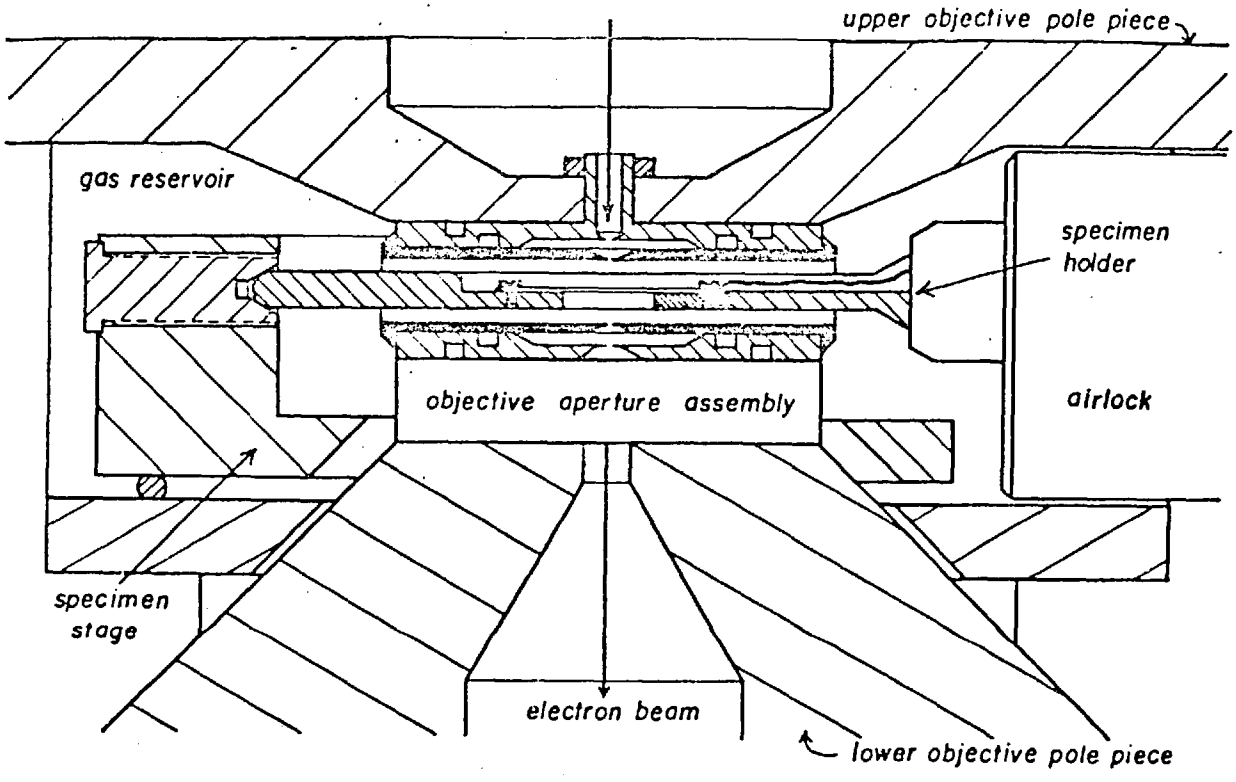


Figure 3.1. General outlay of the environmental cell in the H.V.E.M. (After Swann et al (161))

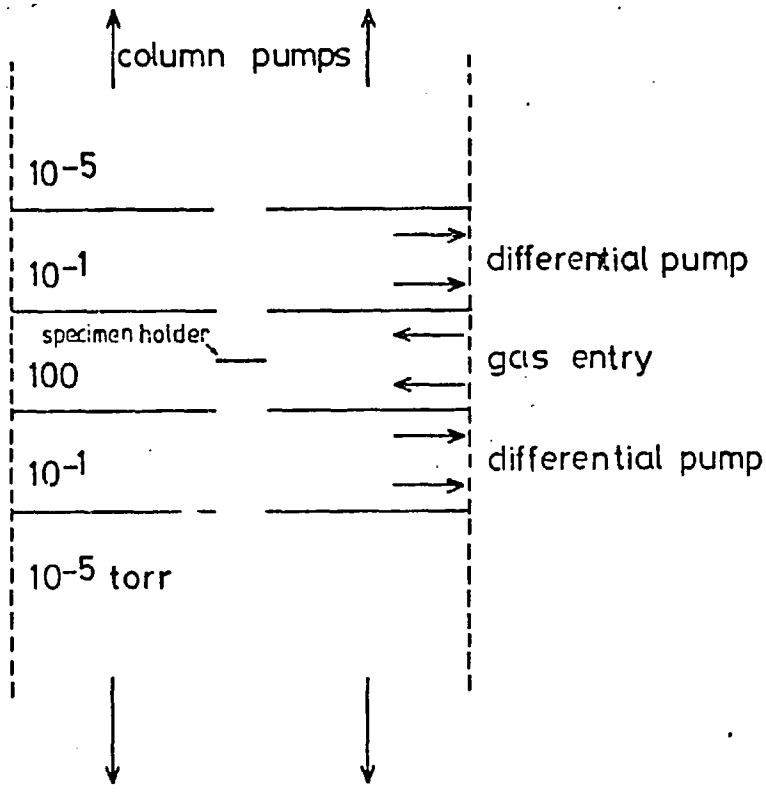


Figure 3.2. Schematic representation of experimental arrangement which allows high pressures to be attained within the specimen chamber.

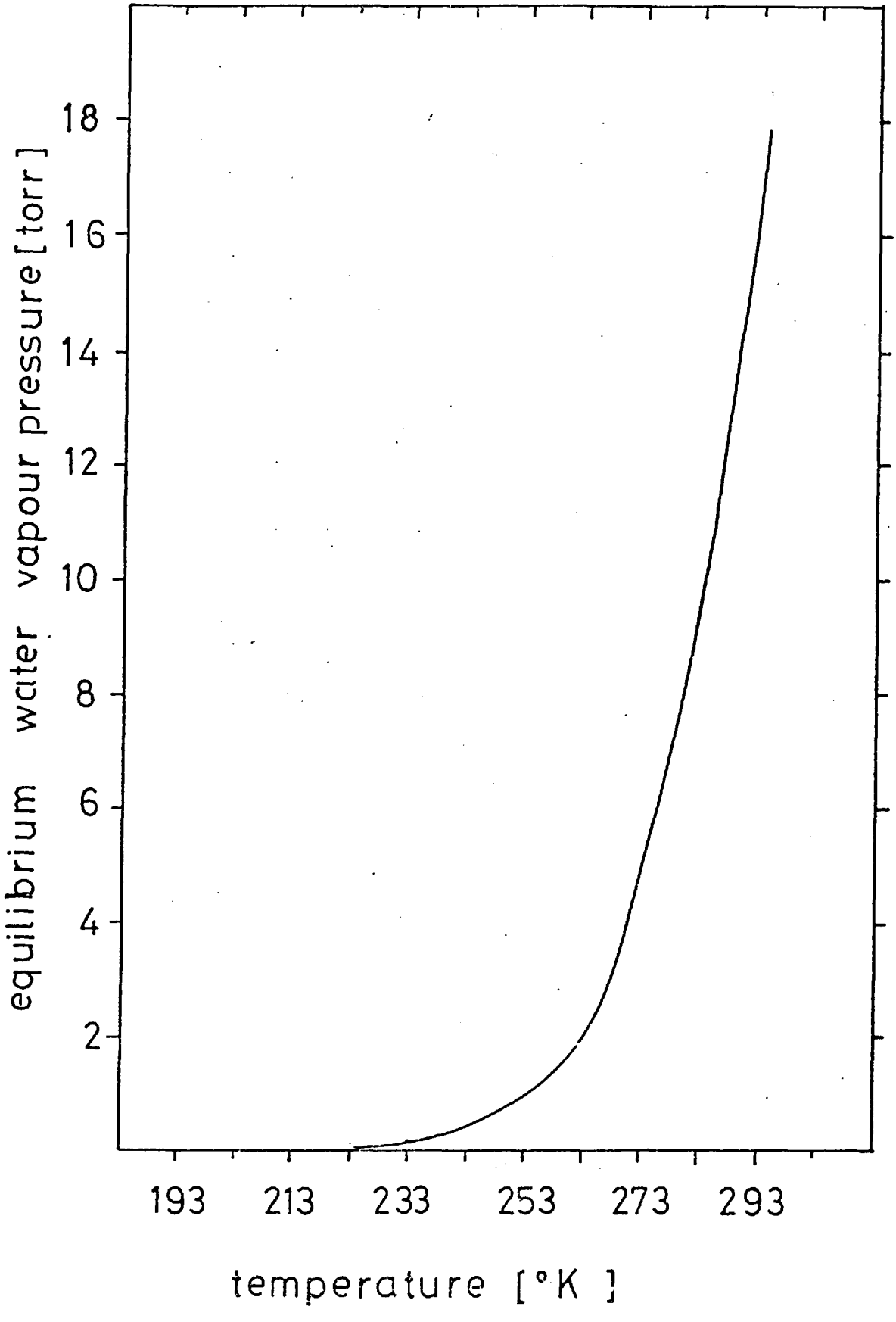


Figure 3.3. Variation of water vapour pressure with temperature.

data however, were confined to Bragg angles less than about 10^{-2} radians due to the limits set by the cell apertures. It was therefore not possible to identify the hydrated film resulting from the reaction. Normal bright field operation was not affected.

3.7.2. Temperature

In conjunction with the environmental cell both cooling and heating stages may be used (160, 161). A liquid nitrogen cooled stage was used, in this work.

There were a number of factors that made use of the cold stage desirable. Firstly it allowed accurate control of the specimen temperature. This was considered important in view of the fact that excessive beam heating effects were undesirable and could not be easily accounted for. Secondly use of subzero temperatures led to reaction rates that were sufficiently slow to allow easy image recording. This also permitted the examination of the early stages of the reaction.

The lower limit of usage was set by the heating effect of the gas which entered the chamber at a temperature of about 293K. Heat gains due to the light helium gas are significant and contribute to the radiation and conductive heat gains from the pole piece that are dominant when cold stages are used under high vacuum conditions.

The temperature of the moist environment also determines the equilibrium activity of the water vapour in the system. At room temperature the vapour pressure of water is 22.87 torr (2340 Pa). This is reduced to 2.5 torr(260 Pa) at $-10^{o}C$ and to only 3×10^{-2} torr (3.95 Pa) at $-50^{o}C$. (Figure 3.3.) Therefore a variation in temperature of the stage not only leads to a change in the reaction kinetics via the "1/RT" factor of the Arhenius equation but it also changes the activity of any water vapour present in the system.

A temperature of 253K was generally used with selected experiments over the temperature range of 213-293K. The estimate of the vapour pressure inside the cell is difficult since the pressures read from Figure 3.3. represent values expected to be found if the entire system were at any particular temperature. Clearly that condition was only fulfilled during experiments carried out at ambient temperature. Under all other conditions the system was under non equilibrium conditions where the inlet temperature of the gas was close to room temperature while the specimen was at the lower set temperature. It is likely that the cell

walls were also at high temperature, i.e. the temperature of the objective lens pole pieces ($20^{o}C$). The values of water vapour pressure indicated in Figure 3.3. therefore represent the lower limit of the existing vapour pressure and would only be true for gas immediately in contact with the body of the stage. Since the reaction occurs between the sample and any water molecules which are in contact with it, however, these values would be expected to be good approximations to the relevant vapour pressure.

Temperature measurement was obtained by means of a thermocouple placed in the stage body adjacent to the specimen. It is likely that the specimen was at a slightly higher temperature as the limiting heat transfer process is conduction between the stage body and the clamping ring holding the sample. Estimate of the temperature difference is difficult but is likely to be very small due to the proximity of the thermocouple to the specimen and the high conductivity of the all metal system at that point.

3.7.3. Electron Flux Density

The electron flux density was controlled and generally kept at a value of $5 \times 10^{+3}$ A/m^2 or less. Local beam heating at this flux density is minimal and any temperature rises are small. Fukamachi and Kikuchi (162) concluded from their experiments that at a current density of 3×10^{3} A/m^2 the temperature rise in an aluminium sample was less than 10K. Makin (163) using a copper sample recorded a temperature rise of less than 1K of a result of direct beam heating. This was considered negligible compared to the contribution from radiant heating from the objective aperture which was found to be several times greater.

The rate of any irradiation damage processes is also directly related to the electron flux density. The effect of this on the reaction will be discussed in detail at a later stage.

3.7.4. Image Recording

Video recordings on an IVC recorder, of the specimen image was carried out using a JAI 730 camera. This provided a continuous record of the reaction enabling successful recording of rapid changes, e.g. dislocation motion. A degree of image intensification was obtained in the system used. The minimum useful screen intensity which could be used was increased by a factor of 100 (164). This was important as it facilitated examination of thick regions and minimised electron beam induced phenomena.

3.7.5. Contamination

The most common source of contamination in electron microscopes is oil vapour originating from the diffusion pump and O-ring grease. Carbon is deposited on samples as a result of a complex interaction between the oil molecules beam and specimen surface.

In the EM7 HVEM silicone oil vapour is found in the camera chamber which travels up to the specimen area. With the gas reaction cell installed the diffusion of such vapour into the specimen chamber was considerably reduced as a result of the limiting effect of the cell apertures. Two other factors helped to reduce contamination in the gas reaction cell. Firstly the outward flow of gas from the high pressure region virtually eliminates "back streaming" of oil vapour past the apertures. Secondly, the cold stage holder acted as an excellent "cold finger" in a similar manner to that of cold traps in conventional microscopy. The fact that the holder was at a slightly lower temperature than the specimen increased the probability of contaminants depositing on the stage in preference to the thin foil.

Any residual contamination in the gas reaction cell is derived from the translator and aperture drives (156). To minimise such contaminants overnight pumping of the entire system was carried out prior to any series of tests.

3.7.6. "In-situ" straining

The opportunity of applying a stress to the sample in the presence of water vapour in the gas reaction cell offers a unique facility for studying stress corrosion cracking of Al-Zn-Mg alloys. It was the purpose of this part of the research programme to assess the feasibility of such experiments.

A straining stage made by GATAN Inc. was examined and its performance in the environmental cell was investigated. The load is applied to the specimen by a relatively strong spring which is relaxed by the thermal expansion of a wire. The wire is heated by the passage of a regulated DC current which can be accurately controlled. A load of 2 Kg is possible and the maximum crosshead displacement is of the order of 1000 microns.

The most crucial aspect of "in-situ" deformation studies is specimen preparation and insertion into the stage. Samples must be thin enough to be electron transparent and allow realistic levels of strain to be attained but at the same time be sufficiently robust for handling.

Handling damage of the thin foils proved the limiting process. The most satisfactory specimen geometry is shown in Figure 3.4. Following spark machining of the grip holes the samples were chemically polished down to a thickness of 0.1 mm. They were then electropolished using a commercially available system to produce electron transparent regions. The resulting geometry allowed easy handling of the sample due to the thick material surrounding the thin areas. The thick material at the edge however, considerably reduced the amount of strain that could be applied for the maximum load. Cutting of the thick edge by a surgical scalpel was unsatisfactory and led to considerable deformation of the foil.

The stress distribution in a sample with a central perforation under tension is non uniform and is shown schematically in Figure 3.5. The stress distribution in the sample was further complicated by the presence of notches or discontinuities which acted as stress concentrators. These were present on most foils and were due to the surface preparation technique.

3.8. Bulk Surface Studies

The samples used to examine the surface reaction between the alloys and water vapour were given the standard surface preparation treatment outlined in section 3.5. and then stored in a dry dessicator for 24-72 hours. In order to ensure that standard "clean", surfaces were indeed present a large percentage of the specimens was examined using secondary electron imaging in the JEOL 100CX microscope prior to exposure. To investigate possible artifacts introduced by electron irradiation of the surfaces during scanning electron microscopy at this stage, the results from these samples were compared to those that were not examined. No differences were found.

Exposure of the samples was carried out as before in sealed vessels at 70°C, or in an autoclave at 110°C. (The limitation to a temperature of 110°C during the surface reaction studies was imposed as a result of equipment failure). Specimens were simply placed in clean, open ended tubes which allowed free access to water vapour. They were then removed, dried in a vacuum dessicator and inspected in the JEOL 100 CX microscope under secondary electron imaging conditions. Use of thinned material permitted examination of samples in the transmission mode. Diffraction data could thereby be obtained.

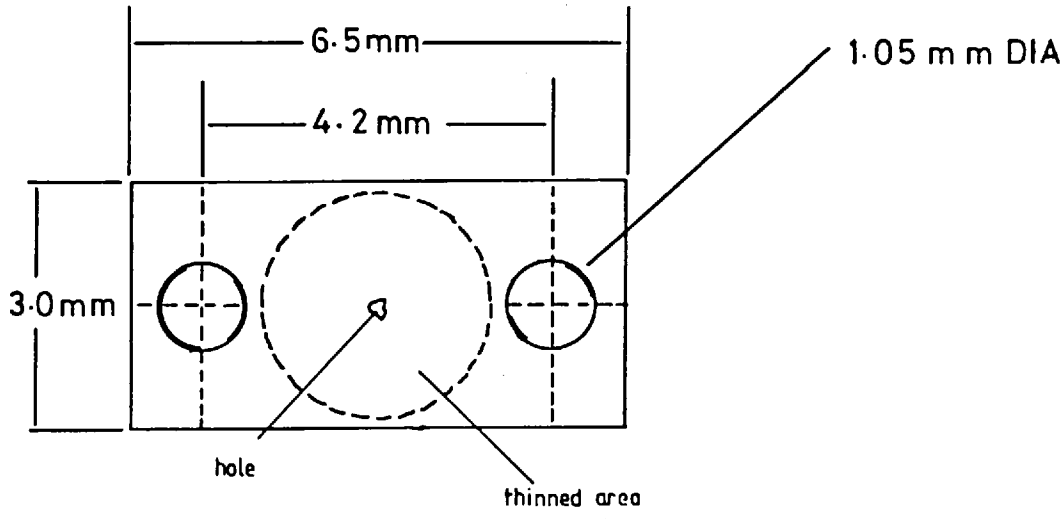


Figure 3.4. In-situ straining sample geometry.

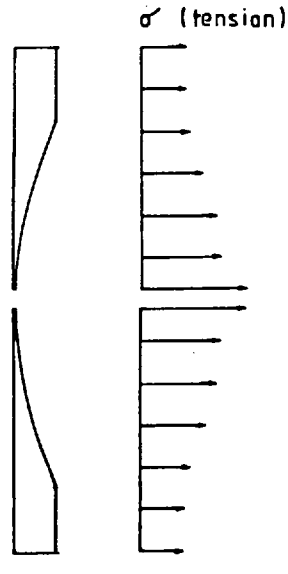


Figure 3.5. Stress distribution in a sample with a central perforation under tension.

Some samples were examined and then re-introduced to the test environment for continued exposure while others were examined only at the end of the test period. Possible artifacts produced by test interruption could therefore be assessed.

It was found that following prolonged exposure tests the hydrated oxide formed on the surface gave rise to significant charging of the specimen. It was then necessary to vapour deposit a layer of gold ($\sim$150-200Å thick) to obtain satisfactory images.

4. RESULTS

4.1. Exposure Tests

4.1.1. Isochronally aged 6/3 base alloy exposed at 70°C

In order to investigate the effect of ageing condition on the exposure characteristics of the 6/3 base alloy solution treated tensile samples were aged dry for 24 hours in the temperature of 70-200°C and then exposed to water vapour saturated air (w.v.s.a.) at 70°C. The time of exposure was fixed at 72 hours. Tensile tests were then performed on these samples and similarly aged dry control specimens.

The results are summarised in Figure 4.1. It was apparent that embrittlement of the underaged alloy had occurred as a result of the exposure to w.v.s.a.. The ductility of the "wet" samples appeared to be significantly lower for all treatments up to 140°C but above this temperature there was no difference, within experimental error, between the dry and wet sets of data.

The change in ductility of the dry samples is caused by the precipitation reactions which take place on ageing. Minimum dry elongation was observed in specimens aged at about 120°C for 24 hours: the alloy is close to peak strength at this ageing condition. Figure 4.1. shows that the insensitivity of the alloy to the exposure environment is closely related to the onset of overageing which occurs as a result of the treatments at 140°C or higher. This observation is in very good agreement with results reported in the literature concerning resistance to stress corrosion cracking (1,2,3).

Transmission electron microscopy showed that the only significant difference between dry and wet material was the presence of a strain field image (characteristic of "bubbles" (141, 142)) on grain boundary particles in samples which had been aged above 120°C (Figure 4.2.) No bubbles were detected in material aged at lower temperature and bubble formation in material aged at 120°C was sporadic. At all times bubbles were associated with grain boundary particles.

The average grain boundary precipitate sizes were found to be approximately 70A at 70°C, 200A at 120°C and 350A at 150°C. At 200°C the particle size increased to a value greater than 750A. Accurate measurements of particle sizes were difficult since their size was a function of the character and orientation of the grain boundaries on which they were formed. For instance high angle boundaries exhibited

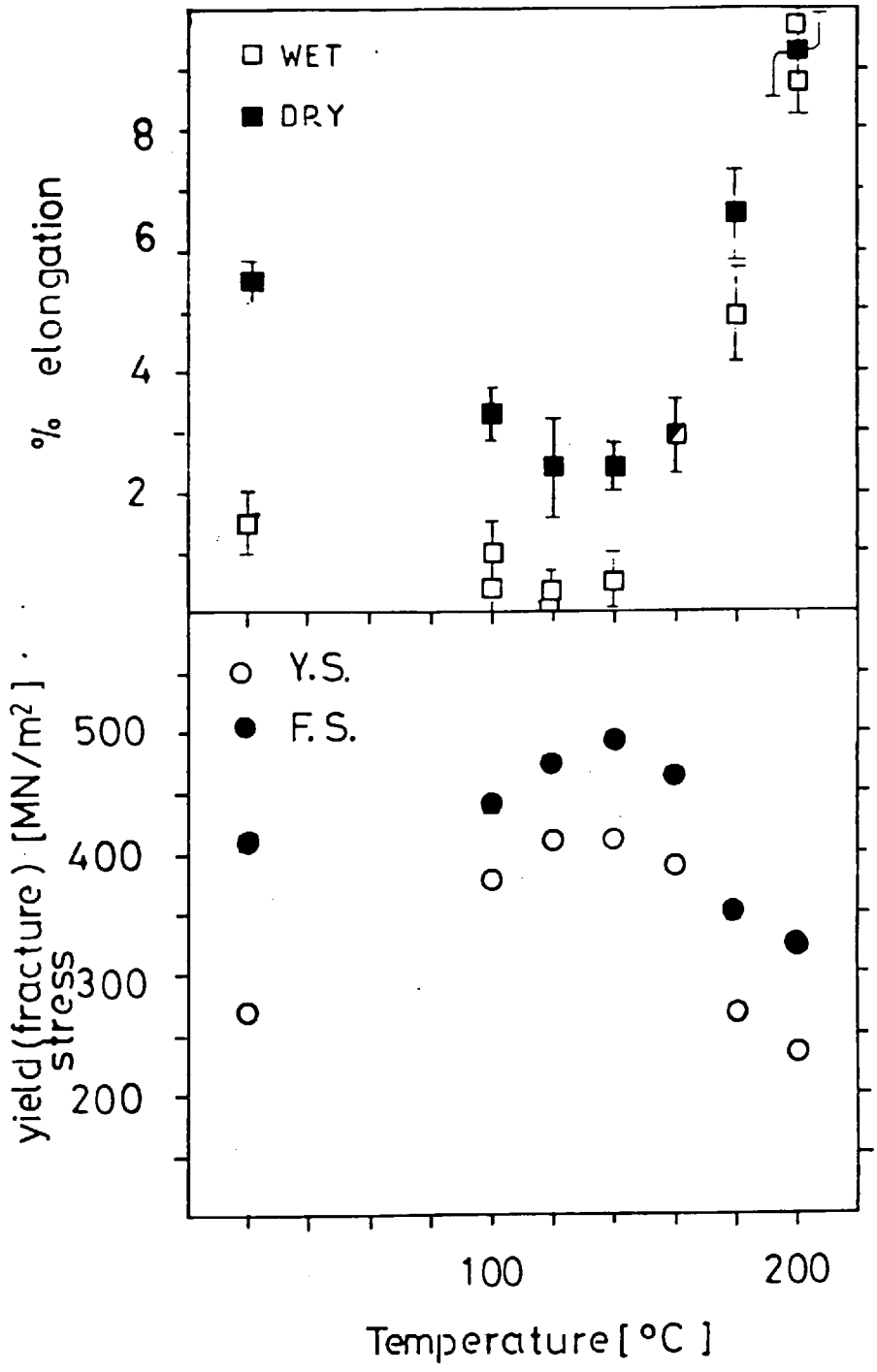
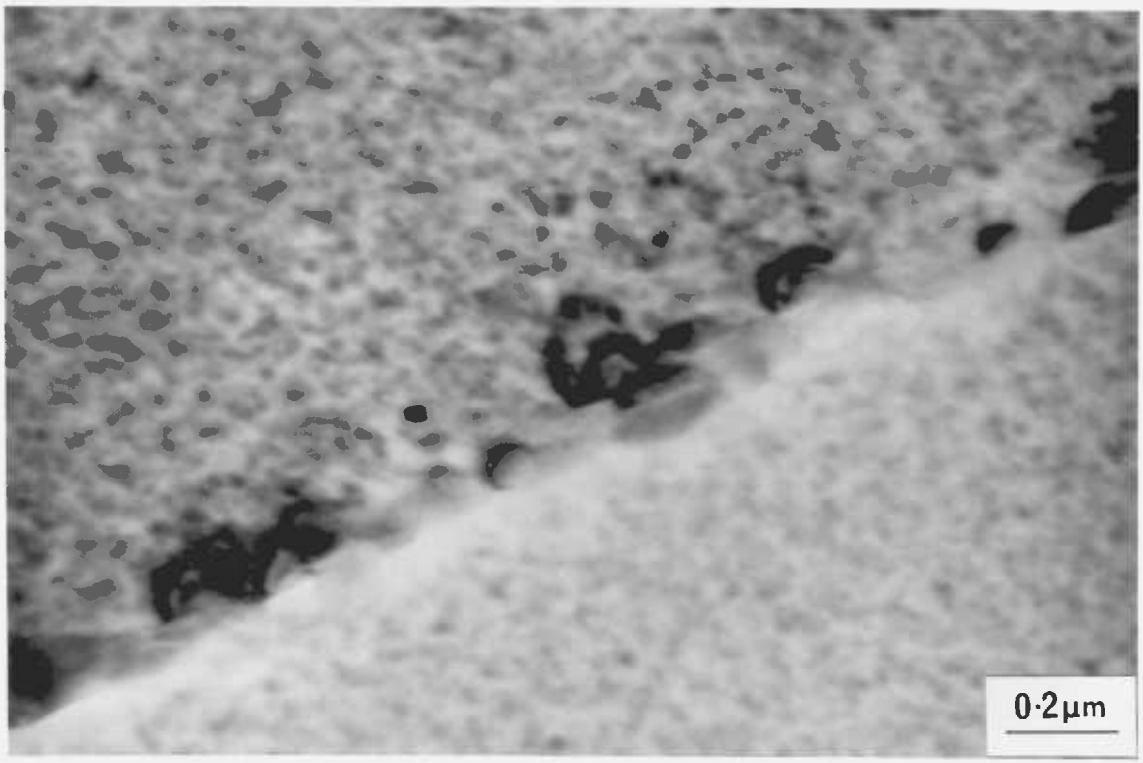


Figure 4.1. Variation of ductility and yield stress of 6/3 base alloy samples exposed to w.v.s.a. at 70°C for 72 hours with prior ageing temperature. (Ageing time 24 hours).

Figure 4.2. (a) Hydrogen bubbles at grain boundary precipitates of an Al-6%Zn-3%Mg alloy tensile sample dry aged at 120°C for 24 hours and subsequently exposed to w.v.s.a. for 72 hours. Note that not all grain boundary precipitates exhibit hydrogen bubbles.

(b) Hydrogen bubbles at the grain boundary precipitates of a similarly exposed bulk sample but previously aged at 200°C for 24 hours.


0·1μm


0·2μm

larger precipitates than low angle interfaces. A distribution of sizes around a peak was found and the figures quoted are mean values taken over a number of inclined boundaries. Inclined boundaries oriented away from Bragg conditions offer the most accurate sites for measurement since under these conditions contrast depends primarily upon atomic number and thus the true size of the zinc rich particles is clearly defined.

4.1.2. Isothermal exposure of 6/3 base alloy at 120°C: solution treated condition.

Isothermal exposure tests, at 120°C, were carried out on material initially in the solution treated condition immediately after quenching. In accordance with the procedure adopted in the isochronal tests, control samples sealed in tubes, were placed in the same autoclave.

At 120°C precipitation from the supersaturated solid solution occurs leading to an age hardening effect. This is clearly shown by the mechanical behaviour of the dry samples (Figure 4.3). The precipitation processes occurring involve the formation of a uniform dispersion of the metastable η' phase in the grain interiors with a narrow precipitate free zone adjacent to the grain boundaries which contain a dispersion of larger η particles (Figure 4.4.).

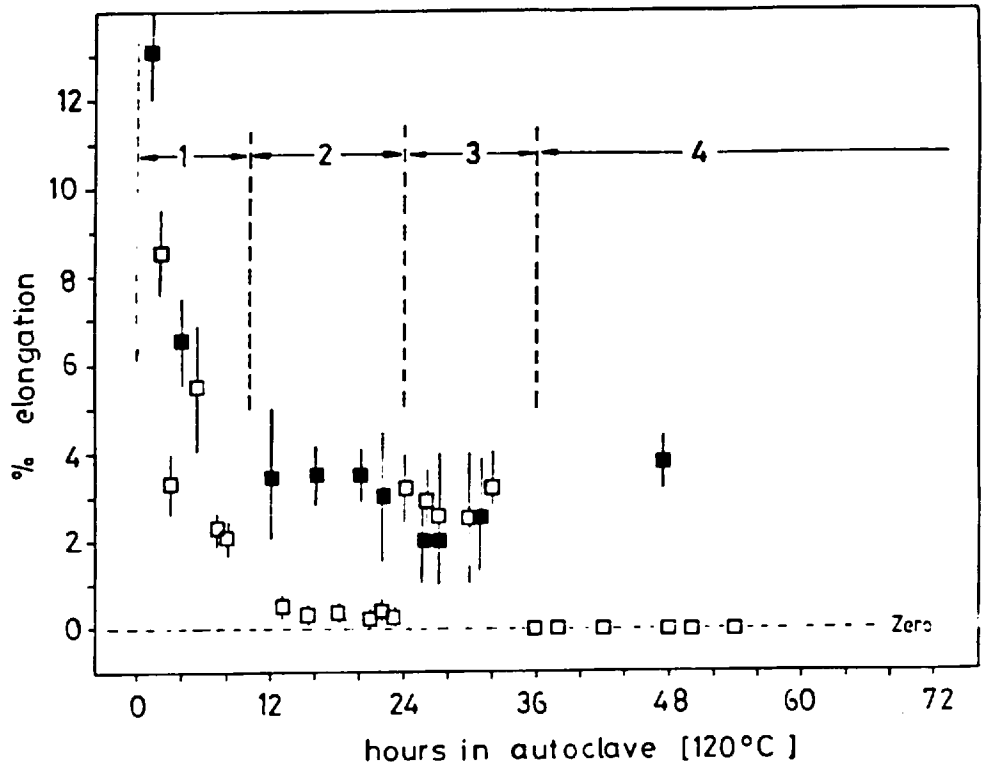
The mechanical behaviour of the specimens exposed to water vapour at 120°C is significantly different (Figure 4.3.). Up to a time period of 6 hours the recorded elongation of the wet samples closely follows that of the dry. Beyond this exposure time the two sets of data deviate, the wet samples exhibiting progressively lower ductility values. This region of falling ductility is termed stage 1. The corresponding fracture stress values over this region show a steady increase and reflect the progress of the precipitation hardening reaction.

At exposure times between 10 and 24 hours the wet samples are essentially brittle. The recorded elongation is constant and less than 1% (typically 0.3-0.5%). This is significantly lower than the ductility of the dry samples (typically 2-3%) but indicates that some plastic deformation precedes fracture. The fracture stresses determined in this regime, designated as region 2, are effectively constant (Figure 4.3.).

After about 24 hours there is an abrupt recovery of ductility, the elongation values now being very close to those measured for the dry samples. This stage, region 3 extends up to 36 hours. The fracture stresses of both dry and wet samples are comparable in this region.

Figure 4.3. (a) Variation of ductility of "as quenched" samples with time of exposure to steam at 120°C (open squares). Similarly treated dry control samples (sealed in glass tubes and placed in the same autoclave) exhibit the elongation values shown by the filled squares.
Each point represents an average of six experimental values. Error bars indicate the standard deviation calculated for each set of data.

(b) Corresponding fracture stress values.


% elongation
12
10
8
6
4
2
0
1
2
3
4
Zero
0
12
24
36
48
60
72
hours in autoclave [120°C]

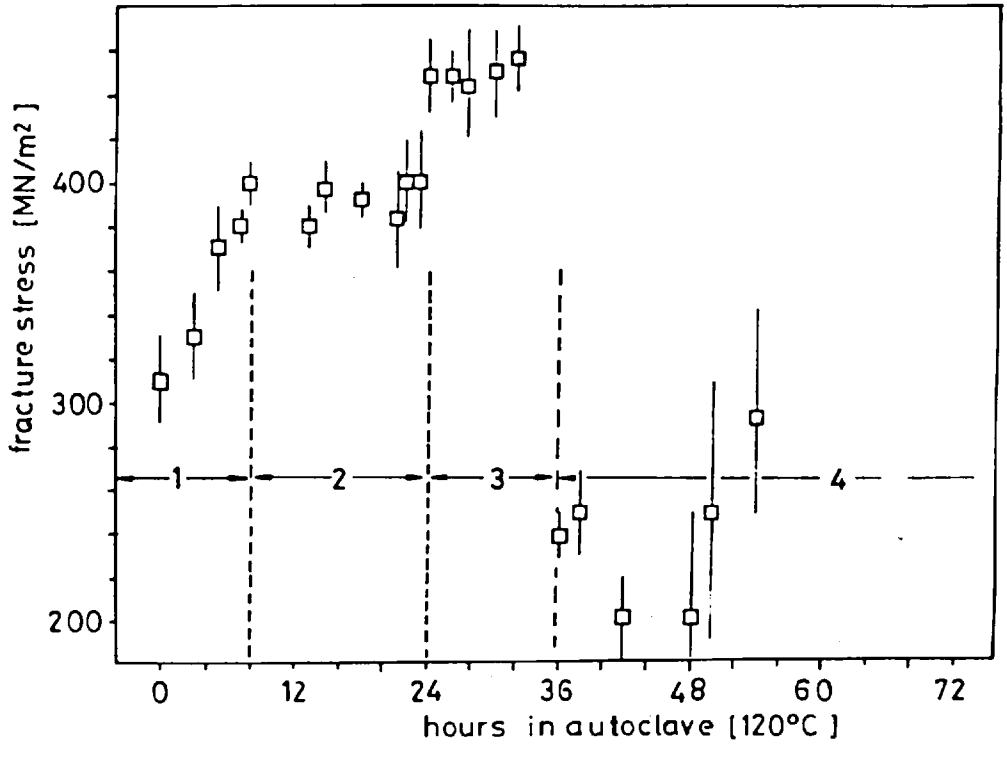
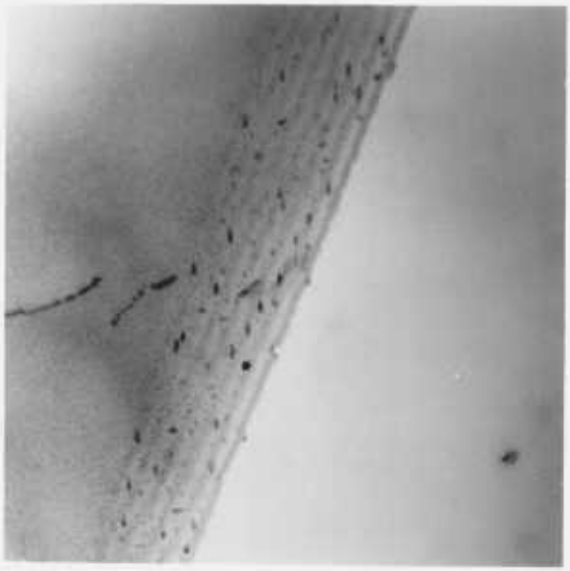
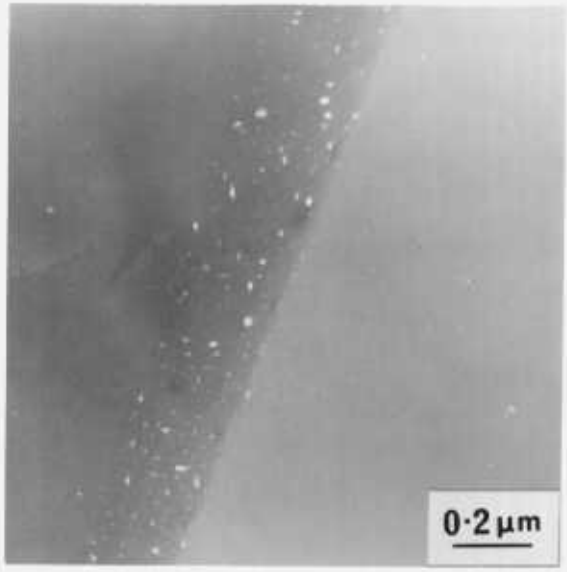

fracture stress [MN/m²]
400
300
200
1
2
3
4
0
12
24
36
48
60
72
hours in autoclave [120°C]

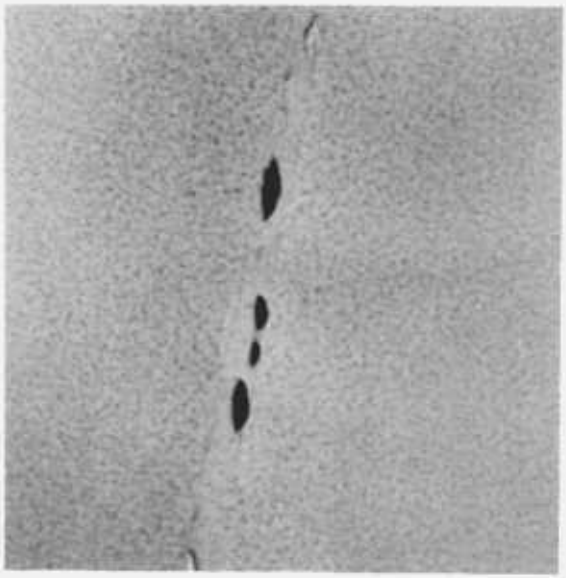
Figure 4.4. (a) Bright and Dark field micrographs of a sample aged dry at 120°C for 8 hours showing precipitation of η ($MgZn_2$) at grain boundaries.

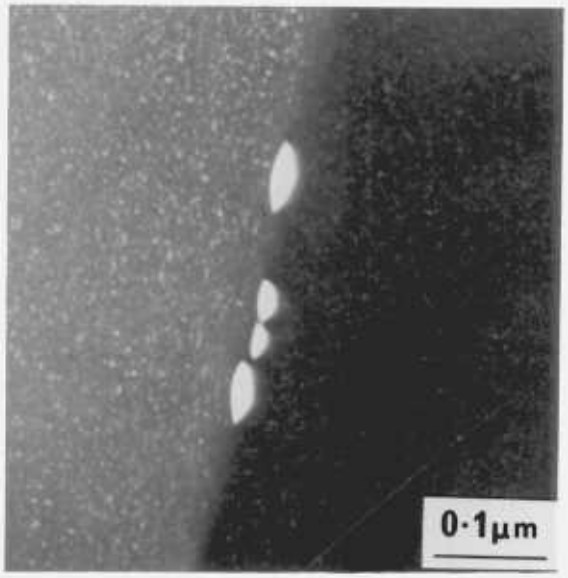
(b) Bright and Dark field micrographs showing grain boundary and matrix precipitation following 38 hours ageing at 120°C.

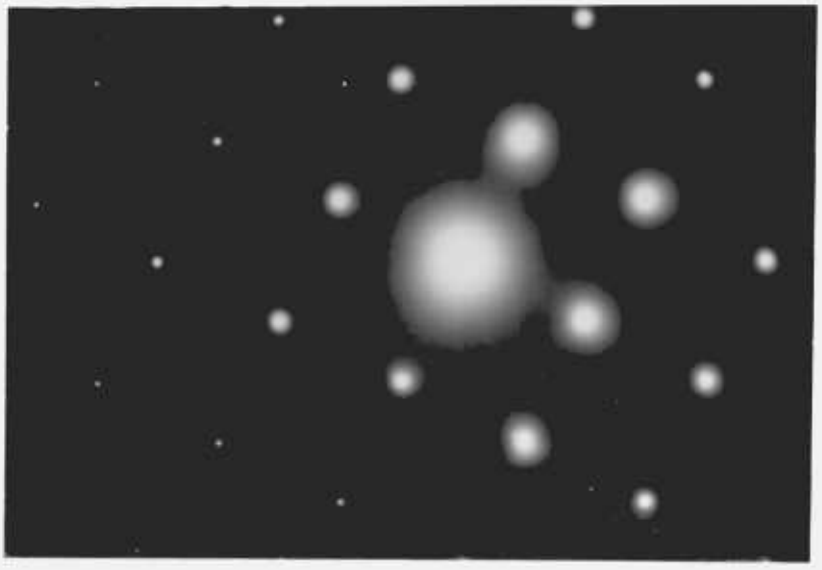
(c) [100] zone in an aged sample of Al-6Zn-3Mg alloy. (2 hours at 120°C). Weak η′ reflections appear along the [220] matrix directions.




0·2μm




0·1μm



At the end of region 3 the samples revert to a totally brittle character. Fracture occurs at very low stresses and no measurable ductility is recorded, i.e. they are elastically brittle. Considerable variation in fracture stress was found in region 4 (Figure 4.3.)

The degree of embrittlement in any of the four stages of behaviour was not found to be a function of the strain rate employed during the mechanical test. No reproducible differences between the recorded elongation at different strain rates were detected in any partially or fully embrittled specimens in the region of $10^{-3}s^{-1}$ - $10^{-5}s^{-1}$.

Embrittlement under all conditions was fully reversible. Full ductility could be restored by repeating the heat treatment cycle at any stage.

Fractography of the samples used in these experiments revealed some fundamental differences between different samples.

Dry control specimens show a normal ductile transgranular dimpled fracture surface in the as quenched condition. This progressively transforms to a mixture of ductile intergranular and transgranular fracture. The percentage of intergranular failure increases with increasing ageing time but dimpling of the fracture is observed in all cases.

Wet specimens of region 1 exhibit fracture modes closely relating to the dry ones but with an increasing number of intergranular facets. The intercrystalline failure mode takes over as region 2 is encountered and persists completely through this region without any evidence of ductile dimpling. However, there is some evidence of microplasticity in the form of emergent slip steps (Figure 4.5.). Plastic deformation appears to have been very limited, the majority of fracture surfaces exhibiting a "clean" faceted failure. At times approaching 24 hours evidence of transgranular crack initiation was found but the favoured fracture mode appeared to be one of grain boundary decohesion (Figure 4.6).

The abrupt recovery in ductility at the end of stage 2 was found to be associated with a change in the fracture mode. Fractography of samples in region 3 revealed that the fracture surface consisted of three distinct regions (Figure 4.7). At the periphery the fracture remained brittle and intergranular. Then followed a band of transgranular brittle fracture whilst the specimen interior exhibited a transgranular ductile fracture mode.

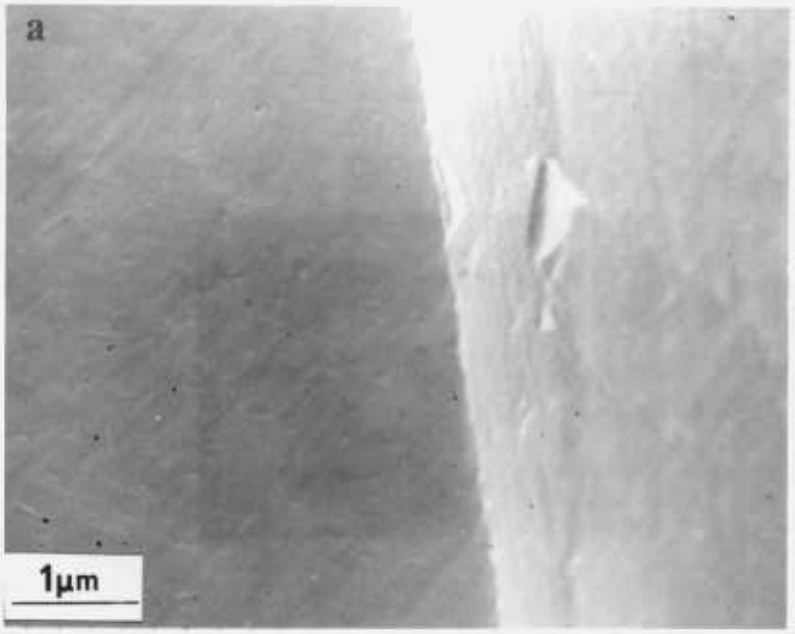
The onset of region 4 was associated with a further change in failure mechanism. The fracture was found to have reverted back to an

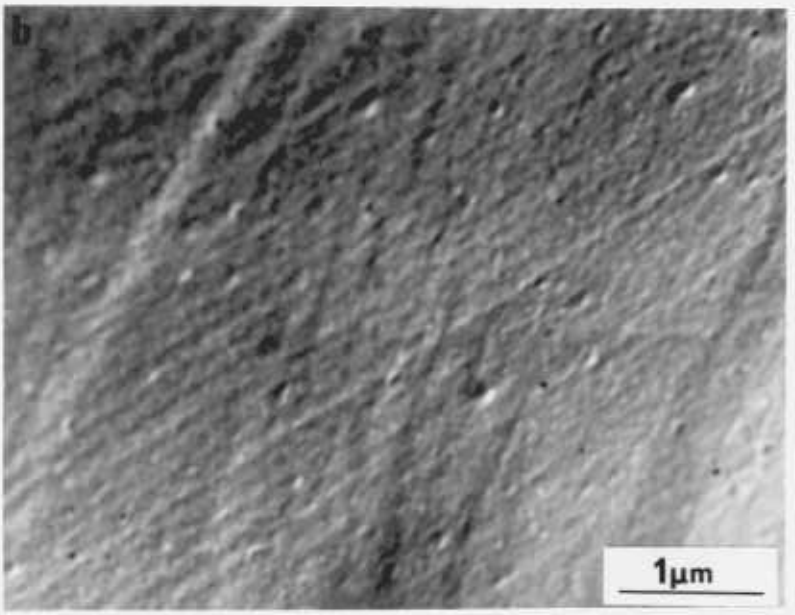
Figure 4.5. Fractography of exposed samples corresponding to exposures in region 2 of Figure 4.3.

(a) Intergranular fracture in a sample exposed to steam at 120°C for 18 hours. Note microplasticity.

(b) Higher magnification of same sample showing emergent slip steps and grain boundary precipitates.

Figure 4.6. Fracture surface of sample exposed to steam in the autoclave for 22 hours.
Transgranular crack nuclei present but fracture still dominantly intergranular.


a
1µm


b
1µm

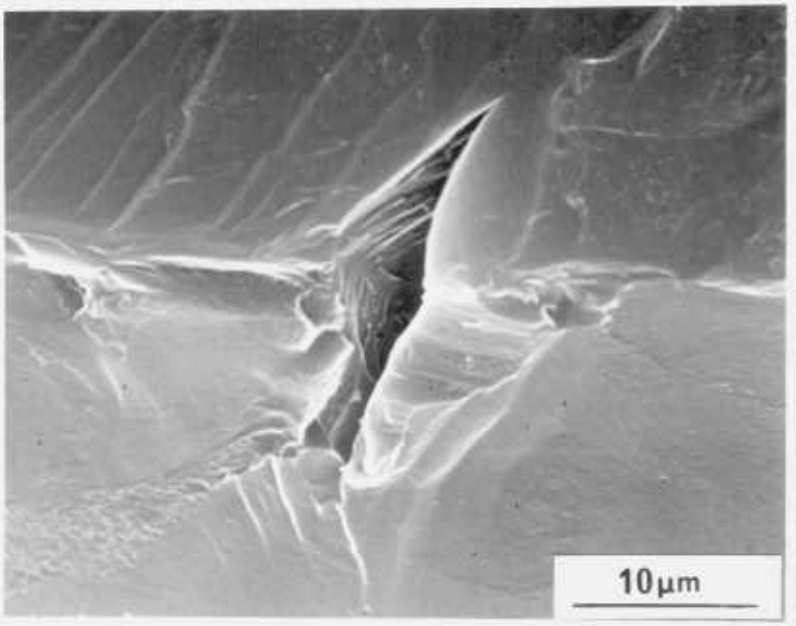
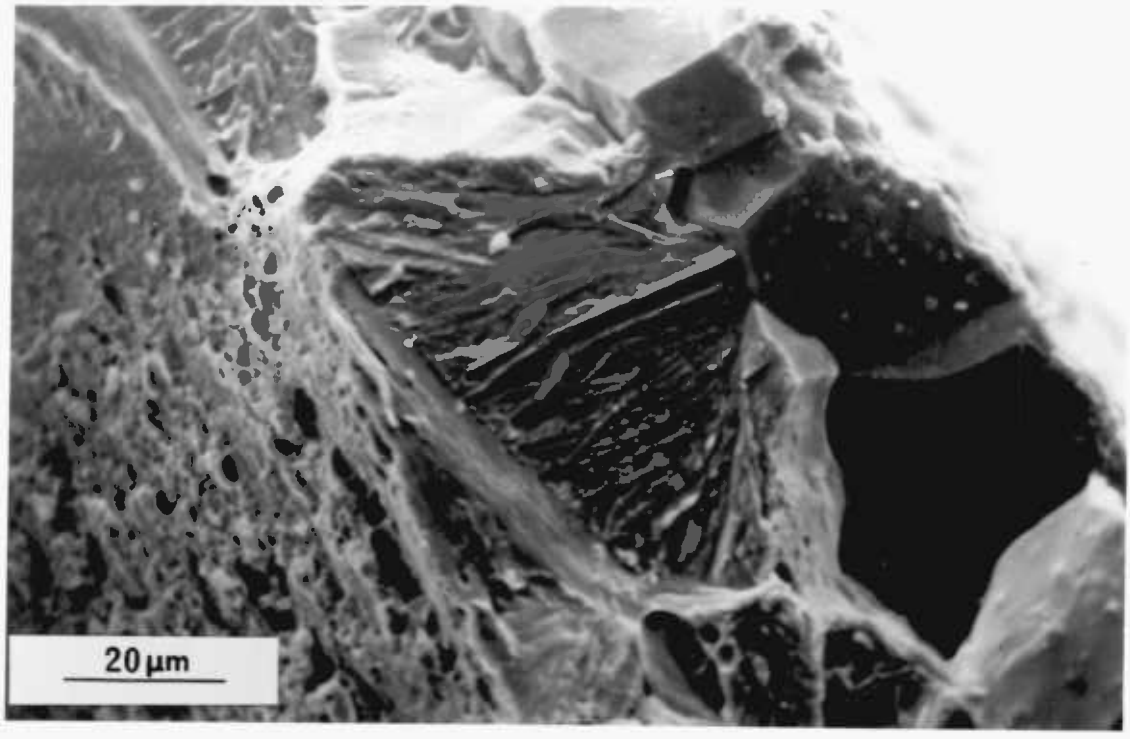
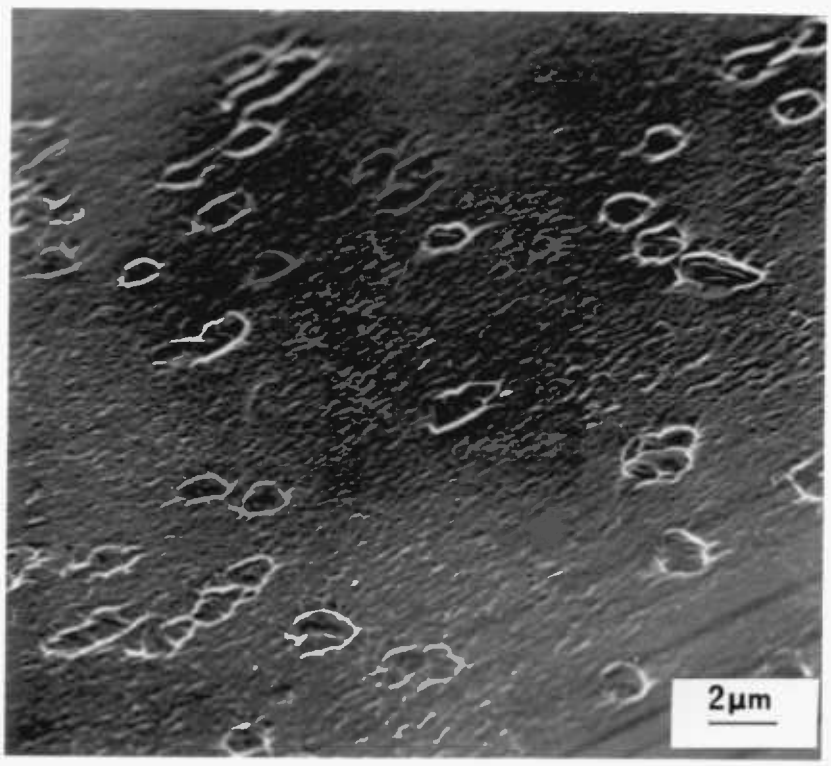

10µm

Figure 4.7. Fracture surface typical of failure in region 3 of Figure 4.3.

Figure 4.8. Intercrystalline failure in region 4. Fracture surface contains a large number of crater shaped depressions.


20 µm


2µm

intercrystalline form (Figure 4.8). In contrast to region 2 however, significant yielding was not apparent as evidenced by the absence of slip steps. The fracture surface was not smooth however, and contained precipitates, some of which were surrounded by crater shaped depressions.

Transmission electron microscopy showed the development of the metastable η' precipitates in the matrix during exposure at 120°C. Grain boundary precipitation of the equilibrium η phase also occurs and the η particles reach an average size of about 200A after a treatment of 24 hours. (This again represents an average size measured from a number of different boundaries.)

Careful examination of thinned bulk tensile test samples in regions 1, 2, 3 and 4 was carried out using CTEM. No hydrogen bubble formation was detected in either region 1 or 2, but bubbles were found in samples from region 3 (Figure 4.9). At the beginning of stage 3 not all η particles were associated with bubbles when initially examined, but subsequently developed them after some seconds exposure to the electron beam (Figure 4.10). Considerable care was therefore required to positively confirm the existence of bubbles prior to electron irradiation. The standard procedure adopted was to select a grain boundary and tilt to the appropriate diffracting condition (e.g. g = 220) with the electron beam confined to a narrow region of the boundary. Photography was then carried out on the immediately adjacent area at a low electron flux density. In this way the presence or absence of bubbles and any growth under the beam could be assessed.

At late times in stage 3 and throughout stage 4 bubbles were present "ab initio" on the majority of grain boundary particles (Figure 4.11). It was also found that in samples exposed to steam for periods greater than 24 hours, i.e. up to region 3 or longer, intragranular dislocation loops were formed on examination under the electron beam at 100 kV (Figure 4.12). This was similar to displacement damage effects found in dry samples but only at accelerating voltages above the threshold for displacement damage, 160 kV. (See section 5.4.1.).

Additionally bubbles were observed on dislocations attached to grain boundaries in samples that had been exposed to water vapour (Figure 4.13).

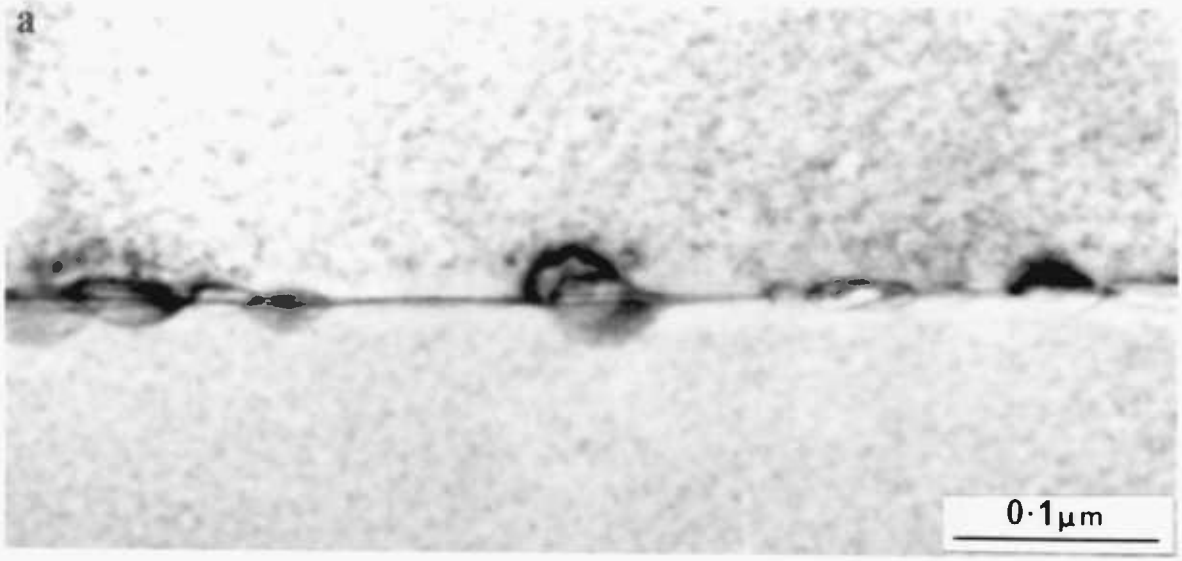
4.1.3. Isothermal exposure of 6/3 base alloy at 120°C: aged condition.

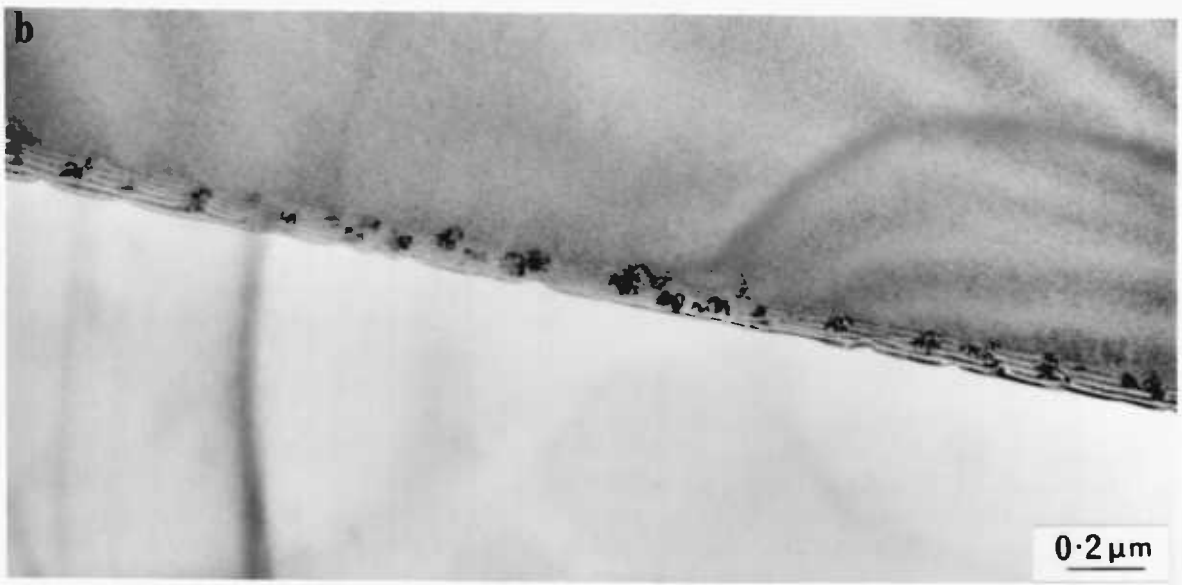
It was clearly significant that the recovery in ductility in stage 3 is associated with the development of the grain boundary η particle

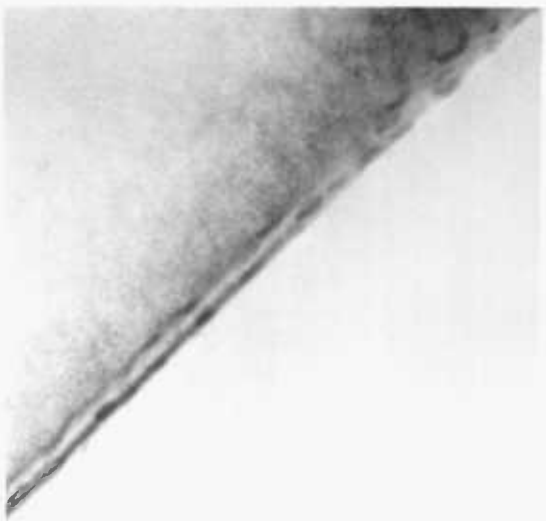
Figure 4.9. (a) Transmission electron micrograph of tensile sample exposed to water vapour in the autoclave for 26 hours. Hydrogen bubble formation at grain boundary particles.

(b) Hydrogen bubbles at boundary of similarly treated sample. Majority of grain boundary particles exhibit hydrogen bubbles.

Figure 4.10. Development of bubbles at grain boundary particles as a result of exposure to the electron beam. Bulk sample exposed to water vapour in the autoclave for 24 hours.


a
0·1μm


b
0·2μm



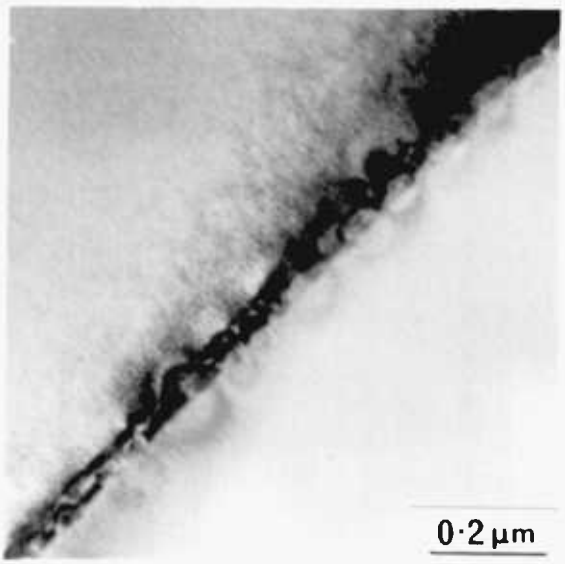
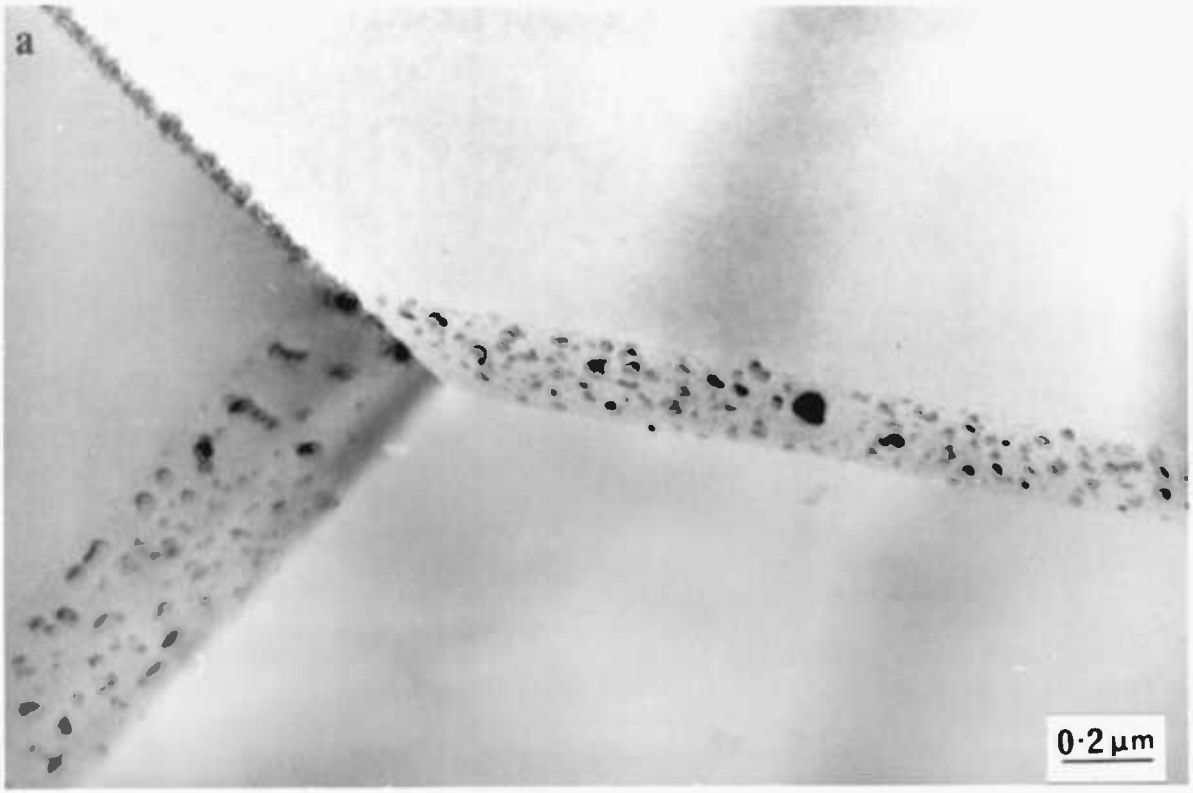

0·2μm

Figure 4.11. (a) Hydrogen bubbles in a tensile sample exposed to water vapour in the autoclave for 32 hours. Note very high density of bubbles.

(b) Hydrogen bubbles in a sample taken from region 4 exposure times (56 hours at 120^{o}C).


a
0·2 µm

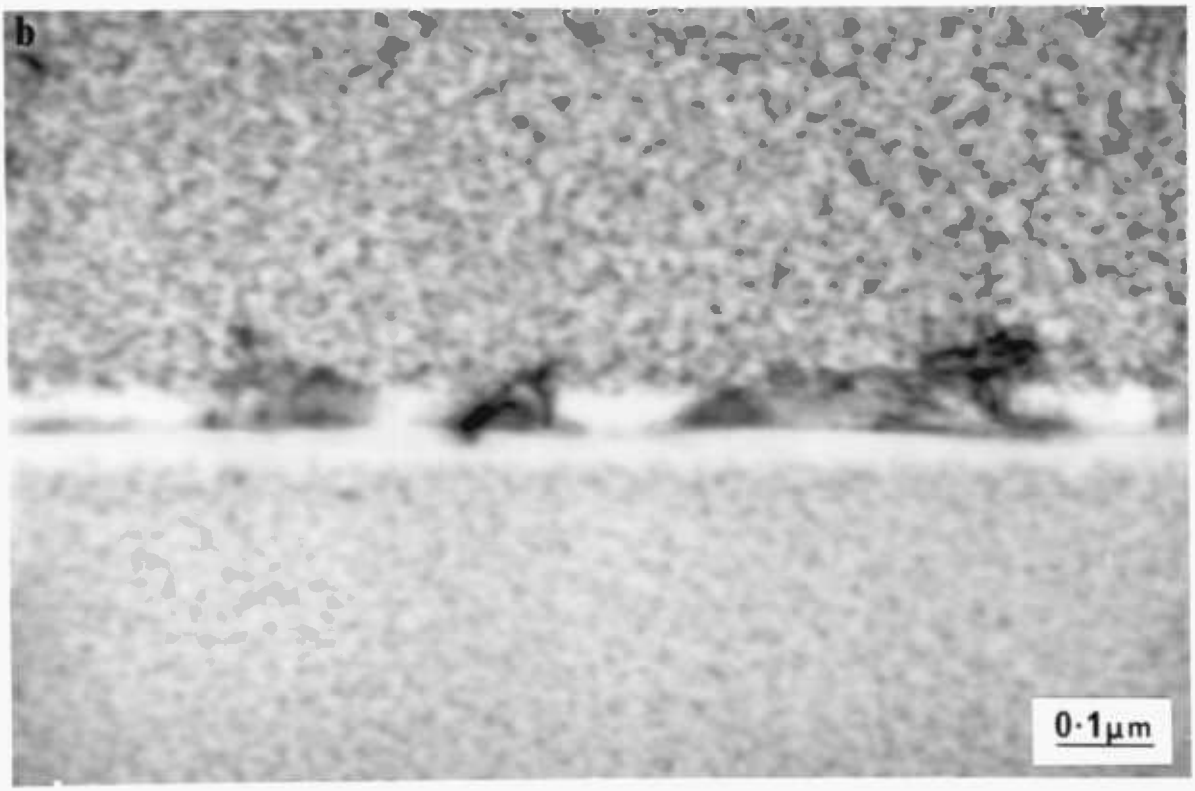

b
0·1µm

Figure 4.12. Intragranular dislocation loops induced by electron irradiation with 100 kV electrons in a sample exposed for 26 hours in the autoclave. No such loops were noted in non-exposed samples.


1m


2

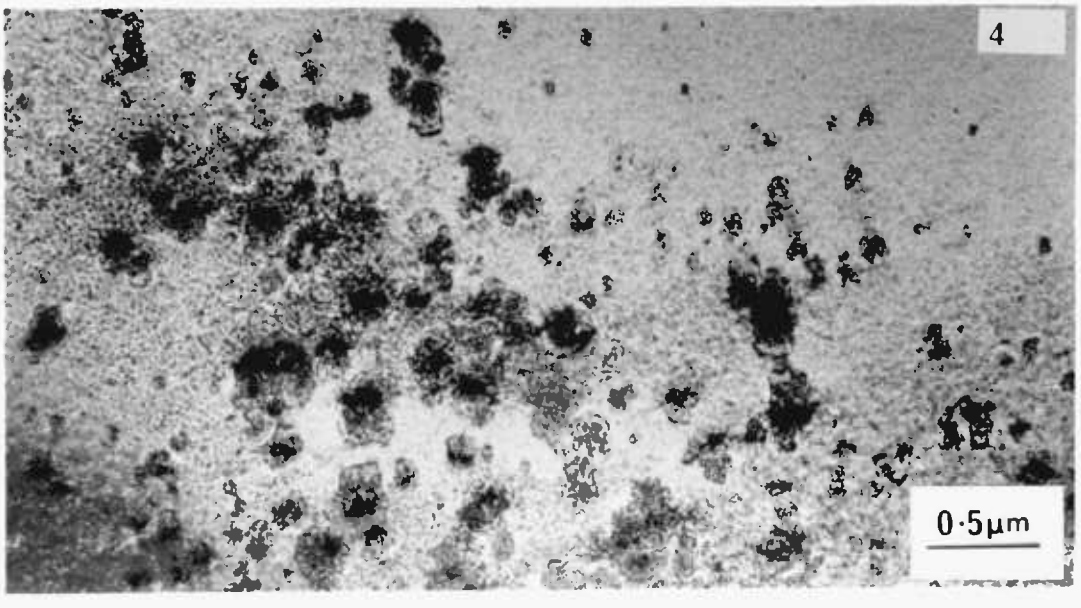
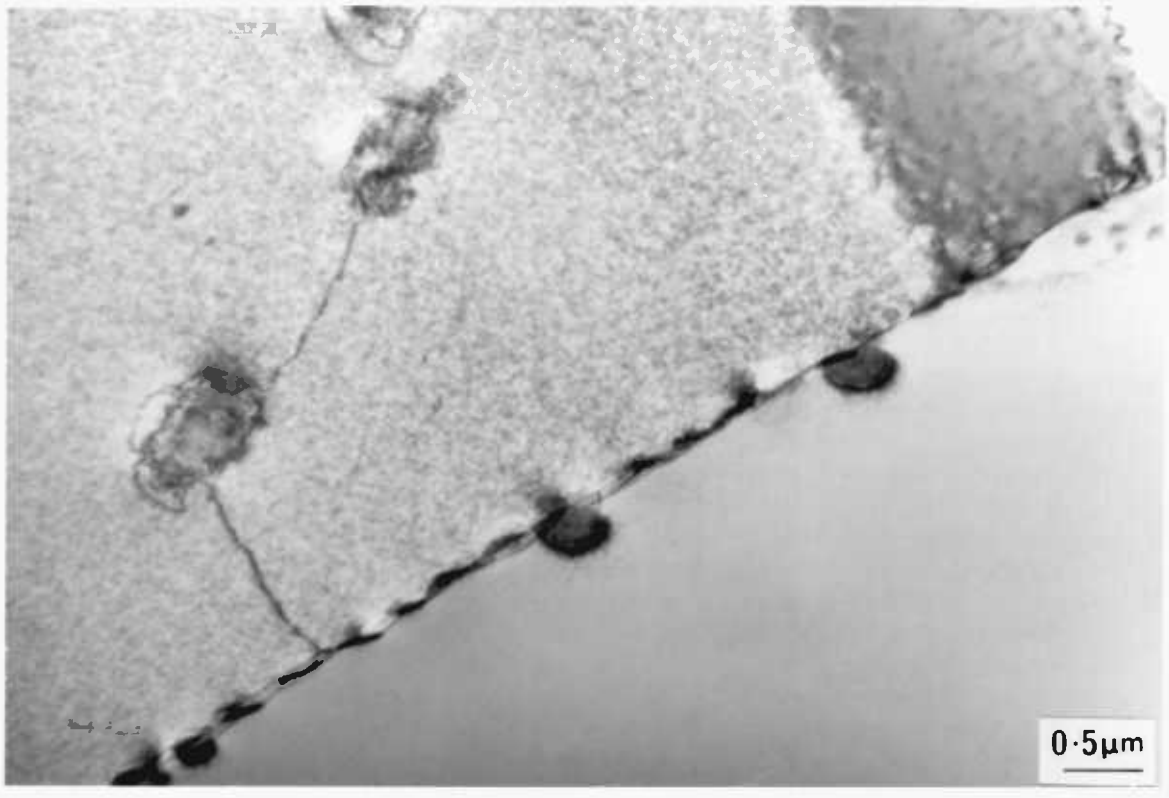
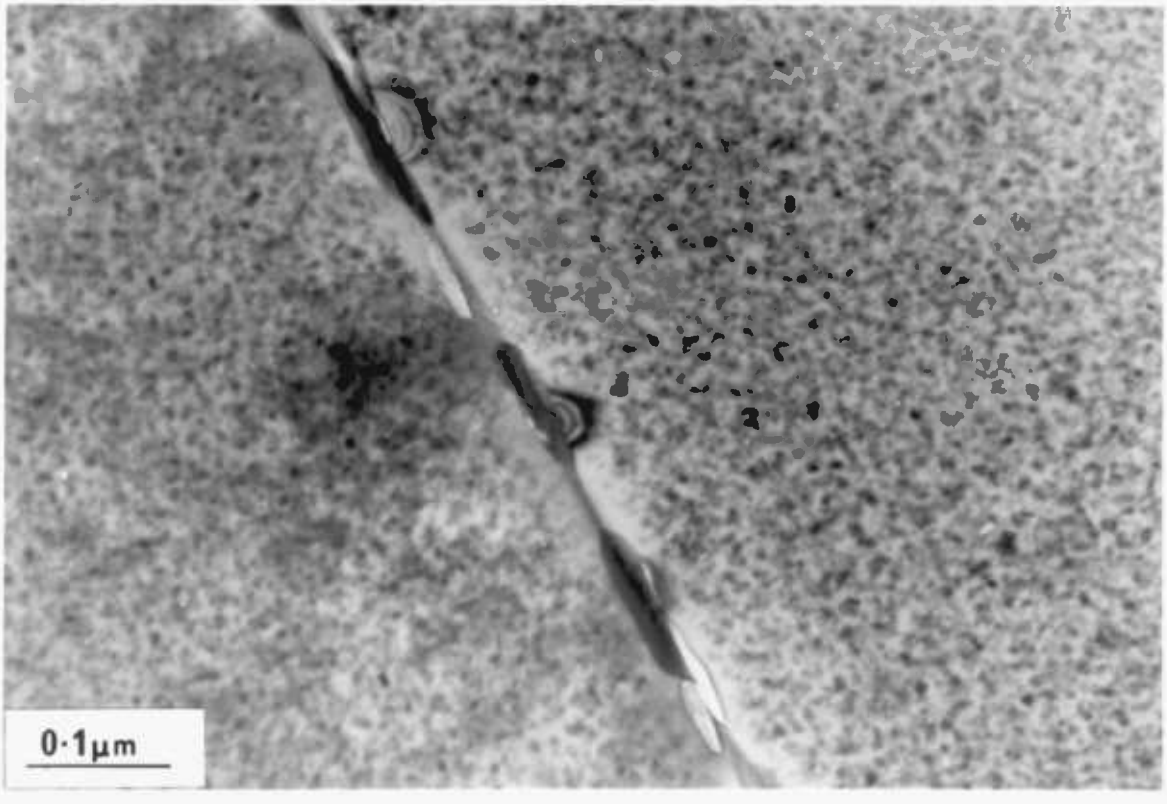

4
0·5μm

Figure 4.13. Hydrogen bubble strain fields on dislocation lines in an exposed sample. Hydrogen bubbles also visible along the grain boundary.

Figure 4.16. Hydrogen bubbles in a tensile sample aged dry for 18 hours at 150^{o}C and subsequently exposed to water vapour in the autoclave for 23 hours.


0·5μm


0·1μm

dispersions and the growth of bubbles on these particles. Both precipitation and exposure to water vapour were taking place simultaneously in the experiments reported in the previous section since samples were initially in the as quenched condition and thus supersaturated with solute. In order to separate these variables some samples were pre-aged under dry conditions either for 18 hours at 150°C or for 92 hours at 125°C. The average grain boundary precipitate sizes resulting from these heat treatments were 250A and 800A respectively. Thus both microstructures exhibited particle sizes greater than the minimum size previously noted to be associated with bubble nucleation. Both microstructures would be expected to be relatively stable on exposure at 120°C. Samples were then exposed to water vapour at 120°C and mechanically tested. The results of such exposure tests are shown in Figures 4.14 and 4.15. It can be seen that the prior heat treatment of 92 hours has resulted in a microstructure which is highly resistant to embrittlement. Within the limits of accuracy of the measurements no embrittlement occurred for exposure times up to 120 hours.

The behaviour after ageing for 18 hours at 150°C however, was distinctly different. Yield strength, fracture stress and elongation remain constant up to about 30 hours exposure. There follows a rapid drop in ductility to zero and a corresponding reduction in fracture stress to a level comparable to the yield strength of the material (Figure 4.15). In these experiments electron microscopy showed clearly the presence of bubbles on the grain boundary precipitates within the ductile failure regime as well as in the embrittled condition (Figure 4.16).

4.1.4. Isothermal Exposure of 6/3 Cu alloy at 120°C

The as quenched condition of the copper containing alloy exhibited an equiaxed structure but with a smaller grain size than that found in the high purity alloy (30μm in comparison with 100μm). Microstructurally the two alloys behaved in a similar manner on ageing, i.e. a sequence of supersaturated solid solution → metastable phases → stable phase with the generation of larger grain boundary precipitates at the interfaces which are associated with precipitate free zones (Figure 4.17). Copper enhances the precipitation kinetics of the G.P. zones and stabilises the metastable η' phase at temperatures below 120°C (see Section 2.3). The grain boundary precipitates were still the equilibrium phase. The only difference between the 6/3 base and 6/3 Cu alloys was the occurrence of very large particles in the latter only visible under the light microscope at low magnifications. It is possible that they were S phase

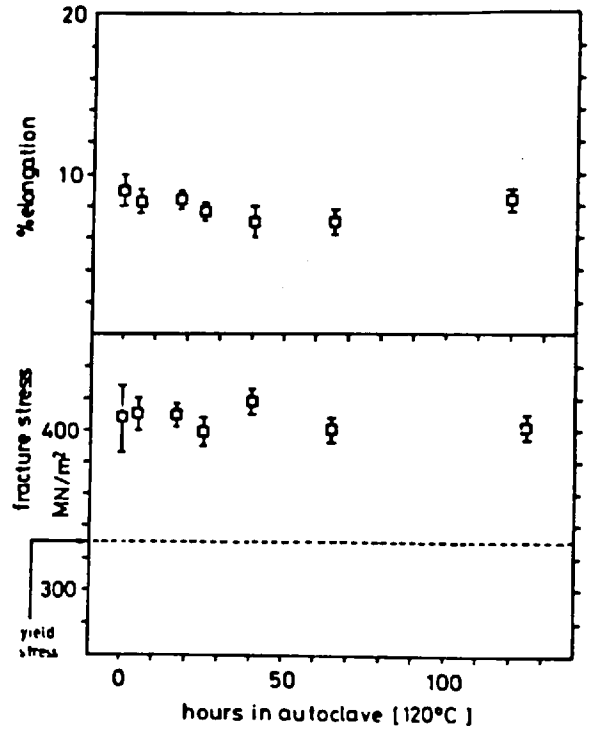


Figure 4.14. The variation of ductility and fracture stress on exposure to water vapour at 120°C of samples solution treated and aged for 92 hours at 125°C.

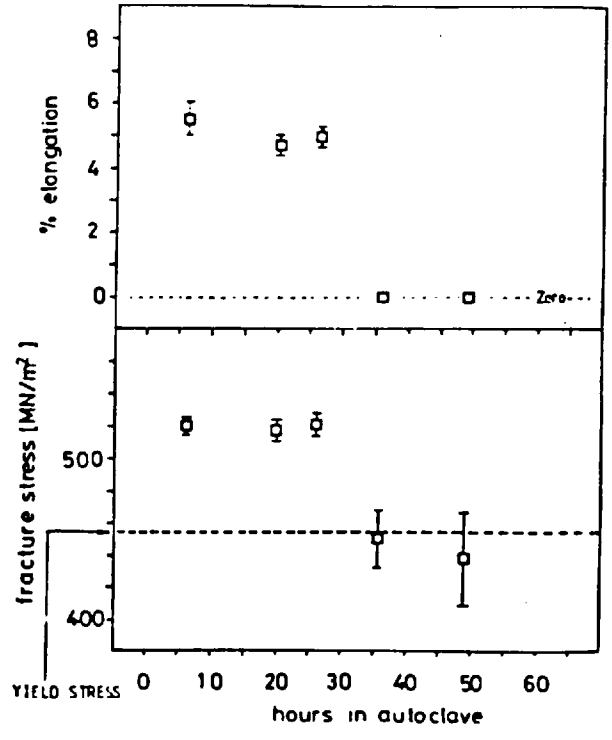
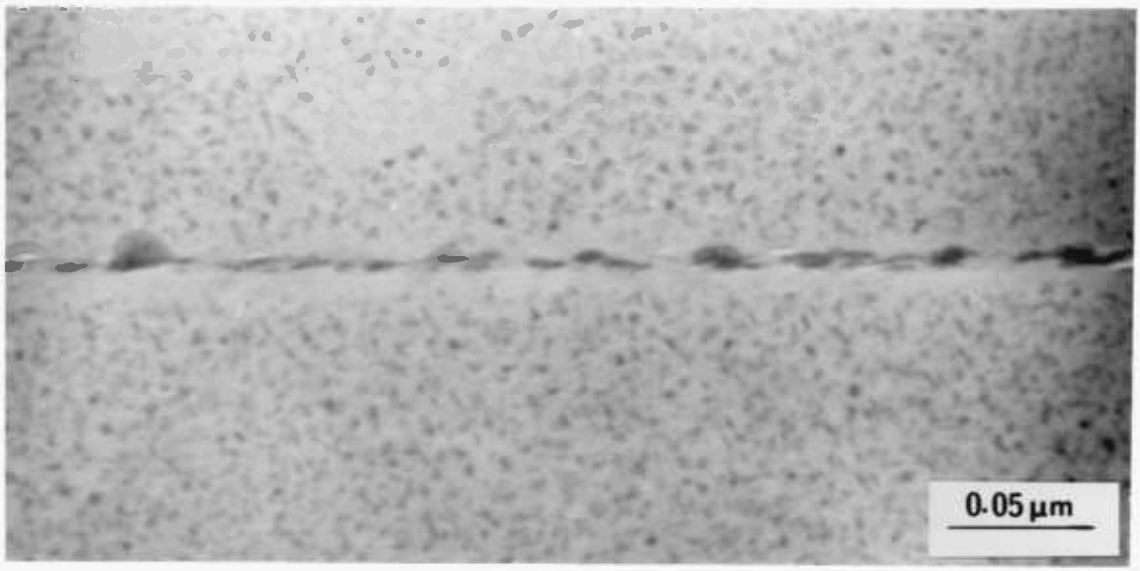
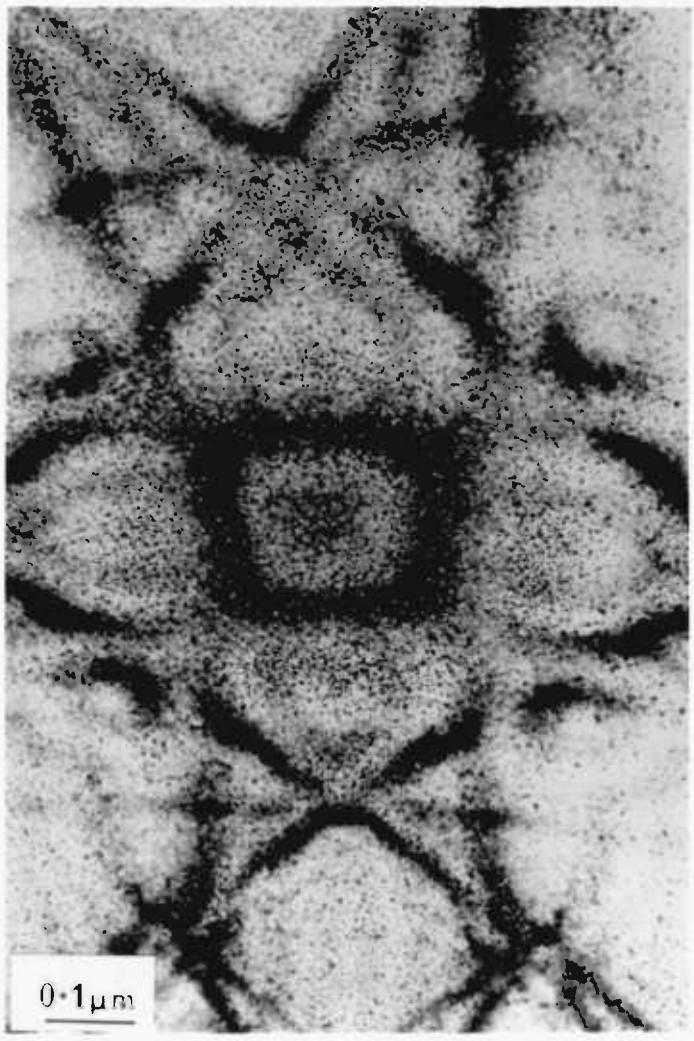


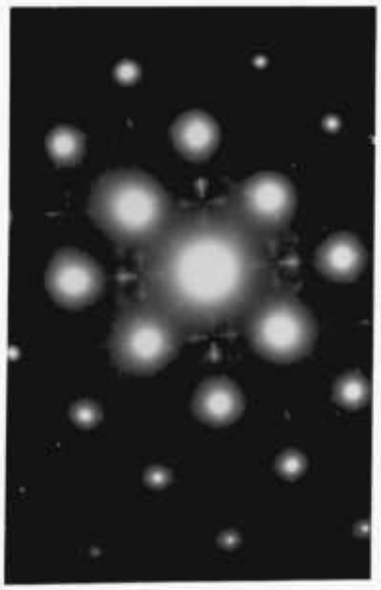
Figure 4.15. The variation of ductility and fracture stress on exposure to water vapour at 120°C of samples solution treated and aged for 18 hours at 150°C.

Figure 4.17. Sample from 6/3 Cu alloy showing grain boundary precipitates, a narrow P.F.Z. and matrix precipitation. Solution treated at 450°C, quenched and aged at 120°C for 7 hours.

Figure 4.18. [100] zone in overaged sample of the 6/3 Cu alloy with associated diffraction pattern. Precipitate stops show the presence of both η and η'. Sample solution treated at 450°C, cold water quenched and aged at 120°C for 174 hours.


0·05 µm


0·1 µm



intermetallics which did not dissolve during solution heat treatment (8). None were observed under the electron microscope and thus positive identification could not be made. Figure 4.18 shows the matrix precipitates and associated diffraction pattern of an overaged 6/3 Cu alloy.

The exposure characteristics at 120°C of this alloy are shown in Figure 4.19. Within experimental error no embrittlement was detected even under prolonged exposure times. Both dry and wet samples show similar elongation values which are considerably higher than those of the high purity alloy.

Extensive fractography showed that the dominant mode of fracture in the absence of water vapour was one of ductile intergranular failure associated with ductile dimpling (Figures 4.20 and 4.21).

Samples exposed to water vapour differed from the control specimens in a number of ways. Firstly for any given time at 120°C the proportion of intergranular failure was greater for wet samples (Figure 4.22). Secondly, over the range of 20-92 hours the occurrence of transgranular cleavage type fracture was detected (Figure 4.23). This was limited to the periphery of the specimens (Figure 4.24). The greatest proportion of such cleavage fracture was found in the region of 40-56 hours with only minute amounts at 92 hours. Such cleavage fracture was first detected in samples exposed for 20 hours (Figure 4.25).

No such cleavage fracture was found in any dry samples under any conditions.

The third and vital difference between the wet and dry specimens was the density of subcritical surface cracks (i.e. cracks that did not contribute to fracture). Wet samples were found to contain significantly greater numbers of such cracks compared to dry specimens (Figure 4.26). These cracks were both of an intergranular and transgranular form and in specimens exposed to steam for long periods virtually all grain boundaries were cracked.

Close examination of the subcritical cracks revealed that they were not caused by intergranular corrosion. This is evident in Figure 4.27, which shows only slight evidence of intergranular corrosion. Slip steps and grain boundary precipitates are clearly visible and show no signs of attack.

The surface of exposed samples was found to be covered by a thick hydrated oxide film of pseudoboehmite (see Section 4.4) (Figure 4.28).

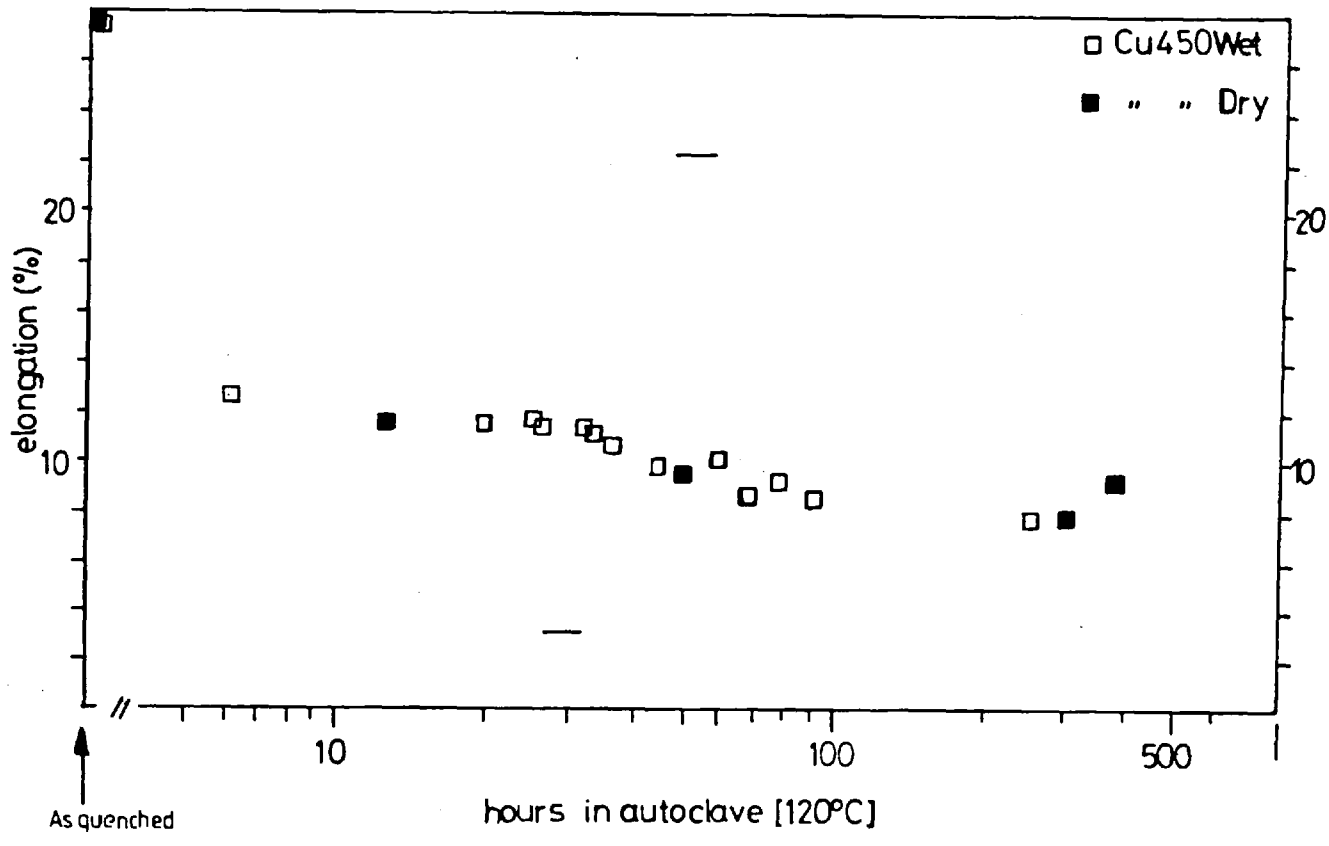
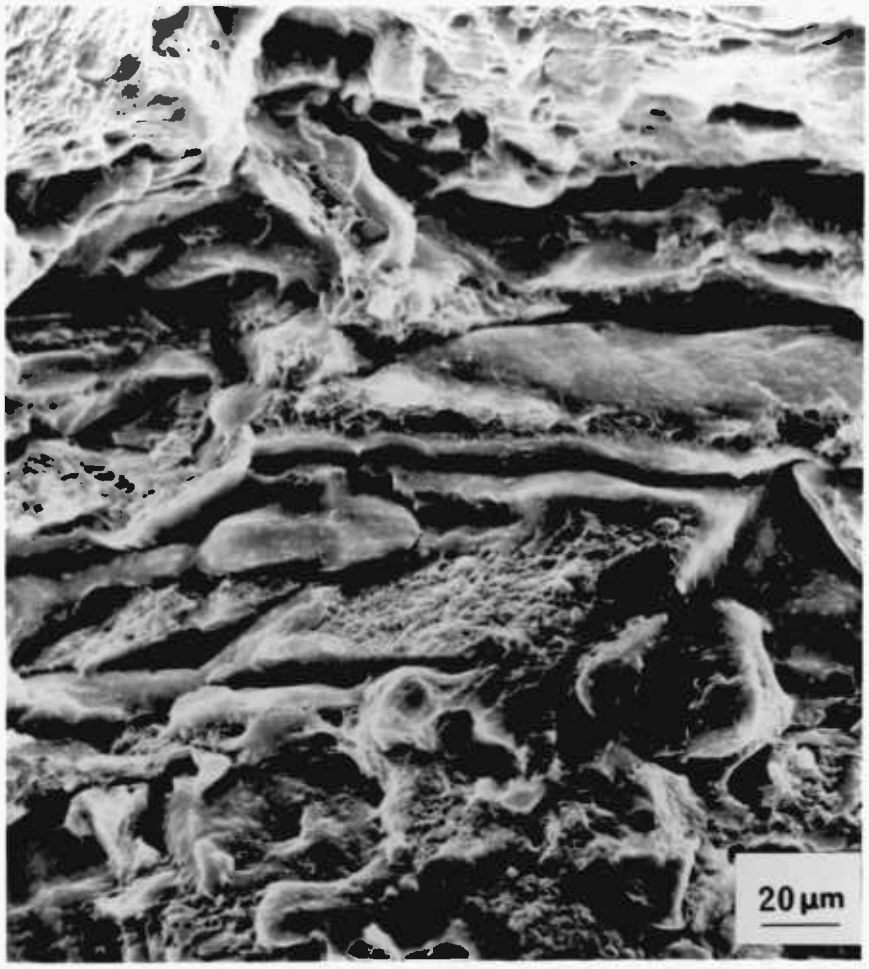


Figure 4.19. Variation of ductility of as quenched 6/3 Cu alloy with exposure to water vapour at 120°C.

Figure 4.20. Ductile intergranular failure of 6/3 Cu sample aged dry at 120°C for 12 hours.

Figure 4.21. High magnification of the fracture surface of a 6/3 Cu alloy aged at 120°C for 12 hours showing extensive dimpling.


20 µm

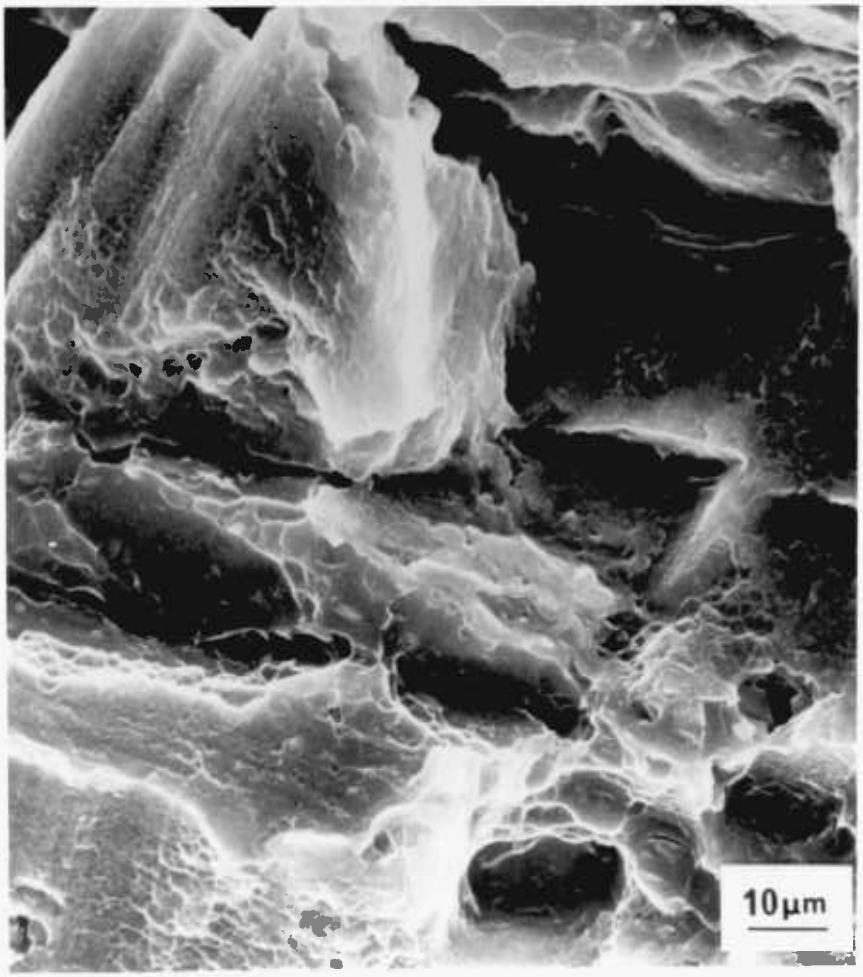

10 µm

Figure 4.22. Comparison between "dry" (a) and "wet" (b) fracture surfaces in the 6/3 Cu alloy treated for 250 hours at 120°C.

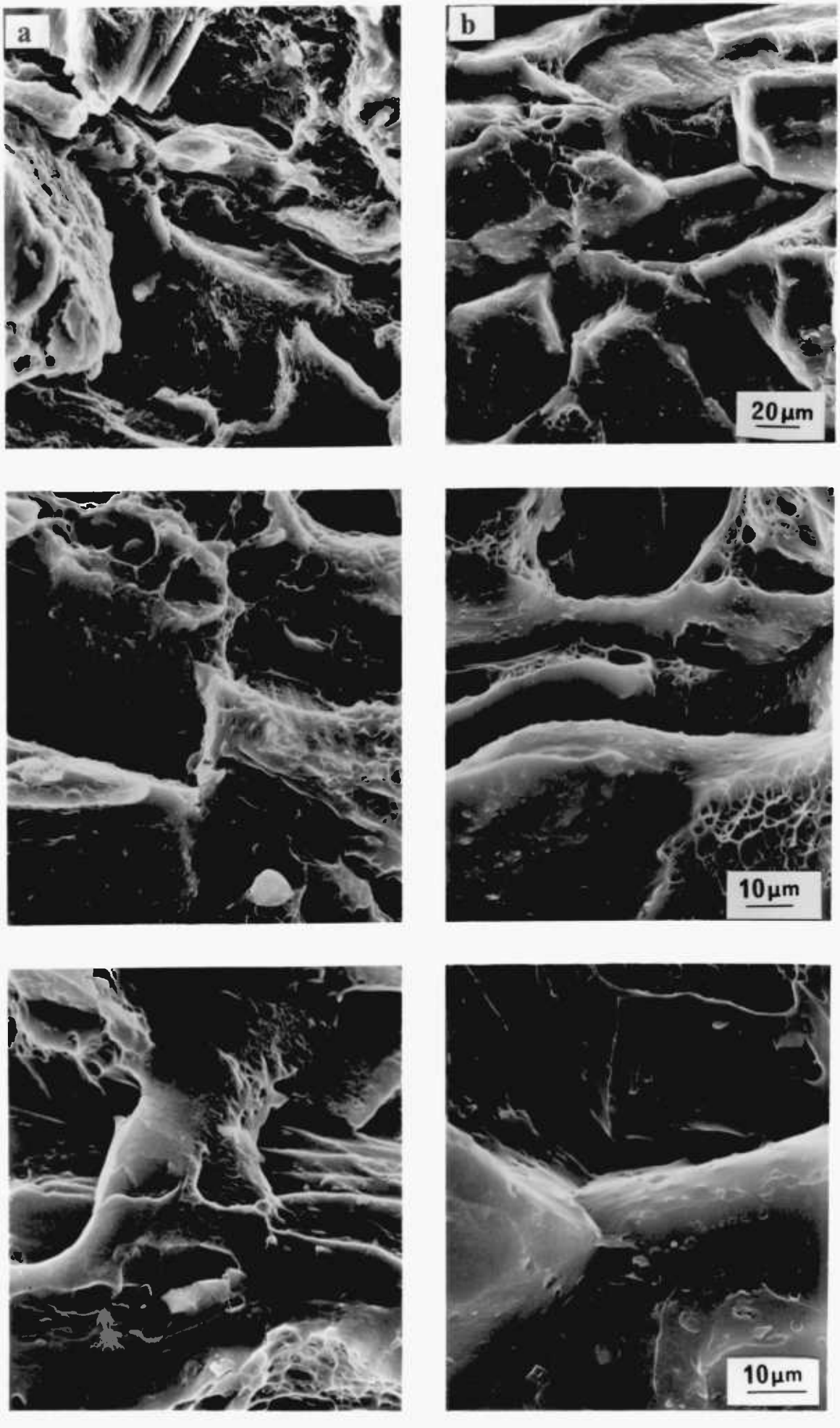
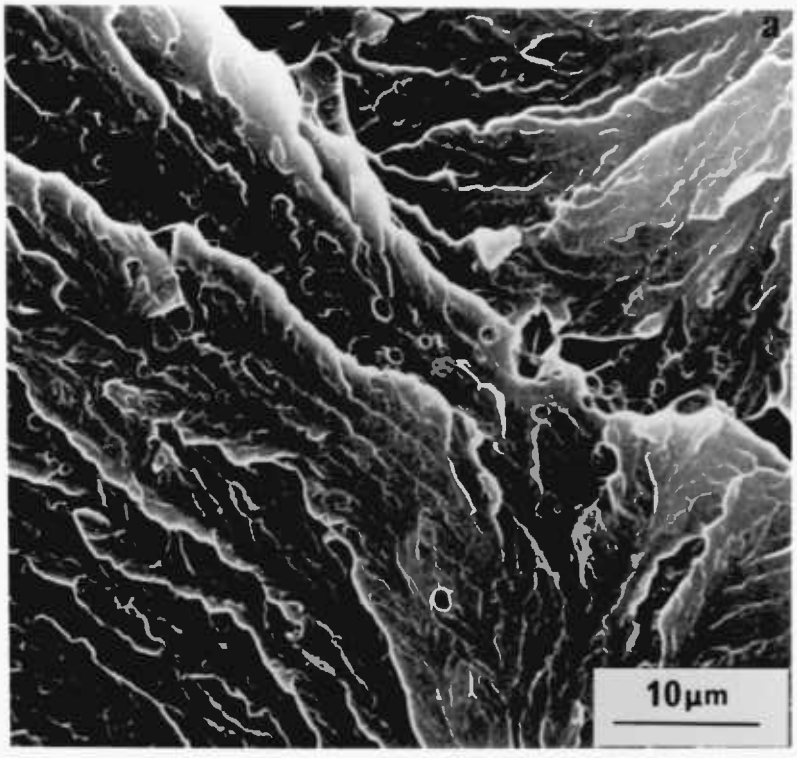

a
b
20µm
10µm
10µm

Figure 4.23. Transgranular cleavage failure in the 6/3 Cu alloy. Solution treated, water quenched and exposed to water vapour at 120°C for 56 hours.


a
10µm

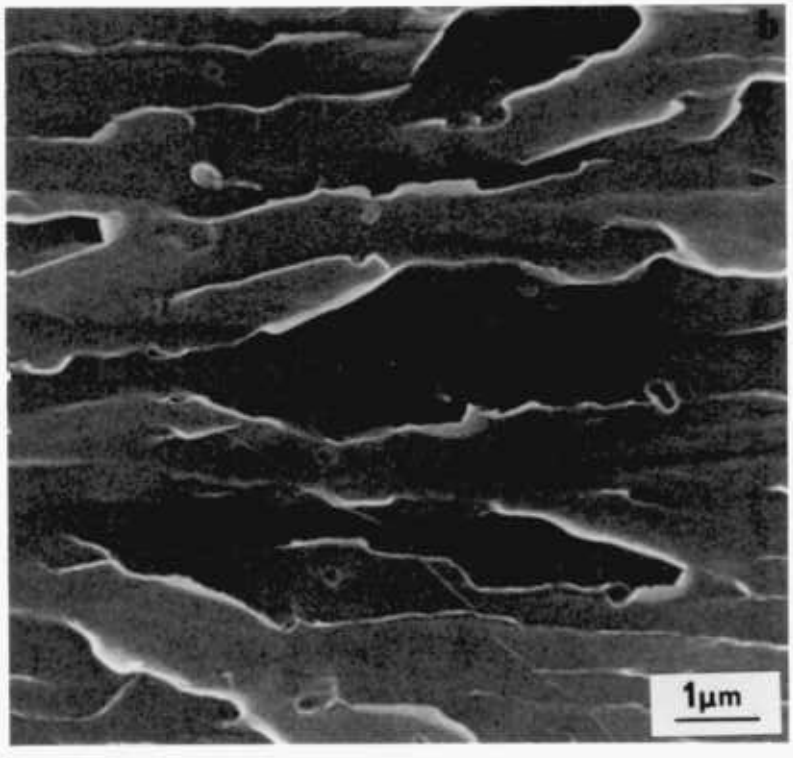
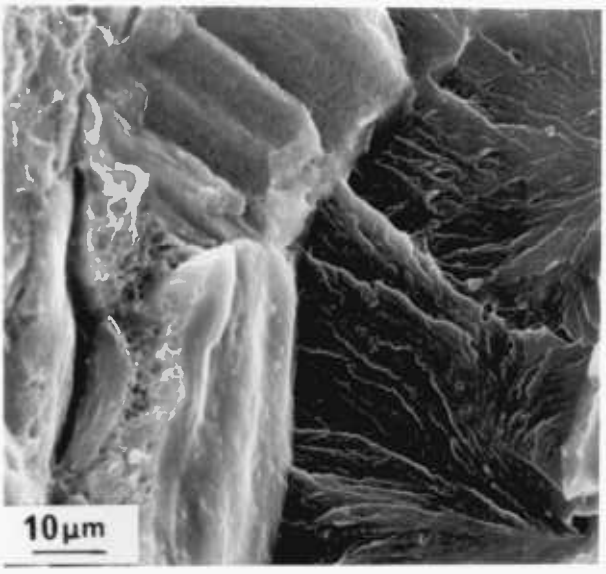

b
1µm

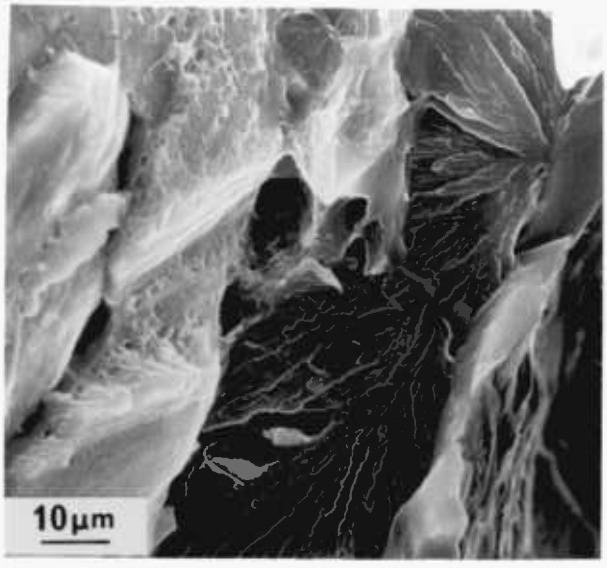
Figure 4.24. Transgranular cleavage fracture at the periphery of samples of the 6/3 Cu alloy exposed to water vapour at 120°C.

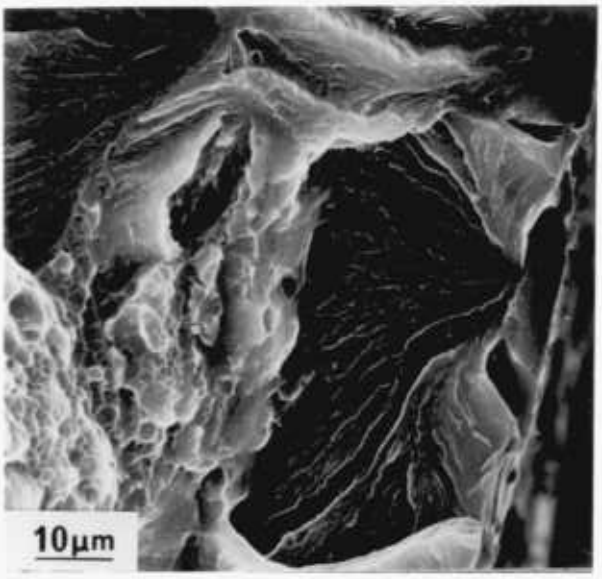
(a) 26 hours exposure

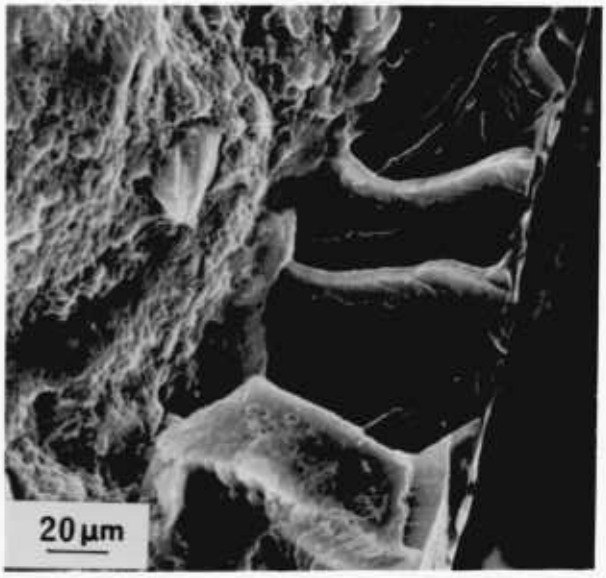
(b) 48 hours exposure

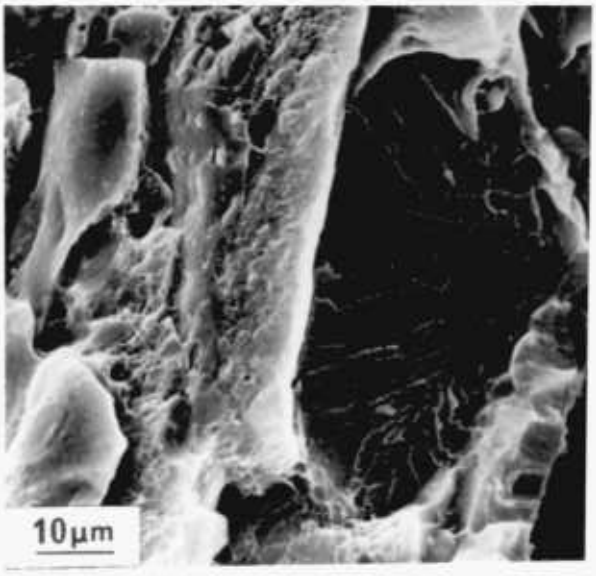
(c) 92 hours exposure

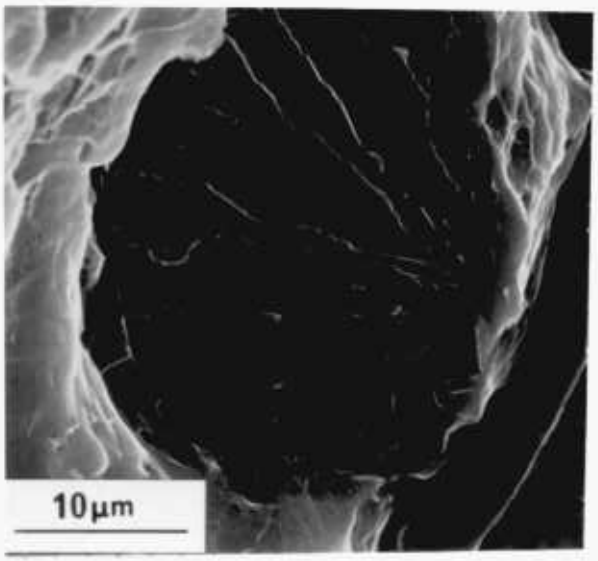

10μm


10μm


10μm


20μm


10μm


10μm

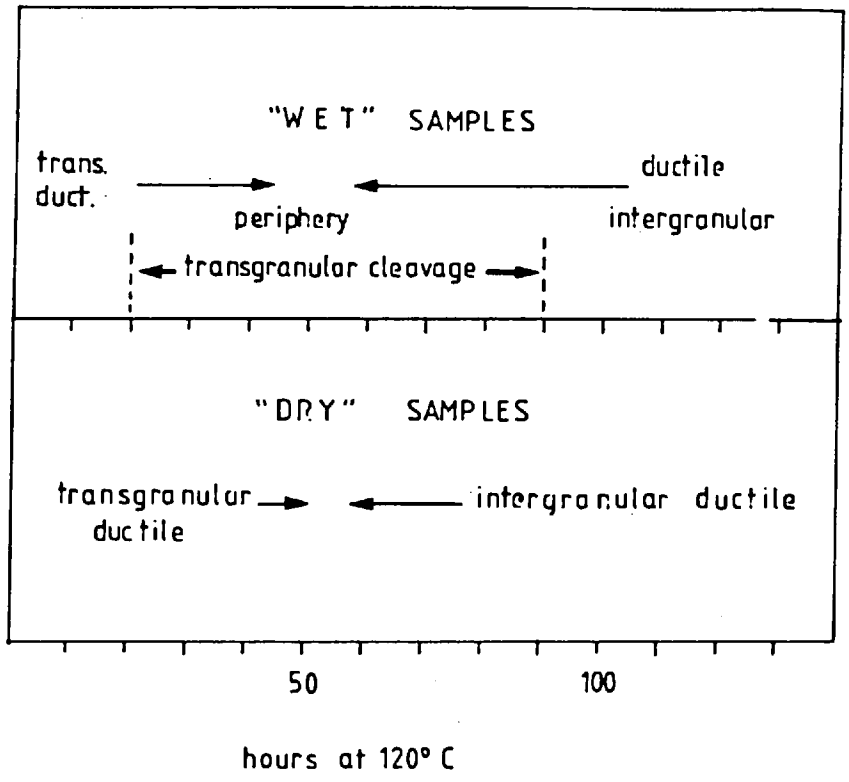
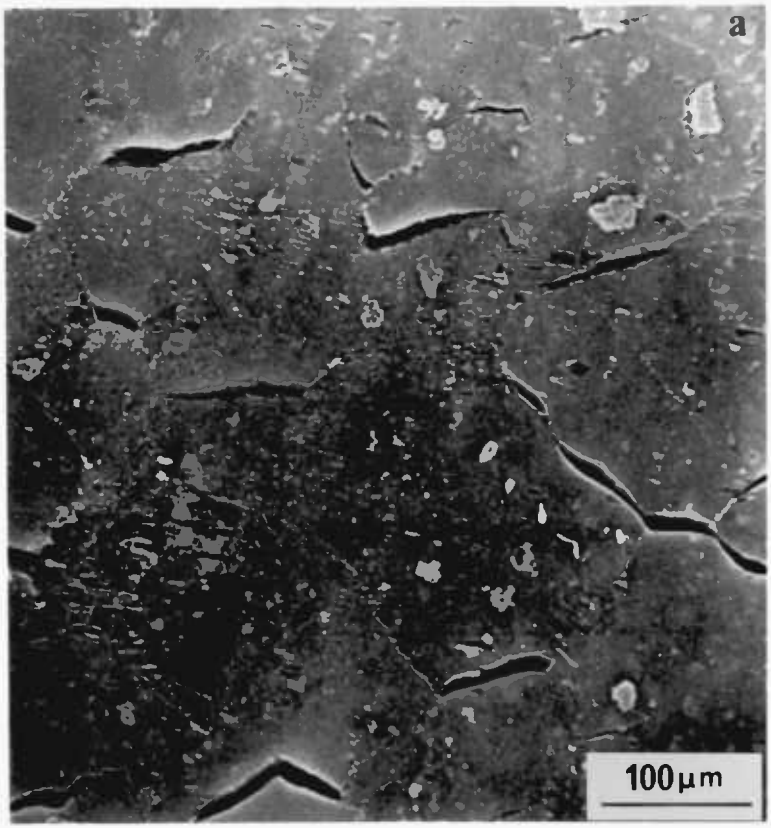


Figure 4.25. Range of occurrence of transgranular cleavage fracture in the 6/3 Cu alloy.

Figure 4.26. (a) Extensive grain boundary cracking following pre-exposure and mechanical testing of 6/3 Cu samples.
Cracks not present before the application of stress.
6/3 Cu alloy exposed to water vapour in the autoclave for 56 hours.

(b) Higher magnification of same sample showing both intergranular and transgranular surface cracks.


a
100µm

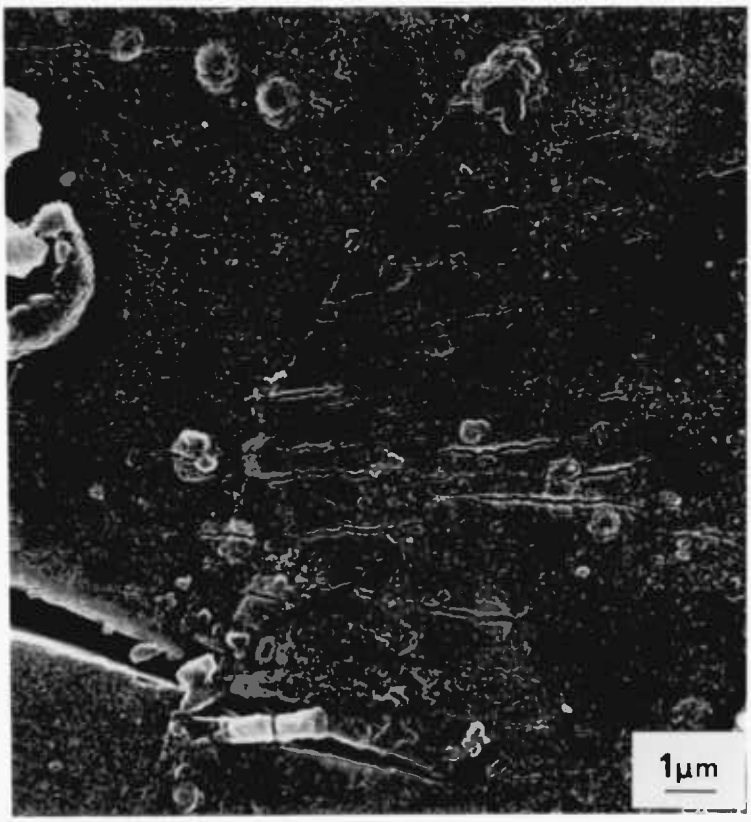
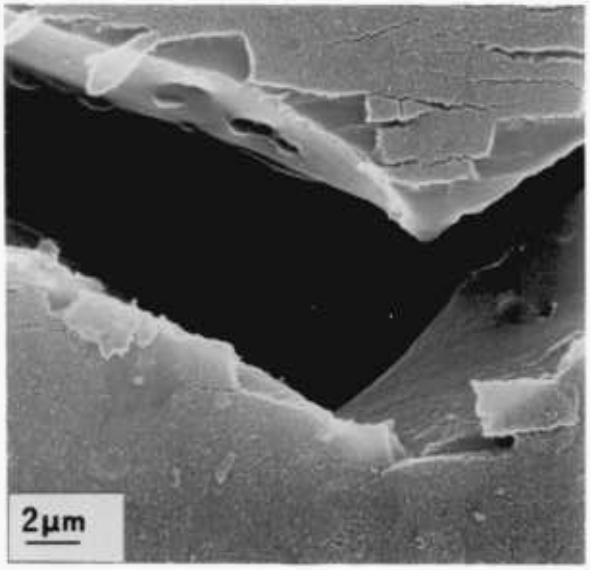
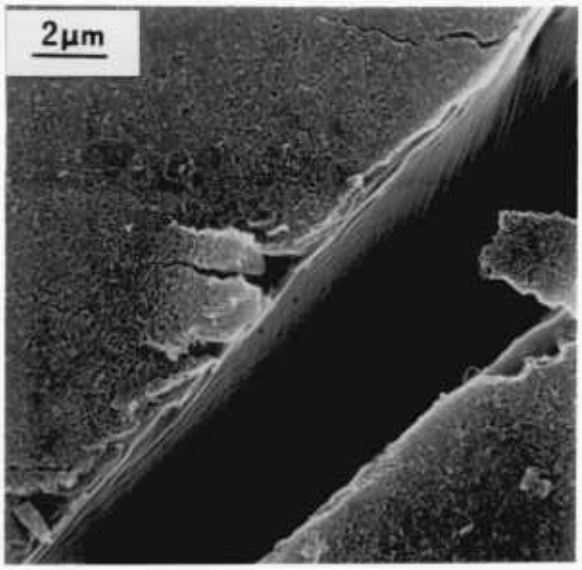
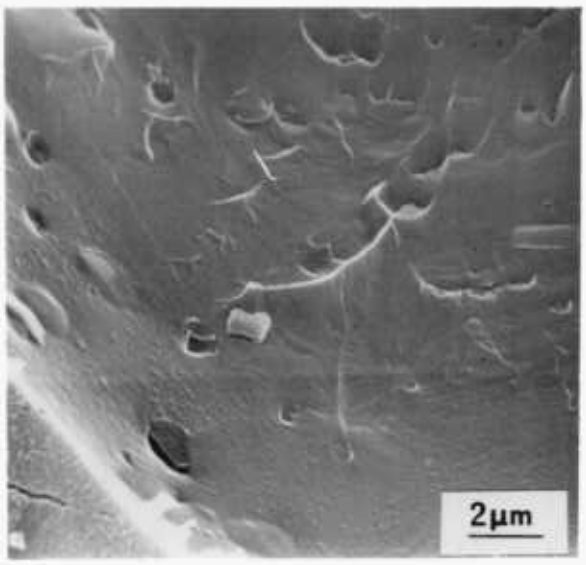

1µm

Figure 4.27. Intergranular subcritical cracks in the 6/3 Cu alloy showing very little intergranular corrosion attack. Grain boundary particles and slip steps clearly visible. Surface hydroxide is cracked following the application of stress.


2μm


2μm


2μm

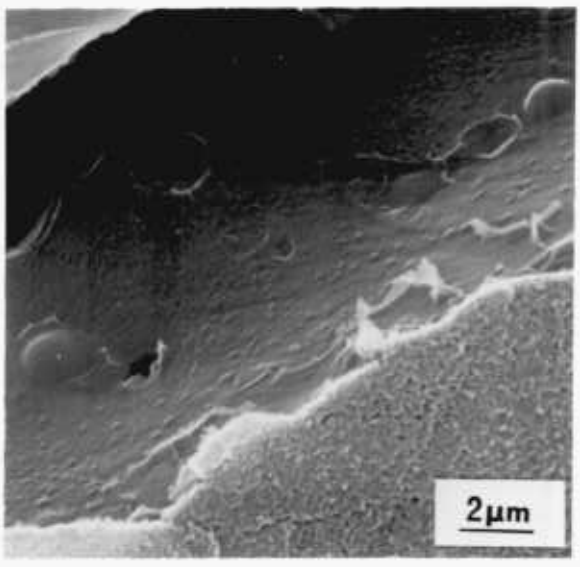
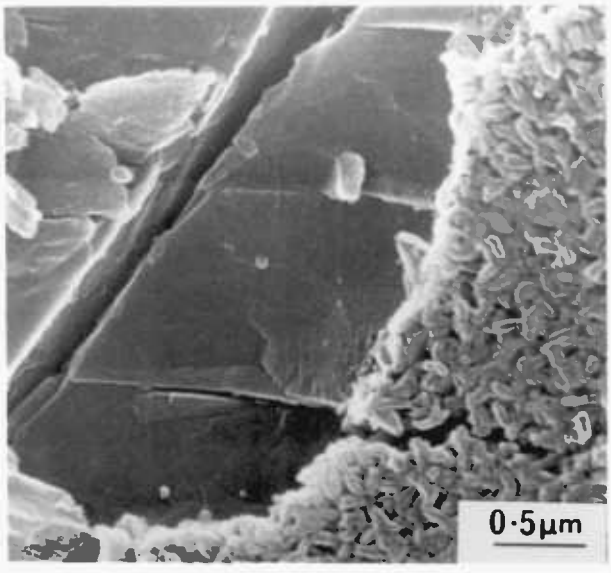
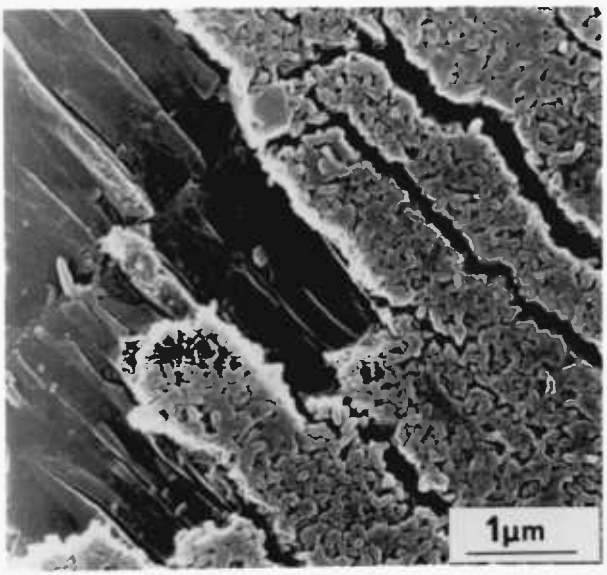

2μm

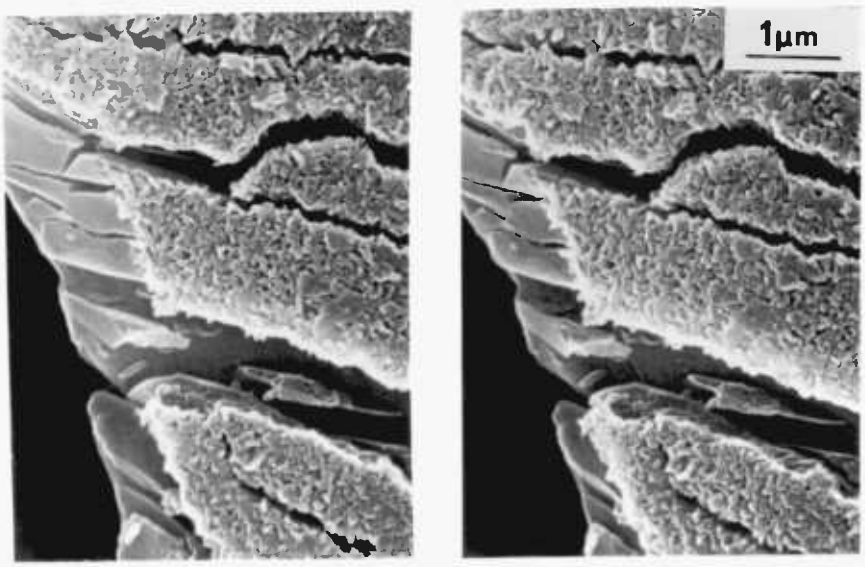
Figure 4.28. (a) Surface cracking of a 6/3 Cu alloy exposed to water vapour at 120°C. Note crystallographic nature of transgranular cracks.

(b) Similar transgranular cracks on both sides of a grain boundary that intersects the surface. Note that different cleavage planes crack in each grain.

(c) Stereo pair of surface cracking showing very thick columnar hydroxide which has cracked as a result of cracking in the underlying metal.


0·5μm


1μm


1μm

It is significant to note that this oxide has been cracked along crystallographic directions (Figure 4.28) which can be correlated with transgranular cracks running along the underlying metal.

All exposed samples examined by transmission electron microscopy exhibited hydrogen bubbles at the grain boundaries (Figure 4.29).

In order to compare directly the effect of copper on the embrittlement characteristics, experiments were carried out using 6/3 Cu samples which had a grain size similar to that of the high purity 6/3 base alloy. This was achieved as outlined in Section 3.1 by solution treating such samples at 500°C followed by a period at 450°C. It was considered necessary to equilibriate the system back at 450°C in order to minimise differences in the vacancy concentration, quench rate and resultant solute profiles at interfaces, between the above samples and the 6/3 Cu samples treated at 450°C only. It appears however, that this was not entirely successful as it was noted that the size and density of the S phase was greater, in the 500°C solution treated material.

Exposure of samples was then carried out in the normal manner. The results of the tensile tests are shown in Figure 4.30, which also includes the results from the 450°C treated samples for comparison purposes.

It was clear in these experiments that the large grain (100μm) samples of the copper bearing alloy were now severely embrittled following exposure to steam. The ductility of the dry samples also decreased with the increasing grain size but these values were consistently higher than those of the wet samples which became completely brittle after about 40 hours exposure (Figure 4.30). It is of interest to note that this time is very close to that found for complete embrittlement in the 6/3 base alloy.

4.1.5. Isothermal exposure of the 6/3 Cr alloy at 120°C

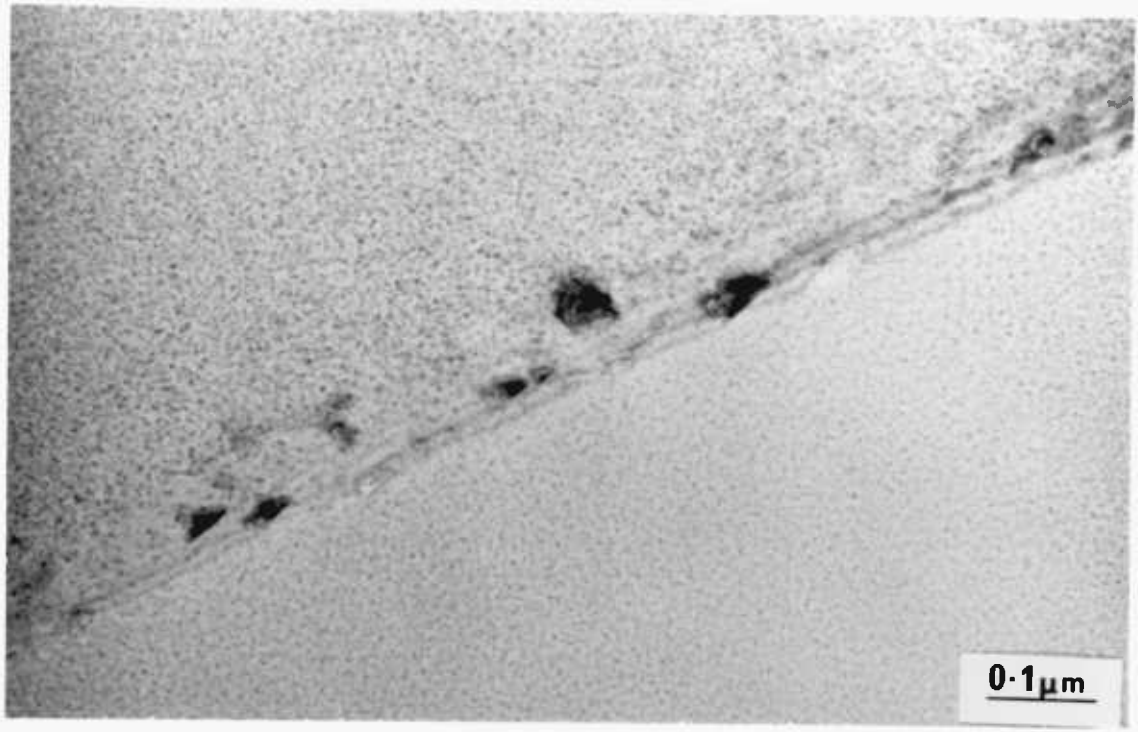
Exposure of the Cr containing alloy to water vapour at 120°C was found to have a minimal effect on ductility if samples were subsequently tensile tested at a strain rate of $\sim 10^{-3} s^{-1}$.

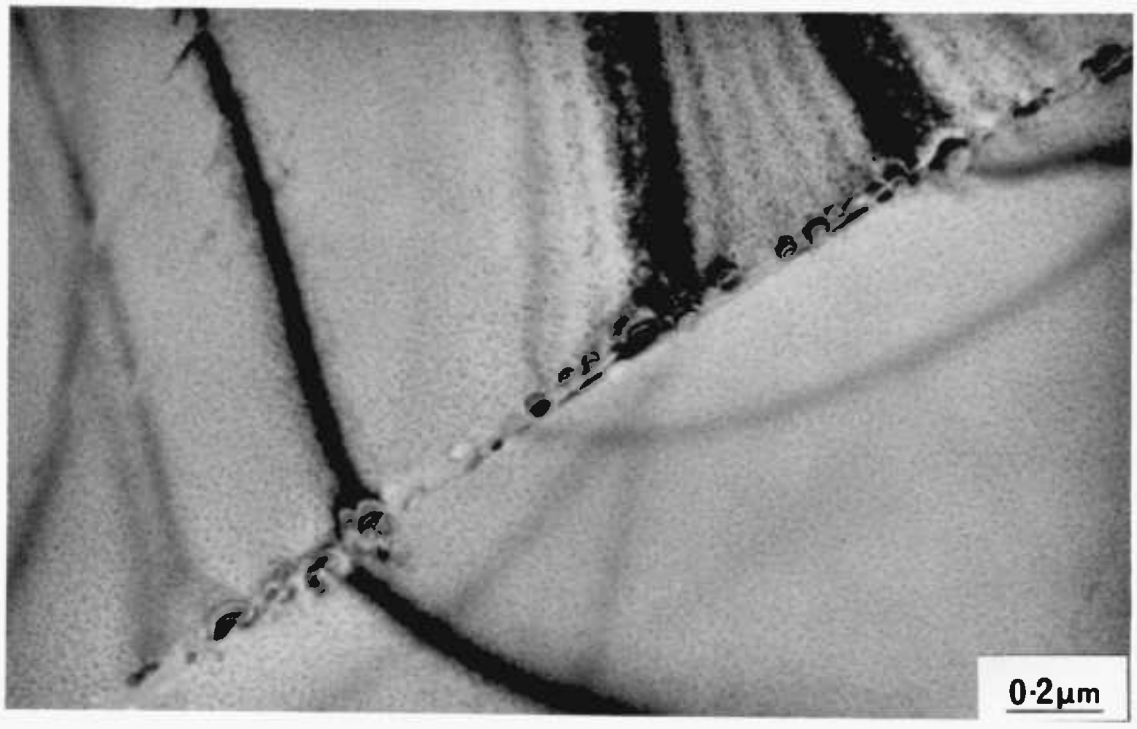
Deviation from the results of the dry samples was slight and only apparent after prolonged exposure times ($\sim$ 500 hours) (Figure 4.31).

However, the fractography carried out in the SEM revealed differences between dry and wet material. The wet samples of the Cr bearing material showed multiple surface cracking (Figure 4.32) but no significantly greater

Figure 4.29. Hydrogen bubbles in the 6/3 Cu alloy.
(a) Exposed to water vapour at 120°C for 22 hours.

(b) Exposed to water vapour at 120°C for 53 hours.


0·1μm


0·2μm

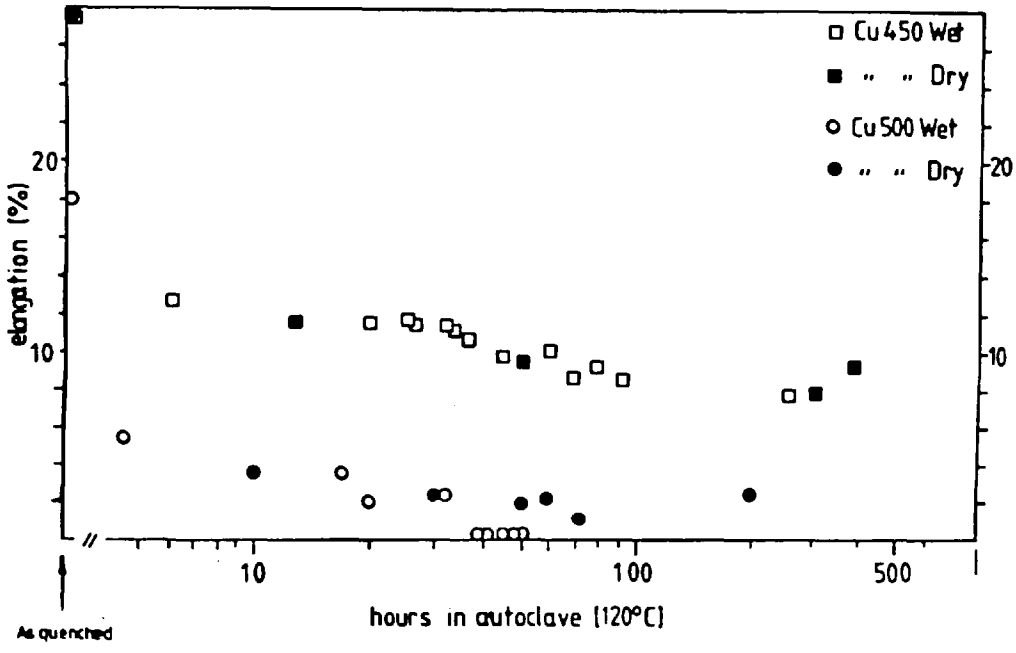


Figure 4.30. Variation of ductility with exposure of 100μm grain size 6/3 Cu samples to water vapour at 120°C. (Open circles) Similarly heated dry samples are also shown (filled circles) and the behaviour of the smaller grain samples reproduced from Figure 4.19.

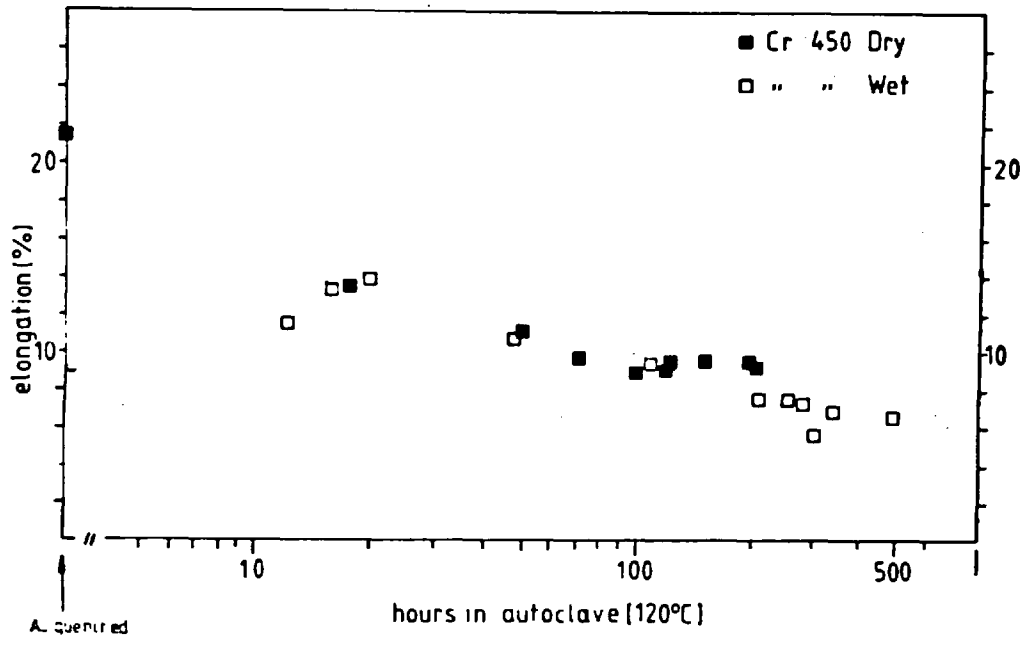
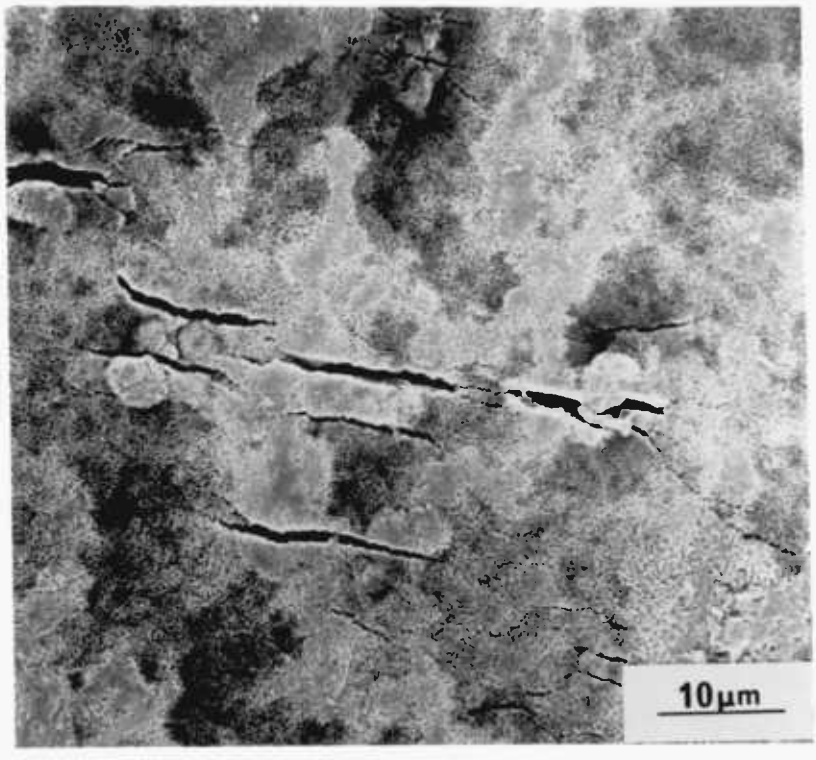
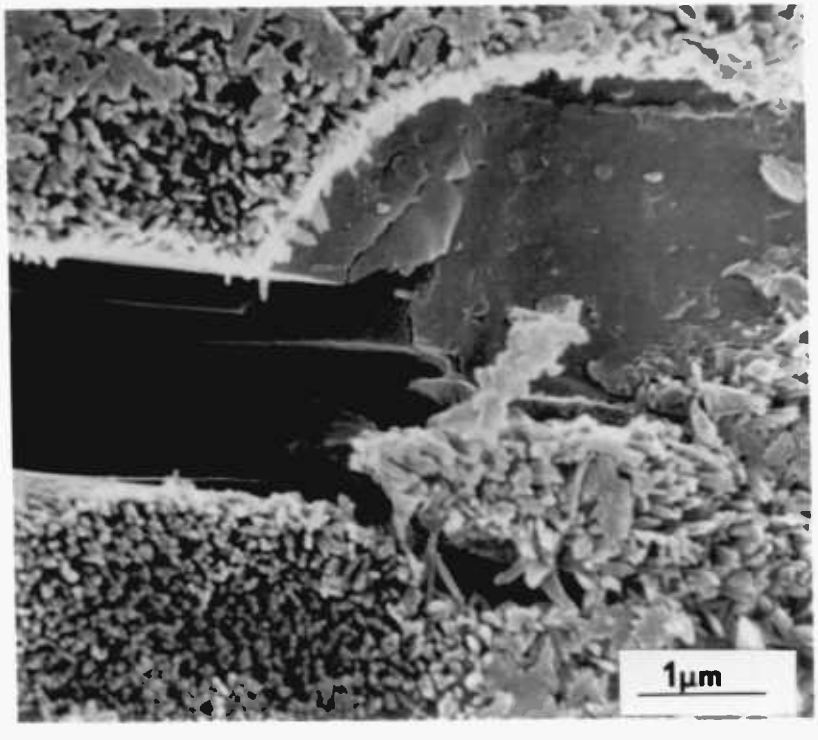


Figure 4.31. Variation of ductility of 6/3 Cr alloy samples with exposure to water vapour at 120°C.

Figure 4.32. Surface cracking in exposed and tensile tested samples of the 6/3 Cr alloy.


10μm


1μm

amounts of intercrystalline fracture (Figure 4.33), than the corresponding dry controls. Both transgranular and intergranular crack nuclei were found but it was evident that all transgranular cracks propagated in a ductile manner.

Selected samples of this alloy were tested at strain rates below the normal $10^{-3}s^{-1}$ with appropriate precautions to exclude laboratory air moisture (see Section 3.1). At strain rates below $10^{-4}s^{-1}$ it was found that significant embrittlement of the alloy could be detected (Figure 4.34). Similarly treated dry samples did not show any such embrittlement thus eliminating the testing environment as the cause of the effect. Fractography of these samples revealed a more clearly brittle intergranular fracture surface (Figure 4.35).

No cleavage type failures were found in any samples (dry or wet) of the Cr bearing alloy at any strain rates.

4.2. Cathodic Charging

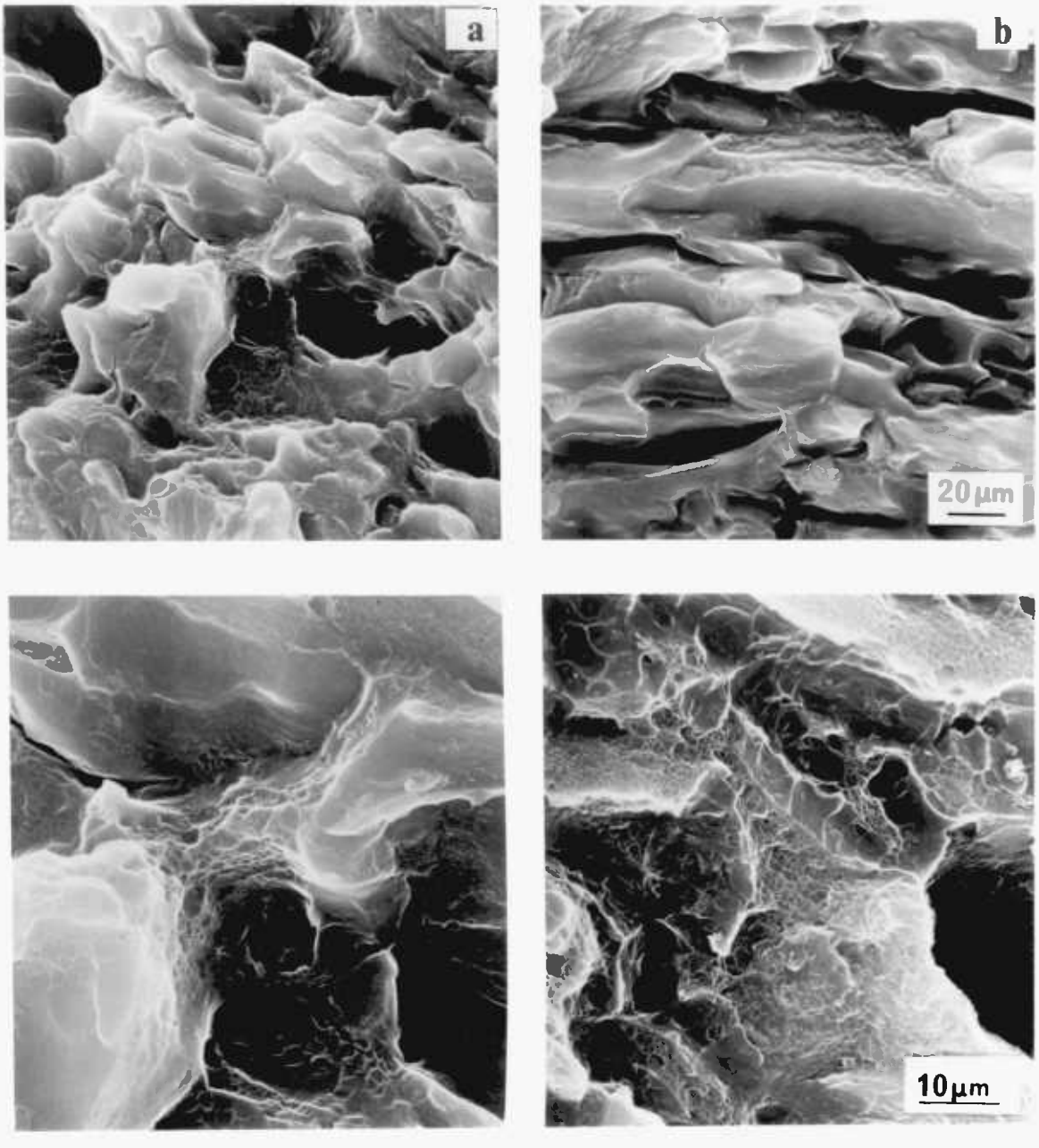
Selected samples of the copper containing alloy were cathodically charged. These were given the standard solution treatment at 450°C followed by a cold water quench and naturally aged at room temperature for three weeks. They were then cathodically charged using the conditions described previously, thoroughly washed and immediately mechanically tested.

The results of the tensile tests are shown in Figure 4.36. It was found that as a result of cathodic charging a drop in elongation was apparent together with a corresponding reduction in the fracture stress.

4.3. "In-situ" Electron Microscopy

The "in-situ" reaction between all the alloys and water vapour saturated helium was found to occur preferentially at sites under electron irradiation (Figure 4.37). The reaction, in the first instance, took the form of a blistering reaction whereby the oxide partially decohered from the metal substrate forming hemispherical surface blisters (Figure 4.38). On further exposure to the electron beam internal bubbles were formed (Figure 4.39). These were identical to those found in the bulk sample experiments described previously and were contained within the foil surfaces. The occurrence of the internal bubbles was a function of alloy composition and heat treatment (see below). The reaction was found to occur at all accelerating voltages employed. Neither was there a measurable difference in the rate of the reaction when using potentials in the range of 100-500 kV.

Figure 4.33. Comparisons between dry (a) and wet (b) fracture surfaces of 6/3 Cr samples show no significant difference in fracture mode even after prolonged exposure.
Dry samples (a) Aged dry at 120°C for 237 hours.
Exposed samples (b) Exposed in the autoclave at 120°C for 229 hours.


a
b
20µm
10µm

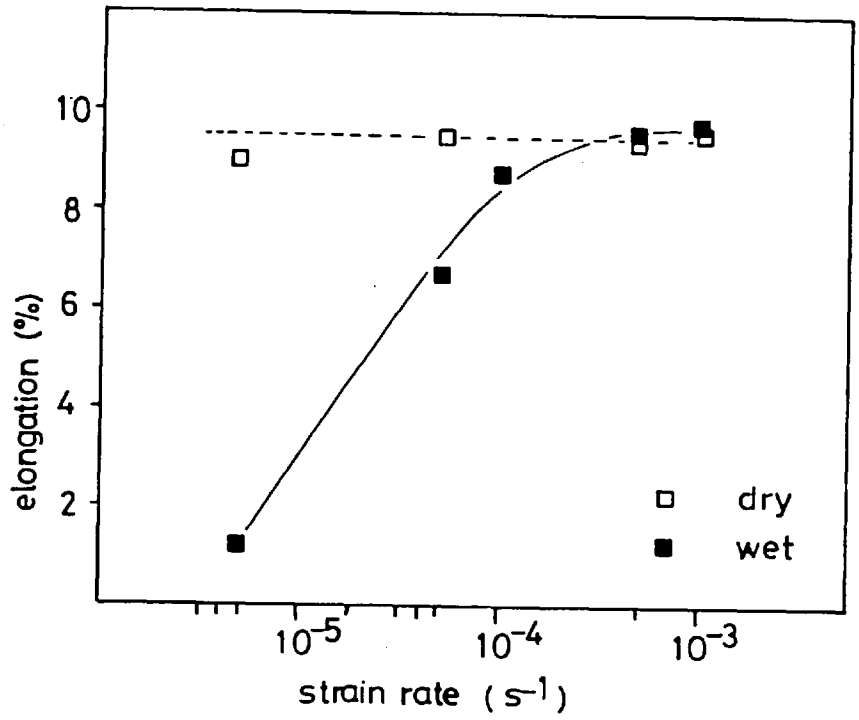
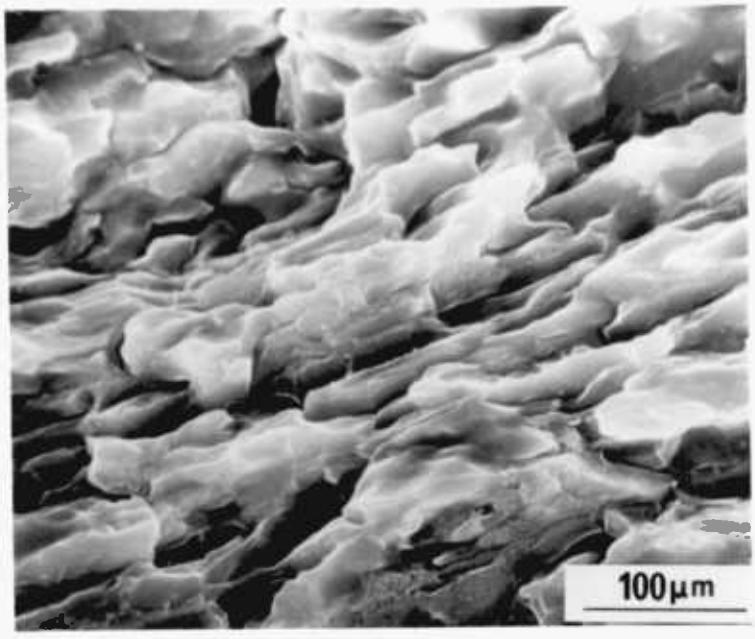
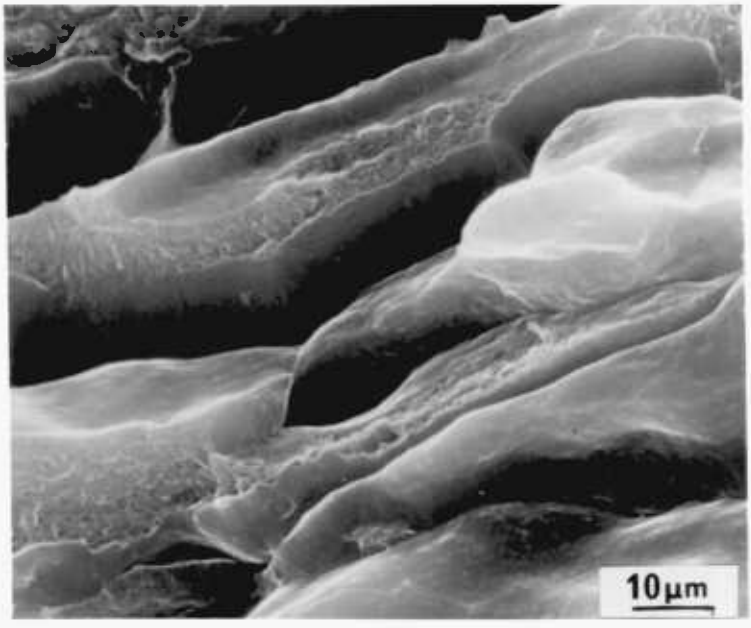
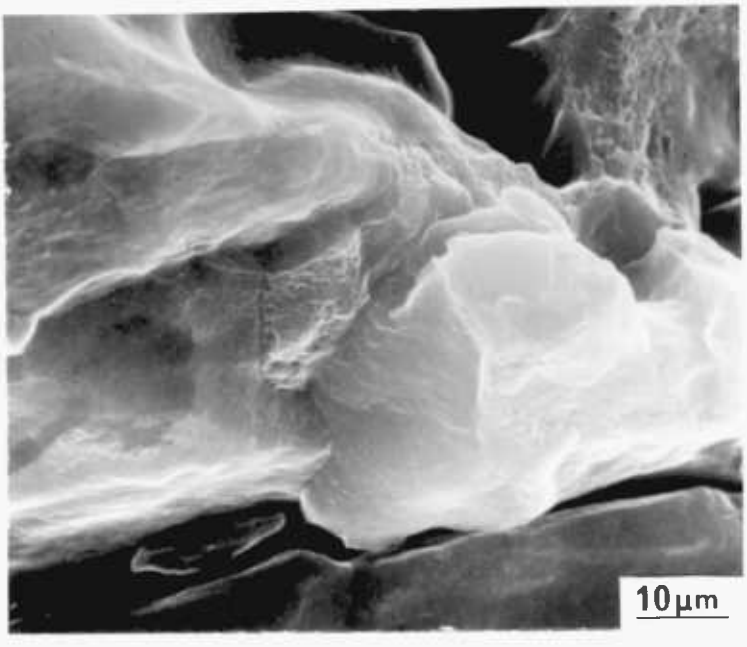


Figure 4.34. Strain rate sensitivity of ductility in 6/3 Cr alloy samples exposed to water vapour in autoclave for 120 hours.

Figure 4.35. Fracture surface of 6/3 Cr alloy samples exposed to water vapour at 120^{o}C for 120 hours and tensile tested at a strain rate of 5 x 10^{-5} s^{-1}.


100µm


10µm


10µm

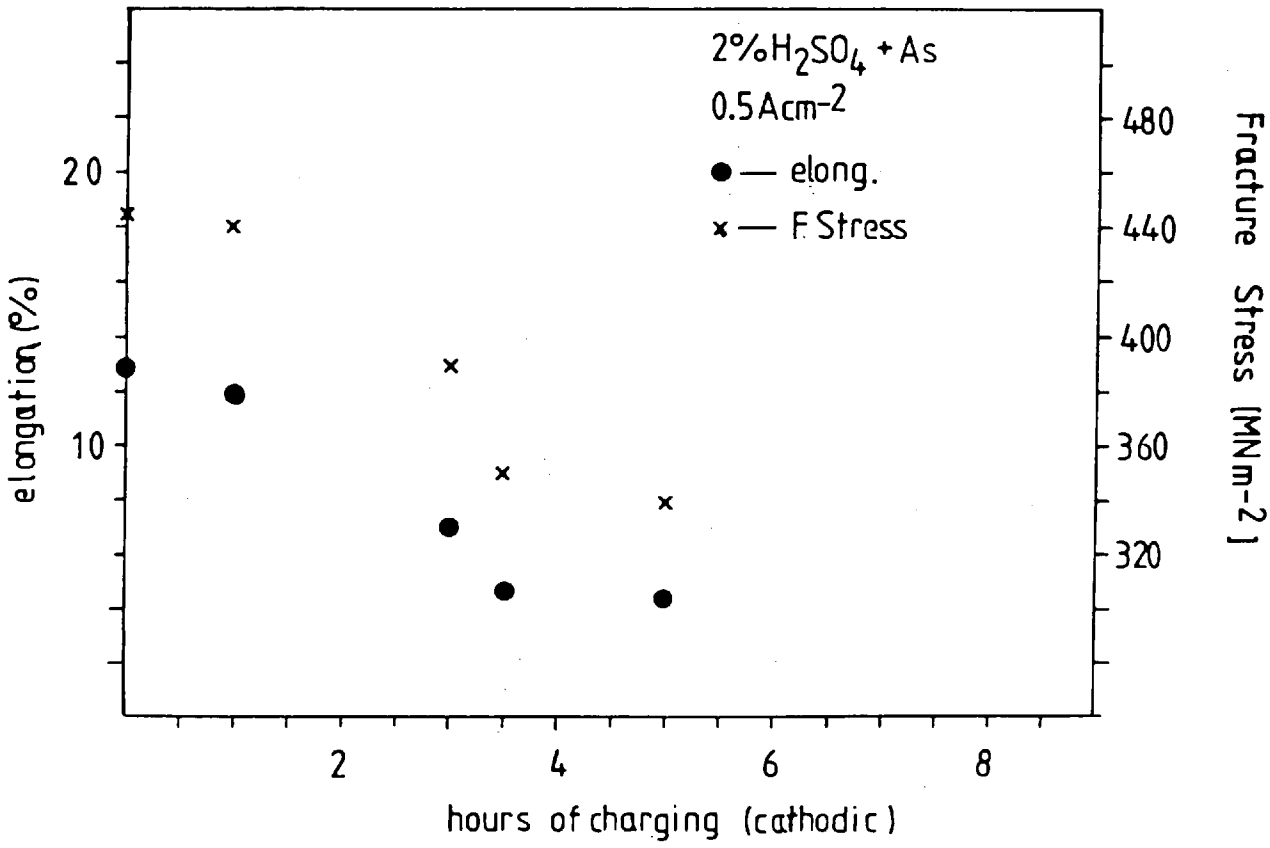
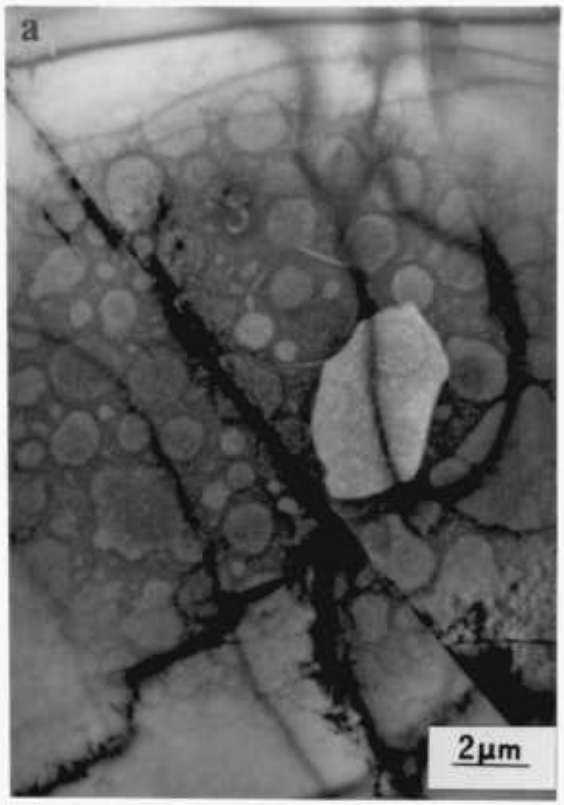
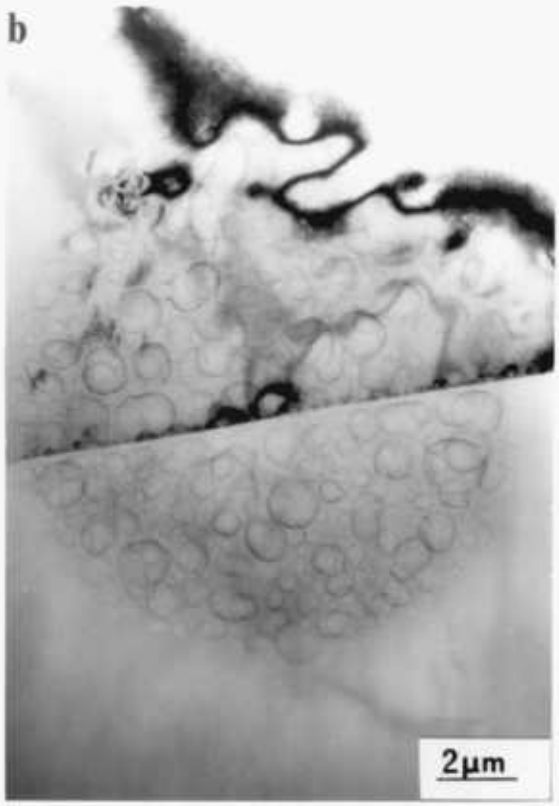


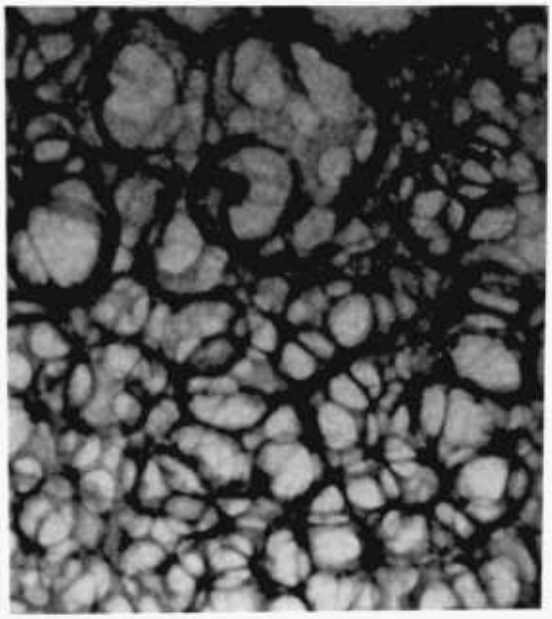
Figure 4.36. Variation of ductility of 6/3 Cu samples with degree of cathodic charging. Each point represents an average of two individual tests.

Figure 4.37. (a) and (b) Surface reaction regions in the environmental cell under the influence of a 500 kV electron beam and water vapour. The reaction is confined precisely to the area under the electron beam and consists of a very large number of surface oxide blisters.
Electron flux density = 5×10^{-3} A mm^{-2}
Temperature = 253 K

Figure 4.38. A S.T.E.M./S.E.M. pair taken on the JEOL 100 CX microscope showing surface blisters induced by reaction in the environmental cell of the H.V.E.M. Blisters form on both sides of the foil.


a
2µm


b
2µm



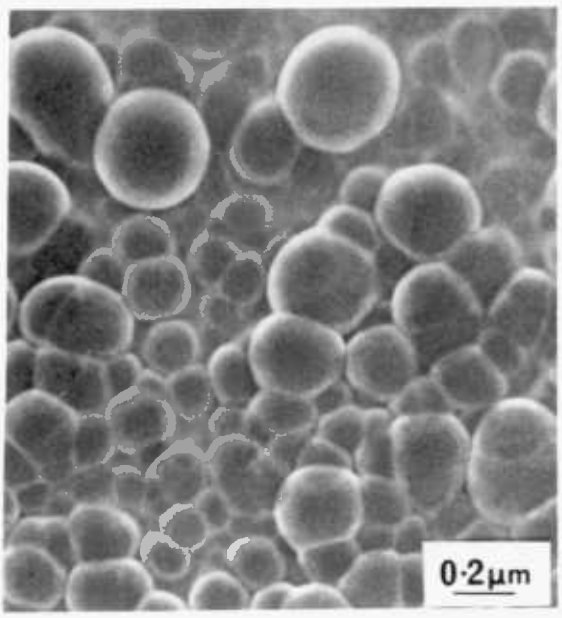
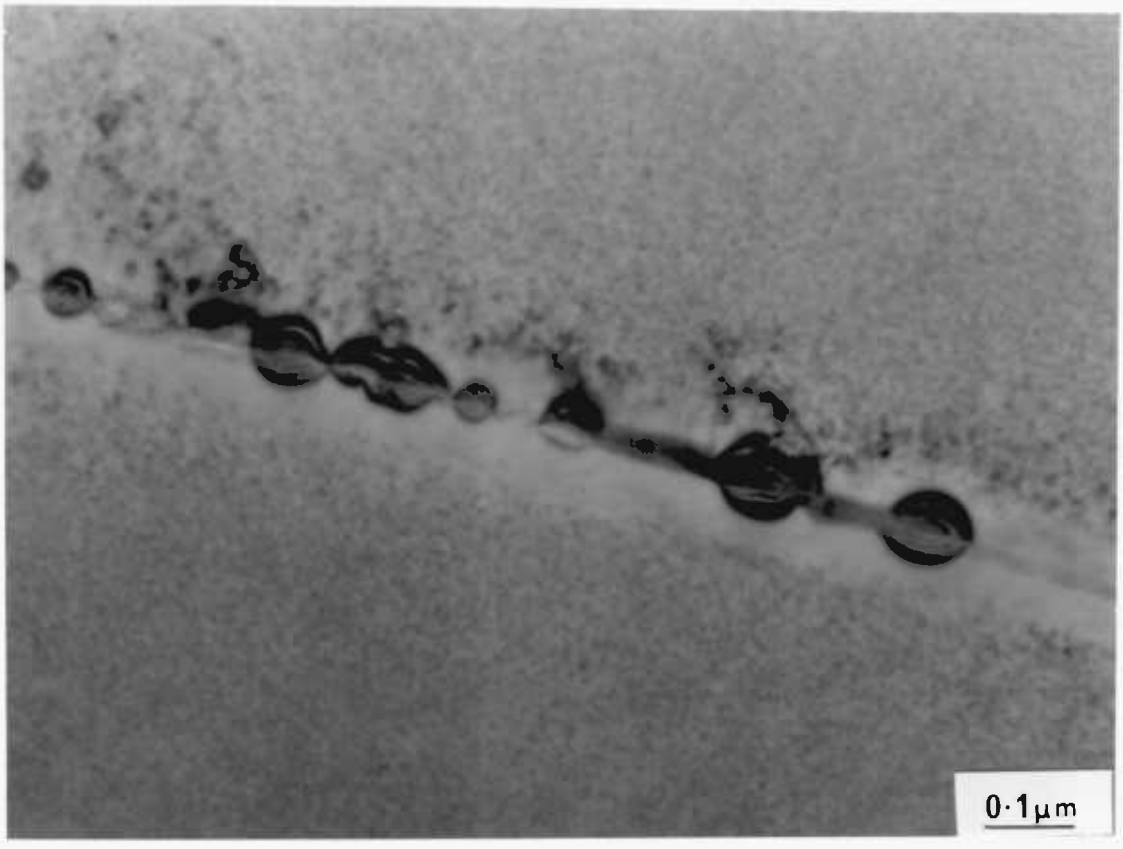
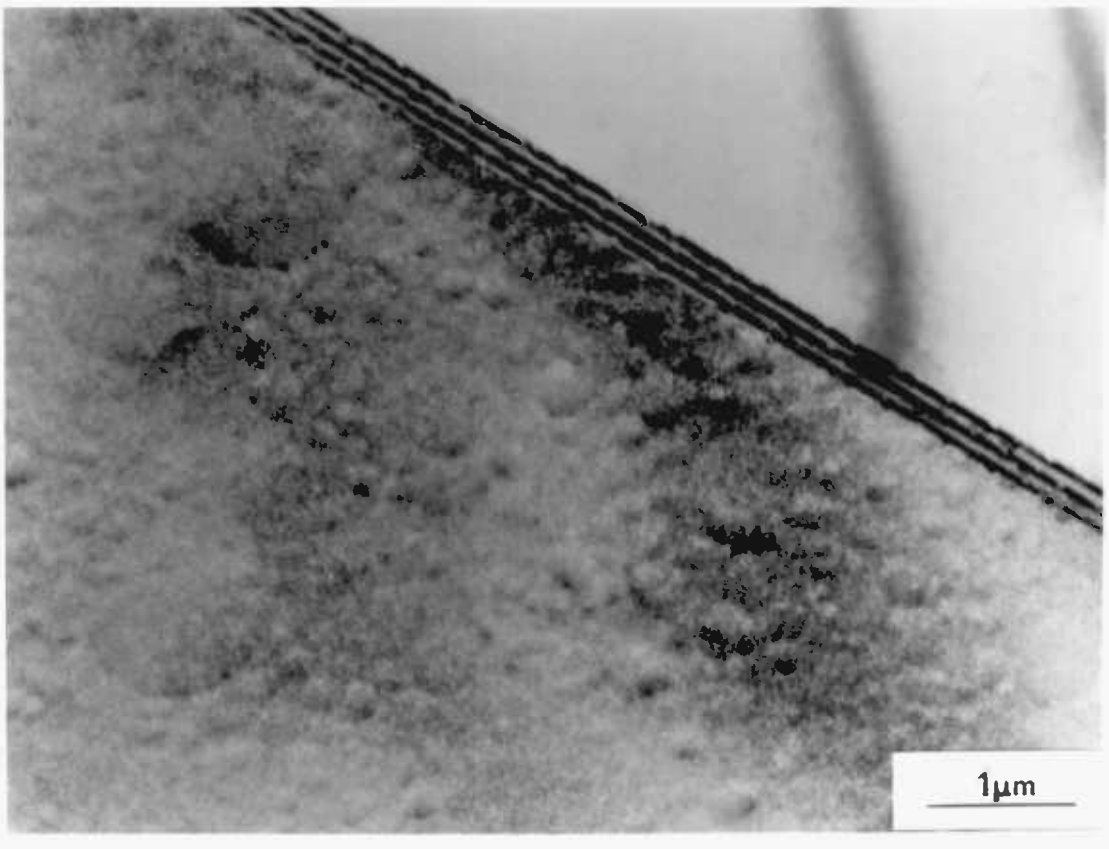

0·2µm

Figure 4.39. Internal hydrogen bubbles produced as a result of the 'in-situ' reaction between water vapour and the 6/3 Cu alloy.
Electron flux density = 5×10^{-3} A mm^{-2}
Temperature = 233 K

Figure 4.40. Fast, continuous surface blistering as a 6/3 base alloy foil irradiated in the environmental cell for 30 seconds.
Electron flux density = 10^{-2} A mm^{-2}
Temperature = 273 K


0·1μm


1μm

The rate of the reaction, however, was critically dependent on the temperature. The reaction at ambient temperature was very fast. In the 6/3 base alloy reaction was detectable after irradiation times of less than 10 seconds at 293K, but this was increased to values greater than 60 seconds at 233K. Accurate evaluation of the onset of the reaction was difficult due to the background image information contained in the foils. Contrast from the second phase particle dispersions was the main contributor to the "background noise" in the aged samples. The "incubation period" values, therefore, are given with reserve and should only be treated as qualitative measures of surface reactivity.

High electron flux densities significantly reduced the incubation period for the superficial reaction, and led to increased reactivity. Comparison of data, such as incubation periods and rates of growth, between the different alloys could therefore only be made at comparable electron flux densities. For this reason the electron flux density was generally kept in the region of 10^{-3}-5 x 10^{-3} A mm^{-2}. At high flux densities (or high temperatures) continuous blister formation fracture and reformation was observed. (Figure 4.40). This occurred at a fast rate and is only clearly visible on the video recordings.

At the low chosen electron flux densities the rate of growth of blisters was reduced sufficiently to allow subsequent measurement of their rates of growth. This was carried out by measuring the diameter of the blisters recorded on photographic plates as a function of time. A typical set of results is shown in Figure 4.41. In this Figure the average diameter of 10 different blisters is plotted against irradiation time. The origin of the time scale measurement was taken as the onset of the surface reaction, i.e. at the end of the incubation period. Blisters showed large variations in size and the results were "normalised" by dividing the volume of any one blister at any time, by the volume of the same blister at the time of the final measurement. This limits the ordinate scale to a range of zero to unity. Furthermore, in order to allow comparison between the rates of growth between the different alloys the time scale was also normalised by dividing all times by the time of the last measurement. Two points on the curve, the origin and (1,1), were therefore fixed. Figure 4.42 shows a pool of results from all three alloys treated so that a normalised volume (d^3/d^3_{max}) is plotted against a normalised time parameter (t/t_{max}). Each point represents an average of not less than 10 different blisters growing under an electron flux density of 10^{-3} A mm^{-2} and at 233K. It is evident from this graph

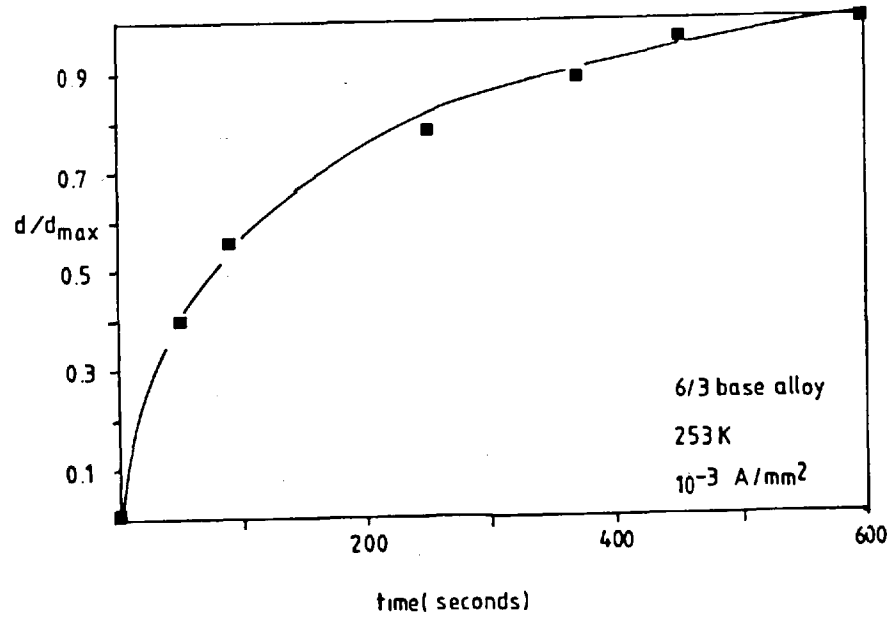


Figure 4.41. Variation of blister size with irradiation time.

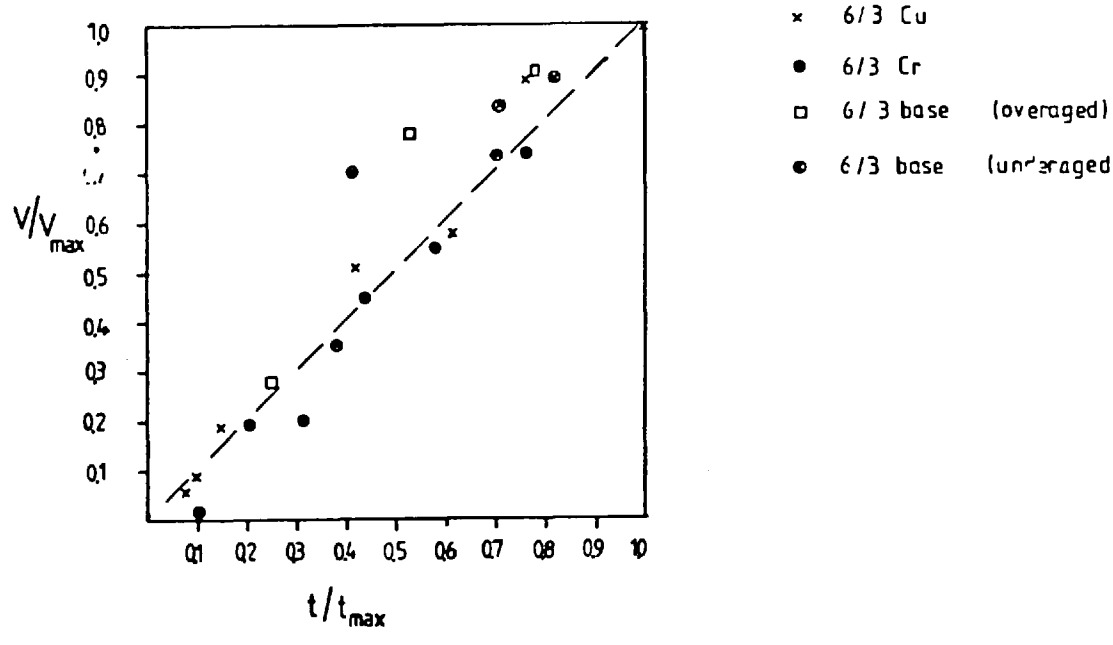


Figure 4.42. Variation of "normalised" volume with "normalised" time for a rangeof alloy samples.

that the experimental points fall on the straight line joining the fixed points indicating that the volume of the blister is directly proportional to the irradiation time.

The blister size, at any time, was a function of temperature. High temperatures gave rise to larger blisters. It was a frequent observation in all alloys that the blisters at the periphery of the reaction area exhibited larger diameters than those in the centre region.

4.3.1. 6/3 base alloy

The first indications of an interaction between examination and hence irradiation of the 6/3 base alloy came in the form of a very fine blistering reaction (Figure 4.43). As mentioned earlier the onset of the reaction was difficult to determine accurately due to the "masking" effect of the underlying microstructure. Further variations between different foils were also evident possibly due to slight variations in initial oxide, temperature and electron flux density.

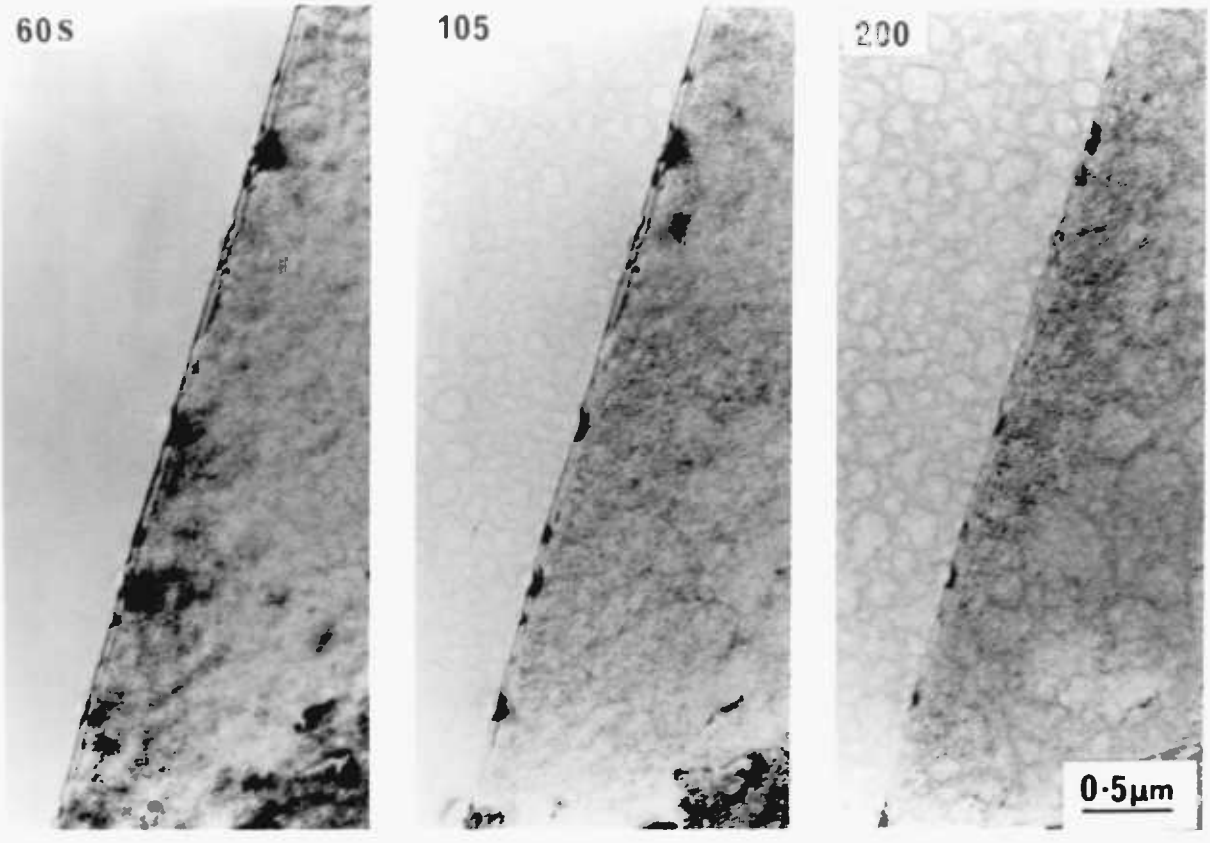
There appeared to be a degree of preferential attack at the grain boundaries (Figure 4.44). In the absence of large particles at the grain boundary (the sample of Figure 4.44 was solution treated and quenched only) the increased chemical reactivity in this region could be due to segregation effects or a reduction in the activation energy for attack at the high energy site of a grain boundary/surface intersection.

In overaged samples it was found that in addition to the surface blisters internal grain boundary bubbles were formed (Figure 4.45). These were confined to grain boundary particles. No such grain boundary bubble formation was detected in underaged material and it was apparent that no bubble nucleation occurred in the 6/3 alloy in the absence of grain boundary precipitates below a size of about 200A. This was in agreement with the results of the bulk exposure tests reported in Section 4.1. Samples with grain boundary particles larger than the critical size exhibited an abundance of bubbles following reaction under the electron beam. Air cooled and subsequently aged samples were particularly good in stimulating bubble formation (Figure 4.46).

Figure 4.47 shows the behaviour of a very large grain boundary particle on exposure to the electron beam. Blistering occurred preferentially at the particle during the early stages of the reaction (arrow 1). As the reaction proceeded general attack and oxide thickening occurred over the entire irradiated area. (This thickening is difficult to

Figure 4.43. In-situ sequence showing the development of blisters following irradiation under the electron beam.
Electron flux density = 10^{-3} A mm^{-2}
Temperature = 253 K
6/3 base alloy solution treated at 450°C, cold water quenched and aged at 120°C for 23 hours.

Figure 4.44. Sequence showing preferential attack at the grain boundary/surface intersections in an as quenched 6/3 base alloy
Electron flux density = 10^{-3} A mm^{-2}
Temperature = 233 K


60 s
105
200
0·5μm

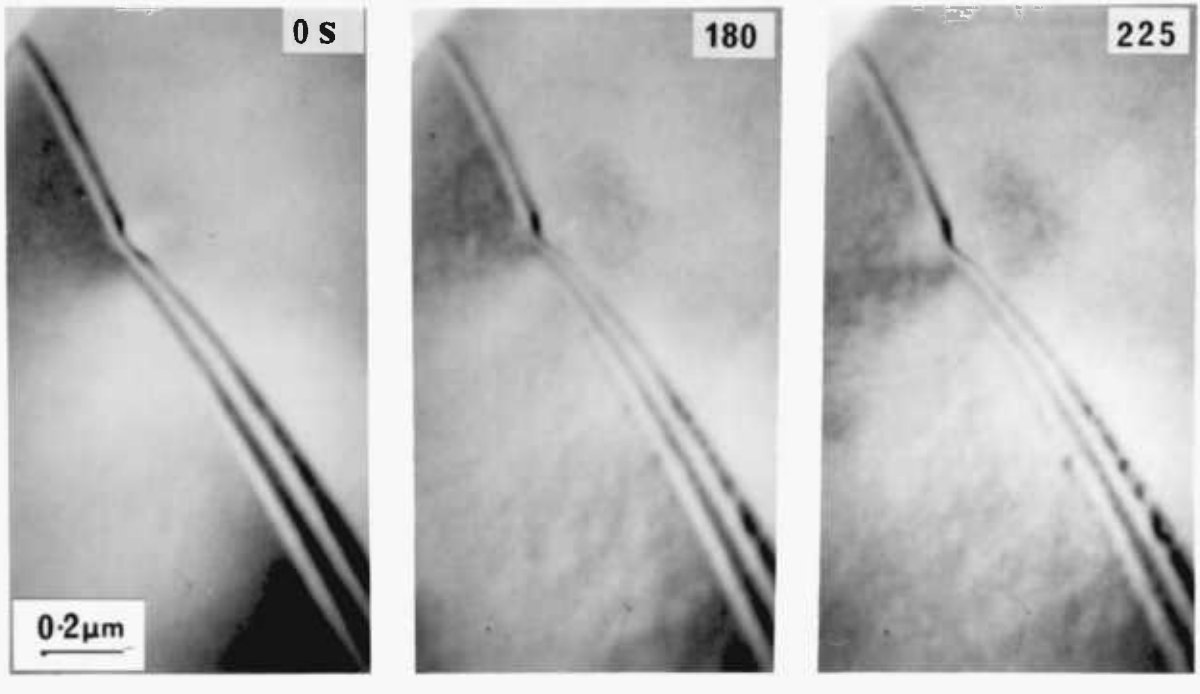

0 s
180
225
0·2μm

Figure 4.45. Stills taken from a video sequence showing the development of internal hydrogen bubbles in an overaged 6/3 base alloy sample.

Note that hydrogen bubbles form exclusively on grain boundary particles.
Electron flux density = 5×10^{-3} A mm^{-2}
Temperature = 233 K

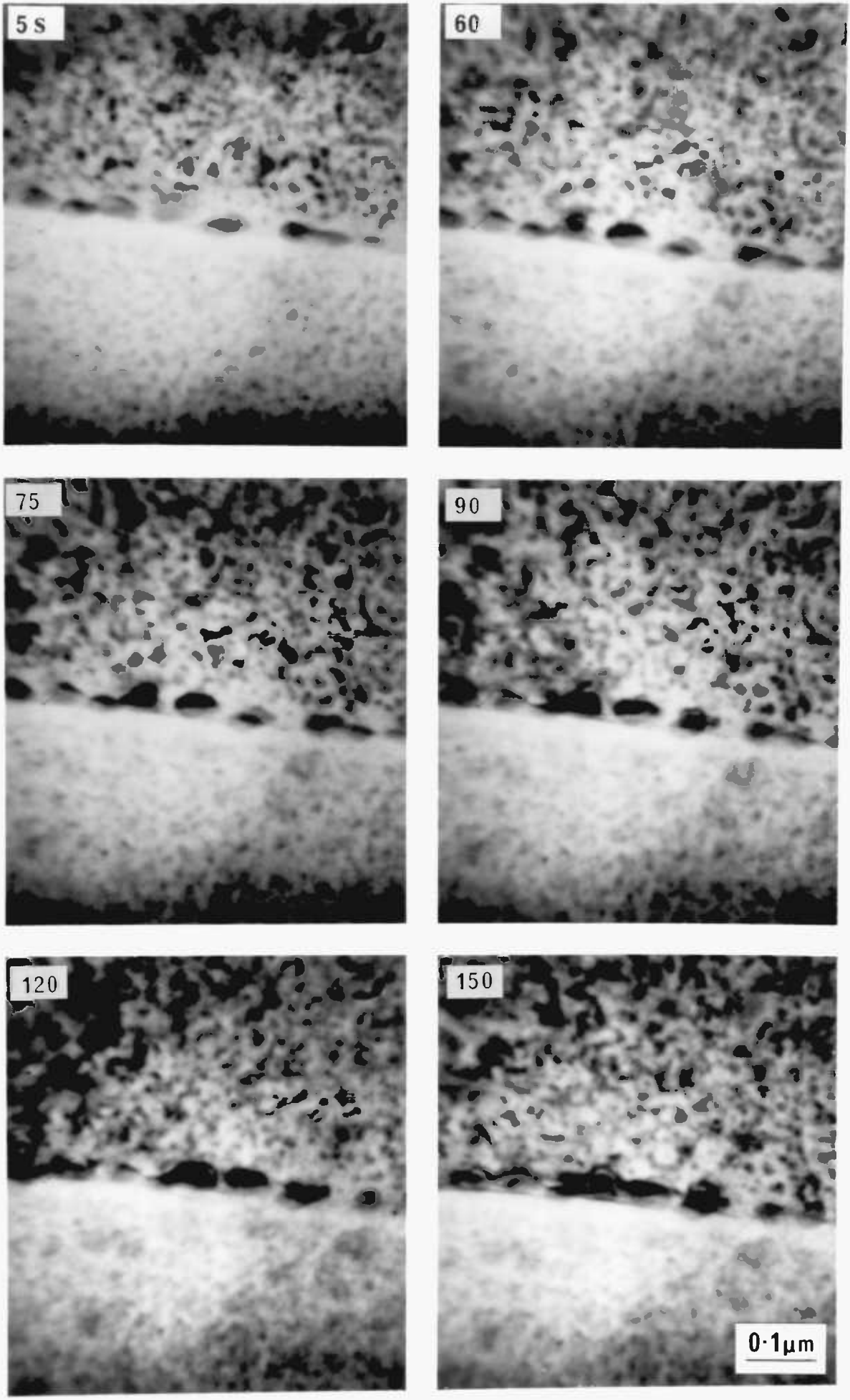

5 s
60
75
90
120
150
0·1µm

Figure 4.46. Stills from a video sequence showing the development of internal hydrogen bubbles.
6/3 base alloy solution treated at 450°C air cooled and subsequently aged at 150°C for 72 hours.
Electron flux density = 10^{-4} A mm^{-2}
Temperature = 233 K

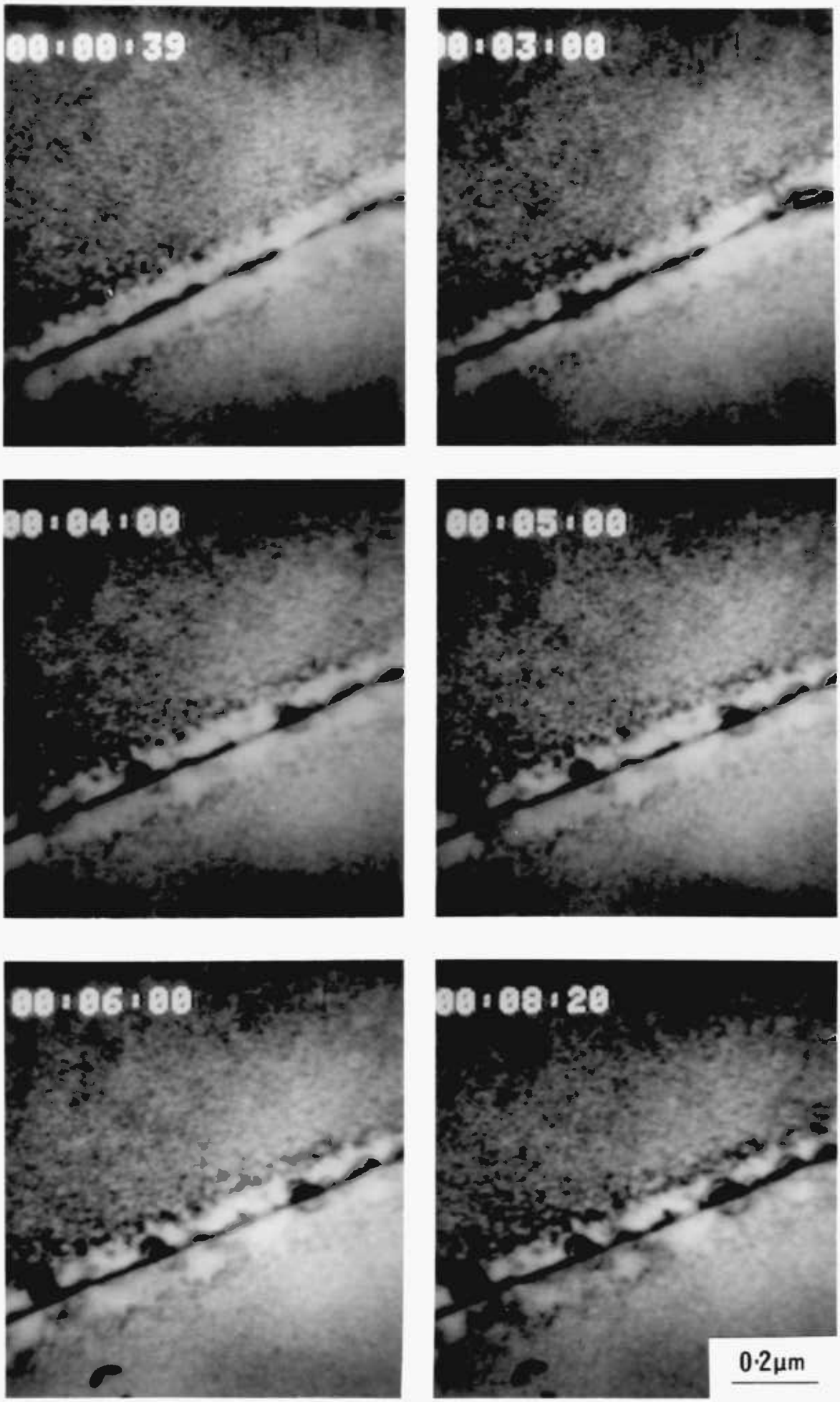
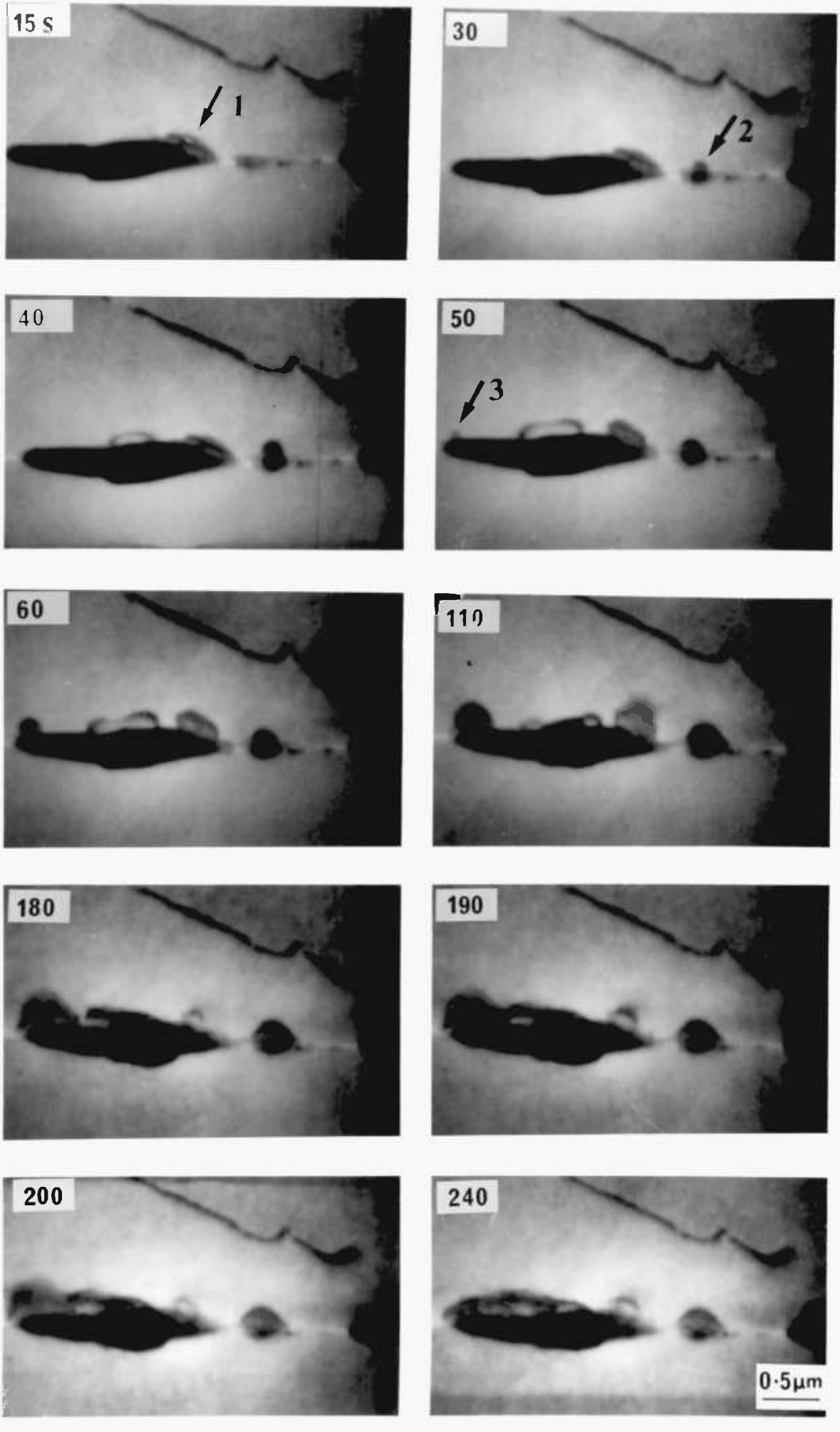

00:00:39
00:03:00
00:04:00
00:05:00
00:06:00
00:08:20
0·2μm

Figure 4.47. Stills from a video sequence showing the reaction events in an air cooled 6/3 base alloy sample.
Blistering reaction first starts on the grain boundary precipitate (Arrow 1). Bubble nucleation first occurs on the smaller grain boundary particle (arrow 2) and at the tip of the large grain boundary precipitate (arrow 3).
Electron flux density = 10^{-3} A/mm^2
Temperature = 253K


15 s
1
30
2
40
50
3
60
110
180
190
200
240
0·5μm

distinguish on the video monitor due to the automatic gain control on the camera compensating for the reduction in image intensity as the oxide buildsup.) It is also evident from this sequence that bubble nucleation occurs first on the smaller precipitate (arrow 2) and at the tip of the large grain boundary particle (arrow 3). The latter bubble appears to be deflated after about 250 seconds, as evidenced by the contraction of the strain field, which is subsequently partially restored. The loss of the strain field could be due to the loss of hydrogen (presumed to be the agent causing the high pressure inside the bubble and hence the strain field) to the surfaces of the foil. An alternative explanation is that bubble grows very rapidly, due to the very high pressure inside it, by decohering a greater part of the matrix/particle interface. The larger volume would then be expected to be at a lower pressure leading to a reduction in strain field image width. On further exposure the pressure inside the bubble would be expected to increase if more hydrogen is introduced into the void. A second example of strain field image reduction and subsequent growth is shown in Figure 4.48.

An interaction between existing dislocations and internal bubbles was noted. Figure 4.49 shows that after the formation of bubbles on the grain boundary precipitate a strain field develops on an adjacent dislocation line. Dislocations away from grain boundary particles did not show such strain fields.

4.3.2. 6/3 Cu alloy

The reaction between the experimental alloy containing copper (6/3 Cu) and water vapour in the environmental cell, was initially found to be hampered by the presence of extensive copper deposits on the foil surfaces. These were traced to copper redeposition during sample thinning in the 20% perchloric acid-ethanol solution. (Similar effects have been reported by other workers (165, 166)). Experimentation using different electrolytes indicated that this effect could be reduced to negligible proportions if a solution of 30% nitric acid in methanol was used. In order to minimise any differences in the nature of the oxide surfaces between the experimental alloys, and thus make comparisons possible, all samples used in the environmental cell were polished in the latter electrolyte under identical conditions.

Whilst showing an overall similar behaviour the progress of the reaction between the 6/3 Cu alloy and water vapour showed some important differences from that of the 6/3 base alloy. Firstly, it was found that at all

Figure 4.48. Stills from a video sequence showing the collapse and subsequent growth of a grain boundary hydrogen bubble.
6/3 base alloy solution treated at $450^{o}C$, cold water quenched and aged at $150^{o}C$ for 72 hours.
Electron flux density = 5×10^{-3} A mm^{-2}
Temperature = 233 K

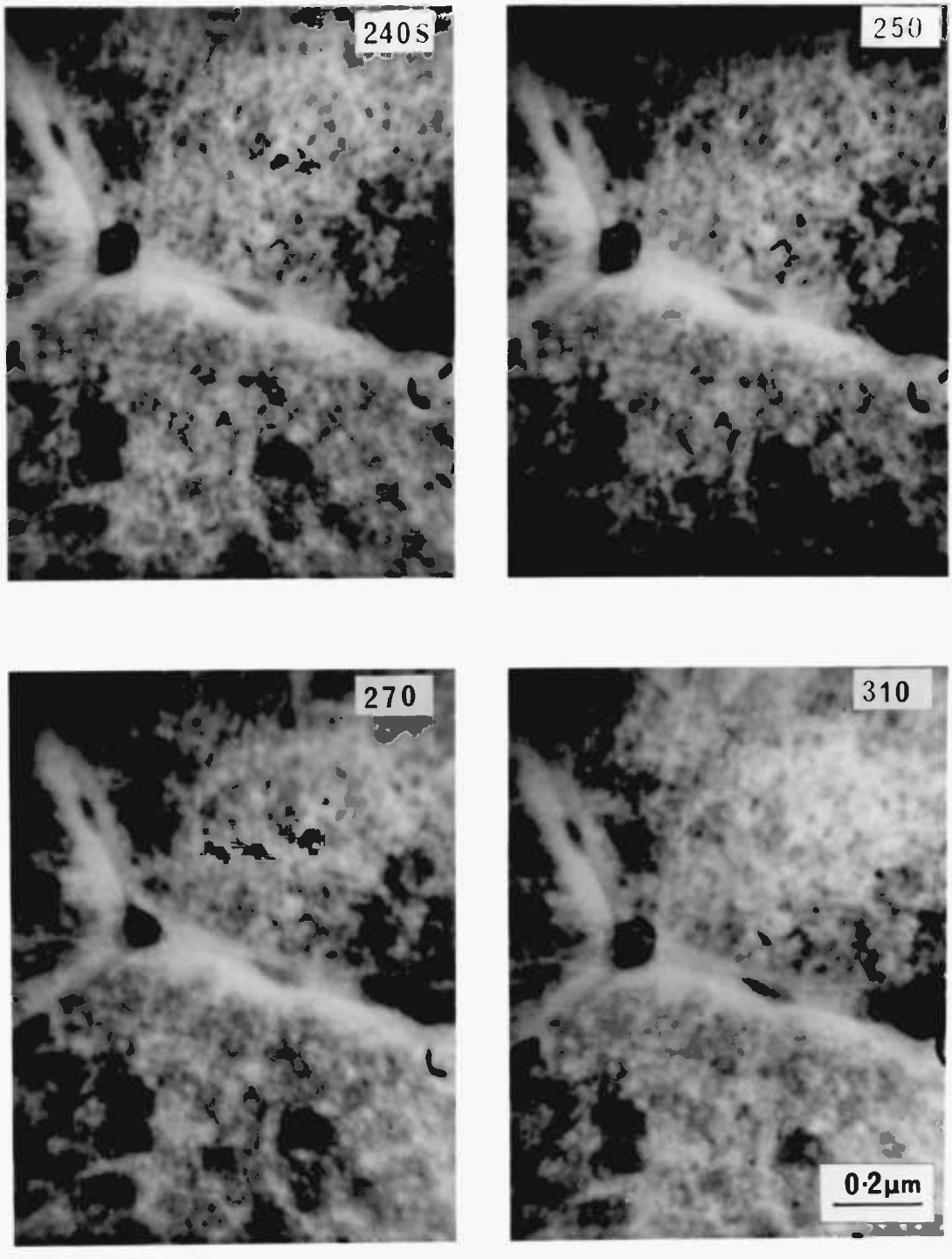
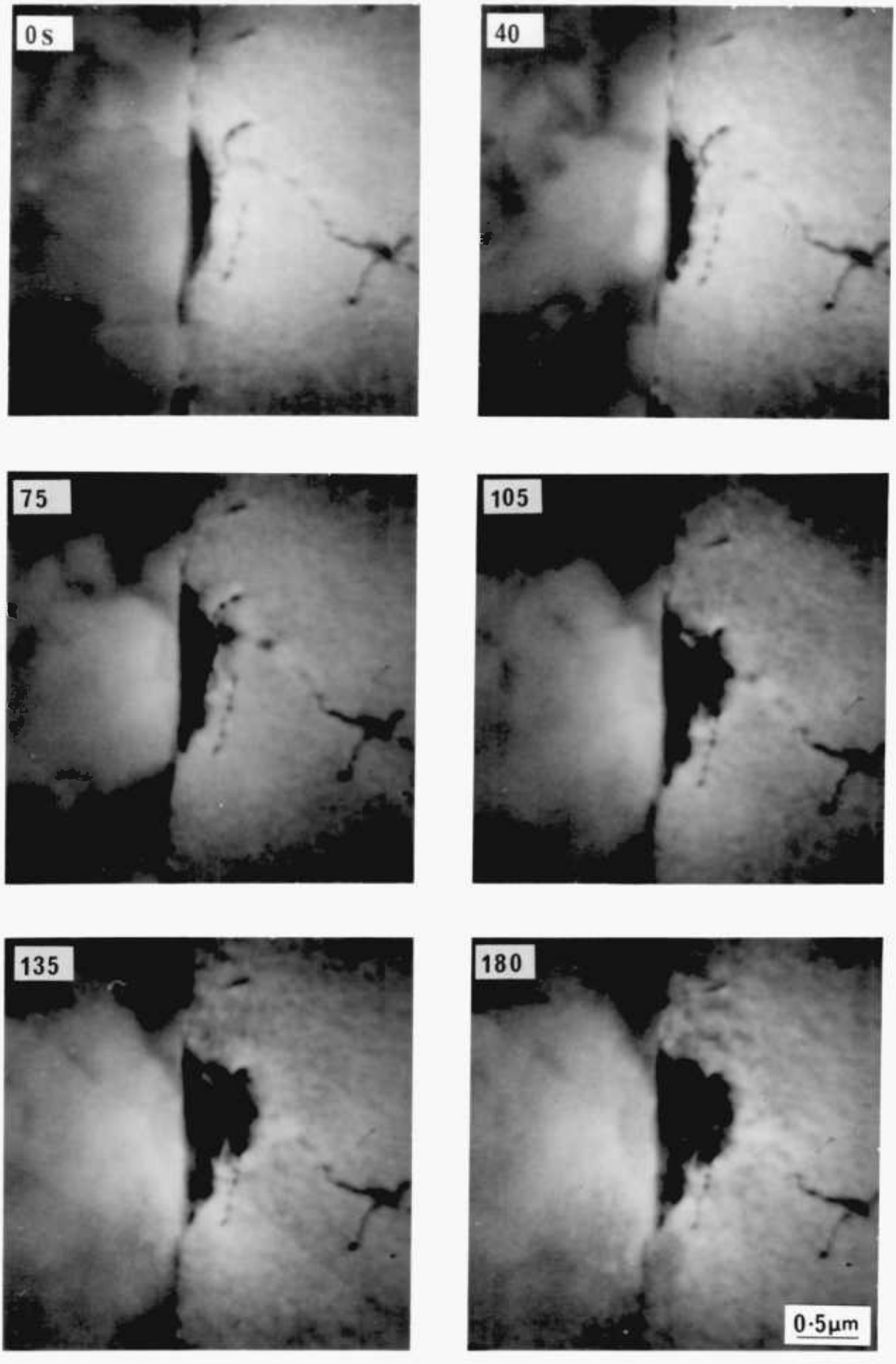

240S
250
270
310
0·2μm

Figure 4.49. Sequence from a video recording showing the gradual build up of strain filed on a dislocation line close to the grain boundary. Note that no such strain field develops on dislocation lines away from the grain boundary.
Electron flux density = 5×10^{-3} A/mm^{-2}
Temperature = 253 K


0s
40
75
105
135
180
0·5μm

temperatures the incubation period for any visible reaction was increased when compared to the 6/3 alloy. The increase showed significant variations between individual foils but was qualitatively reproducible. The initial stage of the reaction showed preferential blistering at grain boundaries (Figure 4.50). Selective attack in this alloy was more pronounced than in the 6/3 base alloy. As shown by Figure 4.50 selective attack is limited to the early stages of the reaction. After prolonged irradiation no distinction could be detected between grain surfaces and the boundary sites.

The most striking difference between the base alloy and the copper bearing quaternary was shown in the bubble formation characteristics. Bubbles were found under all ageing conditions including the as quenched state. Figures 4.51, 4.52, 4.53 are sequences showing the development of bubbles in as quenched, underaged and overaged material respectively, of the 6/3 Cu alloy.

The incubation period for the formation of internal bubbles was significantly longer in this alloy. (Typically 3-4 minutes at 273K and 5×10^{-3} A mm^{-2})

It was clear from the results of both 6/3 base and 6/3 Cu alloys that the growth of any particular bubble was not unlimited. Figure 4.54 shows that following the development of the large bubble smaller bubbles nucleate at closely adjacent sites, and these grow at a faster rate than the large bubble.

In other cases growth of bubbles resulted in the production of dislocation loops (Figure 4.55). These were "punched out" as a result of bubble growth and indicate that the pressure inside the bubbles was sufficiently high to cause local plastic deformation.

4.3.3. 6/3 Cr alloy

The Chromium bearing alloy was set apart from the others by its acute blistering characteristics. The superficial reaction was both very pronounced and associated with short incubation periods (Figure 4.56). It was sometimes observed that the oxide completely decohered from the parent metal (Figure 4.57). In common with the other alloys the blister size was found to be a function of temperature. Figure 4.58 shows that on the same foil two adjacent reaction areas produced at different temperatures exhibit distinctly different blister morphologies. The fact that the foil surfaces, orientation to the electron beam, and pressure were identical clearly shows that the effect is one of temperature.

Figure 4.50. Preferential blistering reaction at the grain boundaries of the 6/3 Cu alloy. Blisters form on both sides of the boundaries.
Electron flux density = 10^{-3} A mm^{-2}
Temperature = 233 K

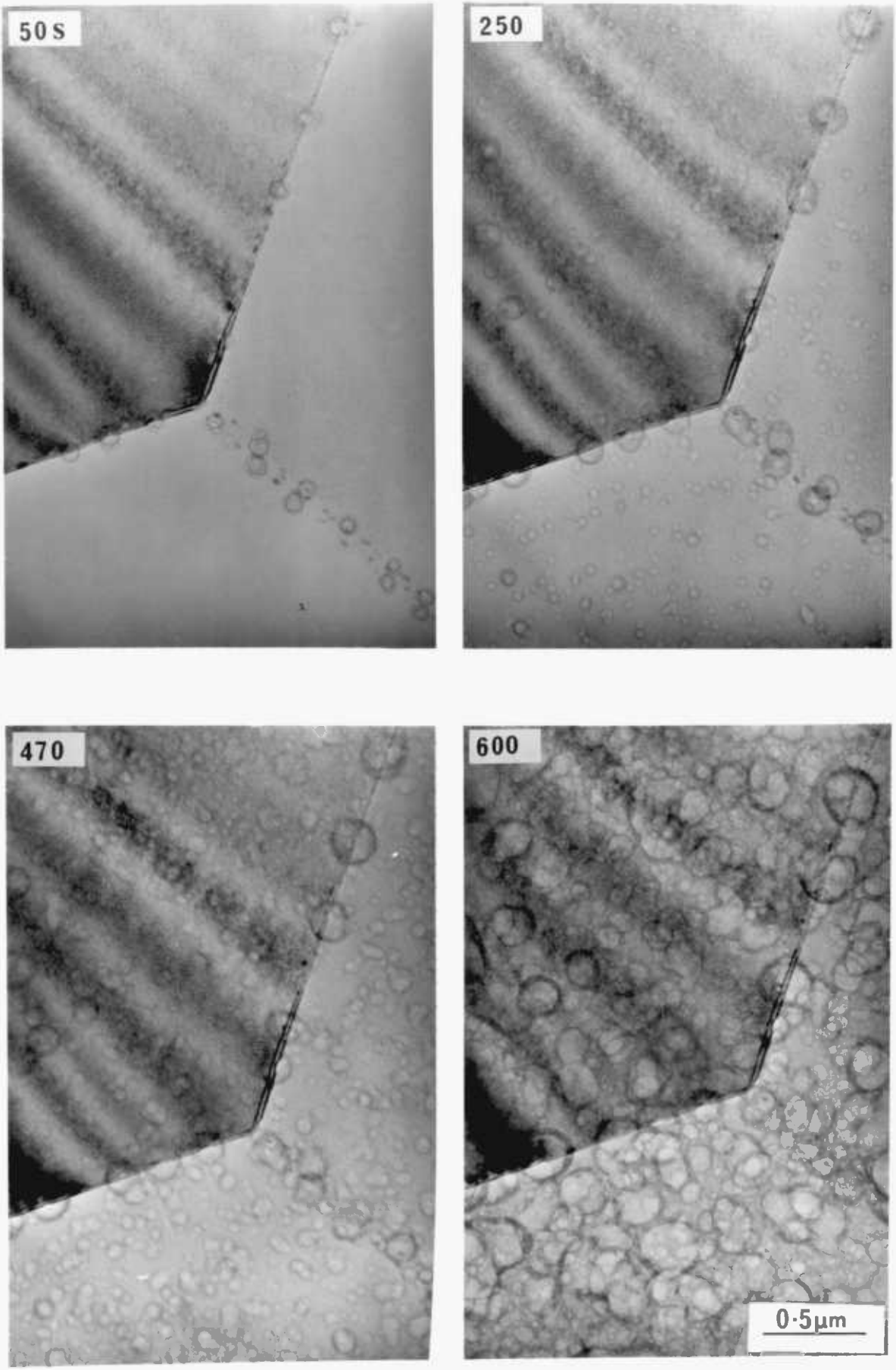
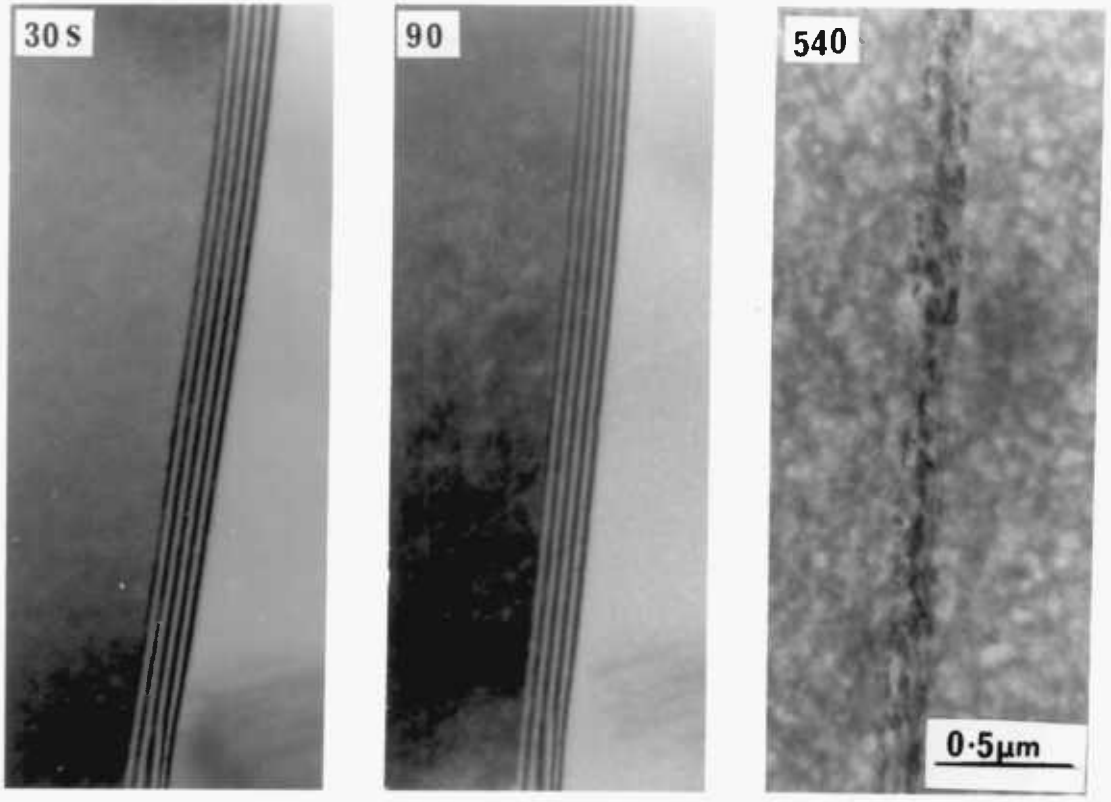

50 s
250
470
600
0·5µm

Figure 4.51. (a) Sequence showing the development of grain boundary bubbles in an as quenched 6/3 Cu alloy sample.
Electron flux density = 5×10^{-3} A mm^{-2}
Temperature = 273 K

(b) Hydrogen bubbles clearly visible at a grain boundary of a different as quenched 6/3 Cu sample irradiated for 4 minutes at 273 K.


30 s
90
540
0·5µm

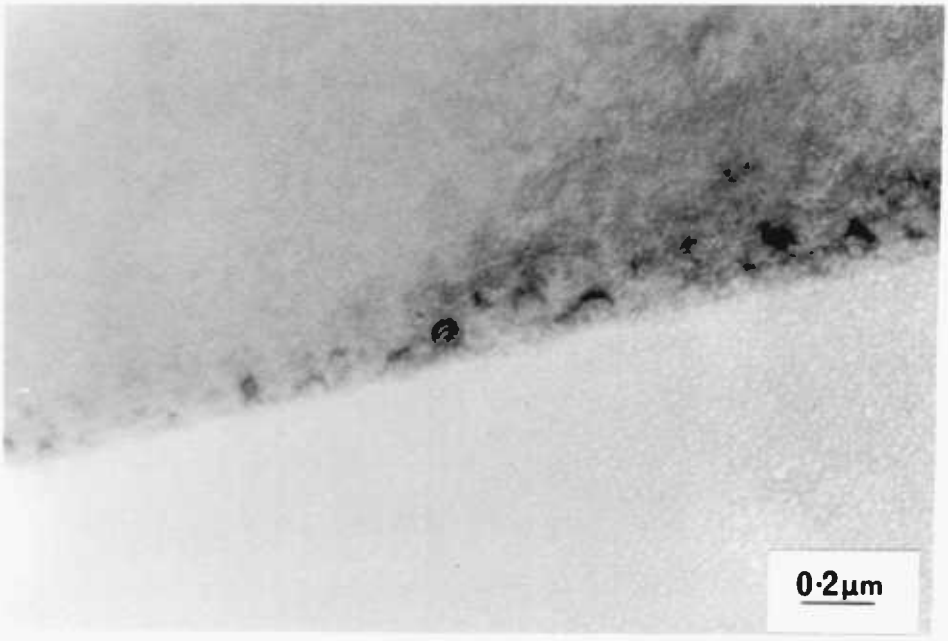

0·2µm

Figure 4.52. Sequence showing the development of hydrogen bubbles in an 6/3 Cu alloy sample aged at 120°C for 22 hours.
Electron flux density = 10^{-3} A mm^{-2}
Temperature = 273 K

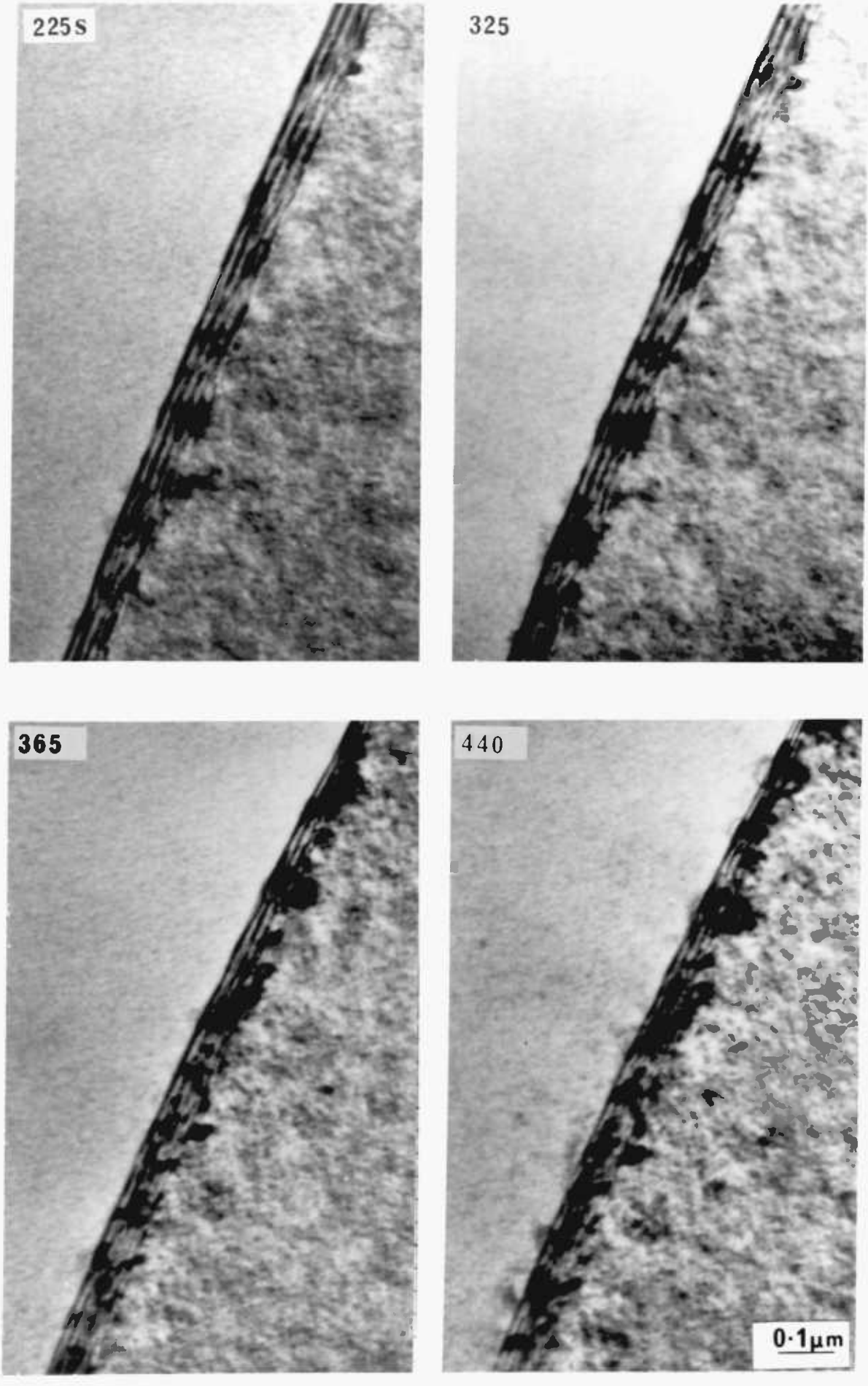

225s
325
365
440
0·1μm

Figure 4.53. Sequence showing the development of hydrogen bubbles in an overaged 6/3 Cu alloy.
Solution treated at 450°C cold water quenched and aged at 150°C for 136 hours.
Electron flux density = 10^{-3} A mm^{-2}
Temperature = 253 K

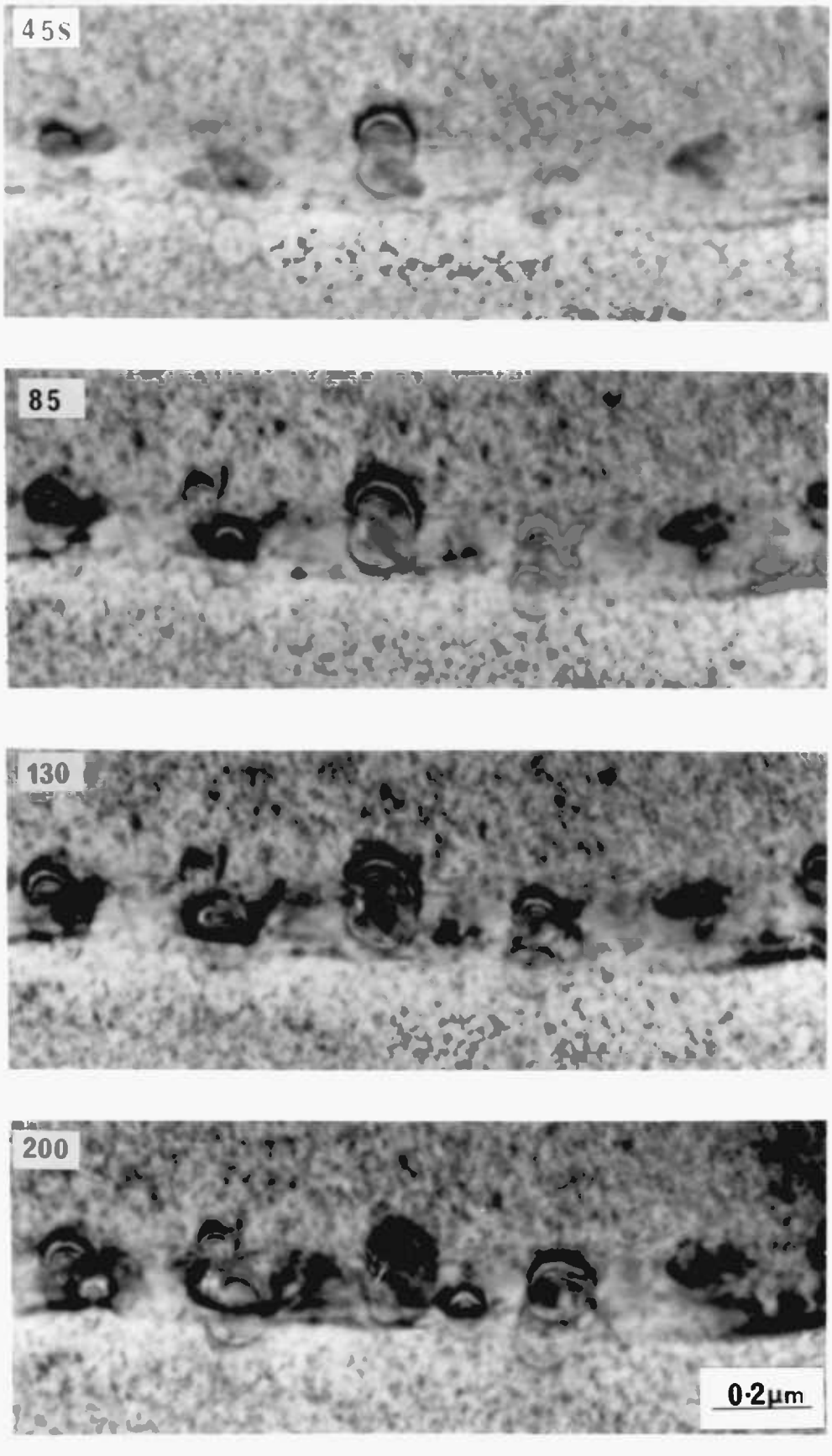

45s
85
130
200
0·2µm

Figure 4.54. Stills from a video sequence showing the development of grain boundary bubbles in an air cooled and aged sample of the 6/3 Cu alloy. Note that the rate of growth of the large bubble is reduced on growth and that smaller bubbles nucleate at closely adjacent sites.
Electron flux density = 10^{-3} A mm^{-2}
Temperature = 253 K

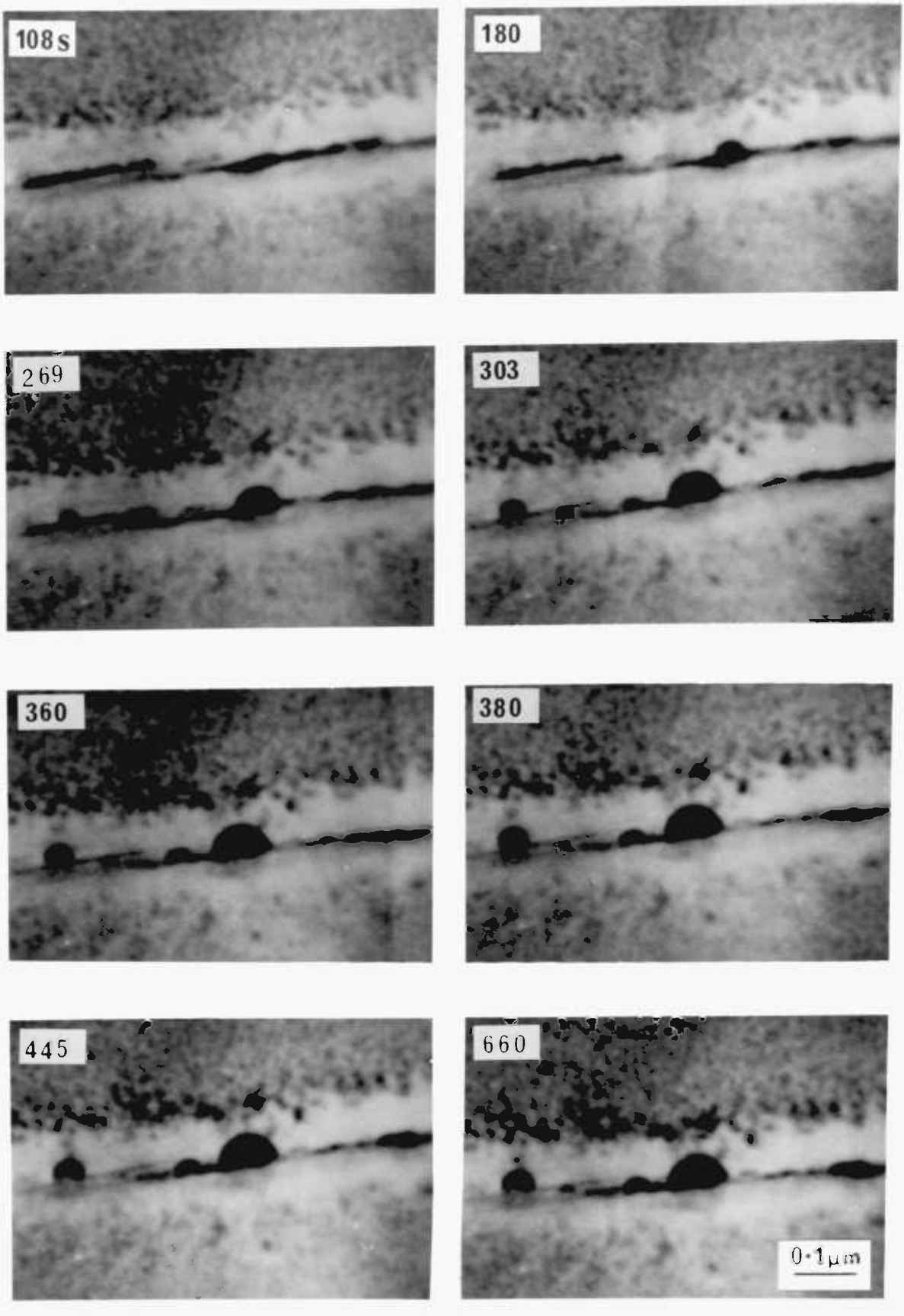

108s
180
269
303
360
380
445
660
0·1μm

Figure 4.55. Stills from a video sequence showing the production of dislocation loops during growth of a grain boundary bubble. There is a movement of dislocations between the still at 4.45 seconds and 4.48 seconds. (This is clearly visible on the original video recording.) Schematic below shows the movement and direction of one of the dislocation loops.
Electron flux density = 5×10^{-3} A/mm^2
Temperature = 253 K


225


228
0·1µm

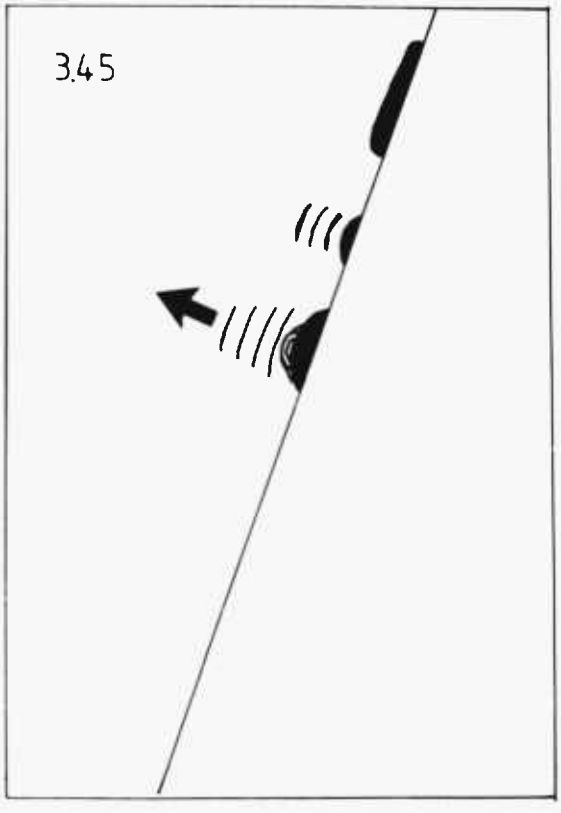

3.45

Figure 4.56. Stills from video recording showing the progress of the superficial reaction on the 6/3 Cr alloy.
Electron flux density = 3×10^{-3} A mm^{-2}
Temperature = 233 K

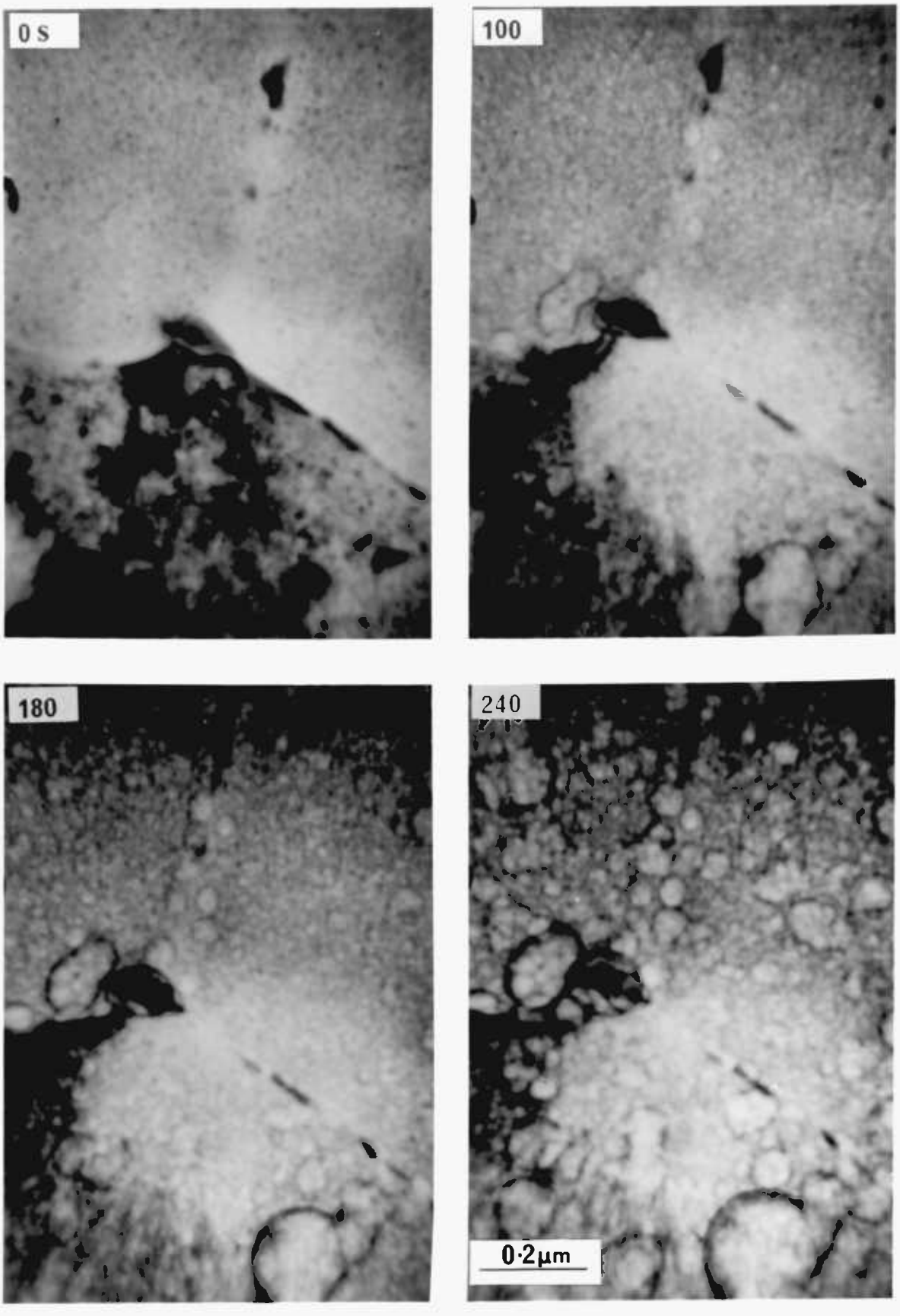
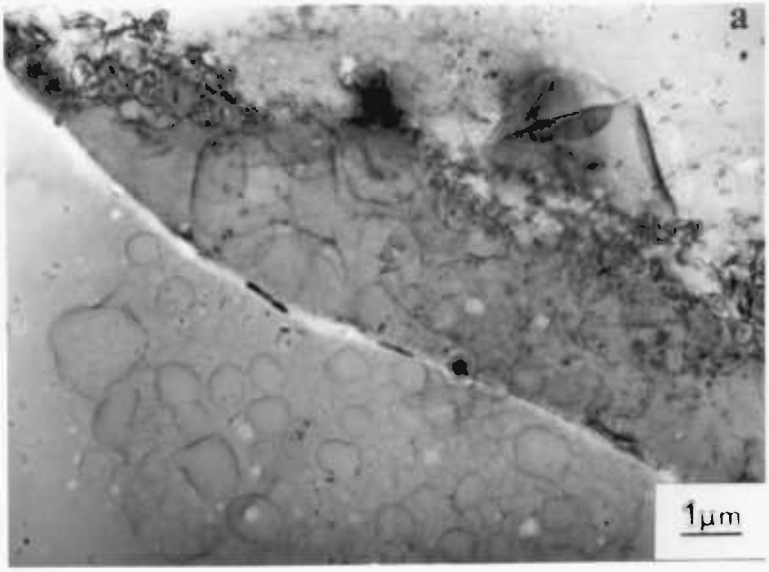

0 S
100
180
240
0·2μm

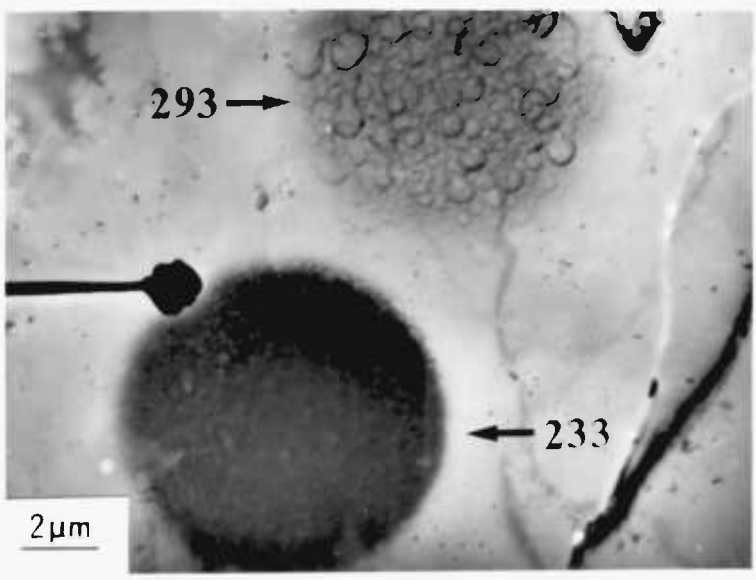
Figure 4.57 (a,b) Complete oxide decohesion following electron irradiation in the environmental cell.
(a) 6/3 Cr alloy solution treated at 450°C air cooled and subsequently aged at 150°C for 18 hours.

(b) 6/3 Cr alloy solution treated at 450°C, cold water quenched and aged at 120°C for 38 hours.

Figure 4.58. Variation of blister size with temperature. The oxide behaves quite differently at the higher temperature giving a significantly larger surface blister size.


a
1μm


b
1μm


293
233
2μm

The blistering reaction of the 6/3 Cr alloy was not found to exhibit any tendency for preferential attack at the grain boundaries. However, if large grain boundary precipitates were present close to the surfaces of the foil then preferential reaction was found at the particles (Figure 4.59).

Bubble formation in the 6/3 Cr alloy was severely restricted. Bubbles were only observed after prolonged irradiation times (Figure 4.60). The detection of bubbles after such high doses of radiation and substantial surface reaction was difficult. In some cases it was observed that bubbles had nucleated some distance away from the main reaction area (Figure 4.60). However, it was not possible to positively confirm the absence of any surface reaction over these sites.

In agreement with the observation made on the 6/3 base alloy any bubbles formed were found only on grain boundary particles. These were either large intermetallic particles or smaller η precipitates produced during ageing treatments (Figure 4.61).

4.3.4. In-situ straining

As mentioned in section 3.7.6 the main limitations in the in-situ straining experiments were set by specimen preparation and handling.

The specimen geometry arrived at (section 3.7.6) allowed sample handling but severely restricted the amount of strain that could be put upon the sample. (Yield stress of the alloys was typically in the region of 300-500 MN/m^2).

Samples stressed to the maximum deflection of the stage showed no evidence of plastic deformation and the reaction with water vapour appeared to be insensitive to the presence of the low elastic stresses present.

Samples which were thinned over the entire gauge length were found to have been damaged during loading into the stage so that the additional stresses imposed in the microscope were small by comparison. However, a number of expected results were apparent. Firstly, it was clear that in the region immediately ahead of a crack (produced either ex- or in-situ) considerable deformation occurred (Figure 4.62). The deformation appeared to be contained within a band.

It was not possible to induce a grain boundary to decohere in situ. Hence no information was obtained concerning intergranular fracture. However, it was observed that in some of the strained samples grain boundaries showed pronounced preferential attack (Figure 4.63).

Figure 4.59. Sequence showing a preferential attack at large T phase grain boundary precipitates produced by air cooling from the solution heat treatment temperature.
6/3 alloy solution treated at 450^{o}C air cooled and subsequently aged at 150^{o}C for 56 hours.
Electron flux density = 10^{-3} A mm^{-2}
Temperature = 233 K

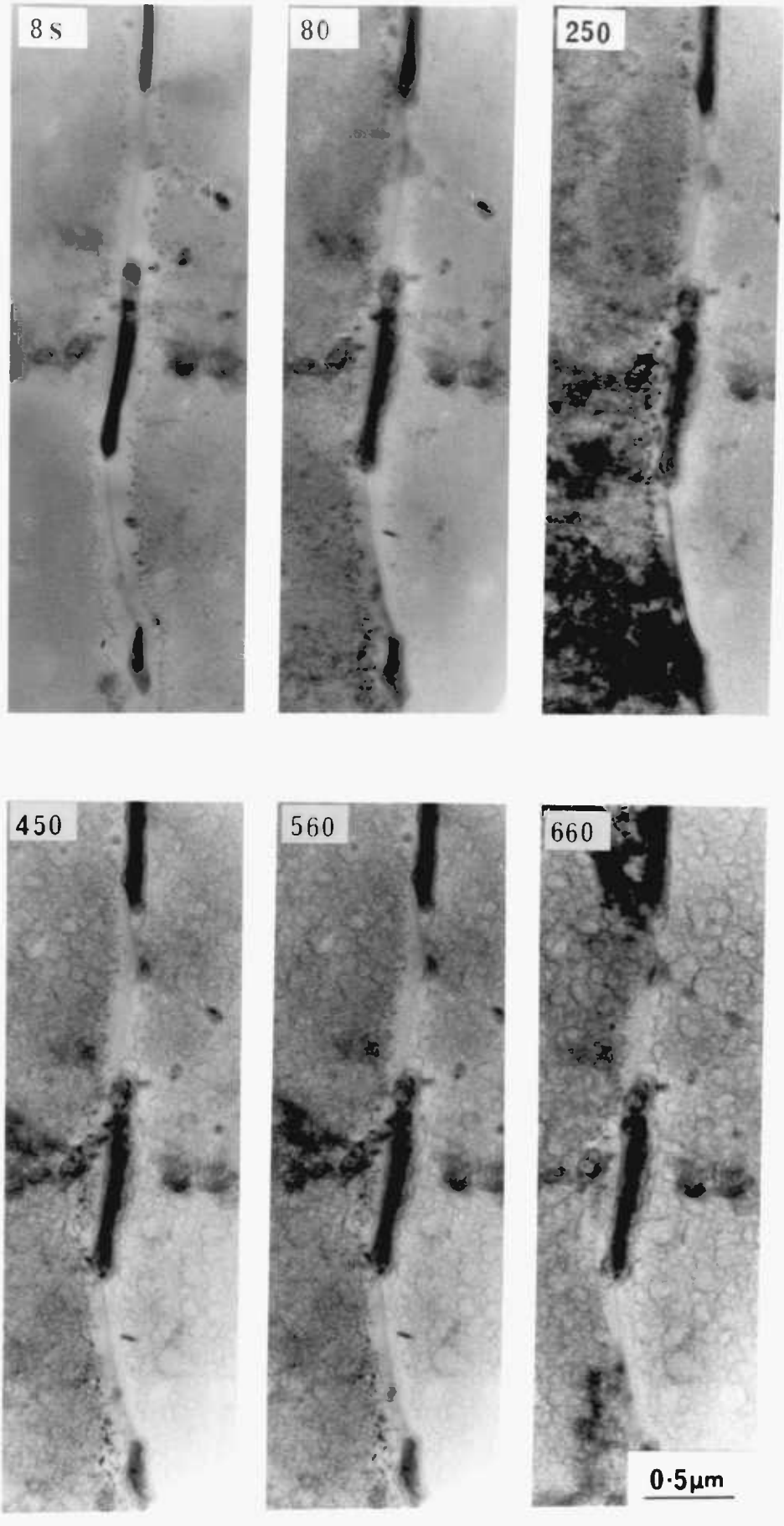
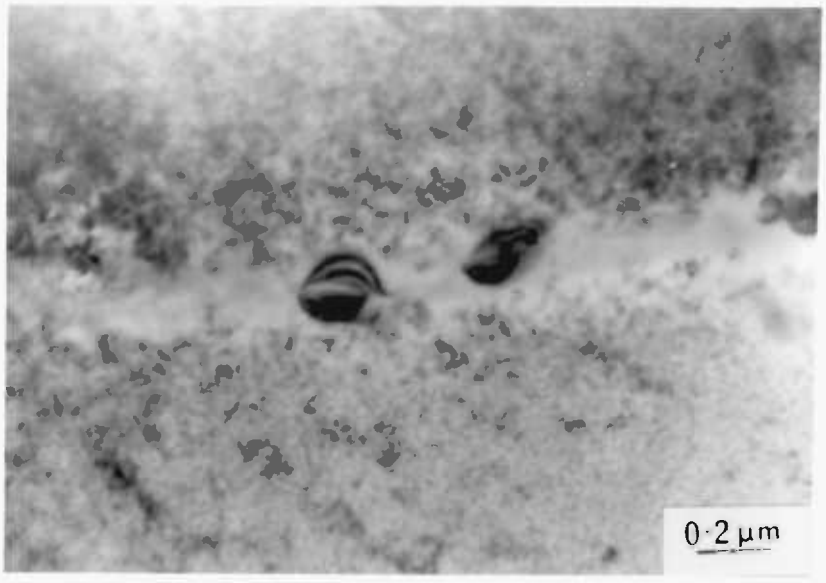
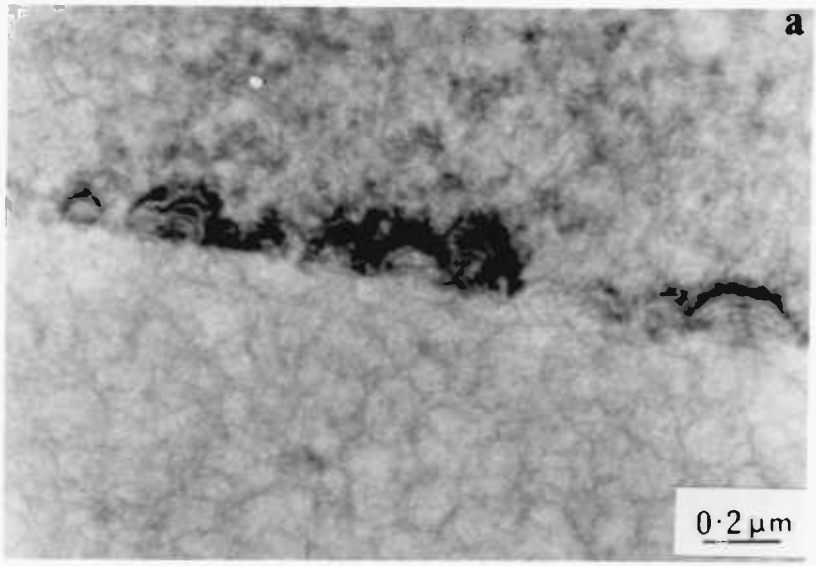

8s
80
250
450
560
660
0·5μm

Figure 4.60. Hydrogen bubbles in a heavily irradiated 6/3 Cr sample.
Hydrogen bubbles visible away from the main reaction zone.
Exposure time = 600 seconds.
Electron flux density = 5×10^{-3} A mm^{-2}
Temperature = 253 K

Figure 4.61. (a) Hydrogen bubbles on η precipitates in a 6/3 Cr alloy.
Time of irradiation $\sim$800 seconds.
Electron flux density = 5×10^{-3} A mm^{-2}
Temperature = 273 K

(b) Hydrogen bubble on a chromium intermetallic in a sample of the 6/3 Cr alloy.
Electron flux density = 5×10^{-3} A mm^{-2}
Temperature = 253 K


0·2 μm


a
0·2 μm

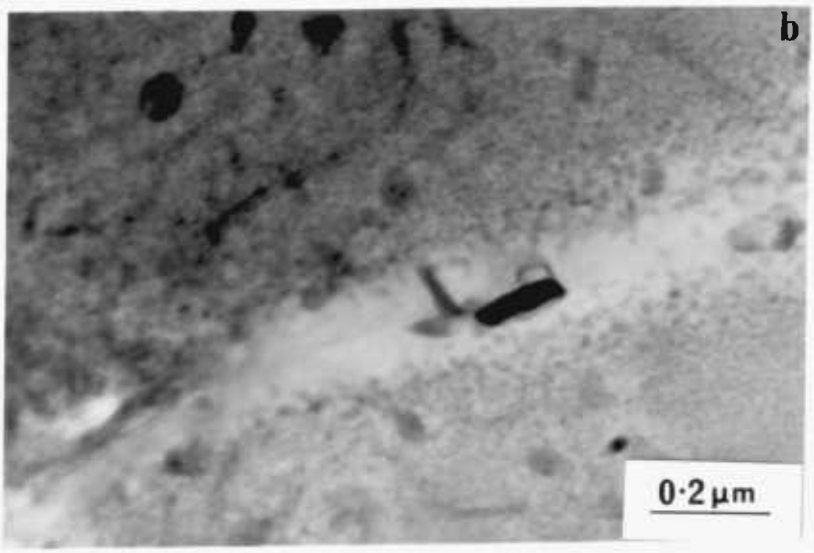
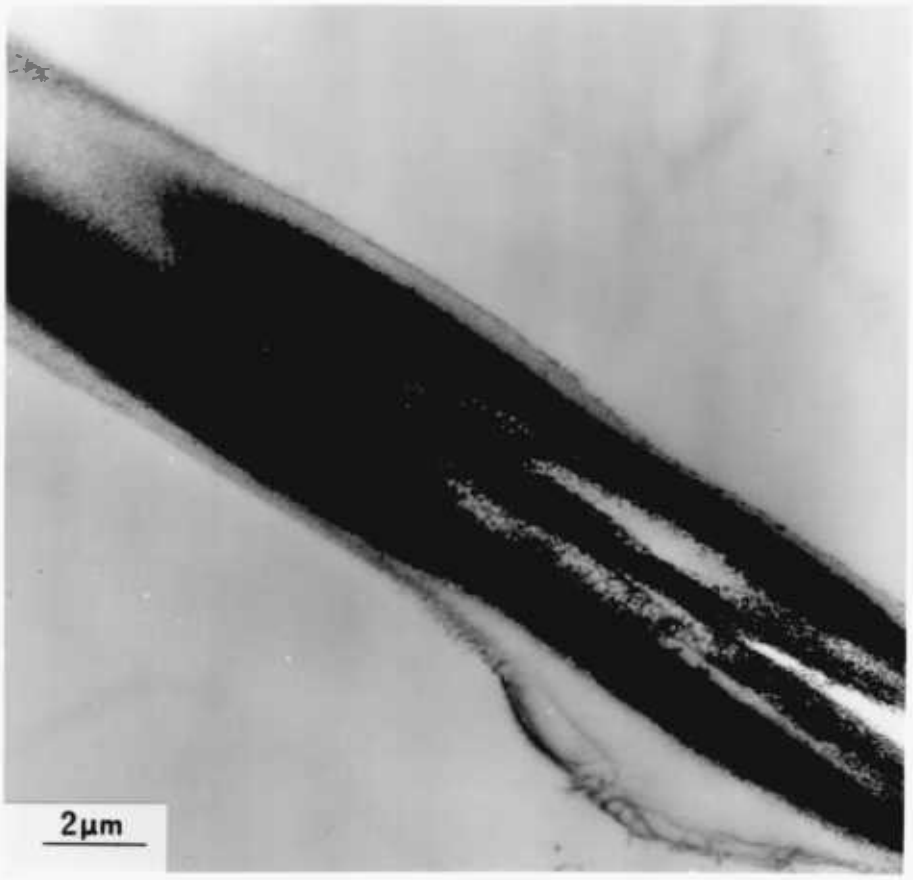
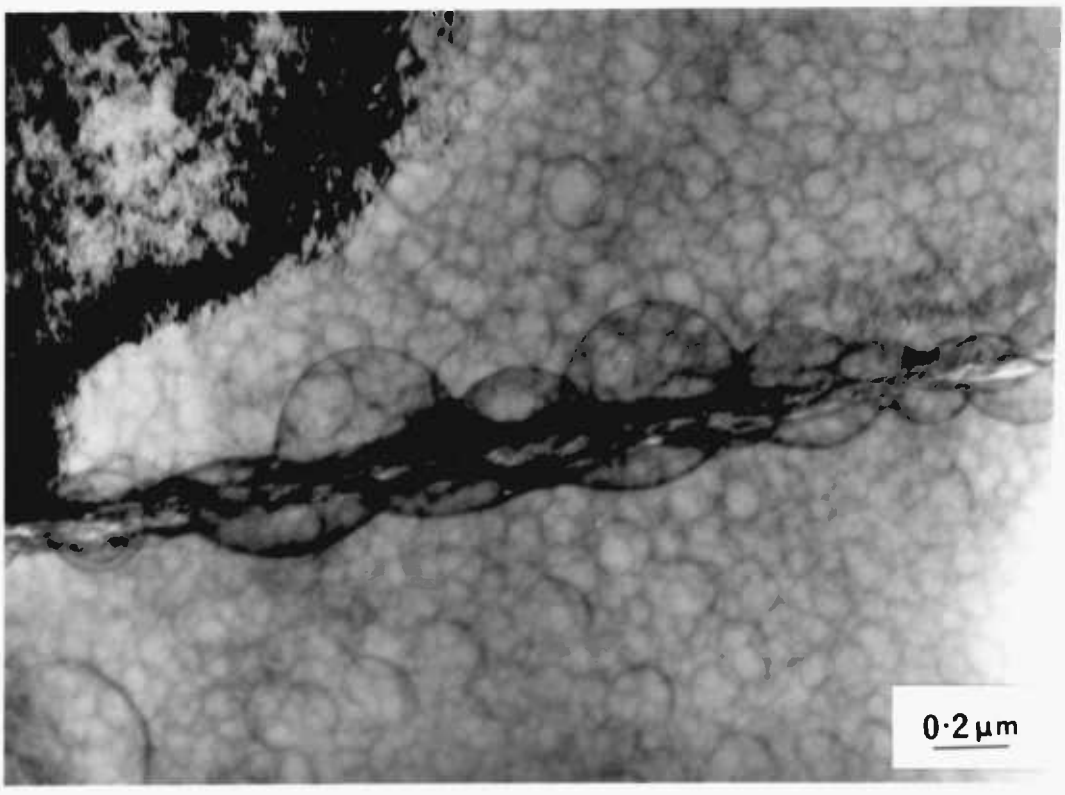

b
0·2 μm

Figure 4.62. Large plastic zone associated with a ductile crack possibly introduced into the sample during loading into the stage. Straining stage crosshead displacement ~500μm.

Figure 4.63. Preferential surface attack at the grain boundary of a stressed sample in the environmental cell. Microcracks are evident in the boundary. Straining stage crosshead displacement ~400μm.


2µm


0·2µm

These appeared to contain microcracks.

In cases where tearing of the samples had occurred it was found that the crack faces constituted very reactive sites (Figure 4.64). This is most probably due to the breakdown of the oxide at these regions.

4.4. Surface Reaction

4.4.1. Reaction of Al-Zn-Mg (Cu/Cr) Alloys with water vapour

The surface reaction studies were carried out on disc type samples. These were chosen because they could be polished under standard conditions (using a nitric acid solution in methanol) and allowed examination of both thick areas (>0.1 mm) and electron transparent regions.

As outlined in Section 3.7 precautions were taken to ensure that as far as possible the initial surface condition of all samples was identical. All discs were allowed to dry in a dessicator after electropolishing for a period of 24-72 hours. They were then exposed to the water vapour environments and subsequently examined in the JEOL 100 CX microscope using secondary electron imaging techniques. The thinned area of the samples could also be examined in scanning transmission and conventional TEM.

The initial step of the reaction between the experimental alloys and water vapour, both at 110°C and 70°C, was found to be one of surface blistering (Figure 4.65). This was not unlike the behaviour found in the "in-situ" reaction (see Section 4.3) and consisted of the decohesion of parts of the initial oxide film from the underlying metal. Blistering was found to occur after a short incubation period, typically 2-5 minutes during which the oxide thickened. It did not show any preference for specific sites at 110°C but slight attack at grain boundaries was noted at 70°C (Figure 4.66).

The blistering reaction was common to all alloys and heat treated conditions.

Combined SEM/STEM work produced some evidence of reaction products within what appeared to be unbroken blisters, (Figure 4.67). However it was not possible to positively confirm the absence of cracks in the blister wall which would have allowed subsequent access of water vapour to the metal. Reaction products inside blisters could easily be seen using secondary electron imaging techniques in cases where the blister wall had clearly been broken (Figure 4.68). Further evidence of oxide

Figure 4.64 (a,b) Preferential surface reaction at the crack faces.
The cracks were produced by tearing during specimen loading into the stage.
Specimen temperature = 293 K
Electron flux density = $\sim 10^{-3}$ A mm^{-2}


a
1μm

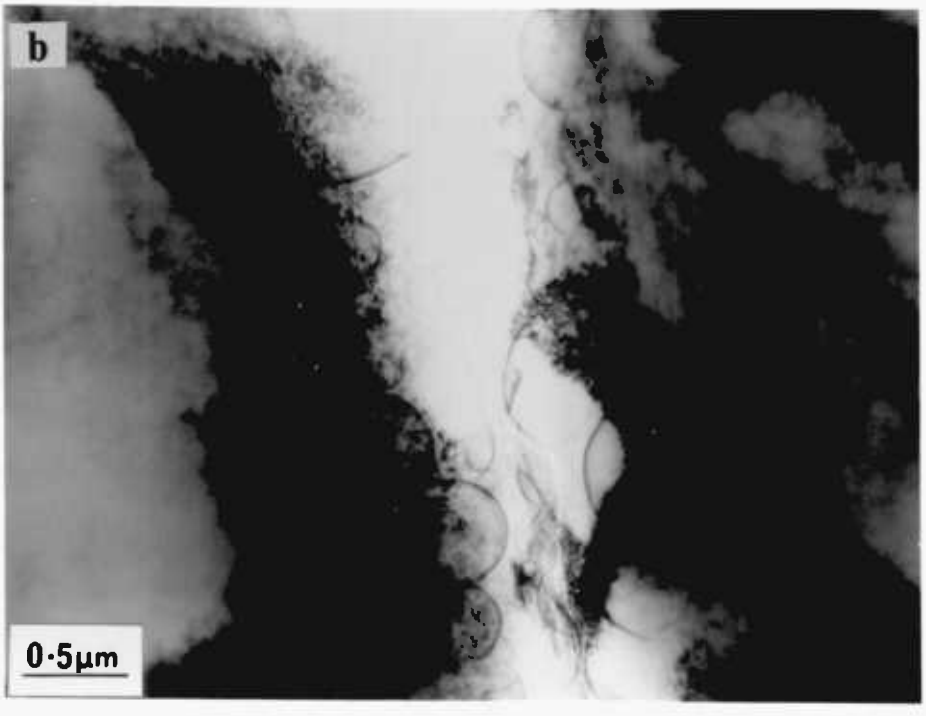
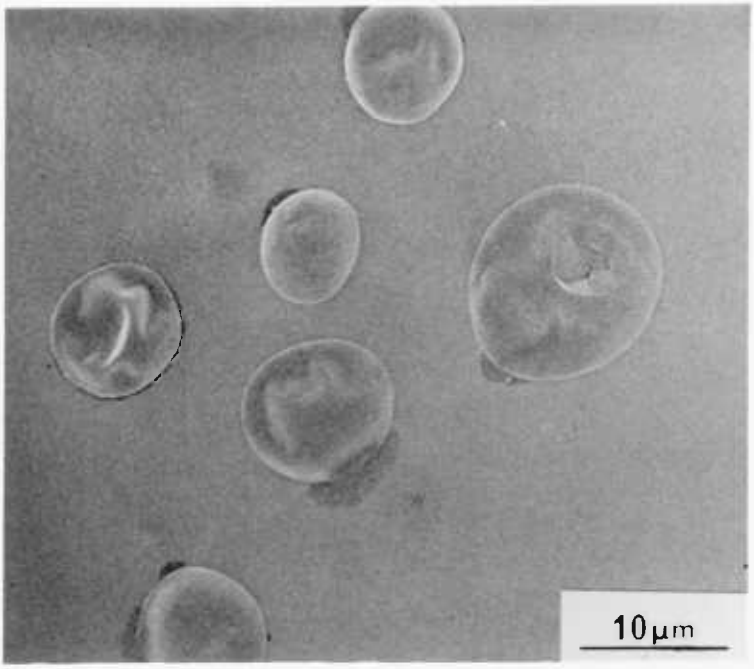
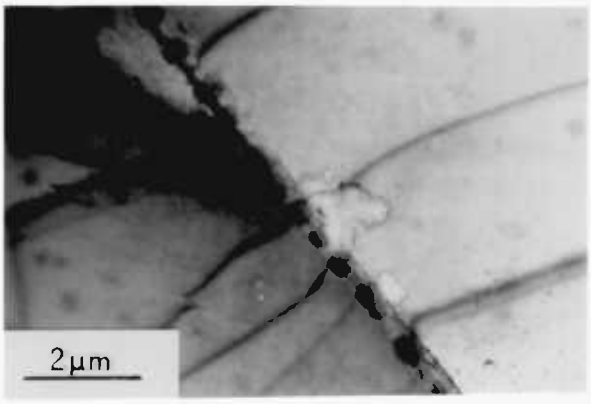

b
0·5μm

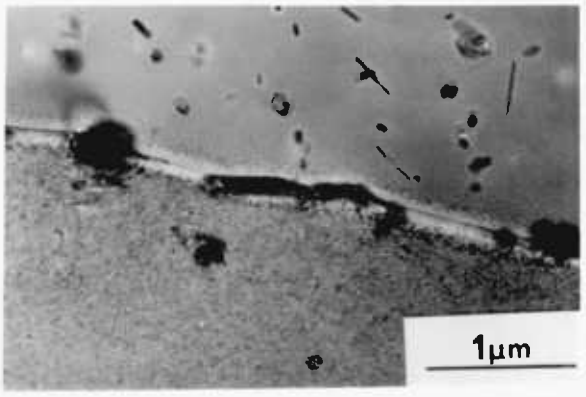
Figure 4.65. Surface blistering in a bulk sample of the 6/3 base alloy exposed to water vapour in the autoclave for 2 minutes.

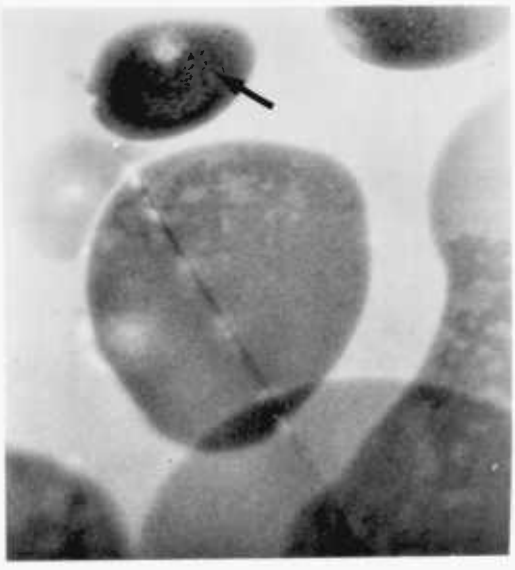
Figure 4.66 (a,b) Slight tendency for preferential attack of the grain boundaries in thin foils exposed to w.v.s.a. at 70°C. 10 minute exposure.

Figure 4.67. S.T.E.M./S.E.M. pair showing reaction products inside blister (Arrow). Whilst the blister appears intact in S.E.M. it is evident from the S.T.E.M. micrograph that this is not so. There appears to be no preferential blistering at the underlying alloy boundary.


10µm


2µm


1µm



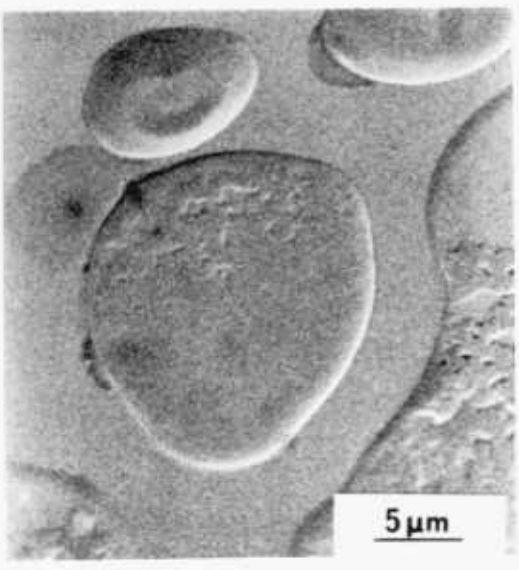
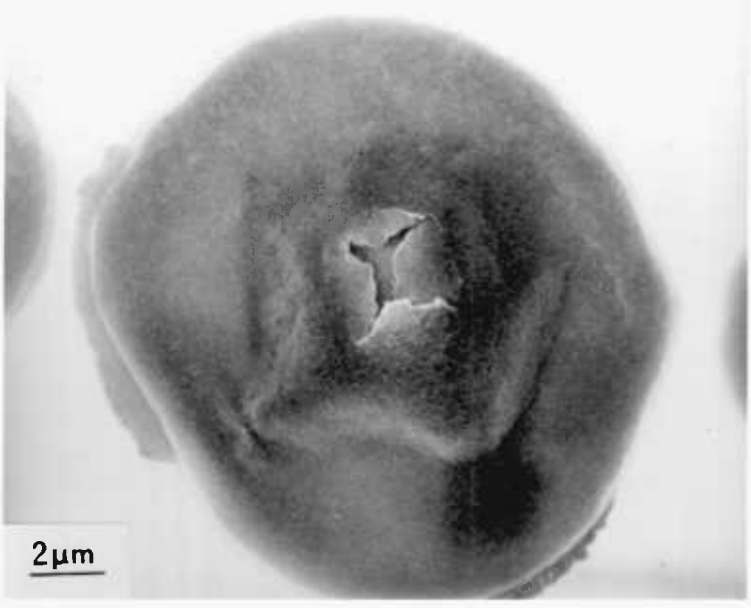
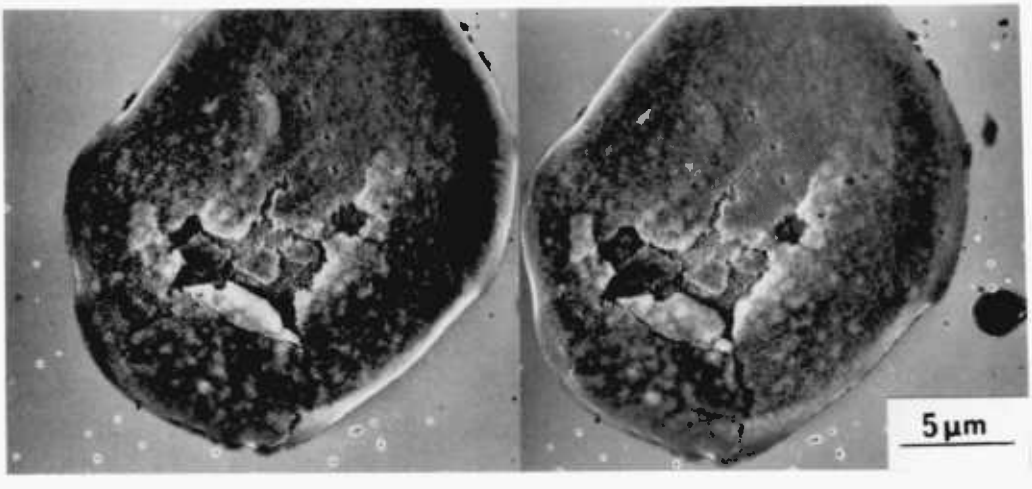

5µm

Figure 4.68. Reaction products clearly visible inside the blister.
Secondary electron micrograph from a 6/3 base alloy sample exposed to water vapour in the autoclave for 5 minutes.

Figure 4.69. Stereo pair showing a broken blister.
Plate like hydroxide is clearly visible inside the blister part of which has collapsed over the fibrils.
Note that the blister wall itself transforms to a product similar to that found inside the blister.


2µm


5µm

growth within blisters is seen in Figure 4.69. This is a stereo pair and shows that part of the blister has collapsed over a layer of an underlying reaction product which appears as a mat of fibrous growth made up of thin blades or lamellae.

On further exposure the blistered areas developed into "islands" of the reaction product (Figure 4.70). The resulting surface then exhibited a series of reaction sites which were surrounded by less reactive regions of relatively featureless oxide. The boundary between the two being sharply marked by the positions of the broken blister walls (Figure 4.71). The blister wall material itself transformed to a morphologically similar hydroxide product irrespective of whether it still formed part of the wall connected to the sample surface or had simply collapsed on the surface (Figure 4.72).

It was clear from stereo microscopy that the blister skin was lying above the fibrous hydroxide layer and appeared to be supported by the latter (Figure 4.73). It was also evident that the blister skin was transformed into the fibrous hydroxide phase at a later stage than the material inside the base of the blister.

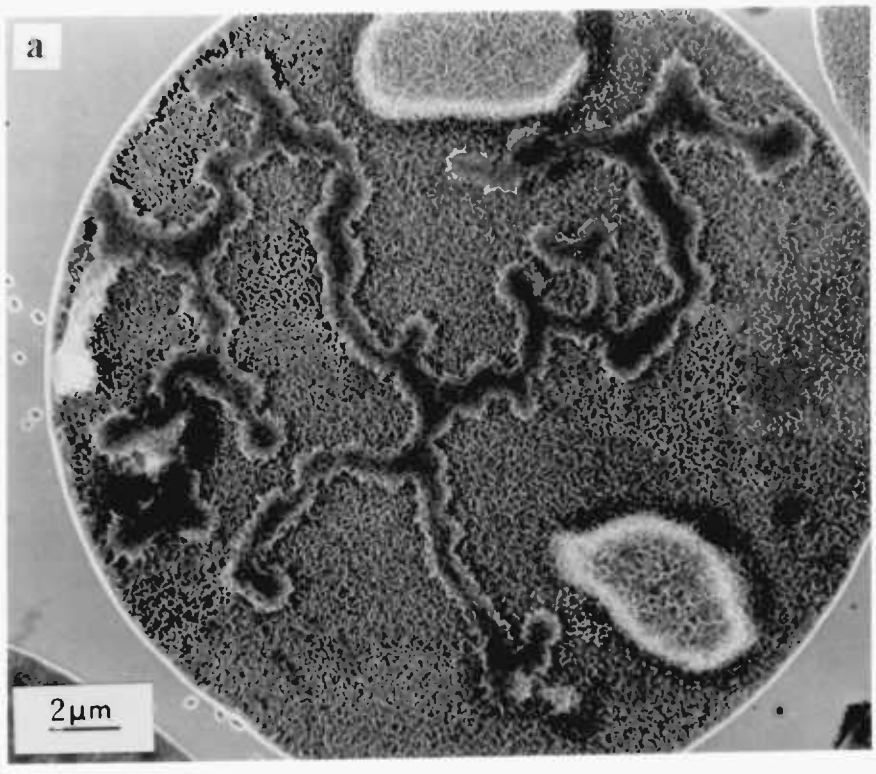
Away from the hydroxide islands formed at broken blisters it was found that film thickening had occurred. The oxide appeared to transform into a globular form which was morphologically different from that found in hydroxide islands (Figure 4.74). At longer exposure times (1-2 hours at 110^{o}C) it was found that platelets of a reaction product, were found to have been formed, (Figure 4.75). These appeared morphologically similar to the fibrous phase present inside the islands but the fibrils were significantly coarser in size (Figure 4.76).

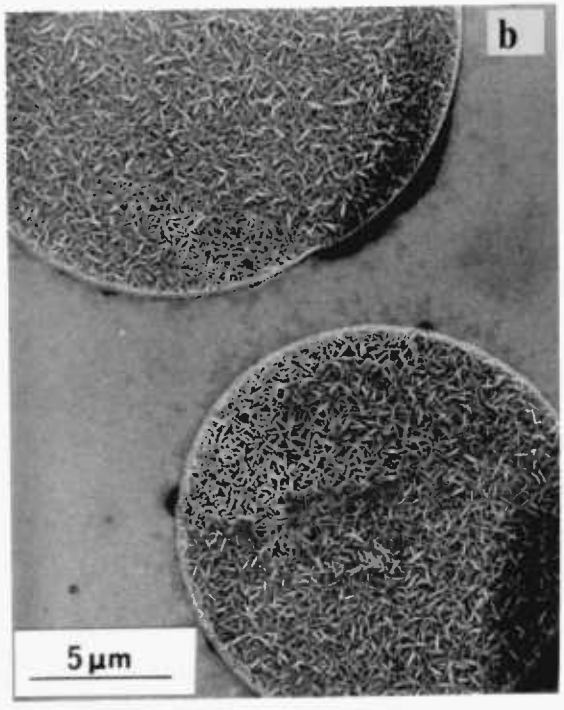
At even longer times ($\sim$12 hours at 110^{o}C) the entire surface of the samples was covered by the fibrous hydroxide phase (Figure 4.77). However, it was clear from stereo microscopy that the history of the reaction was recorded on the surface. Firstly, the transformed remains of the dome walls were found to protrude from the surface, whilst the hydroxide within the islands was clearly of a finer size (Figure 4.78).

The overall sequence of the reaction is shown schematically in Figure 4.79 (a-e)

Identification of the fibrous hydroxide was achieved by employing transmitted electrons from the edge of the disc foil samples to form diffraction patterns. It was found that at these regions the metal was speedily consumed to form a disc of the reaction product.

Figure 4.70 (a,b,c). Reaction 'islands' developed from broken blisters. Micrograph (a) shows remains of the collapsed blister wall over the reaction product.


a
2µm


b
5µm

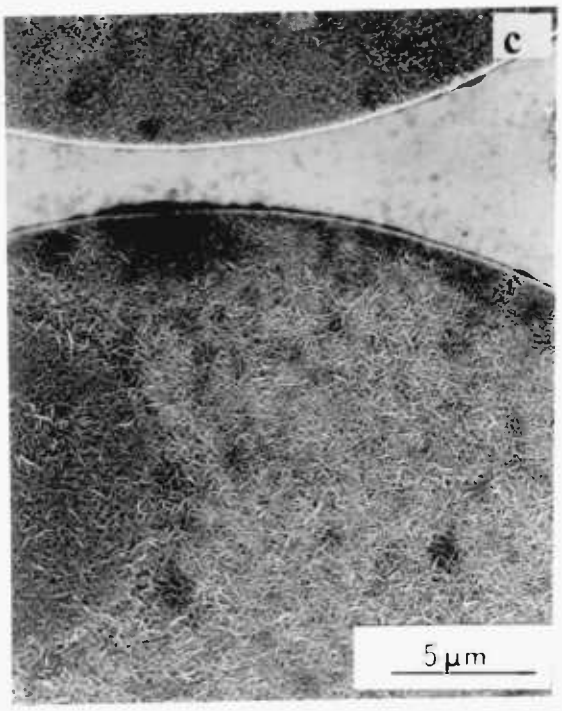
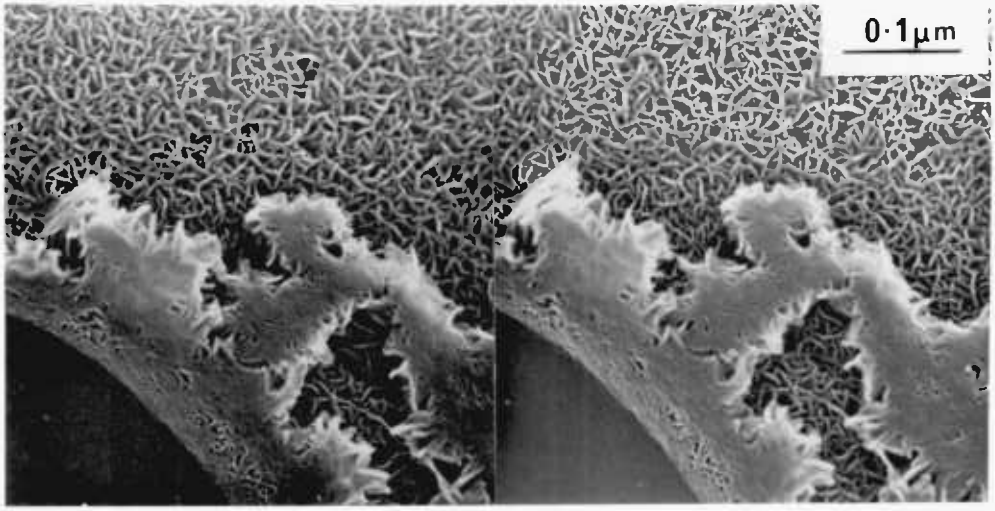
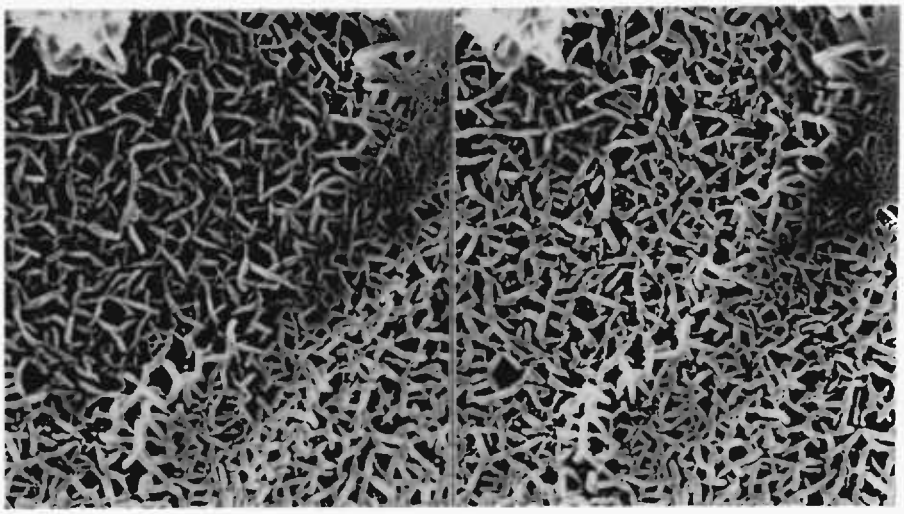

c
5µm

Figure 4.71. Stereo pair showing that reaction site contained within the blister wall. Very little corrosion occurs outside. The blister wall has collapsed over an outgrowing hydroxide product.

Figure 4.72. Stereo pair showing complete transformation of the blister wall to the hydroxide phase. The metal inside the blister has been consumed leaving a very uneven surface. Note also the outgrowing nature of the hydroxide platelets.

Figure 4.73. Stereo pair showing that the collapsed blister skin is supported by the underlying hydroxide.


0·1μm



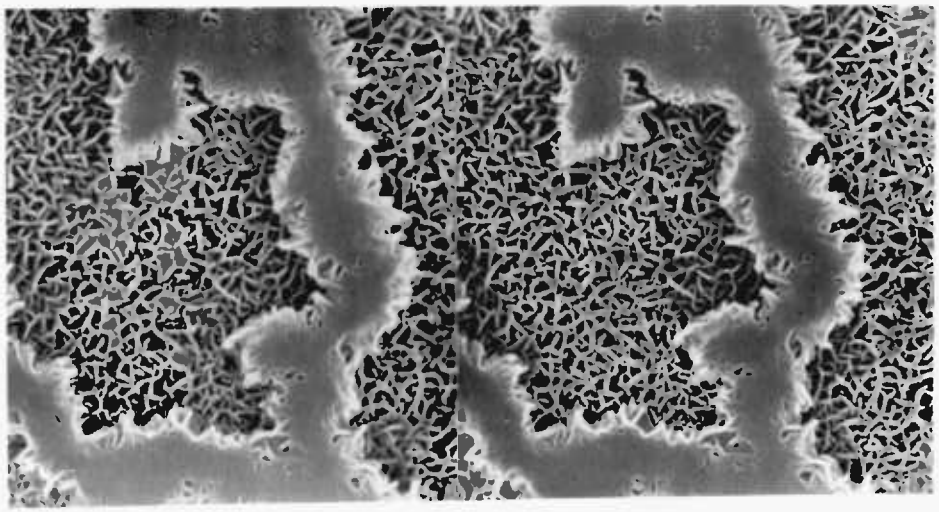
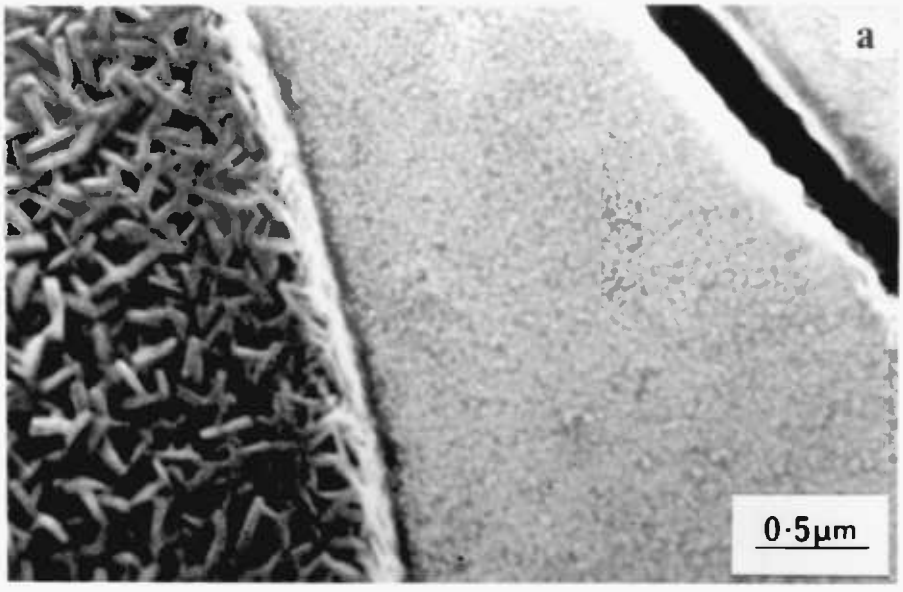
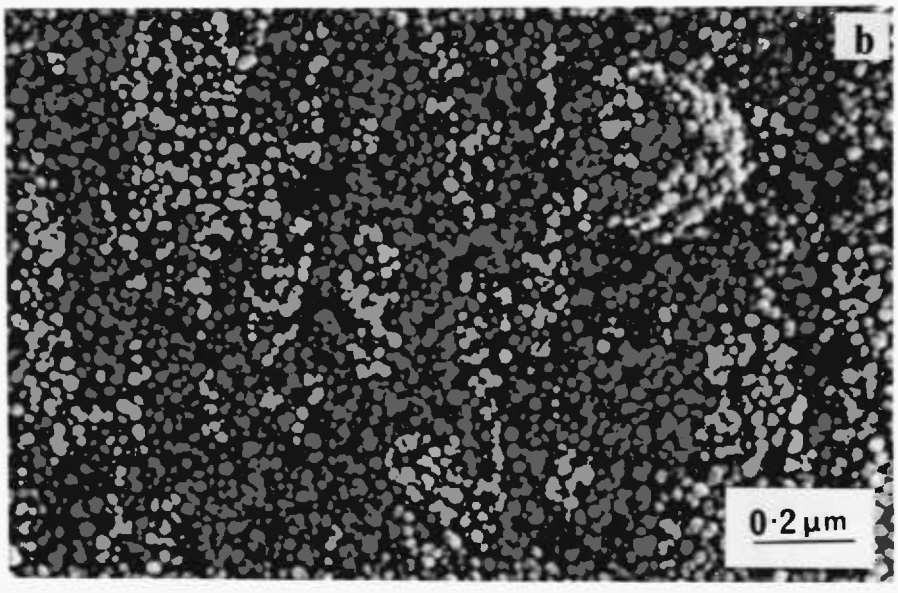


Figure 4.74 (a,b) Oxide away from reaction islands showing distinctly different morphology from that exhibited by the reaction islands.

Figure 4.75. Micrograph showing that the thickened oxide away from the reaction islands gradually transforms to a reaction product very similar to that found inside the reaction islands. Exposure time 1 hour at 110^{o}C.


a
0·5μm


b
0·2μm

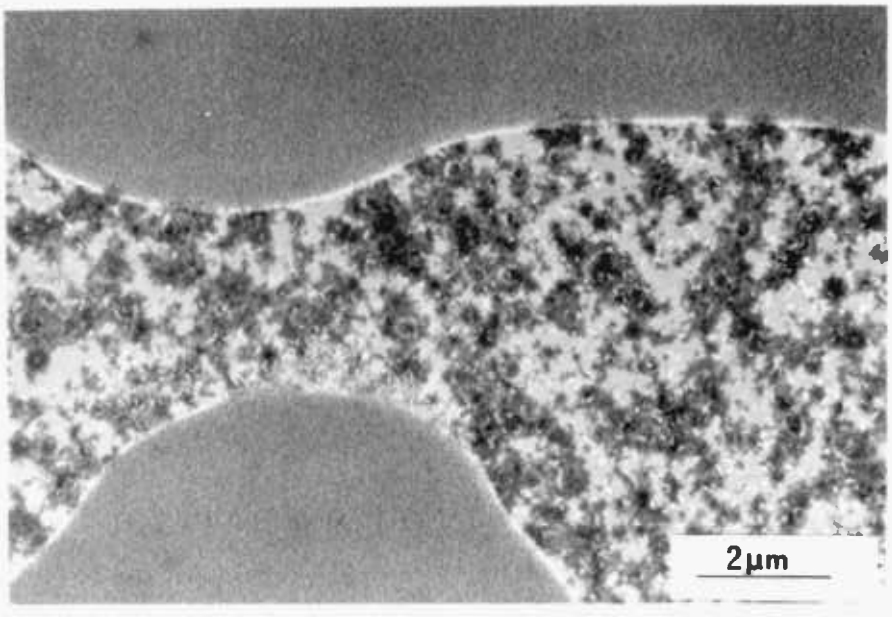
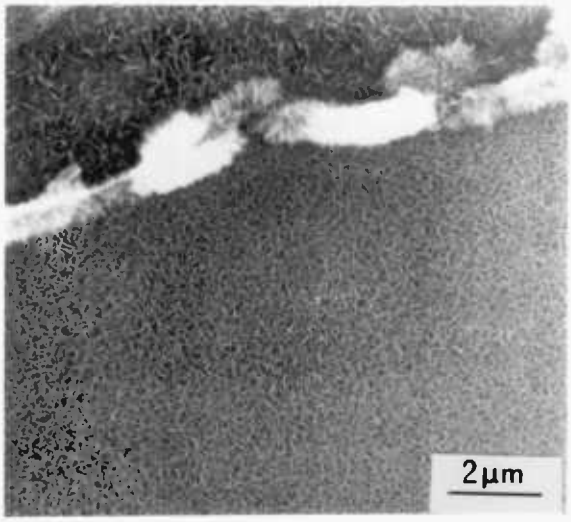
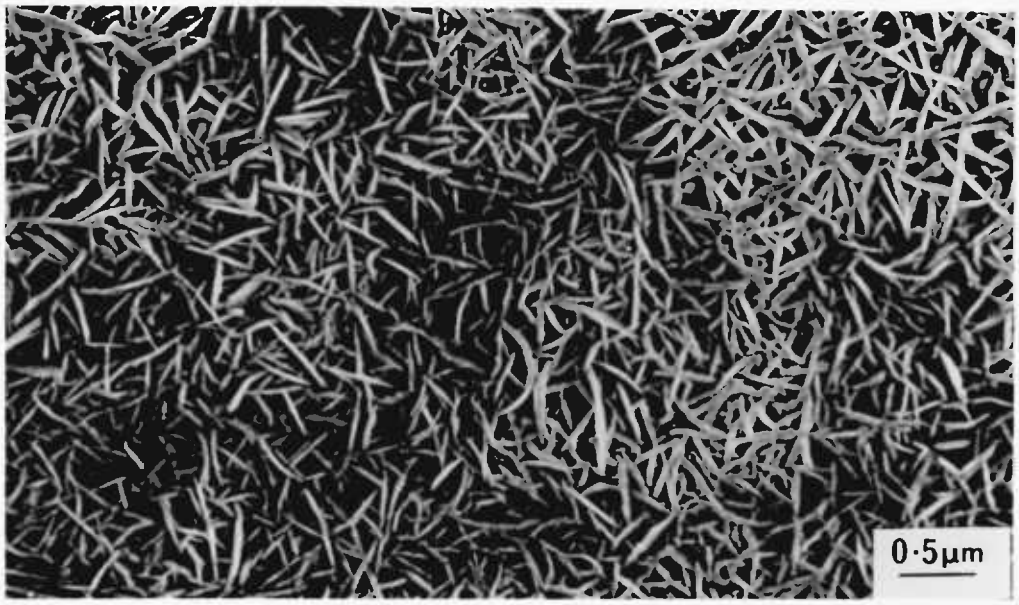

2μm

Figure 4.76. Micrograph showing that the reaction product inside blister is finer than that found outside.

Figure 4.77. Complete coverage by hydroxide after ∿12 hours in the autoclave.

Figure 4.78. Stereo pair taken after a continuous 12 hour exposure to water vapour of a 6/3 base alloy showing that there exists a clearly visible size difference between the reaction product inside and outside the reaction island. The remains of the blister wall are also evident.


2μm


0·5μm

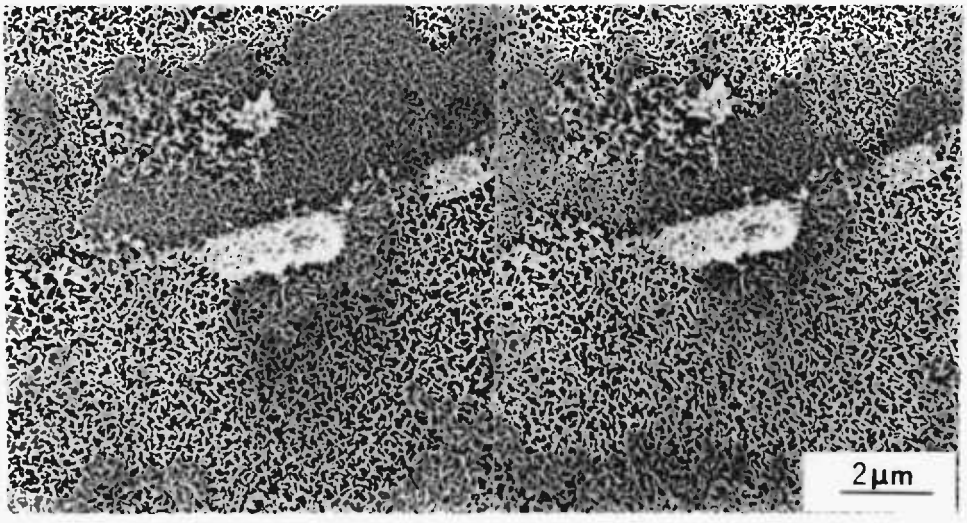
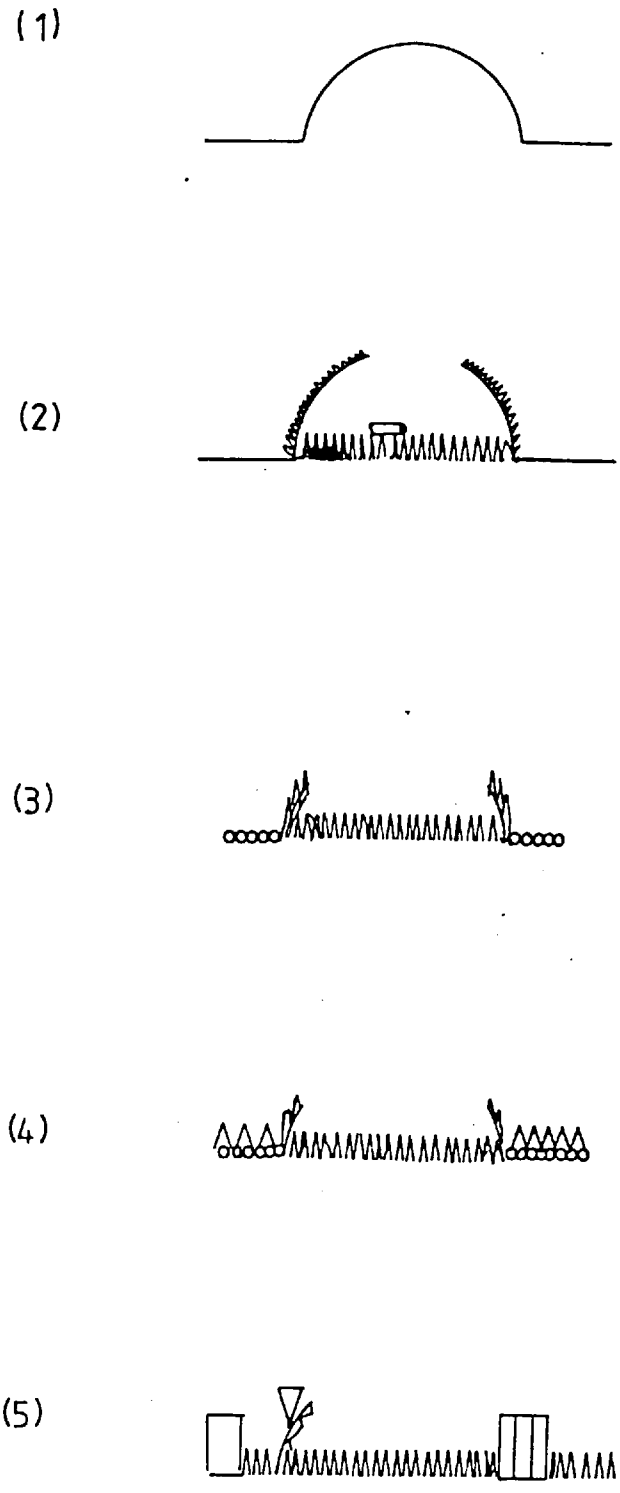

2μm

FIGURE 4.79



Points

(a) Local reaction: surface oxide not reacted: no evidence of reaction within blister.

(b) Collapse of blister walls: beginning to transform but surface not reacting.

(c) Development of hydroxide islands. Reaction on overall surface evident.

(d) Growth of pseudoboehmite outside blister. Collapsed blister wall indistinguishable from underlying reaction product.

(e) Growth of bayerite Crystal both at metal interface + blisters.

Figure 4.79 Schematic representation of the overall surface reaction progress.

This exhibited severe charging under the electron beam. However, some images and diffraction patterns were obtained. Figure 4.80 shows typical bright field images together with the relevant selected area diffraction patterns (SADPs).

The diffraction maxima in the patterns initially consisted of continuous diffuse rings, but became sharper and more spotty with increasing exposure time (Figure 4.81).

Analysis of the SADPs revealed that the rings were closely related to those reported for the boehmite structure (γ-AlOOH) in the ASTM X-ray powder diffraction file.

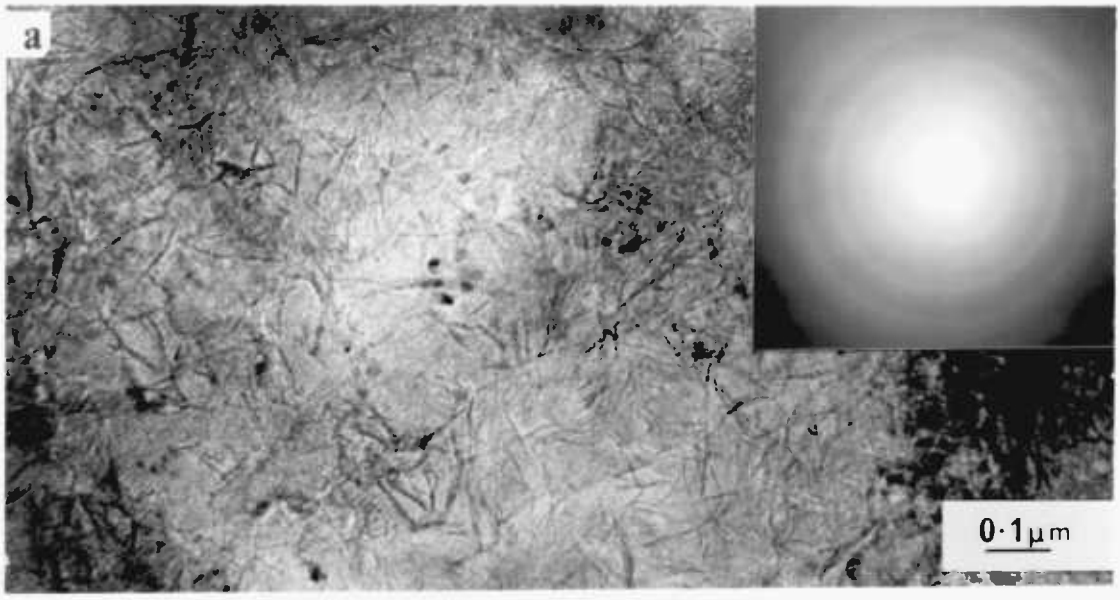
All alloys exhibited the same oxyhydroxide phase but there were evidence in the 6/3 Cr alloy of additional diffraction maxima. These could not be correlated with either boehmite or any other hydrated oxide that may be expected to form (Figure 4.82).

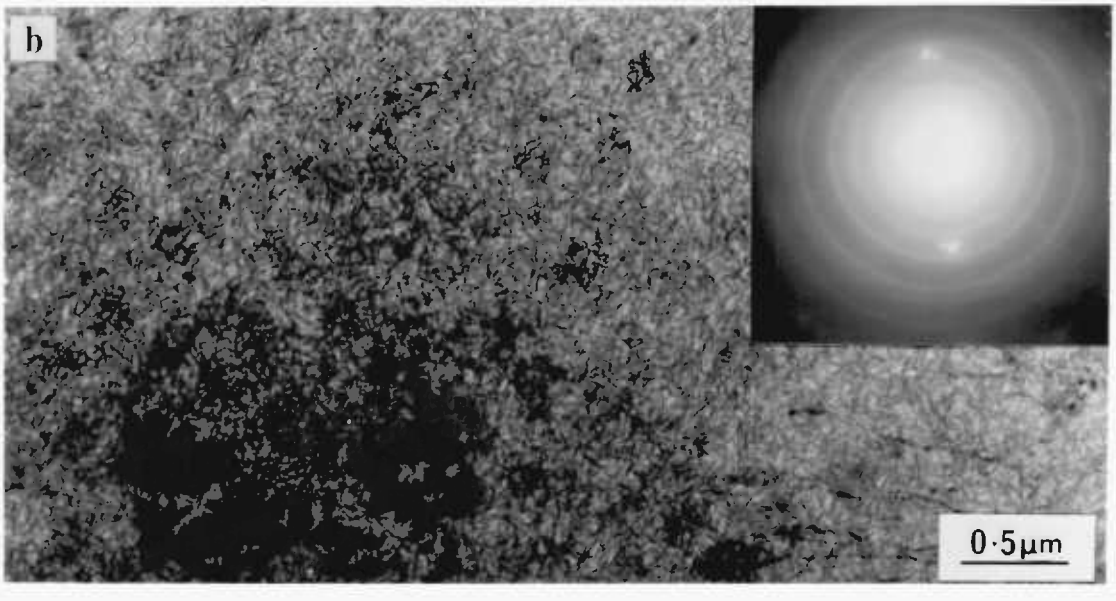
The morphology of the oxyhydroxide was characteristic as shown in the previous Figures (4.73-4.80). At least initially the structure of the crystallites was one of very thin curved lamellae (Figure 4.83). These lamellae were very thin and transparent to 100 kV electrons.

When viewed in stereo, using secondary electrons, the platelets were found to grow out of the surface of the samples (Figure 4.84). The needle like appearance in mono images arises as a result of the specimen orientation to the electron beam. Most of the photographic recordings were taken with the specimen surface perpendicular to the electron beam (for depth of focus considerations) and thus the most prominent aspect of the lamellae was the thickness-width edge. This resulted in the apparent "needle-like" morphology.

Following prolonged exposure to the wet environment however, the outermost parts of the lamellae divided into several fractions and gave rise to true needles or rods (Figure 4.85). Whilst showing variations between individual samples the development of the true needle or rod morphology was dependent on alloy composition. The 6/3 Cr alloy maintained the lamellae for longer periods than either the 6/3 base alloy or the 6/3 Cu alloy. Further a morphological difference between the oxyhydroxide formed on the 6/3 Cr alloy and the others was also apparent. It was found that in the Cr containing alloy isolated parts of the boehmite grew to substantially larger dimensions. Growth occurred from specific points on the surface and exhibited a "radiating star" shape (Figure 4.86). It was clear from transmission microscopy that

Figure 4.80 (a,b,c) Typical bright field images of the hydroxide phase together with associated diffraction patterns.
(a) 6/3 Cu alloy
(b) 6/3 base alloy
(c) 6/3 Cr alloy


a
0·1μm


b
0·5μm

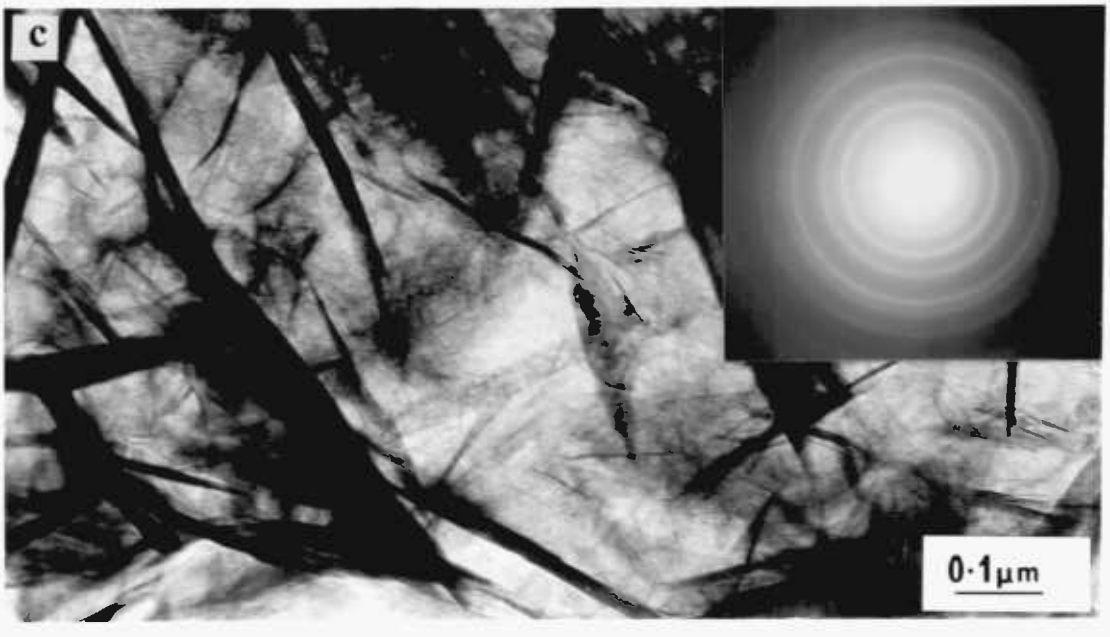
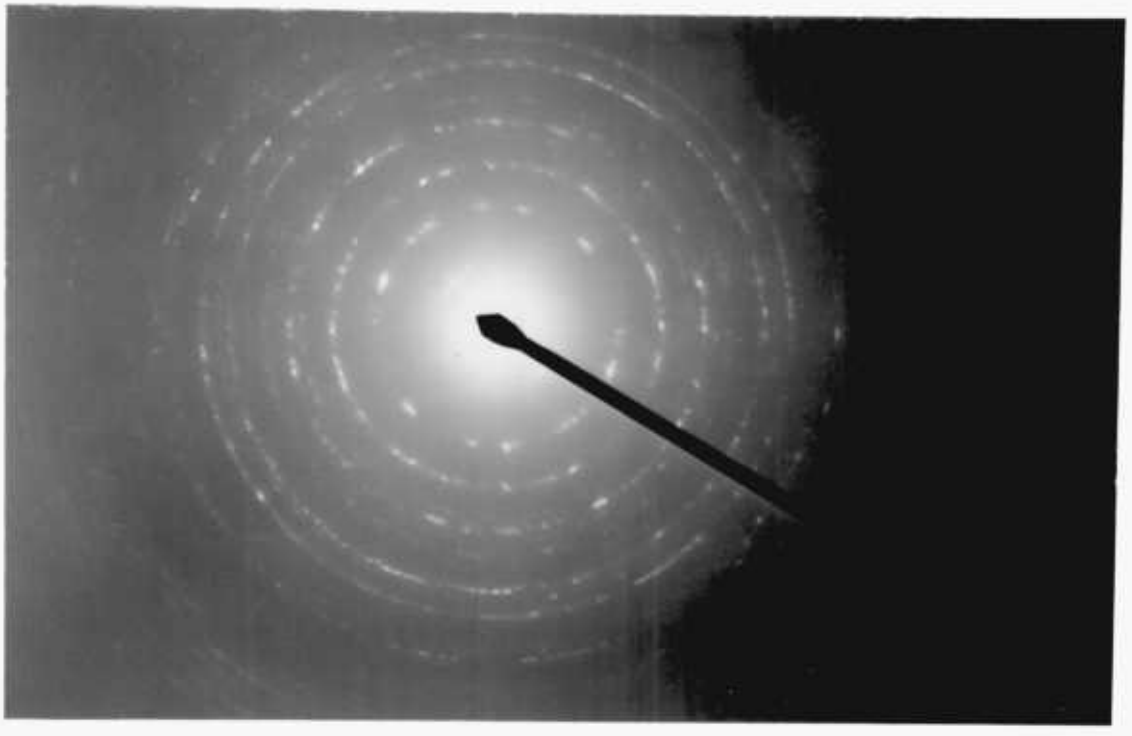

c
0·1μm

Figure 4.81. S.A.D.P. showing well defined boehmite diffraction pattern.
Note the inner ring at 6.2 A.
Al-6%Zn-3%Mg alloy. Exposed for 10 hours at 110°C.

Figure 4.82. S.A.D.P. from a 6/3 Cr sample showing diffraction maxima not consistent with the boehmite structure.



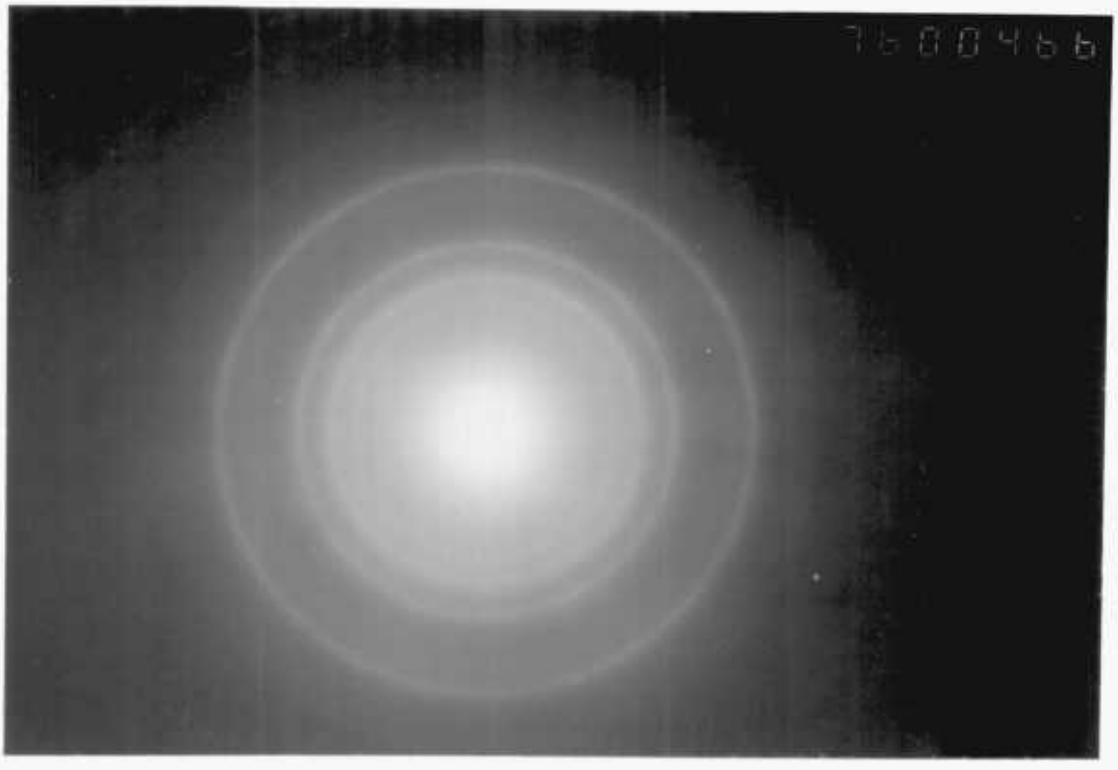
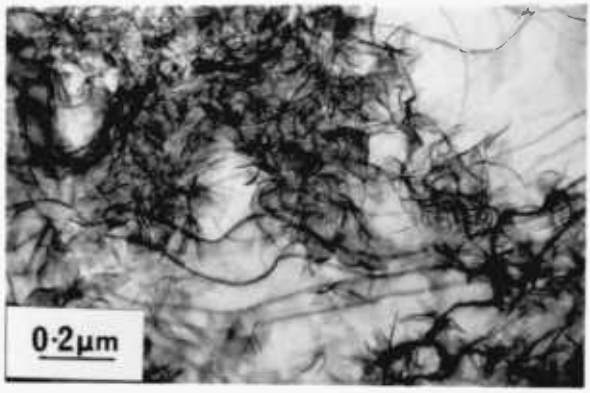
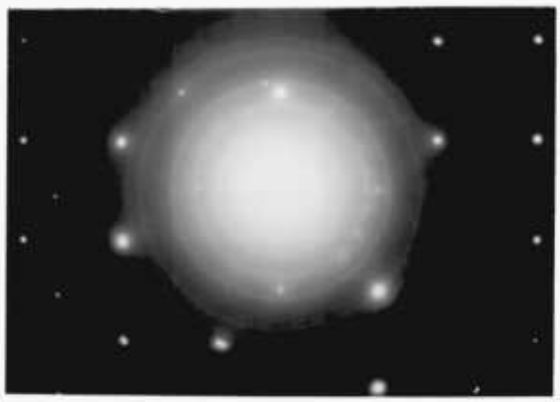

76 00466

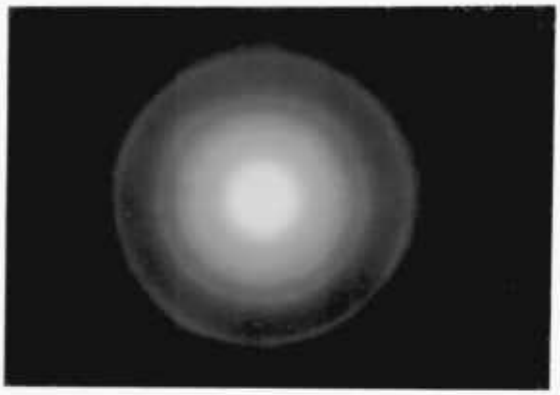
Figure 4.83. Very thin, electron transparent lamellae of hydroxide produced at the edges of the disc samples
(a) 6/3 Cu alloy
(b) 6/3 base alloy

Figuer 4.84. Secondary electron stereo pair showing the very thin electron transparent lamellae making up the hydroxide over the thin regions of the samples.


0·2μm




0·2μm



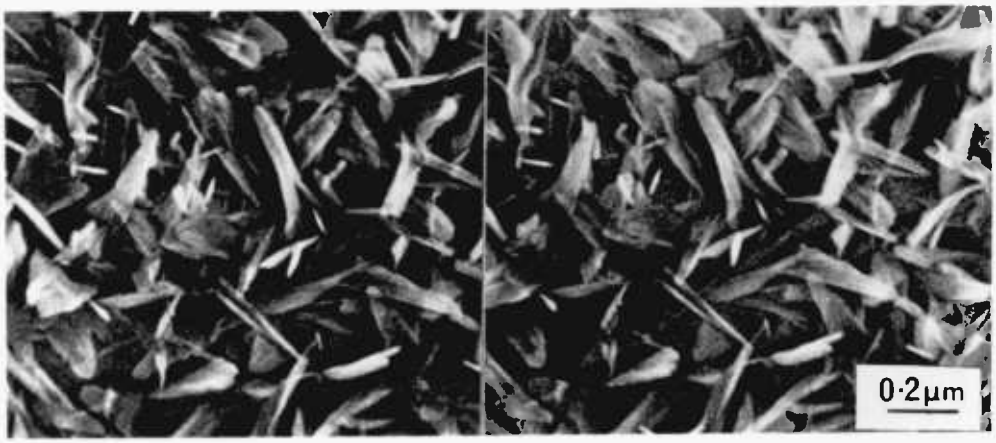

0·2μm

Figure 4.85. (a) Secondary electron image showing the transformation of the lamellae into needles or rods.

(b) Stereo pair showing that transformation occurs at the outermost parts of the lamellae

(c) Stereo pair showing complete transformation of the plate like hydroxide to rods.

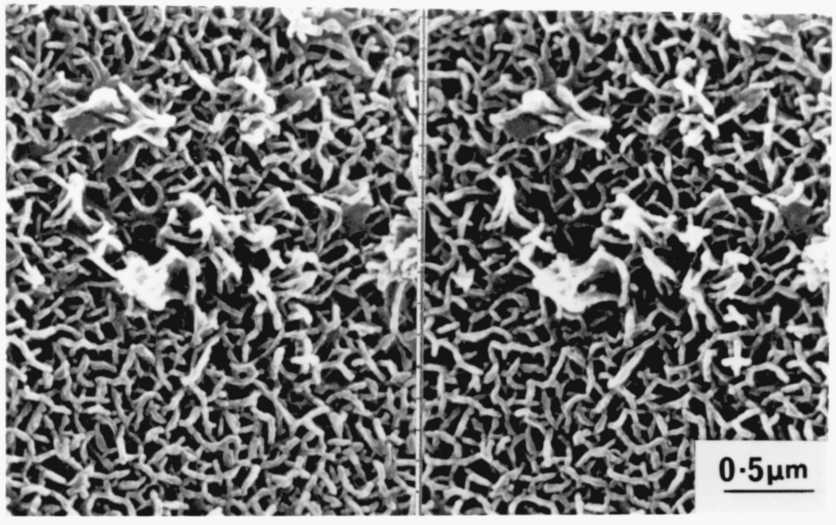

a
1μm


b
0·5μm

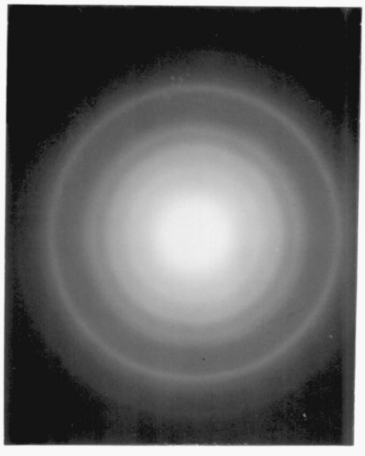

c
0·5μm

Figure 4.86. Stereo pair showing the morphology of the hydroxide product on the 6/3 Cr alloy. Certain areas of hydroxide grow preferentially into a 'radiating star' shape.

Figure 4.87. Transmission electron micrograph showing the nuclei of the radiating star growth particular to the 6/3 Cr alloy. The nuclei for such growth are not associated with grain boundary particles, or intermetallics.


0·5μm


0·5μm



growth had occurred from specific nuclei (Figure 4.87). Figure 4.87 shows an area where attack was slight and clearly reveals that the nuclei associated with this mode of reaction are not related to grain boundary precipitates or intermetallic particles nor any other obvious surface defect. As in the case of the more common pseudo-boehmite crystals during the initial stages of the reaction, these lamellae were very thin and electron transparent. It was not possible to separate the two morphologically different forms of hydroxide using the available diffraction data. The "radiating star" shaped colonies were maintained after prolonged exposures and appeared to grow preferentially (Figure 4.86).

Adhesion of the pseudoboehmite phase to the metal substrate appeared to be weak. The surface layer could be easily removed by adhesive tape or indeed by rough specimen handling. Stereo pairs taken from samples that had been damaged so that the metal/oxide interface was visible showed that the pseudoboehmite lamellae did not penetrate into the metal substrate (Figure 4.88).

In the later stages of the reaction there existed a second reaction product which was found in the 6/3 base and 6/3 Cu alloys alone (Figure 4.89). This took the form of highly faceted crystals roughly triangular or hexagonal crystals or plates (Figure 4.90). The crystals grew to heights exceeding several microns (Figure 4.90).

The existence of these crystals at 110°C was sporadic but large numbers were found at 70°C. The occurrence of this phase was limited to the thick areas of the disc samples and it was not possible to obtain diffraction data from the crystals. Identification was therefore limited to matching the characteristic morphology to that reported in the literature. On this basis it was identified as bayerite.

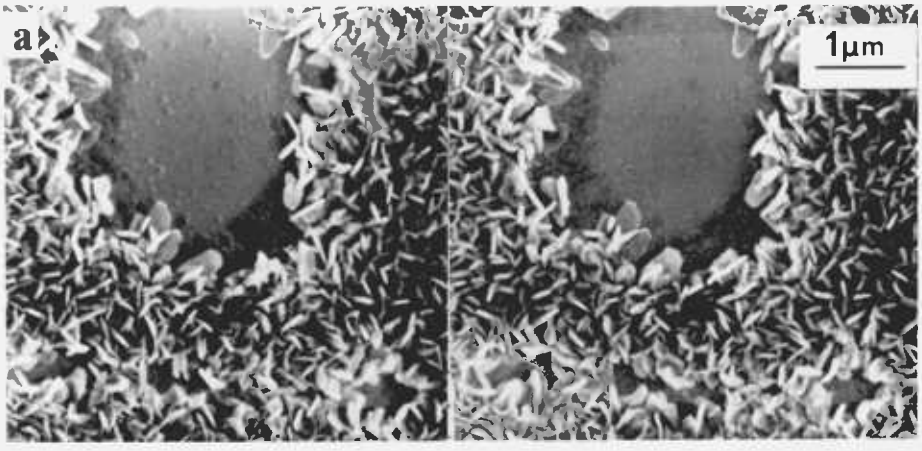
In the majority of cases it was found that the bayerite crystals were formed at sites where there were discontinuities in the pseudo-boehmite layer (Figure 4.91), but in others the existence of a discontinuity was not immediately evident (Figure 4.92).

During the early stages of their formation some of the bayerite crystals appeared to be inverted cones (Figure 4.93). The apex of the cones formed the base of the crystals which grew from the same level as the fibrous hydroxide. However, there were cases where the crystals formed on the surface of the partially or completely transformed blister

Figure 4.88 (a,b)

(a) Stereo pair showing that the pseudoboehmite phase does not have direct access to the underlying metal.
There exists a layer of a thin relatively featureless oxide between the oxyhydroxide and the metal.

(b) Stereo pair from a broken sample which clearly shows that the underlying surface film protruding over the edge.


a
1μm

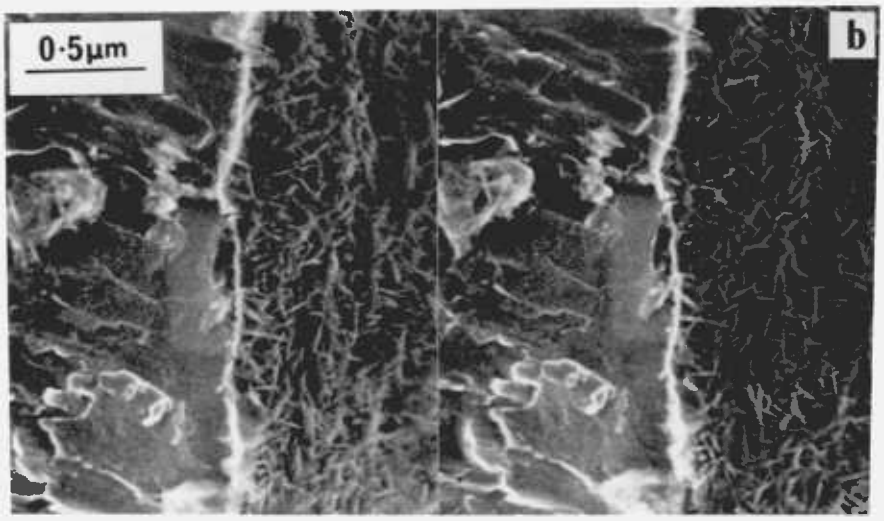
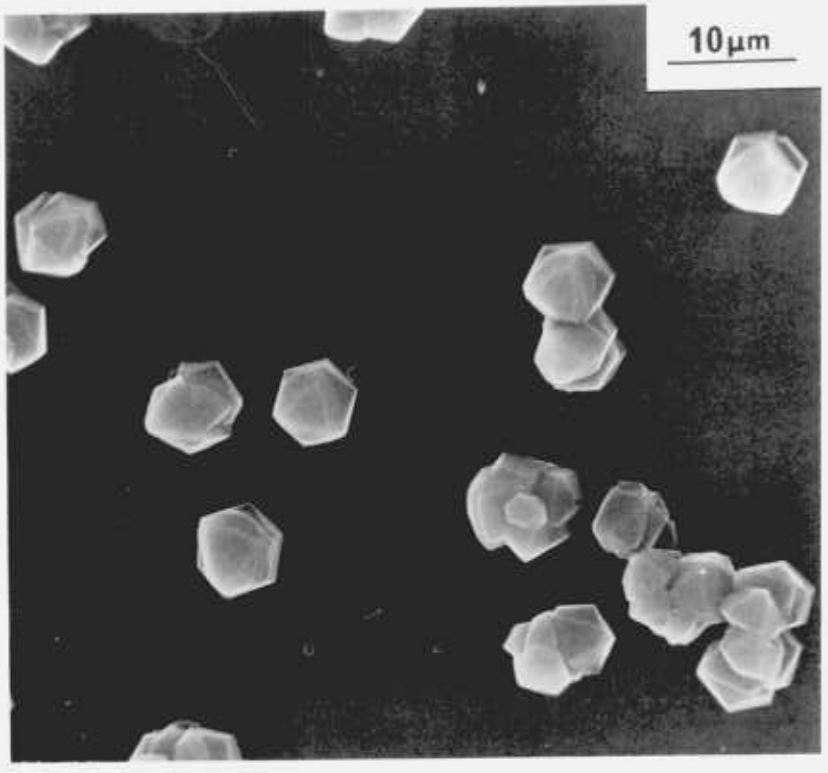

0·5μm
b

Figure 4.89 Highly faceted crystals formed on the surface of the samples and identified by their characteristic morphology as bayerite.


10µm

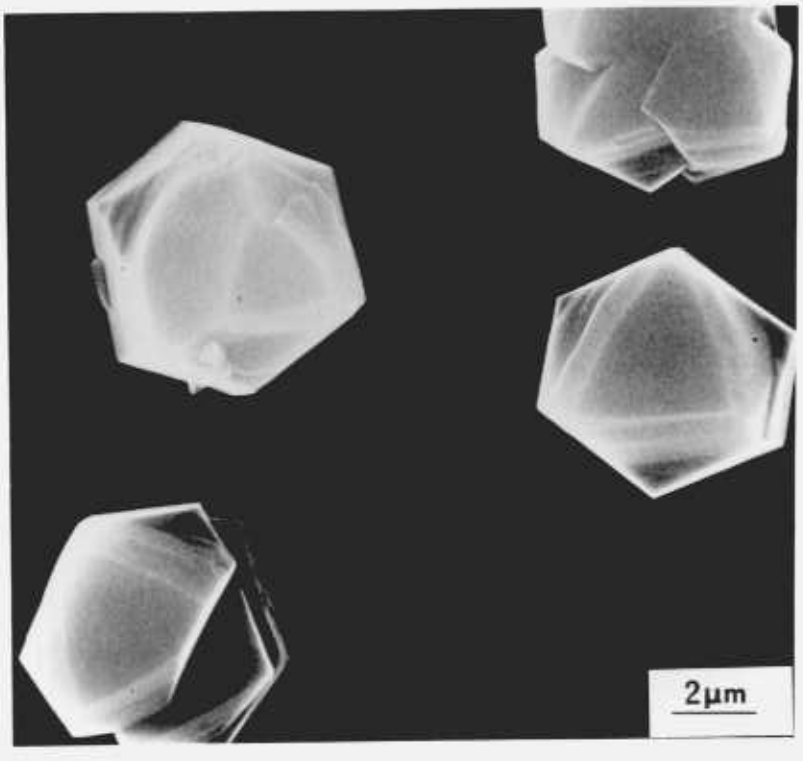
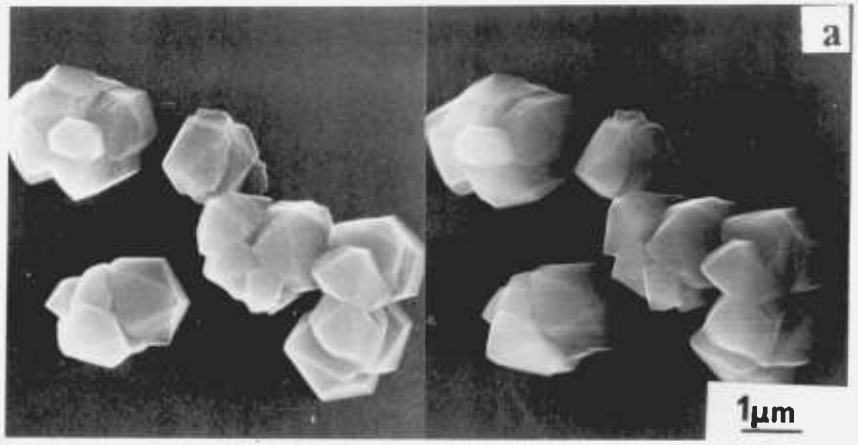
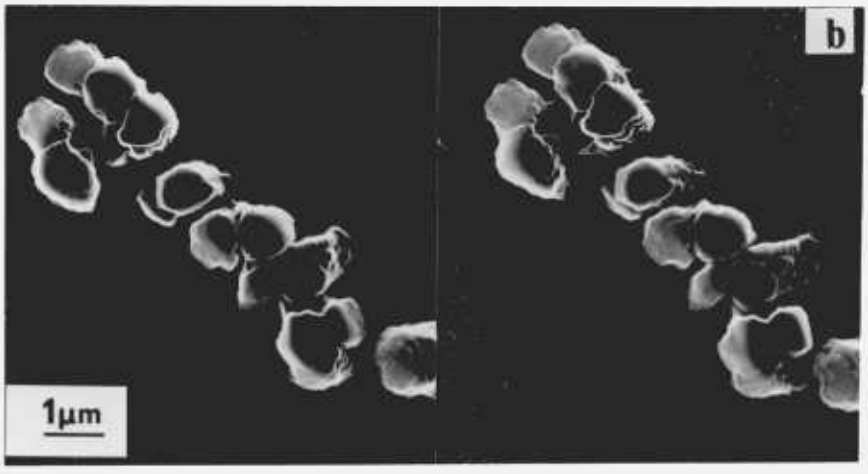

2µm

Figure 4.90 (a,b,c) Stereo pairs showing bayerite crystals in the 6/3 base alloy (a,c) and 6/3 Cu alloy (b).


a
1μm


b
1μm

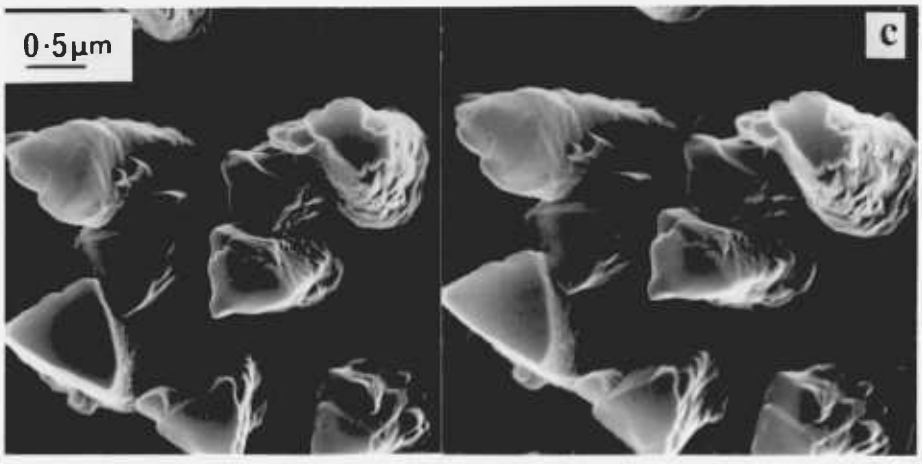
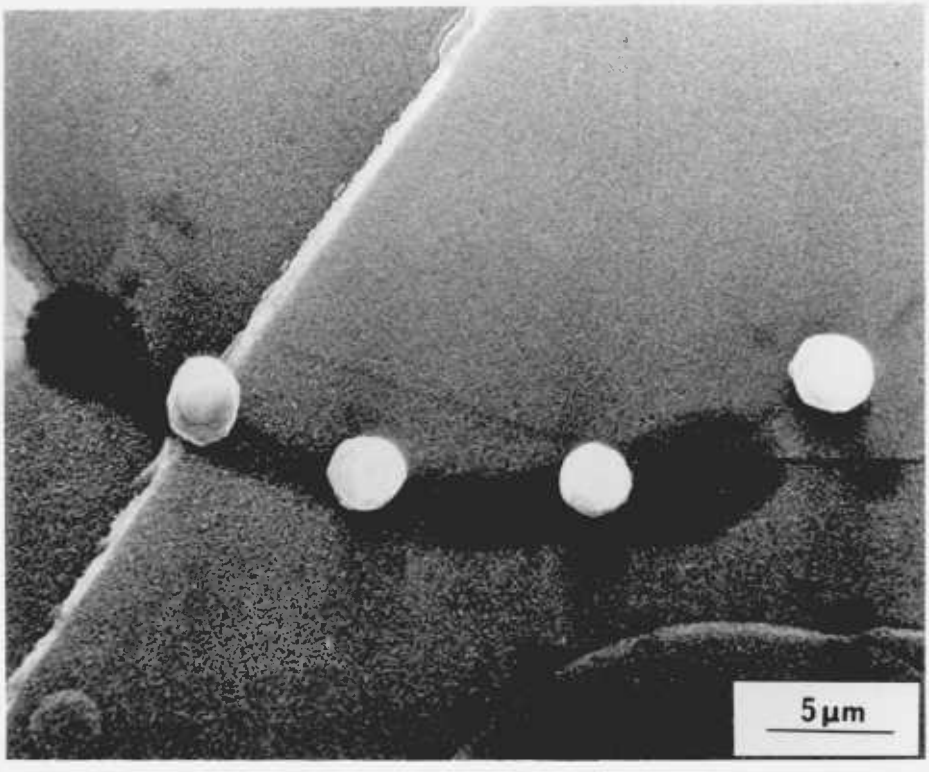

0·5μm
c

Figure 4.91. Bayerite crystals forming at discontinuities in the pseudo boehmite layer (reaction island periphery)

Figure 4.92. Bayerite crystals forming at sites where there do not appear to be any discontinuities in the pseudoboehmite layer.


5µm

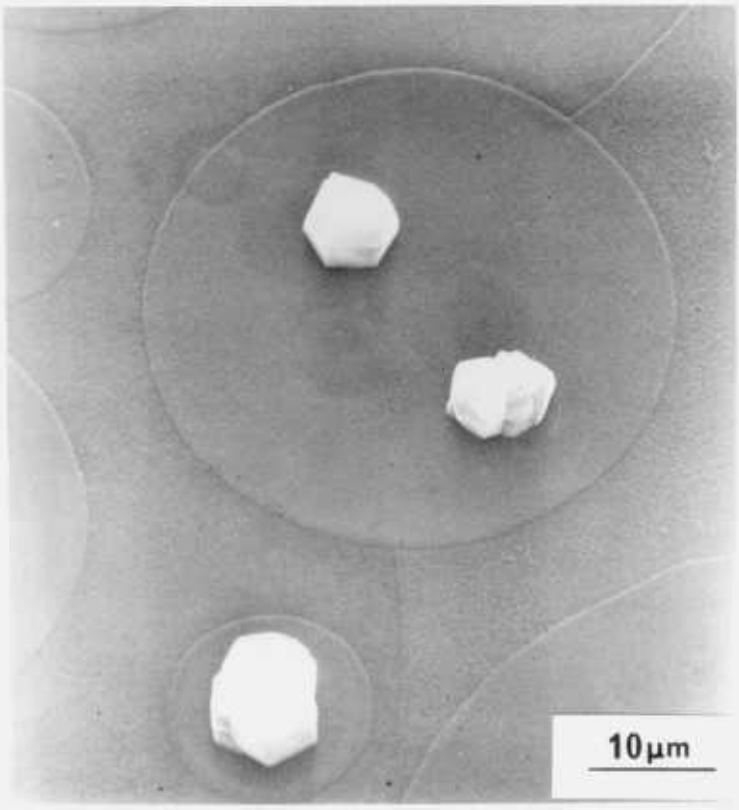
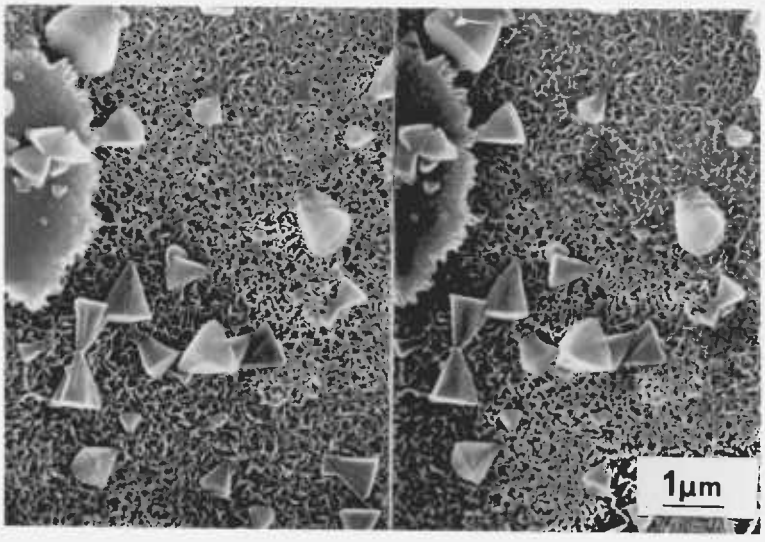
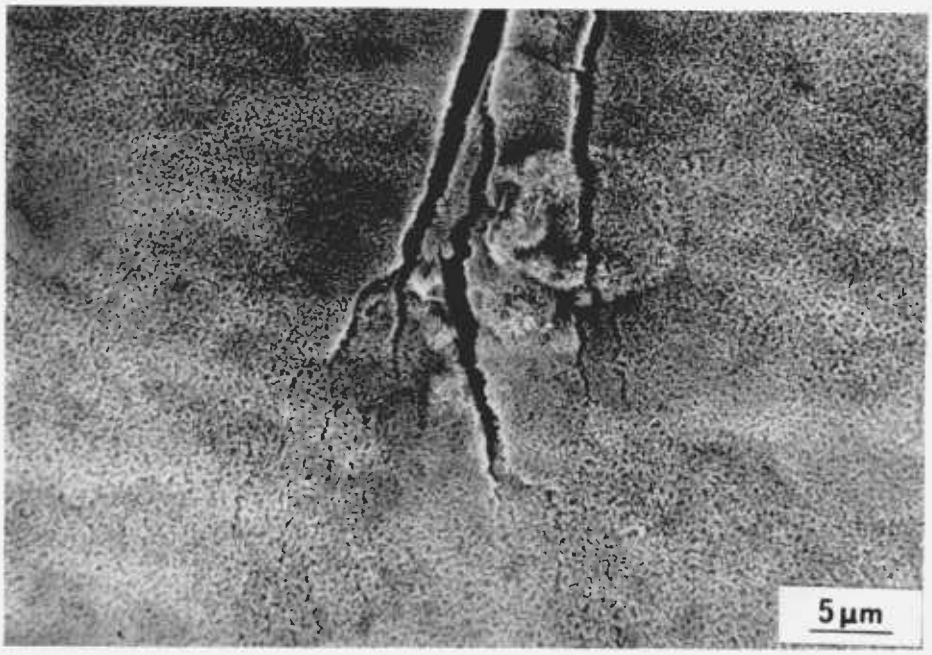

10µm

Figure 4.93. Stereo pair showing bayerite formation over remaining blister skin. It is clear that no access to the underlying metal is possible for those particular crystals. However, the bayerite crystals within the reaction island appear to grow from the same level as the pseudoboehmite phase.

Figure 4.94. Pseudoboehmite hydroxide phase in a chemically polished bulk tensile sample after 32 hours exposure (6/3 Cr alloy).


1μm


5μm

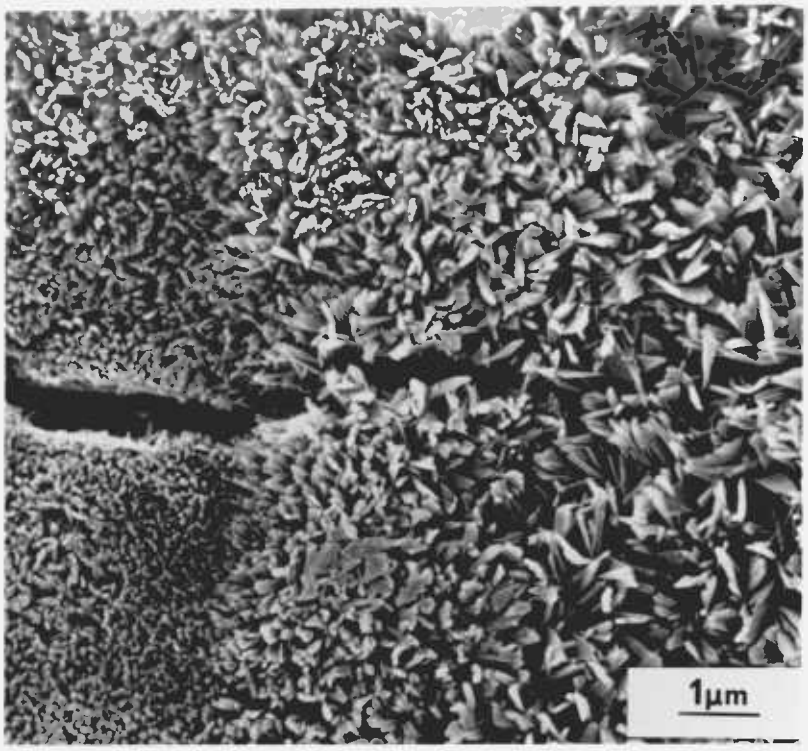
oxide (Figure 4.93). It seems therefore that whilst the formation of bayerite is favoured by access to the underlying metal it can also grow from the boehmite alone.

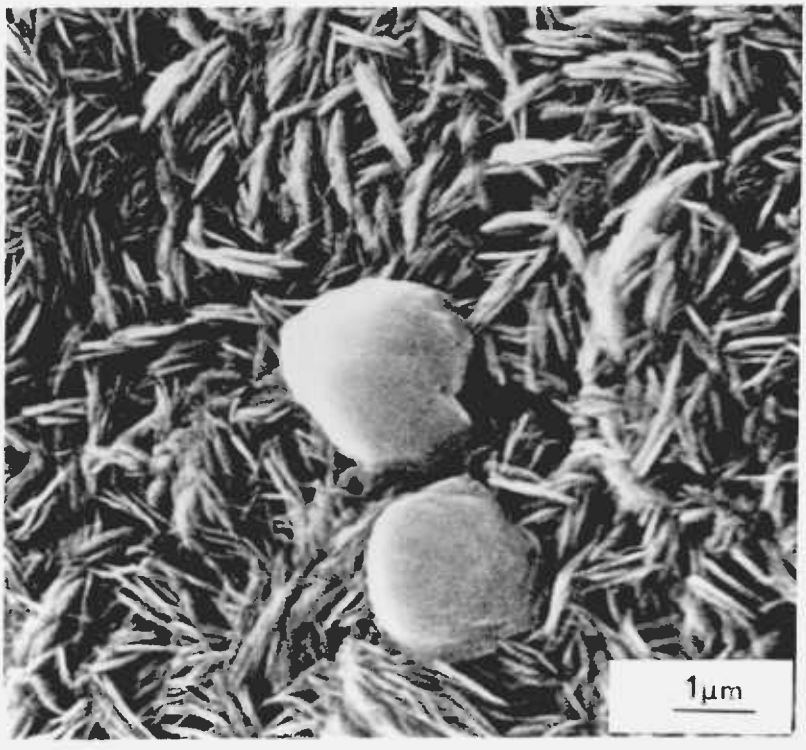
4.4.2. Surface oxide on tensile samples exposed to moist environments

The bulk tensile samples used for mechanical testing exhibited very similar boehmite structures to those found in electropolished samples (Figure 4.94). The boehmite layer was found to have grown substantially and depending upon the time of exposure for any given alloy the surface exhibited a morphology of rods, lamellae or a combination of both (Figure 4.95). The occurrence of bayerite crystals in bulk samples was severely restricted but isolated examples were found (Figure 4.96).

Figure 4.95. 6/3 Cr bulk tensile sample exposed to water vapour at 120°C for 56 hours showing both plate and rod like morphology of pseudoboehmite.

Figure 4.96. Bayerite crystals on the surface of a high purity sample exposed to water vapour saturated air at 70°C for 72 hours. Note that the pseudoboehmite phase is less well crystallised than that produced at 120°C.


1μm


1μm

5. DISCUSSION

It was the principal aim of this work to assess the mechanism of environment sensitive failure of Al-Zn-Mg alloys from a 'metallurgical' point of view. In this respect therefore the actual environment/susceptibility evaluation test used was substantially immaterial provided it fulfilled the necessary criteria for environment sensitive fracture to occur. The choice of water vapour as the corrosive agent was made because, as shown previously (Section 2.7), under most conditions, it is the presence of water molecules that is essential for S.C.C. to occur. In so doing it was not the intention to disregard the possibility of a change in mechanism of failure in different media and the question as to whether any conclusions/mechanisms arrived at from this work can be extended to other environments will be given due consideration in the subsequent discussion.

The employment of 'pre-exposure' tests for evaluation of the environmental susceptibility facilitated metallographic examination of the samples. No post fracture corrosion occurred and fractography could be carried out on clean surfaces. More specifically the role of hydrogen could be examined by utilising 'delayed' effects such as reversibility of embrittlement, strain rate sensitivity of ductility, etc. Consideration will be given to the point that the absence of the simultaneous action of stress during pre-exposure embrittlement tests possibly eliminates one factor in the environment-sensitive failure phenomenon. Thus it is proposed to examine the relevance of the mechanism proposed to account for pre-exposure embrittlement to stress corrosion cracking and to consider modifications which might be needed to extend the mechanism to S.C.C.

5.1. Proposed Mechanism of Failure

On the basis of the experimental results a mechanism has been developed that is capable of satisfactorily explaining the majority of the available data on the environment-sensitive failure of Al-Zn-Mg alloys. In the interests of clarity the mechanism will be outlined here. In so doing it is not implied that alternative explanations and mechanisms will not be examined during the discussion of the results. It merely is hoped that this approach will permit a more concise presentation.

The mechanism is based on the proposals made by Swann and co-workers (42, 76, 77) and considers that failure occurs by a dissolved hydrogen embrittlement event.

The essential steps are shown in Figure 5.1.

5.1.1. Hydrogen production

The hydrogen production event constitutes the primary effect of the environment. Hydrogen is generated as a result of the overall reaction,

$$2Al + 3H_2O = Al_2O_3 + 3H_2$$

This reaction is energetically favourable and occurs rapidly (i.e. the rate constant K_1 is large (Figure 5.1)). It involves a number of steps, beginning with the hydration of the initial film present on the alloy and the subsequent development of a duplex surface film; an amorphous (alumina) inner layer and a hydrated outer product. (pseudoboehmite). The gaseous hydrogen product is generated at very high pressures; (estimated pressure from results $>10^2$ atmospheres; calculated equilibrium pressure 10^{40} atmospheres). Hydrogen discharge occurs at the metal/oxide interface and leads to oxide decohesion and surface blister formation.

The mechanism of hydrogen production involves the transport of ionic species across the amorphous oxide film existing immediately adjacent to the metal under the influence of a concentration profile and an electric field. This mechanism is closely related to that proposed by Draley and Ruther (130). However a hydration step, involving the migration of water, through the outer layer is required. A schematic representation of the proposed events is shown in Figure 5.2.

The hydration event is an essential part of the reaction. It is necessary in order to consume the emerging aluminium ions and constitutes a basic requirement for hydrogen generation to occur.

The diffusion processes through the "amorphous" barrier layer depend on the defect structure. The alloying additions influence the defect structure and thereby the reaction character and kinetics. External sources of defects (e.g. irradiation damage) increase the rate of the reaction by affecting the generation and mobility of the reacting species.

5.1.2. Hydrogen adsorption

A fraction of the hydrogen atoms produced by the reaction at the metal/amorphous oxide interface (Figure 5.2) are considered as "adsorbed" at the instant of the discharge reaction. The exact 'physorption" event is unknown and the adsorbed state of hydrogen is likely to be transient.

The number of hydrogen atoms adsorbed at the metal surface depends on the values of the rate constants K_2 and K_3 (Figure 5.1). No information regarding these values was obtained, but provided the value of K_3 is not

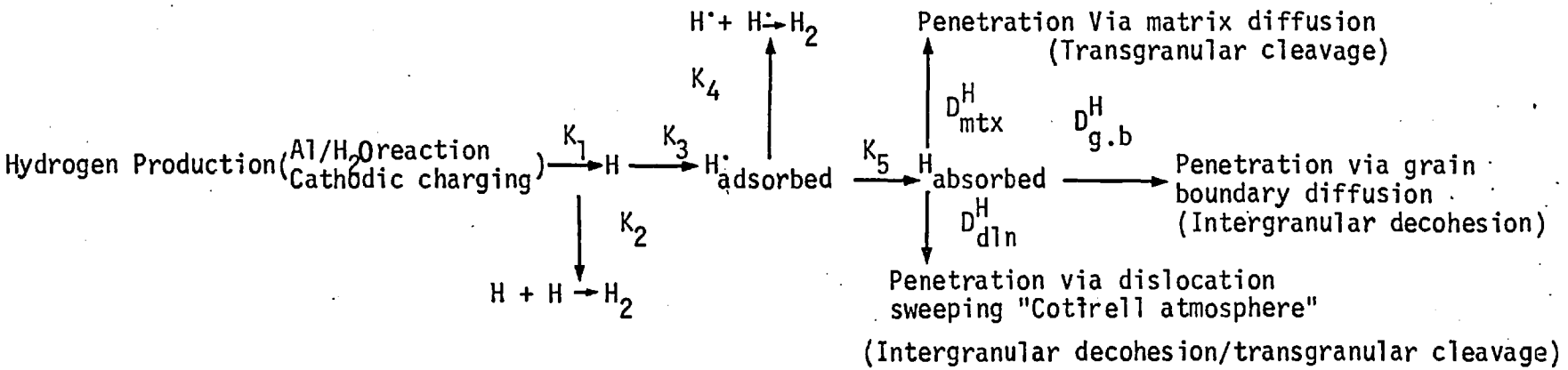


Figure 5.1. Schematic diagram showing the essential steps of the hydrogen embrittlement mechanism. (K_n = reaction rate constant for the n^{th} step.)

Metal	"Amorphous" Barrier Oxide Al_2O_3	Hydrated Oxide Al OOH/$Al(OH)_3$	Water vapour environment
$Al = Al^{3+} + 3e$	$Al^{3+} \rightarrow$	$Al^{3+} + 3AlOOH = 2Al_2O_3 + 3H^+$	H_2O
	OXIDATION EVENT	$Al^{3+} + AlOOH = Al_2O_3 + 3H^+ + H_2O$	
$H^+ + e = H^\cdot$	$\leftarrow H^+$	$Al^{3+} + 3H_2O = Al_2O_3 + 6H^+$	H_2O
$H^\cdot + H^\cdot = H_2$		H_2O (OH^-, H_3O^+)	
		HYDRATION EVENT	
		$2H_2O + Al_2O_3 = 2AlOOH + H_2$	H_2O
		$3H_2O + Al_2O_3 = 2Al(OH)_3$	
		$AlOOH + 4H_2O = AlOOH.4H_2O$	

Hydrogen discharge site
Hydrogen adsorption site

Limit of hydration event
Production of pseudo-boehmite/boehmite

Hydrated oxide/environment interface
Arrival of water molecules

Figure 5.2. Proposed surface reaction mechanism.

orders of magnitude lower than K_2 the high pressure of the gaseous product will ensure that significant amounts of hydrogen will be so adsorbed.

5.1.3. Hydrogen absorption

The adsorbed hydrogen may only follow one of two avenues. Atoms may recombine, form hydrogen gas and be evolved. (An event governed by the rate constant K_4.) Alternatively they may be absorbed into the substrate. (An event governed by the rate constant K_5.) (Figure 5.1.)

The partition of hydrogen between these two alternative paths depends critically on the local surface chemistry. Conditions and agents which catalyse the reaction.

$$H^{\cdot} + H^{\cdot} = H_2 \qquad \text{(i.e. increase the ratio } \frac{K_4}{K_5}\text{)}$$

reduce the amount of absorbed hydrogen. Under conditions where the hydrogen entry step is controlling the environment sensitive failure of the alloys, such catalysis is beneficial. Conversely conditions which favour absorption of hydrogen result in greater susceptibility to embrittlement. On the basis of the present work it is proposed that chromium additions markedly catalyse the recombination of hydrogen and inhibit entry.

The absorption of hydrogen at the surface results in a considerable local supersaturation. Under the influence of the concentration profile thus established, diffusion of hydrogen into the alloy substrate occurs.

There exist three diffusion paths, only two of which are possible in the absence of an applied stress (Figure 5.1). These are matrix, and grain boundary diffusion. (Hydrogen transport via dislocation sweeping is the third transport mechanism, but this is only possible under the combined influence of an applied stress and the water vapour environment.)

Both of these processes do occur as a result of exposure to water vapour. The rates of diffusion are determined by the values of matrix and grain boundary diffusion coefficients, D^H_{matrix} and $D^H_{g.b}$, respectively. Grain boundary diffusion is rapid and leads to a shallow grain boundary concentration profile whilst matrix mobility is restricted. Thus, a steep intragranular hydrogen concentration profile is established.

Hydrogen in intergranular solid solution may, under certain conditions, precipitate and form molecular hydrogen bubbles. In the ternary Al-Zn-Mg system, bubbles are formed exclusively at second phase grain boundary

precipitates of a size above a critical value (200A). However, quaternary additions of copper induce bubble formation even in the absence of second phase particles.

The formation of hydrogen bubbles results in the local depletion of dissolved hydrogen in the adjacent grain boundary regions. They therefore act as traps for the embrittling hydrogen and reduce susceptibility to embrittlement (see below, section 5.1.4.)

The growth of bubbles depends on both the supply of hydrogen and the resistance to their expansion offered by the surrounding metal.

There exists a quasi-static equilibrium between the pressure inside hydrogen bubbles and the concentration of hydrogen in solution at the grain boundary. The higher the pressure of the gaseous hydrogen inside the bubble the higher the concentration of dissolved hydrogen in equilibrium with it.

5.1.4. Effect of absorbed hydrogen on the mechanical behaviour

There exists a critical concentration of dissolved hydrogen (i.e. in solution) both in the matrix and grain boundaries which once attained will induce brittle failure. The attainment of the critical hydrogen concentration in the matrix, C_{Trans}^{CRIT}, leads to brittle transgranular, cleavage type failure. The attainment of a critical hydrogen concentration in the boundary, C_{Int}^{CRIT}, results in low energy decohesion of the boundary. Formation of bubbles therefore increases resistance to embrittlement by reducing the local concentration of dissolved hydrogen.

The stress necessary to induce intergranular decohesion is lower than that needed for intragranular lattice plane separation when both C_{Trans}^{CRIT} and C_{Int}^{CRIT} are exceeded under the conditions of hydrogen entry and partition that prevail.

The embrittlement by the absorbed hydrogen arises as a result of a reduction in the cohesive strength across a grain boundary/matrix interface (intergranular fracture) or due to a weakening of the bonds between cleavage planes (transgranular cleavage). There possibly exists a dislocation/dissolved hydrogen interaction which inhibits significant dislocation ejection at the crack tip: this applies to both transgranular and intergranular fracture.

Intergranular decohesion is achieved as a consequence of the development of some critical stress conditions at a hydrogen weakened boundary. These can be accomplished by the creation of a microcrack either as a result

of the establishment of a dislocation pile up at the boundary or by the formation of a hydrogen bubble. However, fracture will only occur if such crack nuclei can propagate unstably through an embrittled boundary. In a non embrittled boundary plastic deformation leads to crack blunting and ductile failure. The existence of grain boundary hydrogen bubbles therefore will only be detrimental if they are accompanied by the attainment of C_{int}^{CRIT} by the dissolved hydrogen at the boundary. Under these conditions the brittle fracture criteria are satisfied and low energy failure occurs.

Intragranular decohesion (cleavage failure) occurs under analogous conditions. Hydrogen supersaturation interferes with the normal ductile processes and on attainment of a critical stress/strain state, low energy lattice plane separation occurs.

5.2. Discussion of Experimental Results: Surface reaction during exposure

The reaction between the experimental alloys and water vapour at both temperatures examined produced remarkably similar results under all conditions investigated. The essential steps of the reaction are shown in Figure 4.79. The initial step is one of oxide film thickening and the formation of surface blisters. The blisters are produced as a result of the decohesion of the oxide film from the metal substrate.

The occurrence of blisters, clearly visible in all alloys under all conditions examined has been attributed to hydrogen produced by the reaction:

$$2Al\ (ZnMg) + 3H_2O = (Al(Zn\text{-}Mg))_2O_3 + 6H.$$

The occurrence of blisters suggests the formation of hydrogen gas at the metal/oxide interface. The decohesion of the oxide by the hydrogen implies that the pressure within the blister is sufficiently high to overcome the oxide/metal interfacial bond strength. The existence of hydrogen at the metal/oxide interface could be established by one or more of the following events:

(a) Water (either as a molecule or as OH^- ions) penetrates the existing oxide film to react with the underlying metal to yield an oxide and hydrogen.

(b) Hydrogen atoms produced at the environment/oxide interface diffuse through the existing oxide, combine and form hydrogen gas which pressurises the blisters, or

(c) Hydrogen ions (protons) penetrate the oxide and are discharged at the inner interface producing atomic and subsequently molecular hydrogen

(Figure 5.2.).
The results presented earlier support the third alternative, which constitutes a low temperature extension of the mechanism proposed by Draley and Ruther (130) (Figure 2.17).

Penetration by water molecules and subsequent reaction at the metal/oxide interface requires that a reaction product should be formed inside the blister. No such evidence was obtained by combined SEM-STEM imaging techniques. In the cases where reaction products could be clearly observed within the blister in the electron microscope the blister walls had been broken and the 'pseudoboehmite' phase present was most probably produced by direct access of water vapour after the formation and destruction of the oxide layer making up the blister. Also there is no obvious mechanism available for H_2O or OH^- migration through the barrier oxide layer to the metal. Thus, mechanism (a) is unlikely.

Mechanism (b) is also unlikely since there is no driving force for hydrogen atoms to migrate through the oxide. Recombination to form hydrogen molecules at the oxide/environment interface would surely occur. However, proton entry would be driven by the potential gradient generated across the oxide by the build up of electron at the metal/oxide interface as Al^{3+} ions form and migrate outwards (the electronic conductivity of Al_2O_3 at low temperatures is very low (112)). This is the mechanism of Draley and Ruther (130) and is consistent with the observations of hydrogen entry during cathodic charging (51, 78, 79). Also of particular interest here are the observations of Koch (153). He suggests that the embrittlement detected in his samples was due to hydrogen being absorbed from an ionised hydrogen atmosphere. The well known observation that dry molecular hydrogen does not cause failure suggests that it is the ionised species (protons) which diffuse through the oxide and not the neutral hydrogen atoms.

The available literature (section 2.7.1. and 2.7.2.) therefore would not be inconsistent with a mechanism of proton diffusion outlined above (Figure 5.2.) However, no direct proof has been obtained in support of the proton entry mechanism.

The hydration event (Figure 5.2) i.e. the transformation of the initial 'amorphous' (most likely microcrystalline) oxide to pseudoboehmite is important and it is this process that makes water molecules available for the subsequent reaction with aluminium.

The generally accepted view that there exists a barrier layer between the hydrated oxide and aluminium substrate received some support in this work. The examinations by secondary electrons certainly showed that the pseudoboehmite plates do not have direct access to the alloy and that a continuous oxide layer exists between the metal and the pseudoboehmite flakes. A schematic representation of the system is shown in Figure 5.3. which also shows the postulated mobile species. It should be noted that the proton diffusion step (i.e. the Draley and Ruther mechanism) operates across the barrier layer. The diffusion of water through the outer pseudoboehmite layer forms an essential part of the overall reaction and can occur via the interstices within the structure of the pseudoboehmite (Figure 2.16), or via the macroscopic pores between the pseudoboehmite plates (Figure 5.3.).

The total reaction involves the oxidation of the aluminium to AlOOH. The above is a possible mechanism by which the overall reaction may occur given that the oxide consists of a duplex layer in which the mobile species in one are likely to be quite different to those operating in the other. A possible set of reactions are shown in Figure 5.2. The movement of Al^{3+} is driven by the concentration profile across the amorphous layer and is most probably aided by the apparent excess of Al^{3+} in amorphous alumina (106). Some magnesium substitution for the aluminium ions may occur in Al-Zn-Mg. The substitution of aluminium by magnesium in alumina markedly increases the hydrogen (tritium) permeability at least at high temperatures (140), and this may further stimulate the entry of hydrogen into the alloys. This may be the rationalisation of the Scamans et al (77) conclusion that regions of high magnesium concentration in the oxide film (MgO) promote hydrogen entry. The occurrence of slight preferential attack at the grain boundaries on exposure to w.v.s.a. at 70°C may be indicative of the presence of higher concentrations of magnesium at these sites perhaps as a result of a solute supersaturation in the underlying alloy grain boundary.

The actual hydrogen diffusion step through the barrier oxide probably occurs through the defect structure (139). It is perhaps worth noting that the oxide would be microcrystalline and not truly amorphous and that the boundaries between such microcrystals may offer additional paths for diffusion.

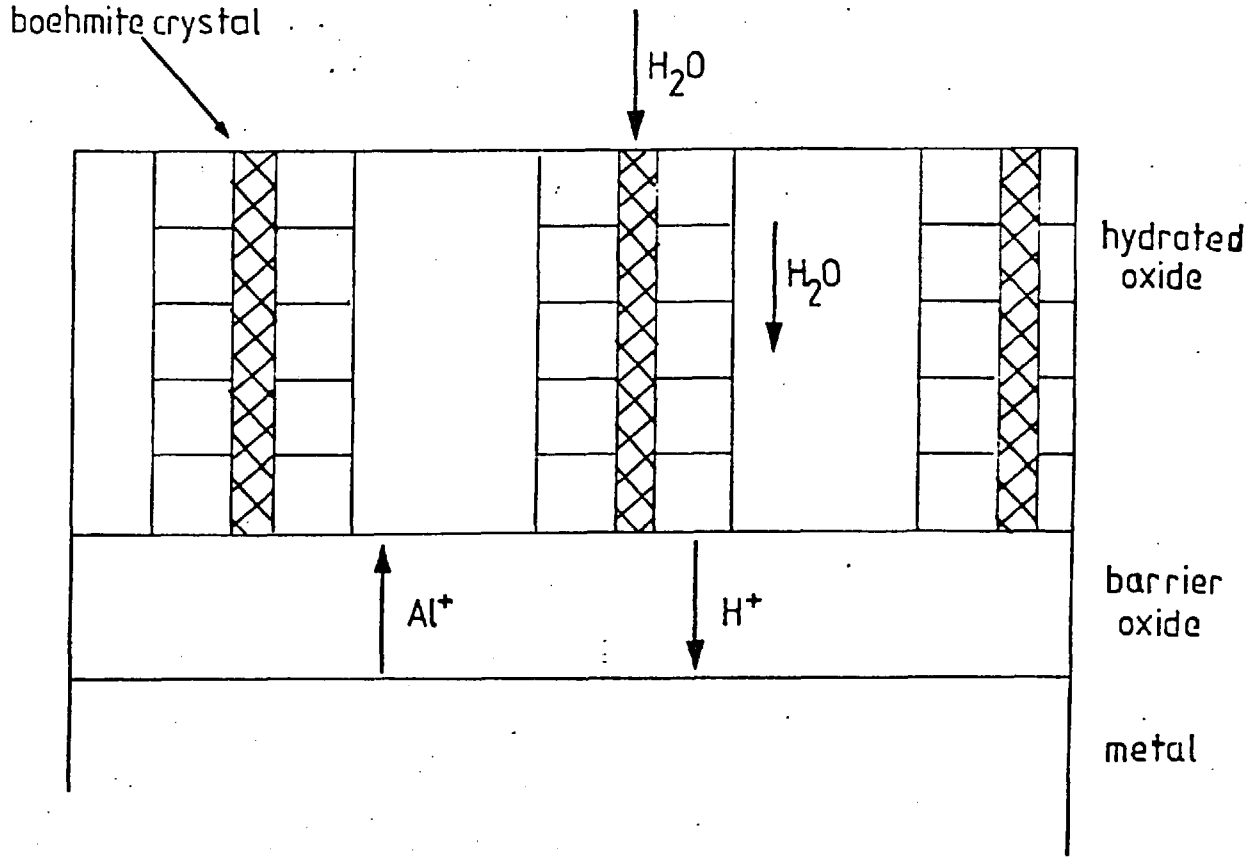


Figure 5.3. Schematic representation of the duplex hydrated oxide on the surface of exposed samples. Arrows indicate direction of diffusing species.

The hydrated film itself was found to be pseudoboehmite (AlOOH) with evidence of some transformation to the Bayerite hydroxide ($Al(OH)_3$) phase after longer exposure times. The morphology of the hydroxide (i.e. one of outgrowing plates) suggests that growth occurs as a result of outward growth rather than a dissolution-precipitation event as suggested by some workers (125). This is important in that it indicates that such plates grow outwards as a result of the reaction of aluminium at the amorphous layer/pseudoboehmite interface and thus is consistent with a mechanism postulating the outward movement of Al^{3+} through the barrier layer to be available at the reaction site. The corresponding cathodic reaction (H^+ production) can then be achieved locally at a site within the hydrated oxide film - presumably at or near the interface with the barrier film where the hydrated oxide is in contact with Al^{3+} ions and the H^+ can enter the barrier layer.

The rationalisation of the occurrence of the reaction islands observed is that at some pressure of hydrogen the blisters are ruptured which then allows access of water to the alloy. Oxidation (corrosion) then occurs rapidly with the subsequent formation of the duplex oxide/hydroxide film. Further growth then occurs by diffusion through the established films. Such behaviour is consistent with the three stage behaviour of the Al-H_2O reaction system (124):

Stage 1 (incubation period) is consistent with the nucleation and growth of hydrogen filled blisters. Subsequent bursting of blisters exposes reactive metal and fast reaction (stage 2). Stage 3 occurs after the establishment of the pseudoboehmite layer and results in the growth of the blade like platelets.

Bayerite then forms either due to a direct transformation from pseudoboehmite alone or more frequently by having access to both pseudoboehmite and metal.

The formation of boehmite lamellae away from broken blisters after prolonged exposure may have two explanations. Firstly it is possible that hydrogen penetrates the amorphous oxide as described previously but instead of forming blisters escapes via some microscopic defect. Alternatively it may be that water, perhaps as OH^- ions is able to diffuse through the microcrystalline barrier layer and form pseudoboehmite. Whichever of these does operate it is evident that the contribution from this mode of growth is small compared to the blister rupture event.

It is evident from the results that the surface reaction between the alloys and water vapour can be influenced by the presence of quaternary additions. Specifically it appears that chromium induces a morphological change in the pseudoboehmite while not, apparently, changing the reaction behaviour. The presence of unidentified oxide rings in the diffraction data indicates that there may be an effect on the structure of the hydroxide product but more data on backpolished samples are needed before positive identification can be made. (The diffraction data were obtained from regions of the foil which had been completely oxidised to produce the hydroxide and may therefore be atypical.) No such effect was noted in the copper containing alloy (6/3 Cu). It therefore appears that chromium additions exert an influence on the surface events and as shown by the 'in situ' experiments one effect is the catalysis of the recombination of adsorbed hydrogen to form gaseous hydrogen at the oxide metal interface (see Section 5.4).

The evidence for hydrogen entry into Al-Zn-Mg alloys following exposure to water vapour containing environments has already been presented (Section 2.7.3.). It is found that following exposure to water vapour Al-Zn-Mg alloys absorb hydrogen (42, 76, 77). Hydrogen was identified both by inference and direct measurement (42, 76, 77). Later it was shown that prolonged exposure leads to the development of internal hydrogen bubbles (141). Extensive, similar observations were made in the present work. In view of the very good correlation between the exposure work of Alani and Swann (141) and Scamans (142) and the present investigation no discussion of comparisons between dry and wet samples is considered necessary here. It is simply pointed out that the results reported in the above publications were routinely verified. Hydrogen bubbles were found exclusively in samples that were exposed to water vapour.

It is possible that such bubbles have been seen in other work also but have gone unnoticed. For instance some excellent examples of hydrogen bubble characteristic strain fields on second phase grain boundary

precipitates can be found in the paper by Unwin and Nicholson on the grain boundary precipitation in Al-Zn-Mg alloys (Reference 22 page 1385). Most surprising the authors completely overlooked the presence of these strain fields which are clearly not associated with the grain particles themselves. (Hydrogen was most probably introduced into their foils as a result of accidental exposure to water during specimen heat treatment, preparation or storage.)

Penetration of hydrogen in Al-Zn-Mg alloys as a consequence of exposure to water vapour at room and mildly elevated temperatures, therefore merely demands the extension of the accepted high temperature behaviour of aluminium (see Section 2.7.2.)

Finally, it is concluded that the 'exposure' step of the current experiments did accomplish its primary objective; it led to the introduction of hydrogen into the samples. The subsequent fracture under a tensile stress must therefore be considered in the context of a hydrogen presence and the question as to whether it has any effect on failure is addressed below.

5.3. Pre-exposure Embrittlement Tests

5.3.1. Isochronal Exposure

It is evident from the results presented in section 4.1 that the mechanical behaviour of underaged samples of the 6/3 base alloy is significantly affected by exposure to water vapour saturated air. "Wet" material exhibits lower ductility than comparably treated dry samples. Overaged samples are insensitive to exposure.

The loss of ductility in the underaged samples could be rationalised by two alternative mechanisms:

(a) Intergranular corrosion/pitting occurs as a result of dissolution of the metal. This produces microcracks which act as sharp notches causing stress concentrations and a reduction in recorded elongation. (Watkinson and Scully (44)). This proposal identifies the anodic reaction $Al \rightarrow Al^{3+} + 3e^-$ as responsible for the observed behaviour.

(b) Ductility is reduced due to an embrittling effect of absorbed hydrogen which is produced as a result of the reaction of the alloy with water vapour. (Swann et al (42, 76, 77)). In this case it is the cathodic event, hydrogen production, that is considered to be more important.

The second suggestion is favoured in the present case for the following reasons:

(i) No significant grain boundary corrosion was apparent before tensile testing.
(ii) Ductility of samples could be fully restored by repeating the heat treatment cycle.
(iii) Chemical/electrochemical polishing of samples prior to tensile testing had no effect on the recorded elongations.

The anodic dissolution mechanism is at variance with the above. Once a crack has been established by dissolution there is no avenue for restoring ductility. Furthermore removal of the surface layer containing the crack by chemical polishing should reverse embrittlement. No such behaviour was noted. In contrast to this a hydrogen embrittlement event consisting of deep penetration of the samples by hydrogen is capable of explaining all of the above.

Hydrogen produced by the reaction between the alloy and water vapour enters the alloy and causes brittle failure during the subsequent application of stress. Embrittlement is insensitive to the removal of the surface material because deep penetration of hydrogen, i.e. rapid diffusion along grain boundaries, is capable of establishing a sufficiently high concentration of hydrogen throughout the section of the sample. (This is quite likely since the thickness of the samples is only 4 or 5 grain diameters.) Reversibility of embrittlement by resolution heat treatment and ageing allows hydrogen to outgas and thus leads to the re-establishment of ductility.

The insensitivity of the overaged samples to water vapour exposure at 70°C can also be explained by the two alternative mechanisms. It could be argued that pitting/intergranular corrosion does not occur in the overaged samples and thus no reduction in ductility occurs. This is indeed the case. No significant attack of the boundaries was noted. However, when considering the overall behaviour it is difficult to explain why localised intergranular corrosion processes should not give rise to susceptibility in overaged alloys which have large anodic particles and yet be detrimental in underaged alloys.

The hydrogen mechanism offers an explanation of the observed behaviour if overaged samples are more tolerant to the presence of hydrogen. The surface reaction studies (section 4.4) have shown that blistering, i.e. hydrogen generation occurs over the entire span of the ageing treatments employed. Furthermore, direct observation of hydrogen bubbles in the overaged exposed samples have shown that hydrogen penetration does occur.

It is significant however, that the onset of insensitivity to exposure was concurrent with the formation of grain boundary bubbles. It may be therefore, (and evidence for this will be given below) that the increased tolerance of the overaged structures is related to the ability of the microstructure to form hydrogen bubbles. If the embrittlement is caused by a critical concentration of atomic hydrogen in the boundary as suggested by Swann and co-workers (42, 76, 77), then the nucleation of gaseous hydrogen bubbles will increase the total amount of hydrogen that needs to be introduced into the sample to reach that critical concentration.

The absence of any hydrogen bubbles in underaged samples indicates that their formation is a function of microstructure. Since no noticable differences in the H generation stage (i.e. surface reaction) were observed the implication is that bubble nucleation is affected by the size of the grain boundary precipitates that exist. These reach a size of approximately 200A before hydrogen bubbles are observed.

The behaviour shown in Figure 4.1 can therefore be explained as follows:
Hydrogen generated as a result of the reaction between all the samples and water vapour enters the material. In underaged samples the presence of hydrogen causes embrittlement of the grain boundaries. This occurs by the mechanism proposed by Swann and co-workers (42, 76, 77). These workers found that formation of hydrogen bubbles was preceded by total embrittlement and from this deduced that it was the atomic hydrogen in the structure that was responsible for the observed damage. It is believed that these ideas form a satisfactory basis for explanation of the embrittlement found in underaged samples in the current experiments. The occurrence of hydrogen bubbles however, in overaged samples before any embrittlement could be detected (Figure 4.2) suggests that embrittlement only precedś bubble formation if there are no suitable sites for bubble nucleation. In cases where precipitates above a certain size do exist (as a result of prior ageing) bubbles form before complete embrittlement. Using this argument the results of Alani (141) can be understood. In his underaged samples lack of suitable (precipitate) sites inhibited the formation of bubbles until such time as the hydrogen concentration was sufficiently high to cause hydrogen bubble nucleation in their absence. In point of fact, it is likely that the hydrogen bubbles he observed did nucleate at second phase particles. This is because his as quenched samples were exposed to w.v.s.a. at 70^{o}C for periods exceeding several days. Under these conditions grain boundary precipitate nucleation and growth would

be expected. The need for exposure of periods of several days before bubble formation (50) may therefore be related to the need to grow the grain boundary particles to the critical size during exposure itself. Attainment of this size then results in the nucleation of bubbles after embrittlement by atomic hydrogen has taken place.

Overaged samples do not show embrittlement due to their increased tolerance to the presence of hydrogen. This tolerance may be directly related to the nucleation of hydrogen bubbles at grain boundary particles above a critical size and/or some other microstructural parameter such as a softer matrix. The data of the isochronal exposure tests alone do not permit the relative importance of the two alternatives to be assessed.

It is of interest to note that the variation of susceptibility (i.e. elongation of 'wet' samples) to pre-exposure embrittlement with ageing condition is very similar to that which may be expected from more traditional S.C.C. tests (1, 2, 3). This highlights the link between pre-exposure embrittlement and S.C.C.

5.3.2. Isothermal exposure

The results of the isothermal exposure tests on the 6/3 base alloy at 120°C (Section 4.1.2., Figures 4.3-4.13) are crucial to the development of the failure mechanism. The mechanical properties measured (Figure 4.3) preclude any possibility of interpreting the embrittlement at 120°C and subsequent recovery of ductility in terms of an anodic dissolution mechanism. A crack formed in such a way could reduce the ductility as shown in stages 1 and 2. However, in the absence of substantial changes in fracture toughness on continued ageing at 120°C there is no way in which recovery of ductility could be obtained. The yield stress, fracture stress and ductility data for dry samples clearly indicate that no such change in fracture toughness may be expected in the region of the stage 2/3 transition. It should also be noted that no significant cracks were detected at grain boundaries in exposed samples. Even in the worst cases only some preferential shallow attack at the boundaries was observed. The interpretation of the behaviour shown in Figure 4.3. based on the hydrogen embrittlement mechanism is as follows:

During stage 1 exposure ductility of the samples falls partly as a consequence of the age hardening reaction and partly as a result of hydrogen accumulation in the grain boundaries. This eventually reaches a critical concentration at which the boundaries become fully embrittled and stage 2 commences.

The brittle intergranular failure in stage 2 is considered to be due to the attainment of this critical concentration of dissolved hydrogen throughout the thickness of the sample. The hydrogen concentration profile along the thickness of the sample is considered as shallow as a result of high grain boundary diffusivity. This is quite reasonable since the grain boundary diffusion coefficient of most metals is reported as being several orders of magnitude greater than the bulk diffusion coefficient (167).

The absence of any hydrogen bubbles in samples exposed for times up to the end of region 2 shows that embrittlement is due to "dissolved" hydrogen and not due to a "planar pressure" effect of the bubbles as suggested by some workers (168).

It is also evident from Figure 3.4 that fracture in region 2 does not initiate until the stress level applied slightly exceeds the yield stress. This is considered to be due to the need to attain a critical strain at the grain boundary leading to the dynamic nucleation of a crack which then propagates in an unstable manner through the embrittled boundary. Microstructurally this may be viewed as the attainment of a critical dislocation "pile-up" at the grain boundary. The planarity of slip produced by the ageing may be significant in this regard.

Kawata and Izumi (32) have recently analysed the mechanism of microcrack ('ledge') formation at grain boundaries in an Al-6%Zn-2.5%Mg alloy and concluded that propagation of such cracks should lead to the separation of the grain boundary itself. Furthermore their observations indicated that ledges in underaged material (such as that in stage 2) have sharp edges. These are developed as a consequence of the planar slip which occurs in underaged Al-Zn-Mg alloys.

The basic assumption at this point is that the dissolved hydrogen in the grain boundary encourages the propagation of the crack initiated at small strains. Since planar slip also occurs in dry samples but no brittle fracture is observed this demands the reduction of the grain boundary matrix cohesive strength (as postulated by a number of workers previously (42)). Assuming that the Griffith equation is satisfied: i.e. when the surface or cohesive energy of the boundary γ_b is reduced sufficiently the crack will grow spontaneously from the crack nucleus generated by slip:

$$\sigma_F^{INT} = \left(\frac{2E\gamma_b}{\pi c}\right)^{\frac{1}{2}}$$

where

E = Youngs modulus

c = Crit. crack length

γ_b = grain boundary surface energy (interfacial energy).

By using this standard Griffith criterion a critical fracture stress σ_F^{INT} may be calculated for a range of values of γ_b (surface energy) and c (crack length) as shown in Figure 5.4.

The observed (constant) fracture stress in region 2 was $\sim$400 MN/m^2 and therefore a combination of c and γ_b is needed which will give a σ_F^{INT} of approximately 400 MN/m^2. If γ_b is taken as 1 J/m^2 (typical of the surface energy of many metals (171)) then the crack nucleus that needs to exist in order to give brittle failure is approximately 2 x 10^{-7} m (2000 A) (Figure 5.4.) This is much too large to be generated by slip. It can be seen from Figure 5.4. that a γ_b value of 0.1 J/m^2 would require a more reasonable value for a critical crack length of $\sim$2 x 10^{-8} m (200 A) to initiate brittle fracture. This may well be attained by a dislocation pile up at a boundary.

If the above analysis applies, then the implication is that hydrogen reduces the value of the grain boundary surface energy by one order of magnitude from that of the lattice. (The surface energy of the aluminium lattice is given as 0.840 J/m^2 (169) and the grain boundary energy will not therefore exceed this value.) This represents a reduction of $\sim$90% and may just be attainable for the case of an embrittled grain boundary. (Large reductions $\sim$50% in grain boundary surface energy have been reported by Hondros (171) due to the segregation of small amounts of bismuth at copper grain boundaries.) Inherent in this analysis is the presumption that the normal crack blunting processes are inhibited or restricted.

In a most elegant and more rigorous analysis McMahon and Vitek (172) have recently shown that the segregation of impurities to grain boundaries of a mild steel can lead to reductions in fracture toughness of the order of 95%. They have argued that γ_b is the principal variable which governs intergranular fracture toughness. It would appear, therefore, that whilst the above system is quite removed from the case under consideration presently, very large reductions in fracture energy are, in certain cases possible as a result of intergranular segregation.

In his theoretical analysis Rice (169, 170) has identified a theoretical regime of conditions that can possibly sustain a brittle "cleavage" interface separation. From these he has calculated that a

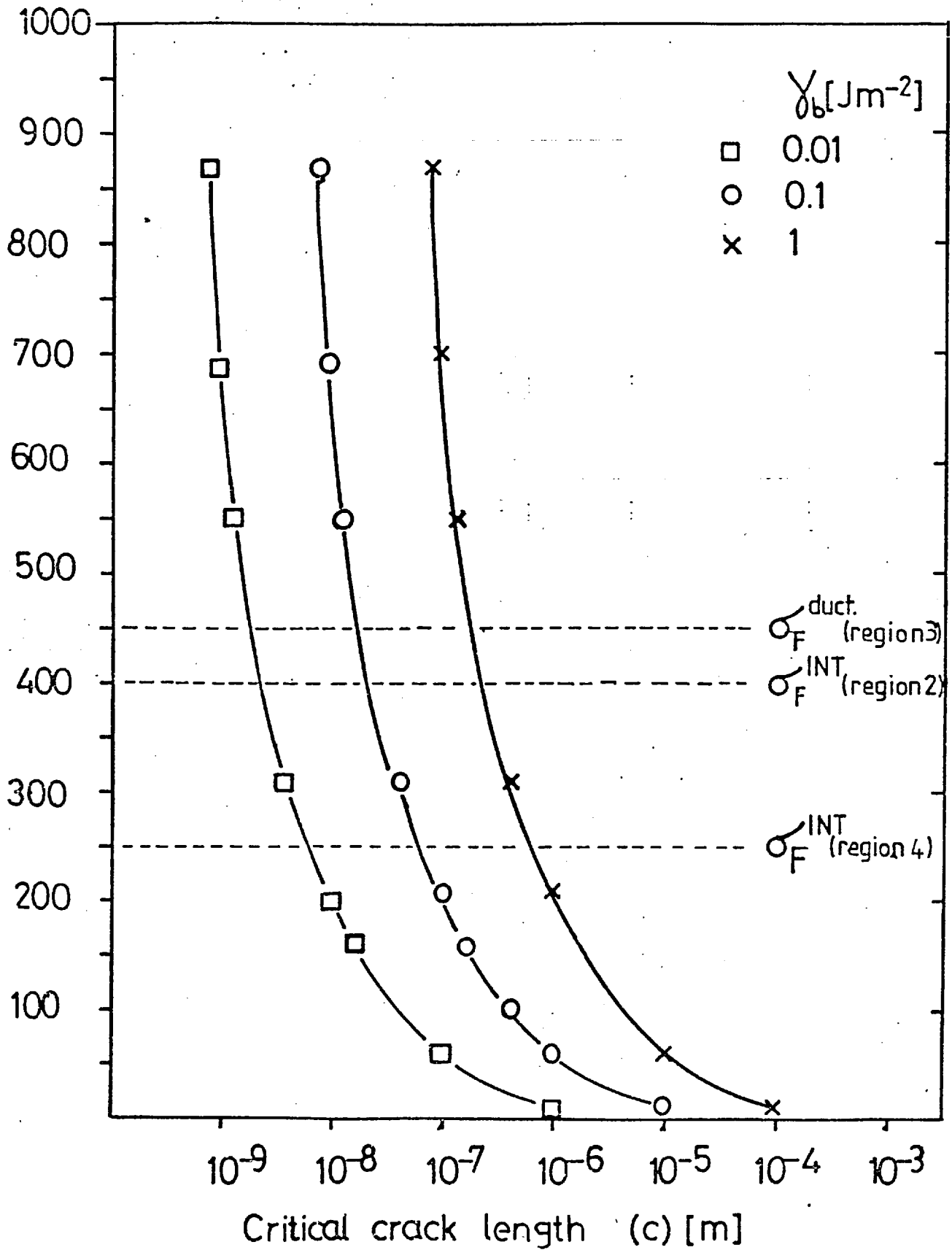


Figure 5.4. Variation of fracture stress with critical crack length for a range of values of grain boundary surface energy (γ_b). (Based on the Griffith Equation)

reduction of approximately 40% in the value of γ_b is necessary for embrittlement to occur. This value is not too dissimilar from that predicted from Figure 5.4.

It should be noted that both Rice's analysis and that given previously based on the Griffith criterion, merely establish the conditions that render a boundary capable of brittle decohesion. Fracture needs to be initiated from a sharp crack. This implies that the conditionsin region 2 must be such that a sharp crack can be established and propagate. The above discussion has shown how such conditions can be developed in the presence of hydrogen.

Accepting that the embrittlement in region 2 is caused by the penetration of hydrogen through the entire thickness of the samples then the hydrogen grain boundary diffusion coefficient at 120°C can be calculated. Using the standard $d = \sqrt{Dt}$ relationship and taking d as 0.2mm (half the thickness of the samples),and t as 10 hours (onset of region 2), the value of D is found to be $\sim 10^{-8}$ cm^2sec^{-1}. It is only slightly higher than the values quoted from other pre-exposure embrittlement work at 70°C (10^{-8} - 10^{-10} cm^2sec^{-1}) (42, 96, 154). It is in good agreement with the value calculated from the Eichenauer and Pebbler relationship (173)

$$D = 0.21 \exp(-10900/RT)$$

where R is in cal/mol and D in cm^2sec^{-1}. In contrast, the Ramsley and Talbot correlation, (174)

$$D = 1.2 \times 10^5 \exp(-33500/RT) .$$

gives a value of 10^{-14} cm^2sec^{-1}.

The discrepancy is possibly due to the fact that Ramsley and Talbot's work refers to bulk hydrogen diffusion whilst Eichenauer and Pebbler's appears to refer to grain boundary mobility.

The estimates of the hydrogen diffusion coefficient in aluminium at room temperatures given by Ells and Evans (175) and Foster, Jack and Hill (176) are $\sim 10^{-10}$ cm^2sec^{-1}. This is in good agreement with reference (173). Not unreasonably grain boundary diffusivity appears to dominate at low temperatures (167).

It should however be noted that hydrogen will, none-the-less, penetrate the interior of the grains while the metal is exposed to water vapour and although the concentration achieved at any time will be orders of magnitude lower than that at the grain boundaries it would be unwise to ignore the effect (see later discussion).

The onset of stage 3, i.e. the recovery of ductility, in Figure 4.3 is clearly associated with the onset of bubble formation (Figure 4.9). In the absence of a significant change in fracture toughness on continuing ageing at 120°C the transition to stage 3 can only be explained by a hydrogen redistribution mechanism. The redistribution is thought to occur as a result of hydrogen bubble formation at suitable nuclei. These are the grain boundary η particles which, significantly, attain a size of about 200A in diameter at the onset of stage 3. This is in excellent agreement with the observations in isochronally exposed pre-aged samples and puts on a firm footing the suggestion that a critical size of η particles is necessary for bubble formation.

Formation of bubbles involves the take up of hydrogen from solution at the grain boundaries and its deposition in a gaseous form. If nucleation occurs over a sufficiently short period, the diffusion of hydrogen down the grain boundaries will not be able to cope with the effective "loss" of hydrogen and for a short period of time the boundary will experience a sharp reduction in the concentration of dissolved hydrogen. The concentration of hydrogen in stage 2 cannot be far in excess of that required for full embrittlement since this is initially achieved after ~10 hours ageing while stage 3 begins after only about twice this time. Therefore even a relatively small reduction in the concentration of dissolved hydrogen would be sufficient to allow the alloy to revert back to its normal ductile mode of failure. This is indeed the observed behaviour.

The most intriguing aspect of failure in region 3 is the appearance of the three discrete regions of fracture:- Intergranular, transgranular cleavage and ductile (Figure 4.7).

The explanation for the outer intergranular layer may be that it is caused by intergranular corrosion during exposure as suggested by some workers (44) or due to hydrogen embrittlement. The latter hypothesis is favoured because of the previously noted absence of corrosion induced cracks and the complete recovery in ductility obtained by resolution treatment. The intergranular zone simply represents the region of highest hydrogen concentration which results from its proximity to the hydrogen source (the surface).

The existence of the transgranular cleavage in the zone adjacent to the outer intergranular periphery, suggests that the hydrogen absorbed by the matrix during exposure leads to the embrittlement of the grain interiors. Absorption of hydrogen by the aluminium matrix was

demonstrated by Gest and Troiano (51) who recorded a reversible increase in the lattice parameter of cathodically charged 7075 samples. Nelson and Pugh (49) associated the occurrence of transgranular cleavage in their samples with the existence of intragranularly held hydrogen. In this work some indirect evidence for intragranularly held hydrogen is provided by the observation of radiation damage of exposed samples with 100 KV electrons (Figure 4.12). Radiation damage phenomena will be discussed in detail subsequently, but it is important to note that aluminium does not damage following electron irradiation if bombarded with electrons accelerated through 166 KV or less (see Section 5.4). Therefore, the irradiation damage observed at 100 KV could not have been caused as a result of direct electron-aluminium collision. Wolfenden (177) has recently shown however that if aluminium is supersaturated with helium then subthreshold damage can occur via an indirect knock on event, in which an absorbed helium atom itself displaced by an incident electron, displaces an aluminium atom. A parallel is therefore drawn between Wolfenden's ideas and the present results. It is suggested that as a result of exposure hydrogen is absorbed into the matrix of the samples. During the subsequent irradiation by 100 KV electron absorbed hydrogen acts in a similar manner to that proposed by Wolfenden (177). Hydrogen atoms are displaced by high energy electrons and on collision with aluminium atoms transfer enough energy to displace the latter. In agreement with the previous work therefore (49, 51) it is proposed that it is the absorbed hydrogen that is responsible for the occurrence of the transgranular cleavage failure in region 3.

The occurrence of the three mode fracture in stage 3 is rationalised by consideration of the hydrogen concentration profiles present in both matrix and grain boundaries.

A schematic diagram showing the form of the hydrogen concentration profiles consistent with stage 2/3 behaviour is shown in Figure 5.5. The assumptions implicit in this figure are:

(i) A shallow hydrogen concentration profile at grain boundaries resulting from a high hydrogen grain boundary mobility,

(ii) A very much steeper profile of hydrogen in the matrix reflecting the significantly lower mobility of hydrogen in the grain interiors,

(iii) Much lower concentrations of hydrogen in the grain interiors than at grain boundaries resulting from the lower matrix mobility.

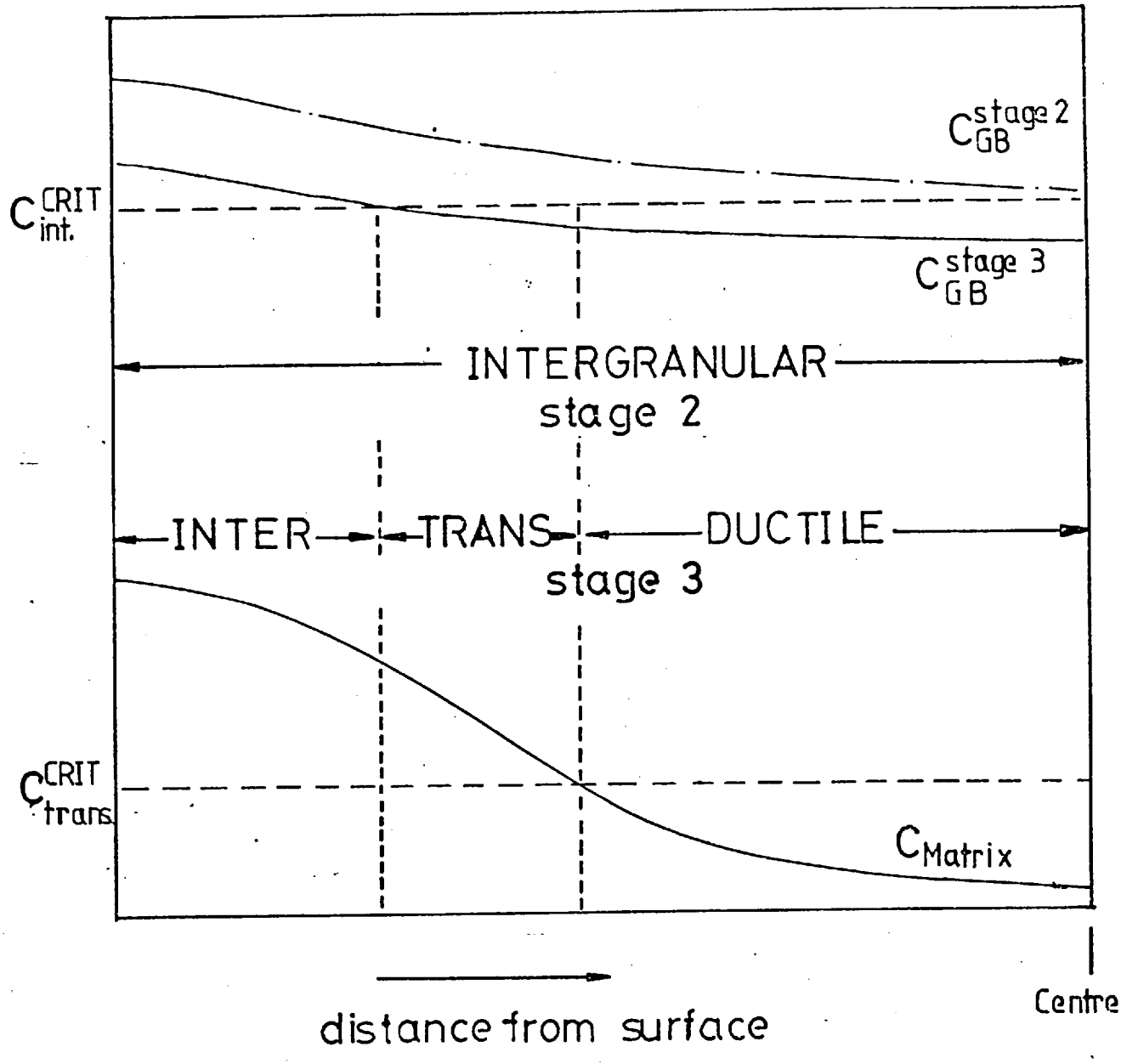


Figure 5.5. Proposed hydrogen profiles existing across the thickness of exposed samples in regions 2 and 3 of Figure 4.3.

(iv) That there exist critical concentrations of hydrogen both in the grain boundaries and matrix (C_{INT}^{CRIT} and C_{TRANS}^{CRIT}) which once exceeded will give rise to brittle intergranular decohesion and transgranular cleavage respectively.

(v) That $C_{TRANS}^{CRIT} < C_{INT}^{CRIT}$, and

(vi) That when <u>both</u> critical concentrations are exceeded $\sigma_{INT}^{F} < \sigma_{TRANS}^{F}$.

Under the conditions such as those illustrated in Figure 5.5 the concentration of hydrogen at the grain boundaries in region 2 is assumed to have exceeded the critical value C_{INT}^{CRIT} throughout the section of the sample and thus failure is purely intercrystalline (Figure 4.5).

In stage 3 the nucleation and growth of bubbles leads to a reduction in the <u>dissolved</u> hydrogen in the boundary. Since the formation of the bubbles is directly related to the attainment of a critical grain boundary particle size, then a roughly equal uptake of hydrogen into bubbles should occur throughout the sample. (Note that since the distance that the hydrogen has to diffuse in order to form a bubble is small (interprecipitate spacing) this transition should be reasonably abrupt.) In the centre of the sample therefore (where the concentration of hydrogen is already lower than the surface) it is possible that the uptake of hydrogen into the bubbles is sufficient to reduce the <u>dissolved</u> concentration below C_{INT}^{CRIT} and therefore a normal ductile intergranular failure may be expected. Away from the centre region (the exact boundary depending on the relative values of $D^{H}_{g.b}$ and D^{H}_{matrix}) a situation can develop where the concentration of hydrogen at the boundaries is still lower than C_{INT}^{CRIT} but in the matrix C_{TRANS}^{CRIT} is exceeded. (No bubble formation takes place on the smaller <u>intra</u>granular precipitates.) This results in transgranular brittle fracture.

At the periphery the concentration of hydrogen remains above C_{INT}^{CRIT} and since the stress needed for intergranular failure is lower than that for transgranular cleavage brittle intercrystalline failure occurs. Hence the observation of the three zone fracture surface.

As exposure continues hydrogen continues to be partitioned between the grain boundary bubbles, solution in the boundary and the grain interior. As the bubbles grow the strain they produce in the matrix increases as evidenced by the increase in strain field contrast and the eventual plastic deformation of the matrix (Figure 4.55).

This implies that the pressure in the bubbles is steadily increasing. This will necessarily result in an increase in the level of hydrogen in solution at the grain boundary in equilibrium with this gaseous hydrogen. Eventually the hydrogen concentration in solution will again rise to the embrittling level C_{INT}^{CRIT}. This triggers the onset of stage 4 when intergranular brittle fracture is again observed. Because of the shallow form of the grain boundary concentration profile the level of hydrogen necessary to induce brittle fracture (C_{INT}^{CRIT}) will be exceeded throughout the majority of the section of the material at approximately the same time of exposure. Hence the stage 3/4 transition will be abrupt. In contrast to region 2 fracture in region 4 takes place below the macroscopic yield stress, indicating that the fracture cracks grow from pre-existing flaws in the material (i.e. no plastic strain is needed to nucleate the crack). The grain boundary bubbles may well act as such crack nuclei and thus serve to lower the fracture stress although not being themselves directly responsible for the embrittlement phenomenon. The crater like depressions seen in Figure 4.8 result from the growth of cracks from bubbles during the tensile test.

It is important to appreciate the difference between the effect of bubbles in region 3 and 4. It has already been indicated that the low energy grain boundary decohesion event is affected by two factors. Firstly the unstable crack must be nucleated and secondly the energy criterion for the propagation of the crack must be satisfied. Therefore whilst both region 3 and 4 can be regarded as having the necessary nucleation points (bubbles/dislocation pile ups) the propagation event is only possible in region 4 where the re-established dissolved hydrogen concentration has reduced the surface energy (γ_b) sufficiently to make decohesion energetically favourable.

It is not known to what extent the pressure inside the bubbles themselves contributes to the final fracture stress in region 4, but since no "planar pressure" (168) effect was noted in region 3 it is likely that, at least, during the early times in region 4 the effect is negligible compared to the applied load. The possibility that at very long exposures to water vapour fracture occurs solely due to the pressure within a very large number of bubbles exists. Some qualitative evidence for such behaviour was obtained following exposure times in the autoclave of several months. (Cracks were observed at sharp edges and drilled grip holes.) However, it is not known to what extent any residual machining stresses were responsible for cracking in these cases.

The implications of the 3/4 transition in Figure 4.3 are that if a sample with an existing grain boundary particle dispersion of size greater than 200A is exposed to water vapour environments the development of bubbles should occur at short exposures and that embrittlement should be preceded by an incubation period during which the formation and growth of bubbles occurs trapping the hydrogen in a gaseous form. This is indeed the case. Figure 4.15 shows that samples aged dry at 150°C for 18 hours (grain boundary precipitate particle ~250A) do not become embrittled during subsequent exposure to steam for periods up to ~38 hours (the 3/4 transition time figure 4.3). Exposures in excess of this period lead to severe embrittlement with fracture occurring at or below the macroscopic yield stress. The transition is abrupt. Furthermore as predicted bubbles are formed before embrittlement (Figure 4.17).

The behaviour is consistent with the previously discussed mechanism. Grain boundary precipitates do act as beneficial traps for hydrogen by forming hydrogen bubbles and embrittlement is caused by the attainment of critical hydrogen concentration in solution.

The results in the more heavily overaged samples (92 hours at 125°) (Figure 4.14) show that within the timescale of the tests (120 hours) saturation of the boundaries does not occur and no brittle failure is encountered. The implication of this is that the large grain boundary precipitates produced (800A) are more effective trap sites. However, as pointed out earlier the growth of the grain boundary precipitates is not independent of the composition and solute profile of the adjacent matrix (P.F.Z.). Therefore, both the nucleation and growth of bubbles may be regarded as indirectly being dependent on the solute profile via the effect of this on the grain boundary particle size. (A more depleted, softer matrix will offer less resistance to the formation of hydrogen bubbles.)

5.3.3. 6/3 Cu alloy

It is well known that copper additions markedly improve the s.c.c. resistance of Al-Zn-Mg alloys (1, 2, 3, 4). The results presented in section 4.14 accurately reflect the above. They show a notable beneficial effect on the recorded ductility (elongation) of the exposed samples when compared to the 6/3 base alloy.

The degree of embrittlement incurred by the 6/3 Cu alloy following exposure is grain size dependent. (Figures 4.19 and 4.32).

Indeed the small grain size material showed no measurable loss of ductility whilst the coarser grain samples were embrittled within ~40 hours exposure. This behaviour is in line with the proposed mechanism: small grain size material will require a total amount of hydrogen to achieve the critical concentration for brittle fracture which is in excess of that needed by a large grain size sample of similar dimensions. This amount will be proportional to the total grain boundary area in any one specimen.

Examining the results from the samples of small grain size it is evident that within the time scale of the experimental observations no embrittlement was revealed. It was also clearly established that the exposure treatment had resulted in the formation of hydrogen bubbles at the grain boundaries. Of the samples examined all were found to contain hydrogen bubbles. Thus, hydrogen penetration did occur but did not cause embrittlement. This behaviour is consistent with the ideas employed to explain the insensitivity to exposure of overaged high purity alloy samples:- Bubbles are nucleated at hydrogen concentrations less than C_{INT}^{CRIT} and act as 'traps' for the absorbed hydrogen. They serve to reduce the concentration of atomic hydrogen at the grain boundaries, and to accommodate any influx on continued exposure. The excellent pre-exposure embrittlement characteristics of the copper containing alloy therefore appear to be related to the ability of the copper additions to stimulate the formation of grain boundary bubbles (see section 5.4).

A noteworthy aspect is that there did not appear to be any need for extensive grain boundary precipitation and growth to occur before the nucleation of hydrogen bubbles.

The occurrence of transgranular cleavage fracture in the exposed alloys indicates that whilst the grain boundaries are not embrittled, C_{TRANS}^{CRIT} has been exceeded within the matrix close to the surface. This situation is analogous to stage 3 of the 6/3 base alloy exposed at 120°C: Hydrogen generated at the surface diffuses into the alloy along both grain boundaries and matrix. However, as a consequence of the enhanced hydrogen bubble formation at the grain boundaries the concentration of dissolved hydrogen remains below C_{INT}^{CRIT}. In the matrix no such trapping is possible and after approximately 20 hours the hydrogen concentration exceeds C_{TRANS}^{CRIT}. On the subsequent application of stress the embrittled outer grains fail by transgranular cleavage. The restriction of the transgranular cleavage zone to the surface regions reflects the low mobility of hydrogen through the matrix: only those regions close to the surface can be supplied with sufficient hydrogen by lattice diffusion.

The consequence of this is that only a small fraction of the sample is embrittled and thus no loss in overall ductility is recorded.

The confinement of cleavage fracture over a range of heat treatments (20-90 hours at 120°C) which may be expected to undergo planar slip, suggests some hydrogen interference with localised deformation processes. For instance, planar slip may be important in the initiation step of the fracture as outlined previously or there may be some other direct hydrogen/dislocation interaction which restricts dislocation glide. No evidence were obtained in this work that can distinguish between the above. However, the presence of a multitude of subcritical crystallographic surface cracks points to a hydrogen/dislocation interaction away from the crack initiation step.

The results from the large grain size samples are in line with those that may be expected from a high purity base alloy containing trap sites, i.e. one that forms bubbles from the onset of exposure. Embrittlement is exhibited after a period of relative insensitivity to water vapour exposure. This period extends over about 40 hours which is in agreement with the 3/4 transus (Figure 4.3) and the behaviour of aged 6/3 base alloy samples containing grain boundary particles of 250A diameter (Figure 4.15). Whilst the almost exact correlation on the onset of embrittlement is quite possibly fortuitous, the form of the behaviour is important and it is a very good indication in support of the proposed mechanism. It shows that copper additions stimulate the formation of hydrogen bubbles which act as relatively innocuous sites for hydrogen accumulation. Embrittlement is only achieved after the pressure inside the existing bubbles rises to a value which is in equilibrium with a dissolved hydrogen concentration of C_{INT}^{CRIT}. Once this is attained in the boundary brittle fracture occurs.

5.3.4. 6/3 Cr alloy

The mechanical tests on exposed 6/3 Cr alloy samples showed no evidence of embrittlement if tested at a strain rate of $10^{-3}s^{-1}$, normally employed in this work. However, loss of ductility was noted at lower strain rates. Such behaviour is similar to that reported by Hardie et al (96) and appears to be only exhibited by small grain size material (10-30μm).

As indicated previously it is not possible to explain such strain rate sensitivity by an intergranular dissolution/pitting mechanism.

Refuge must be taken under a hydrogen embrittlement phenomenon. In terms of an embrittlement mechanism such strain rate sensitivity is indicative of a mobile embrittling agent. This implies that there exists a need to transport hydrogen during the fracture process itself which is consistent with the suggestion that there is a concentration profile across the thickness of the samples. It appears that the level of hydrogen present in the boundary at the onset of the tensile test is below C_{INT}^{CRIT} and that hydrogen is preferentially accumulated ahead of the crack tip during straining. Under this 'stress induced' solubility the critical concentration is achieved locally and low energy intergranular decohesion occurs. This concept is based on the proposals made by Troiano (91) and is in agreement with the results presented by Green (82) (Section 2.6.1.).

The absence of any strain rate sensitivity in the 6/3 base alloy arises as a consequence of the large grain size of that particular alloy. The total grain boundary area that need to be covered by the diffusing hydrogen in that case is significantly lower than in the 6/3 Cr alloy (grain size $\sim$20μm). In the small grain size material the level of hydrogen remains low and a "stress induced" enrichment is necessary to achieve C_{INT}^{CRIT}.

Two direct effects of the Cr addition could be responsible for the insensitivity of the 6/3 Cr to expsure. Firstly, it may arise as a consequence of a reduced rate of entry, or some internal "trapping" enhancement similar to that exhibited by the 6/3 Cu alloy.

The electron metallographic results were consistent in pointing out a surface reaction modification by the Cr additions rather than any internal microstructural effect. Of the C.T.E.M. examinations carried out on bulk samples none showed hydrogen bubbles even though it was evident that a significant amount of surface reaction had taken place. There were good indications that the hydroxide phase on the Cr bearing alloy was morphologically different from those found on the rest of the exposed alloys examined. The detailed examination of the phases present is beyond the scope of this discussion and it is simply pointed out here that even a small amount of Cr (0.14%) is sufficient to induce a change in the surface reaction. The effect of this step on an overall hydrogen assisted fracture is important in that it can influence the hydrogen production or adsorption/absorption events at the sample surface (Figure 5.1).

The "in-situ" experiments give direct evidence in support of such a proposal (see Section 5.4). The literature is in agreement also. An inhibition of the entry of hydrogen in aluminium by metals of high hydrogen overpotential including chromium has been noted by Cochran (138) (section 2.7.2.) and Gruhl (58) has pointed out a direct beneficial effect of Cr additions to S.C.C. which is not related to the precipitate reaction.

It is proposed that, in common with the other alloys, copious quantities of hydrogen are produced at the metal/oxide interface. However, hydrogen is preferentially partitioned to the gas phase, i.e. K_4 is very large (Figure 5.1), so that little hydrogen is absorbed into the alloy: Cr catalyses the recombination of adsorbed hydrogen and this restricts hydrogen entry into the metal substrate. Any absorbed hydrogen is mainly confined to the outer regions of the sample and on straining at a fast rate the crack quickly advances out of the hydrogen affected area. No embrittlement is therefore recorded. At slower strain rates hydrogen transport to the crack tip during straining maintains a high hydrogen concentration which induces a brittle fracture event. Such hydrogen diffusion may be driven under a concentration gradient induced by an increased solubility at the crack tip (Troiano (91)) or via a dislocation transport phenomenon.

5.3.5. Cathodic charging

Limited cathodic charging experiments were carried out as an alternative method of introducing hydrogen into the samples. Insofar as the recorded elongation values were concerned there was a significant reduction in ductility. However, it was not clearly established to what extent alkaline attack was responsible for the reduction in the recorded elongation values, and thus great care is needed in the interpretation of the observed behaviour. Nevertheless the results are considered significant and in support of the proposed mechanism, as the embrittlement was partly reversible and thus can only be ascribed to hydrogen. These experiments establish the proposal that once hydrogen is introduced into the alloys it has an adverse effect on the ductility.

5.4. "In-situ" Experiments

Various aspects of this work need to be discussed in detail prior to the discussion of the experimental results and their implications. In particular the contribution and the effects, if any, of radiation damage processes on the reaction must be assessed before any results/ conclusions are related to bulk behaviour.

5.4.1. Displacement damage

It has already been indicated that electron irradiation of materials above a critical accelerating voltage leads to displacement damage. This involves the 'head on' collision between incident electrons and atoms. As a result of such collisions it is possible for an electron to transfer enough energy to displace a metal atom into a distant interstitial position, giving rise to an interstitial-vacancy pair. (An interstitial atom on a local site will quickly recombine with the vacancy.) The energy required for such an event is a function of the atomic mass of the atoms, the crystal structure and its orientation to the electron beam (158). In the case of aluminium a threshold value for displacement, Td, has been estimated at 16 eV (158, 178).

The maximum energy that can be transferred by a moving electron of energy E is given by (179)

$$E_{max} = \frac{2E(E + 2mc^2)}{Mc^2} \qquad (1)$$

where

M = mass of (aluminium) atom
m = mass of electron
c = velocity of light

At 500 KV the value of E_{max} is ~40 eV (5). Thus the possibility exists for two atom displacements to occur as a result of a single electron collision.

The displacement rate, K, is given by

$$K = \phi\sigma\, Nd \qquad (2)$$

where ϕ = electron flux (electrons cm^{-2})
σ = atomic displacement cross section (cm^2)
and Nd = the number of displaced atoms per primary knock on.

The atomic displacement cross section σ is a function of incident electron energy and can be calculated from the McKinley-Feshbach formula (180). For aluminium irradiated with 500 KV electrons, the value of σ is $\sim 40 \times 10^{-28}$ m^{-2}.

Assuming that Nd = 2, i.e. on average every electron displaces two atoms, and using the measured electron flux density the average displacement rate is found to be $\sim 2 \times 10^{-4}$ displacements per atom per second (d.p.a./sec). This implies that every atom would be displaced once every 5×10^{3} seconds. Duration of a typical experiment was about 600 seconds, therefore one atom in every eight could have been displaced in the course of a single run.

The actual rates of the defect concentration build up however dV/dt, di/dt are given by (181)

$$\frac{dV}{dt} = K - K_V V - \nu_i Z(V + V_o)_i \qquad \text{(for vacancies)} \qquad (3)$$

and

$$\frac{di}{dt} = K - K_i\, i - \nu_i Z (V + V_o)_i \qquad \text{(for interstitials)} \qquad (4)$$

where the terms

$K_V V$, $K_i\, i$ represent respectively the loss of vacancies and interstitials to sinks such as grain boundaries and free surfaces.

$\gamma_i\, Z(V + V_o)i$ represents the loss of defects by mutual recombination.

V, i are respectively the vacancy and interstitial concentrations produced by irradiation, V_o is the thermal equilibrium concentration of vacancies and Z is the number of sites around a defect from which recombination can occur spontaneously. (Z was originally assumed to be unity (182) but later evidence suggests that in copper $Z \sim 100$ (9). No data are available for aluminium but Sharp (181) suggests that for close packed structures in general $Z > 1$ and possibly close to 100.)

K_V and K_i are the proportionality constants for loss of defects to sinks and depend on the jump frequency, jump distance and density of fixed sinks. (Constant for any given material at a fixed temperature.)

The thermal equilibrium concentration of vacancies at any temperature V_o, is given by

$$V_o = \exp\left(\frac{S_V^F}{K}\right) \exp\left(\frac{-E_V^F}{KT}\right) \qquad (5)$$

where K = Boltzman constant

S_V^F = formation entropy

E_V^F = formation energy

(A corresponding expression applies to interstitials)

The entropy term $\exp\left(\frac{S_v^F}{K}\right)$ is ~ 1 (182) whilst the values of E_v^F and E_i^F are given as 0.65 eV and 4 eV respectively (183). Substituting these values into equation (5) the fractional equilibrium concentrations of vacancies and interstitials can be found. (10^{-9} vacancies and 10^{-74} interstitials at 273K) In contrast the concentration of irradiation defects calculated from the previously given displacement rate and assuming 90% loss by recombination is of the order of 10^{-1}. Clearly, therefore, the concentration of irradiation defects in the alloys is significantly greater than the thermal equilibrium value. The effect of this artificial concentration of defects on the reaction observed in the in-situ experiments will be discussed presently. It has been shown (181) that at low temperatures in aluminium mutual recombination is the dominant annihilation process and few defects go to fixed sinks. Of the remaining defects the interstitials are the most mobile and are responsible for the occurrence of dislocation loops. These constitute the visible defects in the electron microscope (184, 185, 186).

The arrival of interstitials at the foil surface (metal/oxide interface) is unlikely to have a significant effect on the surface reaction that occurs between the samples and water vapour. This is because the rate determining step in the oxidation of aluminium is the diffusion of the relevant reaching species through the oxide film. Thus any radiation enhanced diffusion in the metal is of little significance to the surface reaction.

Next, the effect of the radiation produced defects on the internal bubble formation must be examined. At low temperatures vacancy agglomeration resulting in void formation is not observed in aluminium even if the metal is pre-injected with helium (177, 187), or bombarded by α-particles (188). This implies that the growth of hydrogen bubbles at grain boundaries in the in-situ experiments is not caused by vacancy condensation. Furthermore the local deformation of the metal observed to occur during the growth of the bubbles suggests that these are internally pressurised as opposed to being voids. It is proposed that they form as a result of hydrogen, generated by the surface reaction, diffusing away from the surface down the grain boundaries. As such they are not irradiation induced artifacts.

It is interesting to examine the effect of the excess vacancy concentration on the solubility and mobility of hydrogen in the matrix. It has been shown that it is energetically favourable for a proton to become associated with a vacancy in aluminium (189, 190, 191).

During the in-situ experiments therefore the possibility exists for hydrogen to be trapped at the irradiation produced vacancies. This implies that a supersaturation in intragranular hydrogen could be achieved which is in excess of that in pre-exposed but non irradiated material. Any vacancies migrating to the grain boundaries could transport hydrogen to these sites but, as outlined earlier, vacancy mobility is low under the experimental conditions (184) and is further reduced by the association with hydrogen (191). The maximum diffusion distance achieved over a time period of 10^3 seconds in an aluminium sample irradiated at room temperature at an electron flux density of 10^{-5} d.p.a./sec. has been estimated at only 10A (181). The contribution of this form of transport to the build up of hydrogen and subsequent bubble formation at the grain boundaries is therefore likely to be negligible compared to grain boundary diffusion

In summary, it can be concluded that the reaction between the experimental alloys and water vapour in the environmental cell should not be significantly affected by displacement damage processes in the metal. Direct confirmation of this conclusion is provided by the insensitivity of the reaction to changes in accelerating voltage. The reaction occurs below the threshold potential for displacement damage.

5.4.2. Irradiation induced temperature rise

For each point defect created there are many atoms that acquire insufficient energy for displacement but are nevertheless excited as a result of collisions, either direct or indirect,with high energy electrons. The energy transfer as a result of these processes is manifested as heat. A temperature rise is therefore a basic consequence of irradiation and may be regarded as a form of damage (192).

The work of Makin (163) has shown that the temperature rise as a result of direct electron beam heating in a metallic specimen is very small (less than 1K) whilst indirect heating by radiation from the objective aperture constitutes the major contribution to any temperature rise. Fukamachi and Kikuchi (162) using electron flux densities comparable to those in this work, were unable to detect any temperature rise and concluded that the temperature increase in the irradiated area of an aluminium sample was less than 10K (their estimate of experimental error).

On the basis of the above the temperature rise as a result of direct beam heating in the present experiments is estimated as being negligible and is assumed to have no effect on the reaction.

Two experimental observations support the above conclusion. Firstly the variation of reaction kinetics with varying stage temperature shows that the sample was sensitive to the stage temperature and thus any temperature rise due to beam heating must have been small. Furthermore radiant heating from the objective aperture cannot be the cause of the preferential reaction since the reaction area was limited precisely to the area under the electron beam. Whilst radiant heating from the aperture would also be localised (determined by the dimensions of the aperture and its proximity to the sample) the heated area arising from such a source would be larger than the observed reaction area.

5.4.3. Helium injection

In principle it is possible for helium gas injection to occur in this work if the atoms are knocked on by electrons with sufficient energy to produce displacements in the target material. This can lead to surface blistering (193).

Flower (156) has shown convincingly that electron irradiation of silicon, aluminium and magnesium under a helium atmosphere in an H.V.E.M. does not result in detectable gas implantation. That work is directly related to the present examination and reference may be made to it for a detailed discussion. It is considered sufficient here to simply echo the conclusion of the above work: gas injection by displacement events cannot play a significant role in the observed reaction.

A second helium gas effect is theoretically possible. This involves the displacement of atoms via a fast moving helium atom accelerated as a result of electron helium collision. Such displacements can occur below the electron/target atom threshold voltage because of an increased energy transfer process (156, 187), determined by the ratio $4M^2/(M+m)^2$ where M is the atomic weight of the target and m the atomic weight of gas.

The calculated displacement rate as a result of this mechanism at 100 KV is $\sim 10^{-6}$ displacements per second at the highest flux densities used and an order of magnitude lower at the standard conditions (10^{-7}). Correcting for losses by recombination (90%) the concentration of defects produced is of the order of $\sim 10^{-8}$ which approaches the thermal equilibrium concentration of vacancies. This is very low and is

considered insignificant. Support for this conclusion is furnished by Flower (156) who showed that the reaction of pure aluminium with water vapour under the electron beam was identical under both helium and argon atmospheres. Since argon atoms cannot displace aluminium atoms via the above mechanism the effect of helium-aluminium displacements must be small.

5.4.4. Ionisation damage

Ionisation is the cause of the great majority of the energy loss experienced by electrons up to 1 Mv in solid specimens. The rate of energy loss is a function of accelerating potential and decreases by a factor of 2 between 100 kV and 500 kV (194). It consists of the displacement of orbitally bound electrons. In metals the replacement of lost electrons from the localised orbitals occurs very quickly, due to the availability of electrons in the unfilled conduction band. There is thus no permanent damage in a metal.

Electronic excitations in ionic and covalently bonded systems however give rise to various forms of damage (no conduction band to provide replacement electrons). The damage manifests itself in different ways, for example it can lead to the formation of F centres in alkali halides or the degradation of long polymer molecules. Specifically in the case of alkali halides electron-hole recombination events lead to the ejection of halogen atoms into distant interstitial sites. The result of such a process is the formation of two complementary defects. An interstitial atom and a halide vacancy occupied by an electron (F centre). The study of the occurrence, behaviour and effects of such defects has become a very specialised branch of solid state physics which is discussed in detail elsewhere(195). It is of interest to note that the defects that can arise as a result of ionisation damage are not too dissimilar to those produced by direct displacement events (interstitial loops in KI (195)). Indeed in some cases ionisation damage merely represents a different energy transfer process which leads to the same effect (196).

5.4.5. Radiation damage in the oxide

In the current discussion another aspect of the overall damage phenomenon must be examined. This concerns the possibility of damage processes occurring in the oxide covering the samples.

Pells and Phillips (197, 198) have measured an apparent displacement threshold voltage for visible damage in electron irradiated single crystal α-alumina at 390 ± 10 kV. Using absorption and luminescence techniques they were able to correlate this value with the displacement threshold for direct oxygen ion displacement (energy requirement of 75 eV). In contrast to this the aluminium ion was more easily displaced at accelerating potentials above 175 ± 25 kV with an energy requirement of only 18 eV. No visible damage was apparent below 390 kV indicating that it is the agglomeration of oxygen defects that renders the damage visible. Somewhat higher energy threshold values have been reported by Arnold and Compton (199) who indicate displacement energies of 90 eV and 50 eV for oxygen and aluminium atoms respectively.

The information on the effect of ionising radiation on alumina is limited and the damage phenomena are not fully understood. Compton and Arnold (200) report no ionisation damage events in α-Al_2O_3 whilst Turner and Crawford (201) found that neutron irradiated samples were sensitive to ionising γ-radiation. Wilks (202) reports that neutron damaged alumina samples are severely damaged by 100 kV electrons, an observation shared with Hickman and Walker (203). In the latter study it is reported that 80 kV electrons did not produce appreciable damage.

The nature of the radiation induced defects in alumina are in dispute. Most authors (197, 198, 200, 204) attribute the prominent "colour centres" in irradiated alumina to aluminium ion displacement but defect clusters (205) and oxygen vacancies occupied by single electrons (F^+ centres) have also been proposed as alternative explanations.

As indicated earlier the insensitivity of the observed reaction to changes in accelerating voltage suggests that direct displacement damage in the oxide too, had little effect on the reaction with water vapour (threshold voltage for Al^{3+} interstitial production 175 kV). However, the detection of damage centres is subject to large errors and the possibility of damage existing below the detection limits must be considered. For example, the visible defects in electron microscopy are the secondary defects, i.e. the agglomerations of primary vacancies and/or interstitials. If any displaced species (produced either as a result of direct collision or ionisation processes) stay in their primary form, they will remain invisible. Furthermore absorption and luminescence techniques are insensitive to the presence of low concentrations of non clustered defects and are unlikely to detect defect concentrations of less than 10^{14} centres per cm^3 (206).

There are two other major points that make the theoretical treatment of the damage process difficult. Firstly the materials examined were alloys of substantial solute content (at least 9 wt% or primary additions together with impurity traces of other elements, see Table II). The defect structure of the oxide is of course significantly dependent on alloy content (see section 2.7.1) but in terms of radiation damage the existence of impurities in oxides appears to be a major influence (205, 211). Impurity atoms attract and stabilise defects.

The second unusual aspect of this work concerns the presence of water vapour in the environment of the irradiated material, and the subsequent hydration of the oxide. Radiolysis of water by ionising radiations gives rise to a considerable number of radicals (see for example references 207 - 210). Typically reactions take the form

$$H_2O \xrightarrow{h\nu} H_2O^+ + e^-$$
$$H_2O^+ + H_2O \rightarrow H_3O^+ + OH$$
$$OH + e \rightarrow OH^-$$

The existence and effect of these free radicals can only be speculated upon and must be considered in conjunction with other reactive groups that may be present. Such groups are likely to develop on hydration of the 'amorphous' film produced during electropolishing of the samples.

The initial stage of formation of pseudoboehmite from anhydrous Al_2O_3 involves a condensation-polymerisation mechanism (see section 2.7.3.) with the boehmitic group playing an important role:

$$(HO)_2 \{Al - OH + H_2O - Al\} (OH)_3 \rightarrow$$
$$(H_2O)_3 \qquad\qquad (H_2O)_3$$

$$(HO)_2 \{Al - OH \quad Al\} (OH)_3 + H_2O$$
$$(H_2O)_3 \qquad\qquad (H_2O)_2$$

OR

$$(HO)_2 \{Al - OH + OH - Al\} (OH)_2 \rightarrow$$
$$(H_2O)_3 \qquad\qquad (H_2O)_3$$

$$(HO)_2 \{Al - O - Al\} (OH)_2 + H_2O$$
$$(H_2O)_3 \qquad\qquad (H_2O)_3$$

The action of the electron beam on the above radicals is not known. However, the possibility exists for the Al-O or Al-OH bonds to be ionised in a similar manner to that of Si-O-Si bonds. In that case (155, 156) electronic excitation led to bond scission and increased reactivity.

Once the hydration of the oxide has been established the samples exhibit a duplex surface oxide film. This consists of a hydrated outer layer together with a thin 'amorphous' film of alumina immediately adjacent to the metal (Figure 5.3) (section 5.2).

The effect of irradiation of a system such as that depicted in Figure 5.3 is not known. A number of possible damage events can be envisaged:

(a) Scission of the cross linking hydrogen bonds in the outer pseudo-boehmite layer.

(b) Displacement of aluminium and/or oxygen ions in the pseudoboehmite layer (either by direct knock on events or ionisation).

(c) Displacement of aluminium and/or oxygen ions in the amorphous layer.

Any one of the above events is possible at 500 kV but at 100 kV event (a) is the most likely. This is because hydrogen bonding is of low strength. Furthermore the excess water in pseudoboehmite is normally held across the hydrogen bonds suggesting weak polarisation at these sites.

5.4.6. Proposed mechanism for the radiation enhanced surface reaction

It is evident from the available results presented here and elsewhere (155, 156) and the above discussion that the 'in-situ' reaction between water vapour and Al-Zn-Mg alloys is governed by radiation damage to the existing oxide film. Three stages are considered important in the process:

(a) Ionisation of water molecules at the oxide-gas interface.

(b) Ionisation damage across the Al-O bonds in the electropolished film.

(c) Hydrogen bond scission in the pseudoboehmite layer (once this is established) and/or

(d) Cationic defect production in the barrier layer oxide.

The observation of a very short incubation period prior to the initiation of the reaction is a significant one and provides an indication on the damage mechanism operating. Incubation periods at low temperatures are very long, typically 10 min at 50°C (124). The reaction under the electron beam at -40°C occurred within seconds of exposure to moist helium.

Clearly, therefore, electron irradiation enhanced the initial step of the reaction; that of hydration. Such acceleration could have been achieved by ionisation of water molecules close to the surface. An ionised radical such as H_3O^+ or OH^-, or even an 'excited' water molecule H_2O^* constitutes a more reactive species than an H_2O molecule. However, since the incubation period in bulk samples is insensitive to solution pH variations over a wide range of pH values (and consequently H_3^+O and OH^- radicals) (124) the effect cannot be simply due to ionisation of water. The accelerated hydration event must arise as a result of Al-O bond excitation, i.e. ionisation damage. The severed bond would then quickly recombine with the other ionised species (possibly H_3^+O) to give the initial hydrated oxide, i.e. the gelatinous pseudoboehmite. Provided ionisation damage in Al_2O_3 occurs close to the oxide-gas interface the damage centre need not be required to remain stable over long periods of time since the possibility of an ionised water radical being present locally must be high (high electron flux density). A very short lifetime defect would certainly not be detectable by conventional electron microscopy and is quite likely to be beyond the detection limits of absorption techniques. Such defects would be involved in a dynamic creation and annihilation process and would only become of significance if created in the presence of other ionised species. This conjecture is supported by the reports in the literature which state that α-alumina was only sensitive to ionising radiation if it were previously bombarded with high energy neutrons (202, 203, 205). In other words the samples already contained ionic defects which could interact with the dynamically produced damage events of the subsequent ionisation process. Further support is furnished by the observations in this work that electron irradiation of dry samples at 100 kV prior to exposure did not give rise to preferential reaction at the irradiated sites (see Section 4.4). This implies that any defects produced by ionisation damage were of short duration only. It is therefore proposed that the reduction in the incubation period observed arises as a result of the cooperative action of the ionisation events both in the aluminium oxide film and water molecules.

Once the hydration of the alumina is initiated it leads to the formation of boehmite. The occurrence of the cross linking hydrogen bonds in this system are known to enhance water pick up. The ionisation of these hydrogen bonds as a result of electron irradiation is likely to further accelerate the uptake of water leading to rapid reaction and

formation of gelatinous pseudobeohmite. This series of events may be depicted by a simple schematic format as shown below.

$$\xrightarrow{H_2O}$$

$$\xrightarrow{e^- + hv}$$

(i) $\quad O = Al\text{-}O\text{-}H \quad \cdots\cdots \quad H\text{-}O\text{-}Al = O$

$$\xrightarrow{H_3O^+ + e^-}$$

(ii) $\quad O = Al\text{-}O\text{-}H^* \quad + \quad H^*\text{-}O\text{-}Al = O$

(iii) $\quad O = Al\text{-}O\text{-}H\text{--}H\text{-}O\text{-}H\text{---}H\text{-}O\text{-}Al = O$

$$\xrightarrow{+H^+}$$

(The use of the above representation does not imply covalent bonding; hv represents the energy associated with the incident electron e^-; $H^* \equiv$ "excited" hydrogen ligand, $H^+ \equiv$ ejected proton, ----- $\equiv$ hydrogen bond)

The implied reaction from the above is

$$H_3O^+ + AlOOH = AlOOH.H_2O + H^+$$

$$(H^+ + e^- = H^\cdot)$$

and represents the second step in the hydration event.

The reaction can be considered as 'autocatalytic' because it results in the formation of more hydrogen bonds which can be subsequently ionised to give reactive ligands. Blistering implies that the oxide membrane is impermeable to hydrogen gas but not to protons. (The absence of any reaction product within any unbroken blisters suggests that the penetrating species does not contain oxygen, i.e. it is not H_2O, OH^-, H_3O^+) The source of protons is the water molecule which dissociates at the Al_2O_3/AlOOH interface to give rise to H^+. Possible reactions leading to such H^+ production are as shown in Figure 5.2.

$$Al^{3+} + 3AlOOH = 2Al_2O_3 + 3H^+$$

$$Al^{3+} + AlOOH + H_2O = Al_2O_3 + 3H^+$$

$$2Al^{3+} + 3H_2O = Al_2O_3 + 6H^+$$

The above reactions involve the consumption of Al^{3+} which originate from the underlying metal (Figure 5.2). The overall reaction must then depend on the transport properties of the amorphous Al_2O_3 film and involves the outward migration of Al^{3+} ions (anodic reaction) together with the inward migration of H^+ ions which are discharged by the electron

left behind in the aluminium substrate (Figure 5.2.).

The Al_2O_3 formed at interface is then quickly hydrolysed in the manner described previously and thus the reaction is not retarded by the build up of Al_2O_3 in the 'wrong' side of the interface. The implication of such a mechanism is that there should be film thickening during the growth of the blisters. This is indeed what is observed experimentally. The rapid growth of the blisters indicates that the diffusion of protons and Al^{3+} through the Al_2O_3 film must be fast.

The diffusion through this film depends on its defect structure and a modification of this by electron irradiation damage is possible.

The increased diffusion through the amorphous barrier oxide under the electron beam could be attributed to two affects; the first possible explanation is that the accelerated hydration of the outward diffusing Al^{3+} cations generates large amounts of H^+ ions which also diffuse at an accelerated rate in the opposite direction in order to maintain a charge neutrality. The second explanation involves the creation of Al^{3+} vacancies in the amorphous alumina film as a result of displacement by electrons, Such displacements would certainly occur at 500 kV but are not possible at 100 kV. Yet the reaction does not cease or show measurable changes in kinetics. Therefore, whilst a contribution from displacement damage of the aluminium ion would certainly exist in all of the experiments carried out above the threshold voltage, this does not appear to be a necessary criterion for increased reactivity. The alumina structure does in any case contain a large number of vacant aluminium sites (only 22.1/3 of the possible 32 sites per unit cell are occupied) and it may be that these are sufficient to deal with the influx of the diffusing species. A contribution is likely, however, from short duration excitation events such as those described earlier. Since these are likely to increase with decreasing accelerating potential (ionisation damage events) the reaction should not be inhibited by 100 kV electrons. This is indeed the experimental observation. No increase in the rate of reaction was recorded either, but this may well lie within the experimental error (see Section 4.3.4.).

In summary, it can be concluded that the increased reactivity of the experimental alloys with water vapour under the influence of the electron beam arises as a result of radiation damage in the oxide layer. The mechanism of damage is complex and until such time as more detailed data

become available on the damage process in oxides the proposed mechanisms must remain, at least to some degree, a matter of conjecture. Several conclusions may nevertheless be drawn from the above discussion.

1. The acceleration of the corrosion reaction is caused primarily via ionisation damage processes.

2. The simultaneous action of ionising radiation and presence of water molecules is necessary for the reaction to proceed.

3. Radiation damage processes serve only to accelerate the phenomenon. The reaction is radiation enhanced rather than radiation induced.

5.4.7. Surface reaction kinetics

The origin of the experimentally observed rate of growth of blisters is not well understood. Assuming that a very simple stress situation exists, i.e. the force on the blister wall is equal to the force acting on the oxide/metal interface at the hemispherical blister base (156) then it can be shown that

$$2\pi r d\gamma = 2\pi r^2 P$$

where r = radius of blister

d = wall thickness

γ = metal/oxide interface energy

and P = hydrogen pressure inside bubble.

From experimental results we know that

$$r^3 \alpha t$$

$$\therefore \gamma d = P\, t^{1/3}$$

If P is constant then

$$d \alpha t^{1/3}$$

By inspection of the surface reaction sequences it is easy to see that the blister wall thickness increased with time. Unfortunately measurements cannot be made with any accuracy to establish an experimental variation of blister thickness with time. Flower (156) had previously noted such an increase in blister wall thickness with time in pure aluminium. This is at variance with the behaviour of silicon which exhibits a constant thickness wall (155). Flower (156) has also argued that the growth of blisters is governed by brittle decohesion of the oxide/metal interface (section 2.9). Employing his analysis it can be shown that the pressure that may be expected within a typical surface blister is of the order of 10^2 atmospheres.

5.4.8. Deductions from the "in situ" reaction experiments

The results obtained from the "in situ" experiments provide direct evidence of hydrogen penetration into the samples following the reaction between the experimental alloys and water vapour. This observation is of fundamental importance and establishes beyond doubt the hydrogen penetration event in Al-Zn-Mg alloys in the presence of water molecules. Hydrogen embrittlement of Al-Zn-Mg alloys therefore is possible in all environments which contain water. The question is not whether hydrogen penetrates and causes embrittlement but whether there is an alternative mechanism of failure which will induce fracture at a faster rate than hydrogen.

Specifically the in-situ experiments have shown that the reaction between water vapour and the alloys to produce hydrogen is insensitive to the microstructural condition of the sample. Therefore the differences in susceptibility to embrittlement between different microstructural states do not arise as a consequence of modification of the surface reaction or the reaction rate.

There exists a slight preferential attack at the grain boundaries and second phase particles (η or T) that intersect the surface. Hydrogen is therefore produced at a site at which it can be most dangerous by penetrating along the easy diffusion paths provided by the grain interfaces. As suggested in section 5.3.1. there does not seem to be a fundamental difference in surface attack between the underaged and overaged samples that can explain the insensitivity of the overaged samples to water vapour exposure. In both cases any preferential attack should have the same effect since in both cases it is initially confined to the interfaces.

The clear evidence from the in-situ observations is that internal hydrogen bubble formation is a strong function of microstructure. In the 6/3 base alloy samples containing grain boundary precipitates above a critical size (200A) are needed to nucleate hydrogen bubbles. This is in total agreement with the bulk studies. Microstructural states of high pre-exposure embrittlement resistance (i.e. overaged samples) exhibit hydrogen bubbles on exposure in the wet cell. The resistance to embrittlement of these states can therefore be assigned to the availability of suitable sites for the uptake of the absorbed hydrogen. It is the internal redistribution of hydrogen that determines

the overall tolerance to hydrogen. Gaseous hydrogen in bubbles is relatively innocuous. (This concept has been discussed previously and thus will not be dealt with here. It is however pointed out that the previous discussion was developed with the support of the direct observations made in the H.V.E.M. These observations formed an integral part in the development of the proposed mechanism (section 5.1.).)

The direct observation of bubble growth in the H.V.E.M. have provided invaluable information on the "saturation" events responsible for the region 3/4 transition in Figure 4.3, the embrittlement behaviour of the pre-aged 6/3 base alloy (Figure 4.15), and the embrittlement of the large grain 6/3 Cu quaternary. The limit of growth of any one bubble as a result of the resistance provided by the surrounding matrix postulated previously was clearly established. After prolonged exposure the pressure within the bubbles was sufficient to cause localised deformation indicating an internal pressure approaching 10^5 atmospheres. The concentration of dissolved hydrogen in equilibrium with such pressures must be substantial.

One aspect of the internal hydrogen revealed by the "in-situ" experiments that has not been discussed previously concerns the observations of a hydrogen/dislocation interaction. Figure 4.49 shows that such an interaction does exist. A hydrogen "bubble" has obviously nucleated at the dislocation. This is a direct observation of a favourable association between hydrogen and dislocations. Whilst it was not possible to establish the behaviour of such an entity under stress the implications of such an association in the environment sensitive failure of Al-Zn-Mg are far reaching.

"Locking" of the dislocation by the hydrogen is an obvious possibility but similarly movement of the dislocation, if achieved, offers a hydrogen transport mechanism. Donovan (212) has interpreted his results of discontinuous tritium evolution from a strained, supersaturated aluminium sample, as resulting from transport of tritium by dislocations.

Gruhl (80) had previously postulated a dislocation/hydrogen transport step in his pre-exposure embrittlement tests. Certainly the present results establish that hydrogen can be associated with dislocations, but transport by dislocations is clearly not necessary for embrittlement to occur provided other diffusion paths are available to the diffusing species.

The "in-situ" experiments have been instrumental in establishing the characteristics of the quaternary alloys. They have produced evidence which show how the two alloying additions to the basic alloy modify its behaviour.

In the case of the Cu bearing alloy it was clear that bubble nucleation occurred in all the samples examined irrespective of ageing conditions. Even in the absence of grain boundary particles bubbles were formed. By employing the previously given arguments the resistance to embrittlement shown by the 6/3 Cu alloy can therefore be attributed to the ability of this alloy to nucleate and grow hydrogen bubbles so that C_{INT}^{CRIT} is only achieved under extreme exposure conditions. It is not known how copper additions induce bubble formation.

The surface reaction (blistering) events in the 6/3 Cu alloy must be treated with caution in view of the possibility of copper redeposition during specimen preparation (see Section3.5). However, assuming that the precautions taken were successful and minimised any artifacts it can be seen that there is very little difference between the base alloy and the copper containing quaternary. Slight preferential attack at the grain boundaries is similarly evident.

In contrast to the 6/3 Cu alloy the 6/3 Cr quaternary showed a marked blistering reaction which, in some cases led to complete decohesion of the oxide/hydroxide from the metal substrate. This behaviour was exclusive to the Cr containing alloy and has been attributed to the catalysis of the hydrogen recombination reaction at the metal/oxide interface giving rise to excessive H pressure capable of total decohesion of the oxide (Section 5.3.4.). Support for such a preferential partition to the gas phase in this alloy is provided by the observations that internal bubbles were only formed after prolonged irradiation under the electron beam. This suggests that only a small fraction of the generated hydrogen was absorbed by the samples (Section 5.3.4.).

5.4.9. Discussion of the straining stage "in-situ" experiments

The practical difficulties inherent in "in situ" straining experiments have already been outlined (section 3.7.6). These played an important role in limiting the amount of useful information obtained. Nevertheless some interesting results were noted: Firstly it was evident that a substantial region ahead of any transgranular crack had undergone plastic deformation (plastic zone) (Figure 4.62). Such cracks were produced

during specimen loading into the stage and thus reflect the plastic zone size that may be expected in a thin ductile specimen (plane stress conditions). In the case of environment-assisted crack growth the results of Figure 4.64 are of interest in that they show evidence of preferential attack at the crack faces. The cause of the preferential reaction is most probably oxide film thinning or breakdown. It is important to note that the observed blistering indicates hydrogen generation locally at the crack tip. The implications of such localised hydrogen generation in the case of a propagating stress corrosion crack are worthy of consideration. If failure under those conditions is governed by the same mechanism as pre-exposure embrittlement, then it is clear that a build up of hydrogen at the crack tip to induce brittle fracture would only require the diffusion of hydrogen over a short distance. Such diffusion may occur along the boundary if the crack is intergranular or may be transported by moving dislocations as suggested by some workers (213). However, since it was not possible to induce the growth of any cracks in the H.V.E.M. no conclusions can be drawn on this subject.

In cases where grain boundary cracking did occur the production of base metal evidently enhanced the subsequent reaction (Figure 4.63). The events are therefore autocatalytic. Cracking leads to bare metal which quickly reacts to produce more hydrogen which in turn can induce further cracking.

The only difference between these ideas and those of other workers on oxide film breakdown and repassivation control failure models (86-90) is that in this case the direct cause of failure is considered as being the hydrogen generation and diffusion process (cathodic reaction) in preference to the dissolution event (anodic reaction).

5.5. Extension of the Proposed Mechanism to S.C.C.

It is proposed here to rationalise some of the S.C.C. effects from the available literature on the basis of the proposed mechanism and to show that, with minor modifications, it provides a viable alternative mechanism of fracture to the dissolution control models previously advanced.

One of the most important general conclusions arrived at from the review of the literature on S.C.C. of Al-Zn-Mg alloys is that, under most conditions, it is the presence of water molecules in the environment that leads to failure. It seems fruitful therefore to establish the basic mechanism that operates in the presence of pure water and then to examine the ability of such a mechanism to explain the behaviour of the alloys in other environments.

In terms of the overall S.C.C. effects the predictions of the proposed mechanism (Section 5.1) appear to relate very well to the S.C.C. behaviour of Al-Zn-Mg based alloys. On the metallurgical side the hydrogen embrittlement and "bubble trapping" concept is in total agreement with the effect of overageing on the susceptibility of the alloys. Similarly the beneficial effect of copper additions can be rationalised in terms of the enhancement of the bubble formation characteristics in the microstructure.

The conclusion that the direct effect of chromium is one of inhibition of hydrogen entry into the alloy is, to the knowledge of the author, not in disagreement with any available literature. Gruhl (80) concluded from his work that chromium did increase the S.C.C. resistance of Al-Zn-Mg alloys but not by modification of the precipitation hardening reaction. In this respect his findings are in line with the proposed mechanism.

The important step in the S.C.C. behaviour is the effect of the localised corrosion reaction at the crack tip. The system there is complex. Aluminium dissolution does occur but also hydrogen production is achieved. Localised oxide film breakdown and subsequent dissolution at the crack tip region therefore is an important process which will determine the contribution of the anodic reaction to the overall crack growth rate.

Scully (90) has argued that a specific amount of corrosion is necessary to achieve propagation. If too much metal is lost the process

tends to pitting corrosion whilst if the repassivation rate is too fast then not enough material dissolves to cause propagation. This criterion is directly applicable to the present argument and can be readily modified and accommodated in the proposed hydrogen embrittlement mechanism: The "quantum" of corrosion necessary is the amount of hydrogen (produced by the concurrent cathodic reaction) that is needed in any one particular system in order to achieve the critical concentration of hydrogen (C_{INT}^{CRIT} or C_{TRANS}^{CRIT}) ahead of the crack tip. Once this is attained brittle fracture will occur. This demands that the propagation of the crack becomes discontinuous which is in accord with the literature (44, 51, 80). The distance over which C_{INT}^{CRIT} or C_{TRANS}^{CRIT} are attained will depend on such processes as the hydrogen mobility and any tendency for hydrogen to accumulate over a small region ahead of the crack tip. The results of Green et al (81) provide strong support for the latter suggestion, whilst the present work has shown that the generation of hydrogen occurs very close to the crack tip. Therefore the mechanics for the attainment of C_{INT}^{CRIT} locally are available.

The minor modification of the proposed mechanism necessary at this point is the introduction of the idea of an increased hydrogen concentration at the crack tip region. This has already been invoked in dealing with the strain rate sensitivity of exposed samples but it is in any case obvious that the hydrogen concentration will be highest close to the surface where the reaction with water vapour occurs (Figure 5.5). It is also immediately obvious that the crack growth process will depend greatly on the local conditions existing at the crack tip; events that promote absorption of hydrogen will favour acceleration of failure whilst hydrogen loss to the environment will be beneficial.

5.5.1. Metallurgical affects

The effects of most metallurgical parameters can be traced to their effects on the two basic steps that must be satisfied for crack growth to occur. Firstly the entry step must be achieved. Environmental variables will dominate here but as shown in this work metallurgical parameters can also have an effect (e.g. Cr additions). The second criterion that must be satisfied is the attainment of a hydrogen concentration in excess of the internal tolerance of the microstructure at any stress level. This will depend on microstructural properties such as the grain boundary surface energy (γ_b), the presence of suitable traps (e.g. precipitates) and their overall effectiveness (ability to grow

bubbles of hydrogen) and the alloy deformation characteristics, such as planar slip, which will be instrumental in the establishment of the microcrack and its subsequent propagation.

By consideration of the above two criteria it is easy to show, at least qualitatively, that the predictions of the proposed mechanism are in agreement with the majority of experimental observations. Specifically the mechanism is in agreement with the following metallurgical aspects of S.C.C.

(1) Increasing the major solute content (i.e. Zn and Mg) increases the rate of entry of hydrogen by modifying the oxide and possibly also affects the value of γ_b by segregation affects. An increase in susceptibility is therefore to be expected.

(2) The beneficial effects of minor alloying additions can be correlated to their ability to either inhibit hydrogen entry or increase the internal tolerance of the microstructure by stimulating the formation of hydrogen bubbles. In all cases a beneficial derivative can be obtained from a grain refinement effect of the quaternary addition.

(3) Heat treatment determines the size, number and density of available grain boundary precipitates which act as traps and thereby influences the stress corrosion cracking behaviour. Since crack propagation is dependent on the surface energy of the boundary however, any metallurgical effect which modifies γ_b will have a bearing on the observed behaviour. In this regard the solute content of the boundary will have an effect. The solute content (and profile) of the matrix immediately adjacent to the boundary will also determine the effectiveness of the grain boundary precipitates as traps for the embrittling hydrogen.

(4) Planar slip tendencies promote crack nucleation and also appear to be more susceptible to interference by absorbed hydrogen (the occurrence of cleavage fracture in an f.c.c. material in the presence of hydrogen suggests a dislocation/hydrogen interaction inhibiting crack blunting).

(5) Grain boundary particle dissolution is not necessary. Hydrogen production can be achieved as the corresponding cathodic reaction of the dissolution of the P.F.Z. precipitates or interprecipitate grain boundary regions. Nevertheless an enhanced dissolution reaction at the grain boundary precipitates or solute supersaturated zone will be instrumental in providing the embrittling hydrogen locally,and thus influence the S.C.C. behaviour.

5.5.2. Stress effects

The essential difference between pre-exposure embrittlement and S.C.C. is the presence, in the latter, of an applied stress. In addition to promoting fracture the induced strain enhances hydrogen production by oxide film breakdown and may induce local hydrogen accumulation.

The observed crack velocity versus crack tip intensity curves (v-k) (6) can be rationalised as follows. At very low values of k (region 1) the crack velocity increase is associated with the reduction in the amount that γ_b is required to be lowered in order to achieve σ_F. Assuming elastic conditions

$$\sigma_F = \sqrt{\frac{2E\gamma_b}{\pi c}} \qquad \text{(Griffith equation - section 5.3)}$$

and $$\sigma_{Tip} = \sigma_A \, (1 + 2\sqrt{c/\rho})$$

where ρ = radius of crack root

σ_A = applied stress

σ_{Tip} = stress at crack tip

Then at the point of fracture

$$\sigma_A = (1 + 2\sqrt{c/\rho})^{-1} \cdot \left(\frac{2E\gamma_b}{\pi c}\right)^{\frac{1}{2}}$$

Therefore the higher the applied stress the lower the reduction in γ_b necessary for brittle fracture. This explains the strong dependence of region I on metallurgical parameters which control the value of γ_b. Any increase in the value of γ_b will result in an increase in the stress needed to induce fracture.

In contrast to region I, region II (crack growth rate independent of k) is limited by the arrival of the damaging species (80) (H_2O molecules) to the crack tip which controls the production of hydrogen (section 2.6.1). It is less sensitive to metallurgical variables than region I (6). Region II therefore may be regarded as a stage of behaviour determined by the limitations on the local hydrogen generation events.

The ambiguity regarding the existence of a "$K_{I.S.S.C.}$" value is also readily accommodated by a hydrogen embrittlement mechanism. Hydrogen will be slowly absorbed into the alloy continuously until such time as the local critical concentration is achieved. Whether cracking occurs will depend on the ability of the microstructure to tolerate the presence of hydrogen , the tendency of the local hydrogen concentration to be evened out by diffusion and any blunting processes tending to reduce the stress intensity locally. Thus some alloys and microstructural

conditions may exhibit $K_{I.S.C.C.}$ whilst others not.

5.5.3. The role of oxide films

The role of the oxides in the S.C.C. behaviour of Al-Zn-Mg alloys is fundamental and has already been discussed in section 2.7.1. It was shown there that S.C.C. susceptibility can very often be correlated with the ability of the available hydrogen to enter the microstructure. Thus any processes which enhance the penetration of hydrogen through the oxide by modifying its defect structure or indeed lead to its replacement by a less protective film will be detrimental to S.C.C. resistance. Via this argument the effects of specific agents such as Cl^- on the S.C.C. behaviour of the alloys can be explained. Chlorides, bromides and iodides induce the breakdown of the protective oxide and promote the entry of hydrogen. (This necessarily implies that more aluminium dissolution occurs.) Fluoride ions on the other hand provide a more protective film, probably a fluoride modified oxide which restricts the entry of hydrogen.

5.5.4. Concluding remarks

In the above brief discussion. it has been shown how the hydrogen embrittlement (H.E.) model may be used to explain environment sensitive behaviour of Al-Zn-Mg alloys under conditions where anodic dissolution processes have been generally thought to be solely responsible for failure. In addition the H.E. proposals are capable of explaining many other observations such as those from cathodic charging and pre-exposure embrittlement tests which are fundamentally inconsistent with anodic dissolution mechanisms. That anodic dissolution occurs is not in doubt, indeed without it hydrogen production would not take place. However, in no case examined is it necessary to postulate that the anodic event is rate controlling. On the contrary the observations are most readily explained assuming that hydrogen embrittlement is the controlling step. This is true even in cases where localised anodic dissolution takes place since such events promote hydrogen generation and consequent environmental failure.

6. CONCLUSIONS AND SUGGESTIONS FOR FUTURE WORK

It has been demonstrated in this work that exposure of Al-Zn-Mg alloys to water vapour containing environments leads to the formation of hydrogen and its subsequent introduction into the alloys. It has also been shown that under particular conditions the absorbed hydrogen can lead to severe embrittlement of both grain boundaries and matrix.

The overall hydrogen embrittlement phenomenon depends on two factors. It is sensitive to the surface reaction events which govern the entry of hydrogen and to the inherent tolerance of the alloy microstructure to its presence. Modification of one or both of these factors by metallurgical, environmental or stress variables results in a change in the environment-sensitive failure characteristics of the alloys. Specifically the following conclusions have been reached:

1. As a consequence of the exposure of the alloys to water vapour hydrogen is generated at the metal/oxide interface. This leads to oxide decohesion and blistering.
2. The reaction leads to the establishment of a duplex oxide at the surface of the metal consisting of an outer layer of pseudoboehmite (AlOOH) and an inner, very thin layer of amorphous oxide. Eventually bayerite ($Al(OH)_3$) is formed.
3. Growth of the oxyhydroxide phase occurs via a co-operative process of inward diffusion of water through the outer layer and an ionic transfer process across the inner amorphous film. Outward diffusion of aluminium ions through the amorphous layer is compensated by the inward diffusion of protons.
4. Pseudoboehmite growth occurs by transformation of the oxide and not by a dissolution-precipitation process.
5. The surface reaction is enhanced by electron irradiation. Ionisation damage is responsible for the acceleration of the reaction.
6. The cooperative action of ionisation damage and water vapour is necessary for the acceleration of the reaction to occur.
7. Significant hydrogen penetration of the alloys is achieved as a result of the alloy/water reaction.
8. The amount of hydrogen introduced into the samples is affected by minor alloying elements. Specifically chromium additions reduce the amount of absorbed hydrogen by catalysing the formation of gaseous hydrogen at the interface and its subsequent evolution into the atmosphere.

9. Hydrogen is absorbed into the matrix and grain boundaries of the alloy. A hydrogen concentration profile is established in both.
10. The hydrogen profile in the grain boundaries is shallow and results from a high hydrogen grain boundary mobility. In contrast the matrix profile is steep.
11. The attainment of a critical hydrogen concentration of dissolved hydrogen in the boundaries leads to brittle intergranular failure. Similarly the attainment of a critical hydrogen concentration in the matrix leads to transgranular cleavage fracture.
12. The presence of the critical hydrogen concentration in solution at the grain boundaries causes a reduction of grain boundary surface energy of approximately 90%. It is this criterion that controls the susceptibility of the alloy to embrittlement and environment-sensitive failure.
13. Molecular hydrogen 'bubbles' are formed at the grain boundaries of exposed samples. They act as beneficial traps for the absorbed hydrogen reducing the local concentration in solution. They can however act as brittle crack nuclei in an embrittled grain boundary.
14. Formation of bubbles greatly increases the resistance of the alloys to embrittlement. Overaged alloys owe their resistance to embrittlement to the ability of the grain boundary precipitates to form hydrogen bubbles.
15. In the ternary Al-6%Zn-3%Mg and quaternary Al-6%Zn-3%Mg-0.14%Cr alloys hydrogen bubbles are formed preferentially on grain boundary particles under the experimental conditions employed.
16. An addition of 1.7% copper to the ternary alloy markedly stimulates the formation of grain boundary bubbles, even in the absence of grain boundary precipitates. This is the primary reason for the increased resistance to embrittlement by the 6/3 Cu alloy.
17. The nucleation and growth of grain boundary hydrogen bubbles is restricted by the resistance offered by the immediately adjacent matrix regions.
18. There exists a hydrogen/dislocation association. It is possible that this association leads to an interference of normal glide processes.
19. The intimate relationship between pre-exposure embrittlement and aqueous stress corrosion cracking strongly suggests that the environment-sensitive failure of Al-Zn-Mg alloys is determined by a hydrogen embrittlement mechanism. The effects of metallurgical, environmental and stress variables can be rationalised by their influence on the local hydrogen entry processes and the internal tolerance of any one system to the presence of hydrogen.

20. Finally it is concluded that "in-situ" high voltage electron metallography offers a unique technique of studying the environmental degradation and failure of Al-Zn-Mg alloys. Provided adequate account of possible atypical results is taken the technique has the potential to offer a great many insights into the environment sensitive failure of high strength aluminium alloys.

This work has identified two important aspects of the pre-exposure embrittlement characteristics of Al-Zn-Mg alloys: a hydrogen entry step and a reduction in grain boundary surface energy as a consequence of the presence of dissolved hydrogen. Extension of the above ideas to the general S.C.C. phenomenon requires clarification of a number of important points. For instance the following need to be assessed:

What are the processes that control the entry of hydrogen into Al-Zn-Mg alloys in aggressive environments and what is the role of oxides and other surface films on the hydrogen entry event?

In this respect a valuable contribution may be expected from high resolution scanning microscopy. Close examination of the surface following immersion to environments, such as those containing halides in concentrations typical of those at the crack tip, will provide important information on the events possible at the crack tip. Furthermore, combined S.E.M./S.T.E.M. studies may be used to relate surface reactions to particular sites in the underlying microstructure such as grain boundaries, second phase particles and any dislocation substructures. The same techniques may be employed to examine the role of alloying additions on the surface oxides and in particular their influence on the entry of hydrogen. Specific elements, such as nickel, known to catalyse the evolution of hydrogen from aluminium in contact with water in preference to its absorption (see section 2.7) need to be examined for a direct effect on S.C.C. behaviour and surface reaction characteristics. Similarly alloys known to be resistant to S.C.C. should be so examined to establish if their resistance is related to the surface reaction processes, or to some other inherent resistance of the microstructure.

Microanalysis techniques will provide complementary means for determining if particular reactions are governed by solute enrichment or segregation effects.

A further contribution to the understanding of the surface reaction events may be obtained from use of the environmental cell as described

in this work over an extended temperature range and alloy composition. In particular the significance of the observed rate of blister growth on the corrosion reaction and hydrogen entry needs to be assessed.

The role of stress in breaking down the surface oxide needs also to be examined. The localised effect of stress on film breakdown is experimentally difficult to establish but some information may be obtained from the employment of high resolution S.E.M. examination of the fracture surfaces of propagating stress corrosion cracks.

The second factor shown to be important in this work is the internal tolerance of the alloy microstructure to the presence of hydrogen. Here considerable work needs to be carried out in order to establish the relationship between microstructural variables and formation of hydrogen bubbles. For instance, how does the solute profile at the grain boundaries influence the nucleation and growth of hydrogen bubbles in systems where hydrogen bubble nuclei sites are available? Do there exist specific particles which provide more efficient traps than others?

One of the most important problems that must be examined is the localised effect of any absorbed hydrogen on the crack tip deformation characteristics. Thinned samples from propagating stress corrosion cracks should be examined by transmission electron microscopy and compared to those from cracks produced in inert environments. This is a study that is essential to establishing if a hydrogen embrittlement event is responsible for S.C.C. In particular, the exact dislocation hydrogen interaction must be examined. Most valuable information here may be provided by "in-situ" straining devices used in conjunction with environmental cells as described in this work. However, care must be taken to eliminate any effect by irradiation induced defects on the mobility of dislocations. This will necessarily require the employment of accelerating voltages below the threshold for displacement damage in the metal.

A technique worthy of consideration is one employing slow strain rate testing. The significance of the observed strain rate sensitivity of pre-exposure embrittlement and S.C.C. behaviour needs to be examined both in terms of oxide/repassivation considerations but also from a possible hydrogen/dislocation aspect. For instance, is this sensitivity related to hydrogen transport by dislocations or indeed dislocation pinning by hydrogen which then requires slower diffusion of hydrogen to

establish the critical concentration at the crack tip region? Crack tip foils from slow strain rate tests should be used to examine the dislocation hydrogen/interaction.

ACKNOWLEDGEMENTS

Firstly I would like to extend my warmest thanks to my supervisors, Drs. H.M. Flower and P.R. Swann, for their keen interest, encouragement and advice during the course of this work.

Many thanks to all the people in Electron Microscopy, too many to mention by name, for their friendship and for all of the great times we have had together. In particular, special thanks to Mr. R.A.H. Edwards for numerous stimulating discussions and his friendship. I am also grateful to Drs. E.P. Butler, G.M. Scamans, T.J. Baker for many valuable discussions and to Mr. G.W. Briers and Mr. J. Woodall for much technical advice.

Sincere thanks to Mrs. G. Flower for her excellent typing and to Mr. J. Rossdale for dealing so well with so many pictures.

I am indebted to all of my family for their understanding, love and encouragement. Without them it would not have been possible to complete this work.

The financial support by the European Research Office of the U.S. Army is gratefully acknowledged. I would also like to thank Professors J.G. Ball and D.W. Pashley for providing the laboratory facilities.

REFERENCES

1. D.O. Sprowls and R.H. Brown, Proc. Conf. on "Fundamental Aspects of Stress Corrosion Cracking", N.A.C.E. Columbus, Ohio, 466, 1969.

2. M.O. Speidel and M.V. Hyatt, Stress Corrosion Cracking of High Strength Aluminium Alloys in "Advances in Corrosion Science and Technology" (ed. M.G. Fontana and R.W. Staehle) Plenum Press, 2, 115, 1972.

3. I.M. Bernstein and A.W. Thompson, ibid, 7, p.235.

4. M.P. Speidel, Pre-print of ARPA Handbook on Stress Corrosion Cracking of Aluminium Alloys.

5. I.M. Bernstein and A.W. Thompson, Reviews on Coatings and Corrosion, 2, 3, 1975.

6. M.O. Speidel, Proc. NATO Conference on the "Theory of Stress Corrosion Cracking in Alloys", (Ed. J.C. Scully) 1971, p.289.

7. L.F. Mondolfo, Metallurgical Reviews Review No. 153. and "Aluminium Alloys Structure and Properties" Butterworths, London 1976.

8. J. Gjønnes and C.J. Simensen, Acta Met. 18, 881, 1970.

9. P. A. Thackery, J. Inst. Metals, 96, 228, 1968.

10. A. Kelly and R.B. Nicholson, Prog. Mat. Sci. 10 No. 3, 1963.

11. C.J. Peel, Ph.D. Thesis, University of Southampton, 1977.

12. I.J. Polmear, J. Inst. Metals, 86 113, 1957-58.

13. C.E. Lyman and J.B. Vander Sande, Met. Trans. A 7A, 1211, 1976.

14. G. Thomas and J. Nutting, J. Inst. Metals, 88,81, 1959-60.

15. J.D. Embury and R.B. Nicholson, Acta. Met. 13, 403, 1965.

16. N. Ryum, Acta Met. 17, 821, 1969.

17. J.H. Auld and S. Mck. Cousland, J. Aust. Inst. of Metals, 19, 194, 1974.

18. A.J. De Ardo and C.J. Simensen, Met. Trans. 4A, 2413, 1973.

19. N. Ryum, Z. Metallkunde, 66, 377, 1975.

20. A.J. Cornish and M.K.B. Day, J. Int. Metals, 99, 377, 1971.

21. C.J. Peel and P. Poole, RAE Technical Report TR77148, 1978.

22. P.T.N. Unwin and R.B. Nicholson, Acta Met. 17, 1379, 1969.

23. E.P. Butler and P.R. Swann, Acta Met. 24, 334, 1976.

24. P.T.N. Unwin, G.W. Lorimer and R.B. Nicholson, Acta Met. 17, 1363, 1969.

25. M.H. Jacobs and D.W. Pashley, "The Mechanism of Phase Transformation in Crystalline Solids", The Institute of Metals Monograph and Report Series No. 3, p.43, 1969.

26. G.W. Lorimer and R.B. Nicholson, ibid, p.36, 1969.

27. P. Doig, J.W. Edington and M.H. Jacobs, Phil. Mag. 31, 285, 1976.

28. P. Doig, J.W. Edington and J. Hibbert, Phil. Mag. 28, 971, 1973.

29. M.O. Speidel, "Fundamental Aspects of S.C.C." (Ed. M.G. Fontana and R.H. Staehle), N.A.C.E. Houston Texas, 1969.

30. H.A. Hall, Corrosion, 23, 173, 1967.

31. M.O. Speidel, Phys. Stat. Sol. 22, 71, 1967.

32. T. Kawabata and O. Izumi, J. Mat. Science, 14, 1071, 1979.

33. P.T.N. Unwin and G.C. Smith, J. Inst. Metals, 97, 299, 1969.

34. T. Kawabata and O. Izumi, Acta Met. 25, 505, 1977.

35. W. Gruhl, Proceedings of the Symposium on "Aluminium Alloys in the Aircraft Industry" - Turin Technology Ltd. October 1976, p.171.

36. Yoshio Baba, Trans. J.I.M. 11, 404, 1970.

37. W.F. Smith and N.J. Grant, Met. Trans. 2, 1333, 1972.

38. Yoshio Baba, Trans. J.I.M. 7, 224, 1966.

39. C. Baker and D.C. Martin, As in reference 35. p.63.

40. E. di Runo and M. Buratti, As in reference 35, p.125.

41. J.T. Vietz, K.R. Sargant and I.J. Polmear, J. Inst. Metals, 92. 327, 1963-1964.

42. L. Montgrain and P.R. Swann, Int. Conf. on Hydrogen in Metals, (ed. A.W. Thompson and I.M. Bernstein) Metals Park, Ohio, 1974, p.375.

43. W.R. Middleton and R.N. Parkins, Corrosion, 28, 88, 1972.

44. F.E. Watkinson and J.C. Scully, Corrosion Science, 12, 905, 1972.

45. W.Gruhl, Preprint of Contribution to NATO Research Evaluation Conference on the Theory of S.C.C. Ericeira, Portugal, 1971.

46. G.M. Scamans, Scripta Met. 13, 245, 1979.

47. A.J. McEvily, J.B. Clark and A.P. Bond, Trans. ASM 60, 661, 1970.

48. J.C. Scully, As in ref. 6, page 127.

49. L. Nelson and E.N. Pugh, Met. Trans. A. 6A, 1459, 1975.

50. R. Alani, Ph.D. Thesis, London University, 1976.

51. R.J. Gest and A.R. Troiano, Corrosion, 30, 274, 1974.

52. A.R.C. Westwood, C.M. Reece and M.H. Kamdar, Trans. A.S.M. 60 723, 1967.

53. J.J. Gilman, "Cleavage, Ductility and Tenacity in Crystal Fracture" John Wiley New York, 1959, p.193.

54. J.J. Burton and G. Jura, J. Phys. Chem. 71, 1937, 1967.

55. C.F. Old and P. Trevena, Metal Science 13, 591, 1979.

56. H. Nichols and W. Rostoker, Trans. ASM 56, 494, 1963.

57. P. Doig, P.E.J. Flewitt and J.W. Edington, Corrosion, 33, 27, 1977.

58. W. Gruhl, H. Cordier and D. Brungs, Metall, 26, 207, 1972.

59. I.T. Taylor and R.L. Edgar, Met. Trans. 2, 833, 1971.

60. G.M. Scamans, Private communication, October 1979.

61. J.A.S. Green and W.G. Montague, Corrosion 31, 209, 1975.

62. P.K. Pouloe, J.E. Morral and A.J. McEvily, Met. Trans. 5, 1393, 1974.

63. D.S. Thompson, B.S. Subramanya and S.A. Levy, Met. Trans. 2, 1149, 1971.

64. H. P. Van Leeuween, L. Schra and W.J. van der Vert, J. Inst. Metals, 100, 86, 1972.

65. K.G. Kent, J. Inst. Metals, 97, 127, 1969.

66. P.N. Ahler, R. De Iasi and G. Geschwind, Met. Trans. 3, 3191, 1972.

67. E.A. Starke, J. Metals, 22, 54, 1970.

68. A.J. Sedricks, J.A.S. Green and D.L. Novak, Met. Trans 1, 1815, 1970.

69. A.J. Sedricks, P.W. Slatery and E.N. Pugh, Trans. A.S.M. 62, 238, 1969.

70. D.E. Ward and G.W. Lorimer, Contribution to the 3rd Int. Conf. on "Strength of Materials", Cambridge, 1973, Institute of Metals.

71. P. Doig, and J.W. Edington, Corrosion, 31, 347, 1975.

72. A.J. De Ardo and R.D. Townsend, Met. Trans. 1, 2573, 1970.

73. W. Gruhl, Z. Metallkde, 54, 86, 1963.

74. W. Gruhl and D. Brungs, Metall. 23, 1070, 1969.

75. B. Grzemba and W. Gruhl, Metal 30, 521, 1976.

76. L. Montgrain, G.M. Scamans and P.R. Swann, Proc. 3rd Tewksbury Symposium on Fracture, University of Melbourne, June 1974, page 194.

77. G.M. Scamans, R. Alani and P.R. Swann, Corrosion Science, 16, 443, 1976.

78. J. Albrecht, B.J. McTiernan, I.M. Bernstein and A.W. Thompson, Scripta Met. 11, 893, 1977.

79. R.M. Pelloux and J.A. Van den Ayvle, as in ref. 42, p.275.

80. W. Gruhl, Preprint of Contribution to NATO Research Evaluation Conference on "The Theory of Stress Corrosion Cracking in Alloys", (Ed. J.C. Scully) Ericeira Portugal, February 1971, Working Material Vol. 1.

81. M.V. Hyatt, Corrosion, 26, 487, 1970.

82. J.A.S. Green, H.W. Hayden and W.G. Montague, Int. Conf on "H effects in metals" (Ed A.W. Thompson and I.M. Bernstein) Moran Wyoming 1975, A.I.M.E. page 200.

83. J.R. Rice, Contribution to the Int. Conf. on S.C.C. and Hydrogen Embrittlement of Iron Base Alloys Firmini, France, June 1973.

84. W.B. Hilling and R.J. Charles, "High Strength Materials" John Wiley, New York, 1965.

85. M.G. Creager and P.C. Paris, Int. J. Fracture Mechanisms, 3, 247, 1967.

86. T.P. Hoar, As in ref. 1, page 98, 1969.

87. H.L. Logan, "The Stress Corrosion of Metals", John Wiley New York, 1966.

88. D.A. Vermilyea, J. Electrochem. Soc. 119, 405, 1972.

89. T.P. Hoar and F.P. Ford, J. Electrochem. Soc. 120, 1013, 1973.

90. J.C. Scully, Corrosion Science, 7, 197, 1967.

91. A.R. Troiano, Trans. ASM, 52, 54, 1960.

92. R.A. Oriani, Beriche der Bunsengen fur Phys. Chem. 76, 848, 1972.

93. R.A. Oriani and P.H. Josephic, Acta Met. 22, 1065, 1974.

94. R.N. Parkins, "Stress Corrosion Cracking - The slow strain rate technique" ASTM STP 665 (Eds. G.M. Vgiansky and J.H. Payer) page 5 1979.

95. G.M. Ugiansky, C.E. Johnson, D.S. Thompson and E.H. Gillespie, ibid, p.254, 1979.

96. D. Hardie, N.J.H. Holroyd and R.N. Parkins, Metal Science, 13, 609, 1979.

97. H. Buhl, as in ref. 94, page 333.

98. G.M. Scamans, Private Communication, June, 1979.

99. J.C. Scully, Proc. Int. Conf. on Mechanism of Environment Sensitive Cracking of Materials, (Ed. P.R. Swann) Guildford, Surrey, 1977. p.1.

100. F. Keller, and J.D. Edwards, Metal Prog. 54, 37, 1948.

101. M.S. Hunter and P. Fowle, J. Electrochem. Soc. 103, 482, 1956.

102. L. De Brouckere, J. Inst. of Metals, LXXI, 131, 1943.

103. D. Vernon, Trans. Faraday Soc. 23, 117, 1927.

104. C. Wagner and K. Grunewald, Z. Physical Chem. 40, 455, 1938.

105. N.F. Mott, Trans. Faraday Soc. 36, 472, 1940.

106. M.J. Pryor, Oxidation of Metals, 3, 271, 1971.

107. F.P. Fehler and N.F. Mott, ibid, 3, 273, 1971.

108. S.K. Mohapatra and F.A. Kroger, J. Amer. Ceramic Soc. 60, 143, 1977.

109. D. Field, E.P. Butler and G.M. Scamans, Contribution to EMAG Conference, Sept. 1979.

110. A.J. Brock and M.A. Heine, J. Electrochem. Soc. 119, 1124, 1974.

111. R. Eborral and C.E. Ransley, J. Inst. Metals, LXXI, 525, 1945.

112. A.F. Beck et al, Corrosion Science, 2, 133, 1962.

113. M.A. Heine, D.S. Kier and M.J. Pryor, J. Electrochem. Soc. 112, 24, 1965.

114. M.A. Heine and M.J. Pryor, J. Electrochem. Soc. 110, 1205, 1963.

115. T. Vallant and G. Nilson, Cor. Science, 17, 449, 1977.

116. H. Kaesche, Corrosion-Traitements, Protection, Finition 17 389, 1969.

117. F.H. Haynie and S.J. Kelcham, Corrosion 19, 4031, 1963.

118. I.L. Rosenfeld and I.K. Marshakov, Zh. Fiz. Khim. 31, 2328, 1957.

119. B.F. Brown et al, J. Electrochem. Soc. 116, 218, 1969.

120. R.A.H. Edwards, Private communication, 1979.

121. J.C. Scully, Proc. of the A.I.M.E. Conference on Environment-sensitive fracture of engineering materials, Chicago (Ed. Z.A. Foroulis) Illinois, Oct. 1977, p.71.

122. G.M. Scamans and E.P. Butler, Met. Trans. 6A, 2055, 1975.

123. A. Csanady and D. Marton, J. Mat. Sci. 14, 2289, 1979.

124. R.S. Alwitt, Oxides and Oxide Films, 4, 169, 1976.

125. W. Vedder and D.A. Vermilyea, Trans. Faraday Soc. 65, 561, 1969.

126. D. Alderof and G.C. Bye, Proc. Br. Ceramic Soc. 13, 125, 1969.

127. W.J. Bernard and J.J. Randal, J. Electrochem. Soc. 121, 1019, 1964.

128. R.S. Alwitt, J. Electrochem. Soc. 131, 1322, 1974.

129. G.M. Scamans and A.S. Rehal, J. Mat. Sci. 14, 2459, 1979.

130. J.E. Draley and W.E. Ruther, J. Electrochem. Soc. 104, 329, 1957.

131. C.N. Cochran and W.C. Sleppy, J. Electrochem. Soc. 108, 322, 1961.

132. R.H. Hart and J.K. Maurin, Corrosion, 21, 222, 1965.

133. P.E. Blackburn and E.A. Gulbransen, J. Electrochem. Soc. 107, 944, 1960.

134. J.Y. Boos and C. Goux, Contribution to U.R. Evans Conf. on Corrosion, Williamsburg, Virginia, 1971.

135. H. Coriou et al, Proc. Sec. Geneva. Conf. 5, 128, 1958.

136. H. Leidheiser and N. Das, J. Electrochem. Soc. 132, 640, 1975.

137. F. Winter and W. Gruhl, Contribution to D.G.H. Symposium on Heat Treatment, Bad Nauheim, Oct. 1973.

138. C.N. Cochran, J. Electrochem. Soc. 108, 317, 1961.

139. A.L. Andreev, A.F. Vyatkin and A.A. Zhukhovitskii, Russian Journal of Phys. Chem. 48, 1396, 1974.

140. J.D. Fowler, D. Chandra, T.S. Elleman, A.W. Payne and K. Verghese J. Amer. Ceramic Soc. 60, 155, 1977.

141. R. Alani and P.R. Swann, Br. Corros. Journal, 12, 80, 1977.

142. G.M. Scamans, J. Mat. Sci. 13, 27, 1978.

143. F.H. Haynie and W.K. Boyd, as in Ref. 1, p. 580.

144. B. Grzemba and W. Gruhl, Metall. 30, 521, 1976.

145. D. Hardie and T.I. Murray, As in Ref. 99, p.459.

146. J. Bergeseen, Ph.D. Thesis, University of Erlangen, Nurenberg, 1973.

147. T.F. Klimowicz and R.M. Latanision, Met. Trans. 9A, 597, 1978.

148. D.T. Powell and J.C. Scully, Corrosion, 24, 151, 1968.

149. M.O. Speidel, Int. Conf. "H in Metals", (Eds. I.M. Bernstein and A.W. Thompson) Metals Park, Ohio, 1974.

150. B.G. Ateya and H.W. Pickering, ibid. p.207.

151. A.J. Bursle and E.N. Pugh, As in Ref. 121, p.18.

152. J.P. Fidelle, Private communication, Guildford, Surrey, 1977. and A.S.T.M. Special Technical Report 543, 1974.

153. G.H. Koch, Corrosion, 35, 73, 1979.

154. G.M. Scamans and C.D.S. Tuck, As in Ref. 99, p.482.

155. H.M. Flower and P.R. Swann, Corrosion Science, 17, 305, 1977.

156. H.M. Flower, Radiation Effects, 33, 173, 1977.

157. F.J. Humphreys, Acta Met. 25, 1323, 1977.

158. M.J. Makin, "Electron Microscopy in Mat. Science" Academic Press New York, 389-461, 1971.

159. M.J. Goringe, J. Microscopie, 16, 169, 1973.

160. E.P. Butler, Rep. Prog. Phys. 42, 833, 1979.

161. H.M. Flower, N. Tighe and P.R. Swann, Proc. Third Int. Conf. on H.V.E.M. (Ed. P.R. Swann et al) 1974, p.383.

162. M. Fukamachi and T. Kikachi, Jap. J. Applied Physics 14, 587, 1975.

163. M.J. Makin, AERE Report R6957.

164. E.P. Butler, Private Communication, Sept. 1979.

165. G. Thomas, J. Inst. Metals, 1957-1958.

166. M. Ball, Private Communication, Sept. 1977.

167. P.G. Shewmon, "Diffusion in Solids" McGraw-Hill, New York, 1963.

168. H.P. Van Leeuween, Corrosion, 29, 197, 1973.

169. J.R. Rice, Proc. of Int. Conf on "H effects in Materials" (Ed. A.W. Thompson and I.M. Bernstein) Moran, Wyoming 1975, p.455.

170. J.R. Rice and R. Thomson, Phil. Mag. 29, 73, 1974.

171. E.D. Hondros and M.P. Seah, Int. Metal Review 222, p 262, 1977 and Proc. of Symposium on Precipitation processes in solids, 1976, p1.

172. C.J. McMahon Jn. and V. Vitek, Acta Met. 27, 507, 1979.

173. W. Eichennauer and A. Pebbler, Z. Metallk, 48, 373, 1957.

174. C.E. Ransley and D.E.J. Talbot, Z. Metallk, 46, 378, 1953.

175. C.E. Ells and W. Evans, Trans. Met. Soc. AIME, 227, 438, 1963.

176. L.M. Foster, J.H. Jack and W.W. Hill, Met. Trans. 1, 3117, 1970.

177. A. Wolfenden, "Radiation Effects", 21, 197, 1974.

178. G.W. Iseler, H.I. Dawson, A.S. Mehner and J.W. Kauffman, Phys. Rev. 146, 468, 1966.

179. G.H. Kinchin and R.S. Pease, Reports on Progress in Physics, 18, 1, 1955.

180. W.A. McKinley and H. Feshbach, Phys. Rev. 74, 1759, 1948.

181. J.V. Sharp, AERE Report No. R6267, 1969.

182. G.J. Dienes and A.C. Damask, J. Appl. Physics, 29, 1713, 1958.

183. A. Seeger, H. Mehrer, ibid, p.1.

184. M.J. Makin, Phil. Mag. 18, 637, 1968.

185. M. Kiritani, N. Yoshida and H. Takada, J. Phys. Soc. (Japan) 36, 720, 1974.

186. W.J. Yang, R.A. Dodd and G.L. Kulcinski, J. of Nuclear Mat. 64, 157, 1977.

187. A. Wolfenden, Micron, 4, 295, 1973.

188. C.J. Beerers and R.S. Nilson, Phil. Mag. 8, 1189, 1963.

189. N.H. March, J. of Nuclear Mat. 69-70, 490, 1978.

190. J.P. Bugeat, A.C. Chami and E. Ligeon, Phys. Lett. 58A, 127, 1976.

191. Z.D. Popovic and M.J. Scott, Phys. Rev. Lett. 33, 1164, 1973.

192. D.I.R. Norris, Electron Microscopy in Mat. Science, (Ed. E. Ruedl and V. Valdre) Part III, Commission of the European Communities 1975, Luxemburg p.1101.

193. D.J. Mazey, B.L. Eyre, J.H. Evans, S.K. Erents and G.M. McCracken, J. Nuclear Mat. 64, 145, 1977.

194. M.J. Makin and J.V. Sharp, AERE Report, 5570 1967.

195. L.W. Hobbs, A.E. Hughes and D. Dooley, Proc. Royal Soc. London, A332, 167, 1973.

196. L.T. Chadderton, "Radiation Damage in Crystals", Methuen & Co. London, 1965.

197. G.P. Pells and D.C. Phillips, J. Nuclear Mat. 80, 207, 1979.

198. G.P. Pells and D.C. Phillips, J. Nuclear Mat. 80, 215, 1979.

199. G.W. Arnold and W.D. Compton, Phys. Rev. Lett. 4, 66, 1960.

200. W.D. Compton and G.W. Arnold, Disc. Faraday Soc. 31, 130, 1961.

201. T.J. Turner and J.H. Crawford, Phys. Rev. B. 13B, 1735, 1976.

202. R.S. Wilks, J. Nucl. Mat. 26, 137, 1968.

203. B.S. Hickman and D.G. Walker, J. Mat. Sci. 18, 197, 1966.

204. E.W.J. Mitchell, J.D. Rigden and P.W. Townsend, Phil. Mag. 5, 1013, 1960.

205. P.W. Levy, Disc. Faraday Soc. 31, 118, 1961.

206. G.P. Pells, Private communication, October 1979.

207. P. Ausloos (Editor) Fundamental Processes in Radiation Chemistry, Interscience, J. Wiley, New York, 1968.

208. J.W. Spinks and R.J. Woods, "Introduction to Radiation Chemistry" 2nd Ed. 1976, John Wiley, New York.

209. G. Stein, 19th Farkas Memorial Symposium, 27-29 Dec. 1967, p.83, Jerusalem, Israel (Ed. G. Stein, Interscience - Wiley).

210. M. Anbar and D. Meyerstein, ibid, p.109.

211. M.O. Henry, J.P. Larkin and G.F. Imbusch, Phys. Rev. B, 13B, 1893, 1976.

212. J.A. Donovan, Met. Trans. 7A, 1677, 1976.

213. J.K. Tien, As in ref. 82, p.309.

214. N.J. Petch and P. Stables, Nature, 169, 824, 1952.